Technische Universität München
TUM School of Engineering and Design

Numerical and Experimental Structural Beam Analysis for the Development of Helicopter Rotor Blades

Tobias Pflumm

Vollständiger Abdruck der von der TUM School of Engineering and Design der Technischen Universität München zur Erlangung eines

Doktor der Ingenieurwissenschaften (Dr.-Ing.)

genehmigten Dissertation.

Vorsitz: Prof. Dr.-Ing. Florian Holzapfel

Prüfer*innen der Dissertation:

1. Prof. Dr.-Ing. Manfred Hajek
2. Prof. Dr. Carlo L. Bottasso

Die Dissertation wurde am 04.05.2022 bei der Technischen Universität München eingereicht und durch die TUM School of Engineering and Design am 04.10.2022 angenommen.

to my family

Acknowledgement

First and foremost, I thank my wife Franziska and my son Mattis for their everlasting love and support, much needed distractions and periods of rest.

I would like to express my sincere gratitude to my advisor Prof. Dr.-Ing. Manfred Hajek for the continuous support over the last years, the research freedoms and the leap of faith in all projects but also for the certainty of backing and support.
This work would not have been possible without the countless whiteboard discussions, inspirations and joint business trips with my office colleague and friend Willem Rex. Your deep but also broad knowledge were extremely helpful. The same applies for my fellow colleagues and labmates Verena Heuschneider, Florian Berghammer, Markus Rinker, Aaron Barth and Lukas Gaugelhofer, your engineering judgement saved me from mistakes and setbacks.
I also thank Dominik Schicker for motivating me to do my research in the first place and the numerous advises in the development of SONATA. Not less important were the pleasant and friendly working atmosphere at the Institute of Helicopter Technology to which all colleagues contributed. That's why I would especially like to thank Martina Thieme for her humor, and of course for keeping the place running. Nevertheless, regularly lunchtime reunions with Felix Fischer, Svenja Schöder, Stephanie Frankl have sweetened the week also outside the helicopter sphere.

I would also like to thank, Tyler Sinotte and Prof. Olivier Bauchau for the fruitful discussions and for the motivation to persue the experimental measurements of the MERIT rotor blade. Without the large assistance of Daniel Maraite of GOM, who supported us with an ARAMIS SRX sensor and its measurements large portions of this work would not have been possible. Particular appreciation also goes to Marco Morandini of Politecnico di Milano for the altruistic advice and support with ANBA4. I would also like to thank the TUM Laboratory for Product Development and Lightweight Design and TUM Chair of Carbon Composites: with Karl-Ludwig Krämer, Bernhard Lerch, Josip Stokic, Manfred Bauer, Rainer Rauch and Thomas Witteczek for the pragmatic support over the years. Likewise, I am incredibly grateful for the milling skills and precisely manufactured tolerances of the TUM Workshop of the Physics Department and especially Manfred Pfaller and Michael Novotny.

Abstract

Beam stiffness properties of rotor blades differ from the design values due to uncertainties in the manufacturing process and varying material properties but also because the structural model of current predesign methods often has an inaccurate level of detail. This thesis contributes to the improvement of this problem by first developing the structural finite element preprocessor for slender composite structures SONATA to reduce the epistemic uncertainty of the predesign problem, with an increasing representation of the physics.
The second contribution investigates the effects and propagation of irreducible aleatory uncertainties, in the form of material and manufacturing uncertainties, on the dynamic behavior of the helicopter rotor in hover and forward flight.
The third contribution of this thesis is the application and refinement of a strain-based measurement method to experimentally determine beam stiffness properties of the MERIT rotor blade.

Kurzfassung

Balkensteifigkeitseigenschaften von Rotorblättern weichen aufgrund von Unsicherheiten im Herstellungsprozess und unterschiedlichen Materialeigenschaften von den Entwurfswerten ab, allerdings auch deshalb, weil das Strukturmodell gegenwärtiger Vorentwurfsmethoden mitunter einen ungenauen Detaillierungsgrad aufweist. Diese Arbeit trägt zur Verbesserung dieses Problems bei, indem sie zunächst den strukturellen Finite-Elemente-Preprozessor für schlanke Faserverbundstrukturen SONATA entwickelt, um die epistemische Unsicherheit des Vorentwurfsproblems mit einer verbesserten Beschreibung der Struktur zu reduzieren.
Der zweite Beitrag untersucht die Auswirkungen und die Ausbreitung nichtreduzierbarer aleatorischer Unsicherheiten, in Form von Material- und Fertigungsunsicherheiten, auf das dynamische Verhalten des Hubschrauberrotors im Schwebeflug und Vorwärtsflug.
Der dritte Beitrag dieser Arbeit ist die Anwendung und Verfeinerung einer dehnungsbasierten Messmethode zur experimentellen Bestimmung der Balkensteifigkeitseigenschaften des MERIT-Rotorblatts.

Contents

Abbreviations and Symbols

Acronyms

1D	One-dimensional
2D	Two-dimensional
3D	Three-dimensional
AMRDEC	US ARMY Research, Development and Engineering Command
ANBA	Anisotropic Beam Analysis
AREA	Autonomous Rotorcraft for Extreme Altitudes
BSplineLst	Multiple connected B-Splines
C_{TW}	SGL Carbon - SIGRAPREG® C W200 TW2/2 E503/45%
C_{UD}	SGL Carbon - SIGRAPREG® C U600-0/SD-E501/33%
CAD	Computer Aided Design
CAMRAD II	Comprehensive Analytical Model of Rotorcraft Aerodynamics and Dynamics II
CII	Confidence Interval
COV	Coefficient of Variation
CT	Computer Tomography
DAKOTA	Design Analysis Kit for Optimization and Terascale Applications
DIC	Digital Image Correlation
EMC	Electromagnetic compatibility

FBG	Fiber Bragg Grating
FEA	Finite Element Analysis
FFT	Fast Fourier Transform
FS	Full scale
FVC	Fiber Volume Content
HANBA	Hollow Anisotropic Beam Analysis
HART	Higher Harmonic Control Aeroacoustic Rotor Test
HT	High tenacity
ID	Identifier
IM	Intermediate Modulus
iVABS	integrated VABS environment
IXGEN	Intelligent Cross Section Generator
Lay.	Number of Plies
LC	Load-Cell
LE	Leading-edge
LHS	Latin Hypercube sampling
MCS	Monte Carlo Simulation
MDAO	Multidisciplinary Design, Analysis and Optimization
MERIT	Munich Experimental Rotor Investigation Testbed
MLE	Maximum Likelihood Estimate
NDARC	NASA Design and Analysis of RotorCraft
NDT	Non-destructive tests
No.	Number of Samples
NREL	U.S. National Renewable Energy Laboratory
PDS	Product Data Sheet
RCAS	Rotorcraft Comprehensive Analysis System
RCOTOOLS	RotorCraft Optimization Tools
rev	Revolution
RVLT	Revolutionary Vertical Lift Technology Project
S-N	Stress-Life

SC	Shear Center
SD	Standard Deviation
SF	Safety factor
sk	Skin
SONATA	Structural Optimization and Aeroelastic Analysis Framework
sp	Spar
SVD	Singular Value Decomposition
TC	Tension Center
TDS	Technical Data Sheet
TE	Trailing-edge
tr	Transition
TUM	Technical University of Munich
TW	Twill weave
UD	Unidirectional
VABS	Variational Asymptotic Beam Section Analysis
VAM	Variational Asymptotic Method

Symbols

Cw/σ	Blade Loading
E	Young's modulus
G	Shear modulus
Q	Rotor Steady Torque
T	Rotor Steady Thrust
$\mathcal{K}$	Curvature Tensor
$\underline{\underline{D}}_n$	Duplication Matrix
$\underline{\underline{K}}$	Sectional stiffness matrix
$\underline{\underline{M}}$	Sectional mass matrix
$\underline{\underline{NM}}$	Node matching matrix
$\underline{\underline{R}}_e$	Strain Rotation Matrix
$\underline{\underline{S}}$	Sectional compliance matrix
$\underline{\underline{W}}$	Warping displacements under unit loads

$\underline{\underline{Z}}$	Nodal Location Matrix
ν	Poison's ratio
$\underline{F}$	Sectional stress resultant vector
m_{00}	Sectional mass per unit span
m_{11}, m_{22}, m_{33}	Mass moment of inertia per unit span
n_s	Number of random data points
s	Curve coordinate
x_m	Mass center location
x_s	Shear center location
x_t	Tension center location
Ω	Rotor rotational speed
Ψ	Azimuth
Θ_{tw}	Twist angle
α_{crit}	Critical corner angle
α_{pb}	Principal bending axes alignment
α_{ps}	Principal axes of shear alignment
$\underline{\epsilon_c}$	Sectional strains
$\underline{\epsilon}$	Strain tensor
$\underline{\kappa}$	Curvature tensor
μ	Advance Ratio
ω	Eigenfrequencies
ρ	Density
σ	Standard Deviation
τ	Shear stress
θ_{11}	Ply orientation angle
θ_3	Material orientation angle

Sub-, and Superscripts

$()^{(i)}$	Sensor position
$()^{(j)}$	Load case
$()_{(L)}$	Local CBM frame
$()_{(m)}$	Material coordinate sysstem
$()_{(p)}$	Ply coordinate system
$()_{(r)}$	Blade reference frame

$(.)'$	Spatial derivative with respect to the spanwise variable
$(.)_{\mathcal{C}}$	Local DIC coordinate system
$(.)_{\mathcal{G}}$	Global DIC coordinate system
$(.)_e$	Local strain coordinates
$\hat{(.)}$	Nodal quantities

List of Figures

List of Tables

1 Introduction

1.1 Motivation

Since the early 1960s, the use of fiber composites has been responsible for the continuous improvement and thus the success of modern helicopter rotor systems [88].

Rotor blades were originally manufactured in wood for many years. They were designed in a similar way to aircraft wings at the time and were often a mixture of different types of wood, each with properties that the other materials lacked. The service life was enhanced with metallic erosion protection and low fatigue effects were exhibited [82]. The drawback was that they deformed under external environmental influences, causing considerable difficulties. They absorbed water, resulting in lateral unbalances and vibrations. In addition to that, manufacturing required outstanding carpentry abilities [88].
As an intermediate step towards full fiber composite rotor blades followed a time in which metal rotor blades were primarily used. However, they showed low shape flexibility in the manufacturing process and most importantly a low design life due to a high fatigue susceptibility. To counteract the sensitivity of the metals for crack propagation, in the example of the Sikorsky S-61N helicopter, the cavity of the hollow spar was filled with pressurized nitrogen, which escaped in the event of a crack occurring. Pressure gauges on each blade near the hub showed an indication during preflight checkup [172].
In contrast to that, the dynamic strength of fiber composites is very high and the stress-life (S-N) curves are correspondingly flat. Furthermore, nicks result in only slight reductions in the strength and therefore these materials are ideal for the use in dynamically loaded single load path structures such as helicopter rotor blades reducing the risk of a catastrophic failure mode [9].
Their high specific strength and stiffness combined with the possibility to manufacture complex geometric shapes make it the most favorable choice of material [5], [80]. The high elasticity and high fatigue strength made it possible to realize hingeless and bearingless rotor systems with elastic substitute hinges in the blade root reducing the total mass, the number of parts, and maintenance costs of the rotor system.

The previously not available possibility with isotropic metal constructions, to tailor certain structural couplings into the structure gained attention in recent years, as studies showed the significant impact on the aeroelastic behavior to improve performance, aeromechanical stability, and minimize vibration [21], [41].

A large number of constraints and design drivers from various disciplines make the helicopter rotor blade development process difficult, time-consuming, and costly.
Historically, the design and development of improved or entirely new rotor blades is conducted by departments in a company that maintain different simulation codes for the purpose of fulfilling their particular tasks. The aerodynamics department is responsible for performance calculations, aero-acoustics, rotor-wake interaction, unsteady airload prediction, and computational fluid dynamics while the dynamics department focuses on rotor vibratory loads, stability, and aeroelastic models [167]. The structural department determines the elastic properties as well as strength and fatigue characteristics. A Blade and Rotor Design Department often bundle the different aspects while considering materials, manufacturability, and maintainability. [167]
This modular approach narrows the scope of solutions because each department focuses on individual objectives satisfied by individual design parameters. Mutual interactions can only be covered by numerous iterations.
In contrast to that, a multidisciplinary approach offers a more systematic development process that is able to design an improved helicopter rotor [2]. Because of the impact the rotor behavior has on the overall performance of the helicopter and on customer noticeable vibratory characteristics, rotor aeroelastic effects should be considered in the earliest stages of the design process [140].
The entire design process represents a classical aeroelastic problem, where the aerodynamic behavior, structural elasticity, and vibrational dynamics have to be studied simultaneously. The behavior can therefore not be examined with separate analysis of the different disciplines [167]. Integrating all significant disciplines into the design process not only implies that they constrain the design, but also that interactions are defined and accounted for so that those disciplines influence design decisions simultaneously rather than sequentially [2].
Adelman and Mantay [2] describe in 1989 a plan for the development of an integrated multidisciplinary optimization tool that is not only considering limitations from the involved disciplines but accounting for the interactions between them and present a logical path, requirement specifications, validation, and verification procedures.
In 1991, Friedmann [49] presented a survey of multidisciplinary structural design optimization methods applied to rotor blades in order to reduce vibrations of helicopters in forward flight. Friedmann summarizes the research conducted at universities, industry, and government research institutions in the United States. He concludes that an integrated multidisciplinary optimization provides the potential for significant enhancements in vibration reduction that can be accomplished through careful preliminary design and analysis, eliminating the need for additional hardware such

as rotor vibration absorbers or isolation systems [49].
In 1998, Tarzanin [167] reviews 12 years of experience with rotor design optimizations conducted at BOEING. In his survey, he presents multiple approaches, objective functions, and design variables used to develop a rotor design framework. Besides reviewing the optimization-based rotor design process, he states future plans for development at BOEING. The primary objectives are not only to design a rotor with improved characteristics (lower weight, lower loads, less vibration, better aerodynamic performance, and longer life) but also to reduce design cycles and labor hours.
In summary, it can be said that in the last 25 years the endeavor has grown among the industry, academia, and research laboratories to improve discipline integration and mathematically-based optimization [2]. Researchers have repeatedly stated the need for a design methodology and optimization framework that combines the computational efficiency of a beam description in aeromechanic analysis with a rotor blade structural model that is capable of describing realistic composite rotor blade cross-sections with respect to the structural properties, applied load, stress and strain distributions, as well as design constraints [49], [80], [97], [173].

The current state of the art involves three main components which are handled by an optimization framework. The first of the three comprises an aeromechanical rotor analysis which includes flexible multibody dynamics, nonlinear finite elements and several distinguished rotorcraft aerodynamic models. They are often referred to as Comprehensive Analysis. Examples are the widely used *Comprehensive Analytical Model of Rotorcraft Aerodynamics and Dynamics II* (*CAMRAD II*) [76] and the software *Dymore* [12] beyond several others. Both of these codes are presently in use in the rotorcraft industry, academic institutions and government laboratories. The quality of the predictions has been documented in numerous publications.
In this context, the slender characteristic of rotor blades allows the simplification to treat it as a one-dimensional (1D) body due to the much simpler mathematical formulation and reduced computational effort compared to a full three-dimensional (3D) finite element model of the composite rotor blade [42], [175]. While the three-dimensional finite element method is the most accurate approach for realistic rotor blade simulations, it is still not suitable for the preliminary development of rotor blades [42], [94].
In 2010, Yeo [175] assessed the different modeling methods for rotor blade structural dynamics. More precisely, he compared 1D beam analysis using *RCAS* rotorcraft comprehensive analysis with *VABS* calculated 2D cross-sectional mass and stiffness properties with a 3D finite element analysis that was performed using *MSC/Marc* to show the differences of the two methods. He concludes that if the beam length is greater than ten times chord, the agreement in natural frequencies at various rotor speed between 1D beam analysis and 3D FEA is very good. As the aspect ratio decreases, especially the torsional modes start to differentiate.

The goal of beam theories is to describe the inherently three-dimensional structure as a one-dimensional model which contains only sectional quantities that depend exclusively on the spanwise variable (x_1). When modeling a rotor blade as a one-dimensional beam, it is important to ensure that the strain energy in the idealized beam is approximately the same as in an inherently three-dimensional blade. The three-dimensional state of deformations includes not only the axial, torsion, bending and shear deformations of the reference axis of the beam but also the warping deformations of the cross-section. Warping refers to the in- and out-of plane deformations of the cross-section which are much smaller than the deflections of the elastic axis. This allows the separation of the three-dimensional problem into two parts: a two-dimensional local deformation field of the cross section used to calculate the sectional properties, and a one-dimensional global deformation field to calculate the blade response. Hodges et al. [71] note that Berdichevski [18] appears to be the first in the literature to state that the geometrically nonlinear problem of three-dimensional elasticity theory for a beam can be divided into a nonlinear one-dimensional problem and a linear two-dimensional problem. The solution of the one-dimensional equations provides information about the global deflections, which, together with the local deformation field, allow the estimation of the three-dimensional stress state. [80]

In search of a beam theory that unifies all aspects of the deformation into a single system of equations and separates the three-dimensional de Saint-Venant's problem into a two-dimensional analysis over the beams cross-section and a nonlinear one-dimensional beam analysis, the developments by Berdichevski [18] known as the Variational Asymptotic Method (VAM) were refined by Atilgan [6], [7], Hodges [70], Yu [180], [182] and Cesnik [33] which lead to the development of the software *VABS* (Variational Asymptotic Beam Sectional Analysis) for the analysis of initially curved and twisted anisotropic beams.

The second category of methods to solve the de Saint-Venant's problem, i.e. the elasticity solution of a three dimensional beam loaded only at its extremities [183], follows the generalized numerical procedure first introduced by Giavotto et al. [56]. This approach is based on the superposition of the displacement field from two principal contributions, the motion of a reference section of the beam and a three-dimensional in-plane and out-of-plane warping field.
The approach results in a second-order ordinary differential equation along the beam, and according to the de Saint-Venant principle, its solution is composed of two parts: a polynomial part, which is called the "central solution", and a self-balanced exponential part, which is called the "extremal solution". Far away from load application points or support reactions of the beam, the extremity solutions decay exponentially and the central solution defines the behavior of the beam [115]. This approach led to a Fortran code *HANBA* (Hollow Anisotropic Beam Analysis) and was adopted by many research groups who developed derivatives. Among them, *NABSA* [177] and *BECAS* [22], [23]

are worth mentioning.
In 2010, Morandini et al. [115] proposed to remove the a priori assumption of a superimposed rigid section motion and warping displacement to get rid of the unknown and redundant cross-section movement to use the displacement as the only unknown of the problem. Their development led to the Python-based open-source code for ANisotropic Beam Analysis: ANBA version 4.0 (*ANBA4*) [48]. The same approach was later adopted and refined by different authors, including the work from Han and Bauchau [14], [63] which was implemented in their software *SectionBuilder*, an integral part of Dymore.

In the last 20 years, *VABS*, *ANBA* and their variations have become popular tools in rotor blade predesign and represent the second component in multidisciplinary rotor design optimizations [34], [140]. Their accuracy and efficiency has been validated in numerous publications [33], [48], [182]. While a geometric definition of a rotor blade with CAD tools is supposedly technically simple, the transfer to a finite element representation of the cross-section can prohibit automated design optimization. Consequently, most researches have developed individual parametric mesh generators for the cross-sectional analysis, that reduces their structural model to few design variables in the process. This constitutes the third and last component of the design problem.
Hu [73] also stated, that a significant impediment for using *VABS* in the industry is that the ply angle is not readily available from the mesh generator of commercial Finite Element Analysis (FEA) codes [24].

According to Li et. al. [94], the industry is not yet comfortable to use multidisciplinary optimization methods because the analysis and optimization methods struggled with the performance of predicting the behavior accurately to allow a safe and robust final design. Additionally, the current structural rotor blade models are simplified to that extend, that a result of such a design optimization is not precise enough and still has to be refined by manual iterations. Subsequently, the transition to a full three-dimensional description of the result becomes a long and iterative task once again.

The problem resides in the fact that the rotor system behavior can be very sensitive to modifications in some parameters and real problems are rarely described by a set of fixed parameters. For example, it has been reported that the coefficients of variation of the elastic moduli of a composite lamina can be 5 – 15% due to uncertainties associated with fiber and matrix material properties, fiber volume fractions, fiber orientation and undulation, intralaminar voids, etc. [121]. Murugan et al. [118] showed the effect, such aleatory uncertainties (irreducible uncertainty as it cannot be reduced through modeling techniques) can have to the aeroelastic response of the helicopter rotor and vibratory hub loads. A Monte-Carlo analysis revealed considerable deviations from baseline-predictions, with its extreme value of 600% increase of vibratory hub loads because of resonance

conditions. During the extensive studies of the HART I Rotor (Higher Harmonic Control Aeroacoustic Rotor Test), the importance of accurate beam properties became evident as Jung and his coworkers [79] noticed poor agreement between predicted and measured structural loads in both magnitudes and phases. During later laboratory testing [78], they showed a discrepancy of up to 30% for the flap bending stiffness close to the inboard blade root section compared to the predesigned values.

It can be concluded, that the actual blade differs from the designed blade due to uncertainties in the manufacturing process and material properties but also because the structural model of the current methods have to some extent an inaccurate level of detail and miss important structural components (e.g. balance and tuning masses are hardly ever captured). This is referred to as epistemic uncertainty (can be reduced by the increased knowledge or representation of the physics).

Considering these difficulties, the experimental measurement of the cross-sectional stiffness properties is required so that the uncertainties can be quantified experimentally, resulting in a more confident application of analysis and optimization methods in the future. However, this also turns out to be a substantial challenge, since no traditional experimental method is able to determine the generalized Timoshenko 6×6 stiffness properties along an anisotropic nonuniform beam such as a rotor blade [159]. In addition, many of the most common methods make assumptions about partial uniformity and are able to determine only a subset of the sectional stiffness coefficients. An overview of the most common and important experimental methods is given in section 1.3. In spite of the importance for comprehensive analysis, the publicly available stiffness properties for actual helicopter blades is limited and only a subset of the full sectional stiffness characteristics are publicly available for a few existing helicopters such as the Sikorsky UH-60 [43] and CH-34 [136] or of the HART I and II test campaign which resembles the BO-105 rotor [77], [78].

To this day, the recently presented strain based experimental methodology by Sinotte and Bauchau [159]–[161] is the most promising technique that has the potential to meet the requirements for a complete determination of the beam stiffness properties.
This hybrid method relies on the measurement of the surface strain field under six independent measured load cases and combines it with a numerically determined warping displacement field. The strain field is measured using Digital Image Correlation (DIC)- a contact-free, optical 3D deformation measurement method in order to analyze and calculate deformations.
In the demonstration and study of their novel technique, they have used prismatic aluminum and asymmetric composite beams with rectangular cross-section as well as composite beams that resemble simplified rotor blades.

1.2 Objectives

Although there is much untapped potential in the field of multidisciplinary rotor blade design and optimization, I decided for this work to dedicate myself to the improvement of the necessary building blocks of such a design task. The important and fundamental problems of beam structural analysis must be further developed and improved before meaningful numerical design methods can be used for reliable results.
This leads to my research objectives, to improve the current situation of numerical and experimental structural beam analysis for the development of helicopter rotor blades with a holistic perspective. The technical approach to accomplish this can therefore be divided into the following three tasks.

- Develop a generic structural finite element preprocessor for composite beam cross-sections (SONATA) that is able to incorporate all structurally relevant components and allows a rapid translation to a commercial CAD system, while at the same time incorporates a composite manufacturing process to avoid complex constraints and keep the solution within feasible bounds and thus makes it suitable for parametric analysis and multidisciplinary optimizations. The parametric approach, implementation of the finite element discretization as well as the solver integration is to be verified using testcases from literature.

- Study the propagation of material and manufacturing uncertainties of a rotor blade on the beam-properties, the rotating-natural frequencies, the aeroelastic response and vibratory loads in hover and forward flight. As instruments, the previously developed structural rotor blade model of SONATA and a comprehensive helicopter model are used to demonstrate that improvements in numerical and experimental structural beam analysis methods are necessary for the development of helicopter rotor blades and to answer the question whether optimization potentials are eaten up by structural uncertainties.
  Should the modeled material and manufacturing uncertainties have no effect on the rotor dynamics and vibration loads, more accurate numerical and experimental methods to determine the beam properties would be obsolete.

- To evolve and expand on the hybrid experimental strain-based method by Sinotte and Bauchau [160], [161] to experimentally determine the sectional stiffness properties of a modern fiber composite rotor blade. The specimen is the first rotor blade specifically developed for the Munich Experimental Rotor Investigation Testbed (MERIT) with a structure, including a thick carbon fiber C-spar and a trim mass, that is representative of modern fiber composite rotor blades. Furthermore, the manufacturing process resembles the current state of the art. To

increase the significance of the results the constitutive behavior of the selected composite materials is to be identified.
A secondary objective is derived from Sinottes [159] future suggestions to reduced the experimental and postprocessing effort and required time.

These three topics define the structure of the work, in the same order, with a dedicated chapter for each of them.

1.3 State of Science and Technology

In line with the subdivision of the main objectives of this thesis, this section highlights the most important research results on each specific topic, highlighting its scientific relevance.

1.3.1 Parametric Finite Element Preprocessor

In the following, an overview of the three most relevant parametric two-dimensional finite element preprocessors *PreVABS*, *SectionBuilder* and *IXGEN* is given.
All of them share the common principle mentioned before, that the three-dimensional problem is divided into a 2D cross-sectional and a 1D beam analysis as well as the common goal to develop a model for the immediate evaluation of the aeromechanical aspects of rotorcraft configurations with realistic composite rotor blade characteristics in the course of the preliminary design stage [141].

PreVABS Two different parametric finite element preprocessors exist under the name *PreVABS*. The older of the two [39] is a matlab code, copyrighted and commercialized by Utah State University, to explicitly create a finite-element discretization of rotor blade and airfoil sections for *VABS*. It was used in 2010 by Chen [40] to compare different programs for the calculation of inertia and stiffness properties of wind turbine blades. Another notable application was the development of the rotor blades for the AREA Synchropter UAV with 3.3 m rotor diameter developed in 2015 by the author [127], [128].
In the latter, the section curves of the outer geometry are used at various selected radial locations to build up a structural design layer by layer. The resulting structural cross-sectional model was subsequently analyzed with *VABS* for its beam characteristics (mass, center of gravity and shear center, longitudinal, bending and torsional stiffnesses). With the recovery of the three-dimensional stress states initial failure criteria were evaluated.
Figure 1.1b shows the structure of the AREA rotor blade at radial station R250. Certain limitations were encountered in the modeling of the typically thick C-spar, resulting in a gap between the top and bottom in the area of the leading edge, which has a negative effect in particular on the determination of the torsional stiffness and the shear center [128]. PreVabs uses as input parameters airfoil coordinates, web positions and angles as well as chord-wise varying composite laminate buildup schemes to generate a mixed quadrilateral mesh. The finite element modeling process is accurate down to each individual composite layer, starting from the outer airfoil coordinates and translating nodes in normal direction according to each layer thickness inward. The information

of ply orientation, fiber orientation and ply thickness are calculated and recorded for each element [39], [169]. The limitations come from the fact that the layers are parallel curves that contain singularities when the total layer thickness is equal to the radius of curvature of a curve point, i.e. when the parallel curve touches the involute of the given curve (close to the leading edge). Thereby, the modeling process is separating the structure into a upper and lower side skins with no physical connection. Another disadvantage is that the inner structure of filling foam cores, honeycomb structures or trim masses are not regarded.

(a) UAV rotor blade. Adapted from [127]

(b) AREA rotor blade cross-section at R250. Adapted from [127]

Figure 1.1: Examples of rotor blade cross-sections modeled with PreVABS

The complete new developed preprocessor with the name PreVABS (hereinafter referred to as *PreVABS-II*) is a more general and generic two-dimensional preprocessor specifically designed to work with *VABS* that overcomes some of the deficiencies of the earlier *PreVABS*, yet is fundamentally different as it separates the topology definition and generation from the subsequent meshing. The toplogy generation, mesh and visualization capabilities use *Gmsh* [55], an open source finite element mesh generator that leverages the *openCASCADE* CAD kernel.
An early approach and implementation to this idea was mentioned in the literature under the name of *VABS-GUI* [73].
A cross section is composed of different components, which are either laminates or fillers. Each laminate component is composed of one or more segments assigned to a baseline and a preferred direction to either side of it. Layups can be assigned to a portion of the baseline by specifying a start and an end point.

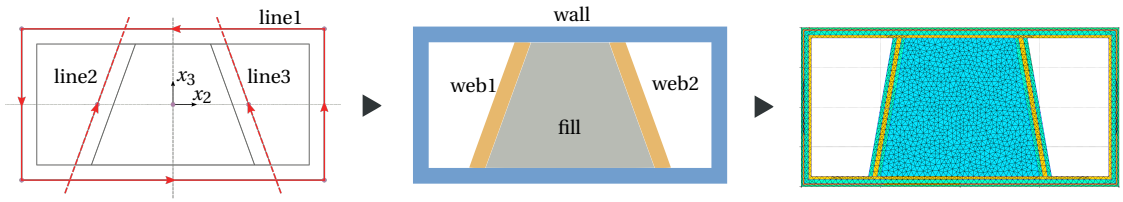

Figure 1.2: Modeling methodology of PreVABS-II. Adapted from Tian et. al. [168].

The geometric definition of these baselines and points make up the wireframe skeleton of the cross section (see figure 1.2). In this very generic approach, its cross sections can be modeled in a similar way to a parametric CAD model. Therefore, there are many different possibilities for modeling and decomposing models to generate the desired topology. The advantages are the large design freedom and the robustness of the proven mesh generator *Gmsh*. *PreVABS-II* is developed by Tian et. al. [168] in Wenbin Yu's research group which is in the process of extending the tool chain

through *DAKOTA* (Design Analysis Kit for Optimization and Terascale Applications) for design and optimization tasks under the name *iVABS* (integrated VABS environment).
It is also noteworthy that Yu [182] and his coworkers have developed *VABS* interfaces for the commercial FEA packages *ANSYS* and *ABAQUS*.

SectionBuilder In order to overcome the conflicting demands of modeling freedom and low modeling effort with optimization suitability, Chakravarty [35], [36] decided to solve this conflict by using two contrasting modeling approaches when developing the *SectionBuilder*. In the first approach "Shape Builder Approach" the cross sections are generated on predefined templates while in the "Component Builder Approach" the cross sections are assembled from several different simplified subcomponents.
The latter approach was used to represent the manufacturing process of rotor blades, where the structural fiber composite components are manufactured in independent curing cycles and subsequently joined by a bonding process. The special feature is that the individual components are defined and meshed independently. The meshes are then connected with a mortar algorithm to create an overall model of the cross-section. This software is fully integrated with a finite element solver within the flexible multibody code *Dymore*. [11]

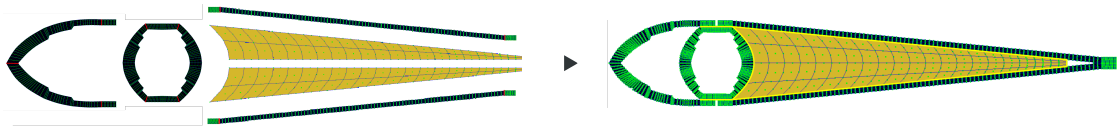

Figure 1.3: Methodology of *SectionBuilder* using an assembly of subcomponents (Component Builder). Adapted from [11].

IXGEN So far, the methods presented have been based strictly on two-dimensional cross sections without the propagation in the spanwise direction being taken into account. Rohl et al. [140] presented in 2012 the cross section mesh generator *IXGEN* (Intelligent Cross Section Generator) that creates not only a three-dimensional surface of the rotor-blade by distributing airfoil cross-sections in spanwise direction but also creates a three-dimensional solid body for each material layer.
It was developed with the support of the US ARMY Resarch, Development and Engineering Command (AMRDEC) by Advatech Pacific and uses *OpenCascade*, the open source CAD geometry kernel to generate the 3D rotor blade geometry and the 2D cross-sectional meshes. Each cross-section uses a predefined topology subcomponents such as spar webs, spar caps, wrap layers, etc. that can be used as design variables during an optimization.
The design environment was applied at the University of Michigan in support of active rotor blade research. Kumar and Cesnik [85], [86] applied the described optimization framework for the aeroelastic analysis and design of an active twist rotor and showed that by using their multidisciplinary

design optimization method, the active twist 4/rev actuator authority can be maximized.
Silva [158] stated in 2018 the plan to integrate *IXGEN* into an *OpenMDAO* Rotorcraft Optimization Framework called *RCOTOOLS* which currently contains a Python interface for the NASA Design and Analysis of Rotorcraft (NDARC) vehicle sizing tool and *CAMRAD II* [113].

1.3.2 Uncertainty Quantification

Over the years, there has been active research to quantify the influence of uncertainties on the dynamic behavior of aerospace structures [38]. Pettit [126] and Beran et. al. [17] provide a thorough overview of the quantification of uncertainties in aeroelastic analysis, design, and testing of fixed-wing aircraft. At this time, however, there is only a moderate selection of studies directly related to helicopter rotors. An overview of the most important references related to this work is described below:

One of the most important and related references is the work by Li [94]. Compared to the traditional multidisciplinary rotor blade optimization proposals, she introduces manufacturing constraints and proposes durability and fatigue analysis in a probabilistic design method to control the impacts of material, shape and load uncertainties on the rotor blade structural performance. By conduction Monte-Carlo simulations she showed the impacts of geometric perturbation (ply waviness on the inner surface) and material property uncertainties for the aeroelastic behavior and the stress distributions. She combined the Monte-Carlo simulation, generating manufacturing and service load uncertainties, and the classical structural design method to find a robust design solution [93], [95], [96].

The studies by Murugan et. al. [116]–[118] are the most comprehensive in recent years to investigate the effects of uncertainties in the material behavior of fiber composites on the aeroelastic behavior of helicopter rotors.
The focus of the studies was on the investigation of material uncertainties on helicopter aeroelastic behavior, natural frequencies, blade tip deflections, vibratory hub loads and stability. The studies contained both simplified composite box beam structural models with balanced symmetric laminates without off-diagonal coupling relation in the beam sectional properties and the consideration of finite element methods by means of the variational asymptotic beam sectional analysis (VABS) to make more valid statements about a realistic anisotropic and inhomogeneous rotor blade structure and thereby reducing the epistemic uncertainty [118]. A rotor, equivalent of the BO105 [118], with a four bladed soft-inplane hingeless design is considered during the studies. The

stochastic analysis is carried out by the means of Monte Carlo simulations.
The calculations revealed considerable deviations from baseline-predictions, with significant increase of 4/rev vibratory loads in resonance conditions.

You et. al. [176] presented a similar study to assess and quantify the influence of normal distributed material properties and manufacturing uncertainties on the aerolastic response and vibratory loads. The manufacturing uncertainties are accounted for by variations in ply thickness, fiber orientation and shear-center position. In contrast to other studies, this study considered the rotor blades to be dissimilar, which contributed to additional non-N_b/rev vibrations in the system. Blade-to-blade dissimilarity and the possible suppression with active rotor control, such as trailing-edge-flaps and active-twist, were studied by Roget and Chopra [139] as well as Pawar and Jung [125]. A recent study by Chatterjee et. al. [38] investigates the problem of manufacturing variability in composite helicopter rotor blades, but instead of a Monte Carlo Simulation, using a variety of machine learning approaches.

To paraphrase Pettit's [126] conclusion for research demands, the ultimate goal of stochastic computational aeroelasticity is an efficient and accurate computation of uncertainty-based factors for realistic structures and flight states.
For helicopters, the rotor-blade structural components have improvement potential to reduce the epistemic uncertainty as they have been insufficiently considered in detail in the few research contributions to date. In particular, with the exception of [117], a finite element sectional analysis method has rarely been used to represent realistic composite cross sections and thus fully populated sectional stiffness matrices of a modern helicopter rotor blade in these studies.
A dynamically balanced design of the initial baseline configuration is equally important as the studies by Murugan et. al. [118] have already shown that otherwise small variations from the baseline design can have a large impact on the dynamic response of the rotor. This would massively distort the results and validity of the study. Sufficient distance of the higher harmonic eigenfrequencies to the rotor harmonics must be ensured in the baseline design. If necessary, means must be found to specifically influence these natural frequencies and distance them from the intersections with rotor harmonics. Usually, this is done by the targeted introduction of additional lumped tuning masses into the structure in such a way that the natural frequencies are a safe distance away from the rotor harmonics. The experienced based engineering rule states that distance to be approximately 0.2/rev to obtain a robust design [171]. In addition, the uncertainty studies and their statements are also only as valid as the original model on which they are based. A validated basis of the baseline comprehensive models and flight states are therefore essential for the significance of the results. This has also not been adequately addressed in previous studies.

1.3.3 Experimental Measurements Methods of Beam Stiffness Properties

In this section, a summary of experimental procedures for the determination of the beam sectional stiffness properties of helicopter rotor blades is given.
As mentioned before, helicopter rotor blades typically comply very well with the beam assumptions of a long and slender structure with one dimension much larger than the other two and smoothly varying cross-sections along its length [175]. In the following, the axis x_1 of the beam is defined along the longer dimension, and x_2 and x_3 define the plane of the cross-section perpendicular to this axis.

The stiffness properties along a beam are generally expressed by a linear relationship (equation (1.1)) between the sectional stress resultant vector $\underline{F}^T = (F_1, F_2, F_3, M_1, M_2, M_3)$ with the axial force F_1, transverse shear forces, F_2 and F_3, twisting moment M_1 and the two bending moments M_2 and M_3 and the sectional strains $\underline{\epsilon_c}^T = (\epsilon_1, \epsilon_2, \epsilon_3, \kappa_1, \kappa_2, \kappa_3)$ with the sectional axial strain ϵ_1, transverse shearing strains, ϵ_2 and ϵ_3, twist rate κ_1 and two bending curvatures, κ_2 and κ_3. The three forces are the resultants of the stress distributions across the cross section of the beam, while the three moments are evaluated with respect to the reference axis of the beam [14].

$$\begin{pmatrix} F_1(x_1) \\ F_2(x_1) \\ F_3(x_1) \\ M_1(x_1) \\ M_2(x_1) \\ M_3(x_1) \end{pmatrix} = \begin{bmatrix} K_{11} & K_{12} & K_{13} & K_{14} & K_{15} & K_{16} \\ K_{12} & K_{22} & K_{23} & K_{24} & K_{25} & K_{26} \\ K_{13} & K_{23} & K_{33} & K_{34} & K_{35} & K_{36} \\ K_{14} & K_{24} & K_{34} & K_{44} & K_{45} & K_{46} \\ K_{15} & K_{25} & K_{35} & k_{45} & K_{55} & K_{56} \\ K_{16} & K_{26} & K_{36} & K_{46} & K_{56} & K_{66} \end{bmatrix} \begin{pmatrix} \bar{\epsilon}_1(x_1) \\ \bar{\epsilon}_2(x_1) \\ \bar{\epsilon}_3(x_1) \\ \kappa_1(x_1) \\ \kappa_2(x_1) \\ \kappa_3(x_1) \end{pmatrix}; \quad \underline{F} = \underline{\underline{K}}\,\underline{\epsilon_c} \tag{1.1}$$

The symmetric 6×6 sectional stiffness matrix K on the right hand of the equation (1.1) describe the constitutive law for the cross-section of the beam containing the desired unknown coefficients. In general, these equations can be fully coupled so that all of the sectional strains affect the values of each of the sectional stress resultants.

The existing measurement techniques to experimentally obtain at least partially the coefficients of the sectional stiffness matrix can be divided into deflection, rotation and strain based measurements.

Deflection-based Methods

As the name suggests, these methods use the measured displacement of the beam subjected to loads in order to determine the stiffness coefficients. To simplify equation (1.1), Euler-Bernoulli assumptions are often used, which provide for beams with a high aspect ratio a sufficient accurate result [13]. According to these assumptions, the cross section of the beam is infinitely stiff in its own plane and thus does not deform under load. The second and third assumptions are that the beam cross-section remains plane and normal to the deformed beam axis. Note, that the third simplification leads to the negligence of the sectional shear deformation terms ($\epsilon_2 = \epsilon_3 = 0$).

With the additional exclusion of the torsional terms, the governing equations for the beam displacement can be formulated as differential equations in terms of three sectional displacements, when the sectional strain tensor is expressed in terms of the beam displacements (e.g.: $\kappa_3(x_1) = d^2\bar{u}_2(x_1)/dx_1^2$). Characteristic solutions of the second order differential equations can be obtained for specific load cases with the knowledge of the boundary conditions.
A typical test case for helicopter rotor blades is a cantilevered fixed-free setup with a clamped blade root that restricts both displacement and rotation (see figure 1.4a).

(a) Cantilevered bending test of the IRI T22/T23 rotor blade with photogrammetry. Adapted from [19].

(b) 3-point bending test of the HART-1 rotor blade. Adapted from [78].

Figure 1.4

For the cantilevered case, the following basic linear solution is obtained that relates the single force to the displacement.

$$K_{55} = \frac{F_{3,\text{tip}} L^3}{3\bar{u}_{3,\text{tip}}} \tag{1.2}$$

The biggest drawback of the method is that the solution is heavily dependent on the boundary conditions and that the equations are derived under the assumption that the slope at the attachment is zero. The integral solution of the equation lead to the fact that slight angle variations at

the attachment result in large deflections of the tip, leading to an underestimation of the actual stiffness.
The second common technique is a 3-point bending test (see figure 1.4b). The blade is supported by two rollers that restricts displacement but allows rotations, while the load is applied at the center. Compared to the cantilevered setup, the assumption of the boundary conditions are usually in better agreement in this case. The drawback is, that only an average stiffness between the ends can be obtained which equals to the assumption, that the beam sectional properties are uniform between measurement locations.
Loads are often applied by weights and deflections are measured with dials or with electromechanical LVDT (Linear Variable Differential Transformer) transducers that convert the linear motion into a corresponding electrical signal or as in the case of Bernardini et. al. [19] and Enei et. al. [46] with photogrammetry.

Application examples of these methods can be found in the HART I [78], [79] and HART II [77] rotor blade experiments. They obtained the flap (K_{55}) and lead-lag bending stiffness (K_{66}) of the blade uniform section using the 3-point bending technique as shown in figure 1.4b. The flap bending stiffness for the root portion of the HART I blade is determined using the mirror-method, a rotation based technique described in the next section.

A different but also a deflection based measurement technique is used by Bernardini and Enei et. al. [19], [46], measuring the beam displacements using photogrammetry by identifying 3D coordinates of labeled point markers on the rotor blade surface in a series of 2D digital images. By measuring the displacements and rotations of the rotorblade at multiple distributed locations in a cantilevered setup (see figure 1.4a) compared to the undeformed reference case, the sectional curvatures $\kappa_2(x_1)$ and $\kappa_3(x_1)$ are obtained by differentiating the displacement distribution along the beam axis x_1 two times. A polynomial interpolation was used to smooth the recovered data to before differentiation.
The peculiarity of this method is, that it is not bound to the previous limitations and assumptions of boundary condition and uniformity. The unknown quantities (K_{55}, K_{66} and K_{56}) evaluated with the Euler-Bernoulli assumptions under at least two different load condition using a least square approach.
The twist angle under torsional moment M_1 is obtained through multiple measurement locations in chordwise direction. Similarly, a polynomial fit of the torsion angle is used to obtain the twist-rate $\kappa_1(x_1)$ by differentiation that is directly associated to the torsional stiffness properties. Since the twist angle is calculated from the multiple distributed point marks in chord direction, this could also be classified under the next category of rotation-based techniques.
A very similar approach was selected for the evaluation of the inboard root section of the HART II

rotor blades. Jung et. al [77] used Digital Image Correlation (DIC) to measure the deflection in that region under load, used a cubic spline interpolation to differentiating the deflection curves and associating them to the desired flap beding stiffness.

Rotation-based Methods

Instead of determining the stiffness coefficients from experimentally measured displacements, rotation-based techniques directly measure the slope or first derivative of the displacement field to determine the coefficients.
The most popular method is the so called "mirror method" which was first introduced by Chandra and Chopra [37]. They determined the bending slope and elastic twist of a composite I-beam at different spanwise stations by measuring the rotations of surface-mounted mirrors in two orthogonal plane. The reflection of a laser was used in this setup to detect the inclination angle.
In the setup of the experimental tests of the HART I rotor blades conducted by Jung et. al. [78] a pair of mirrors was used in combination lasers to determine the flap bending and torsional stiffness of the root section. In order to determine the rotor blade torsional stiffness of the CoAX 2D helicopter, Jaksch [75] used a digital inclinometer.

(a) HART I flap bending experiment using the mirror method. Adapted from Jung et. al. [78]

(b) Digital inclinometer measurements to determine the torsional twist angle. Adapted from Jaksch [75].

Figure 1.5

Strain-based Methods

In strain-based methods, model assumptions provide the relationship between the measured strains, a local measure of differential deformation in the structure, and the applied sectional forces to determine the desired coefficients.

In 2018 Süße und Hajek [166] presented a method that uses axial rotor blade surface strain measurements of distributed fiber Bragg grating (FBG) sensors of four glass fibers to identify not only elastic blade deformation but also to recover the sectional bending stiffness coefficients of the AREA [128] rotor blade at 15 instrumented radial locations.

Compared to conventional strain gauges that measure the change of resistance, FBG sensors are optical interference filters inscribed in optical fibers that measure the strain based on the changing reflected wavelength. They are known to have an better signal-to-noise ratio, are more fatigue resistant and are insensitive to corrosion and electro-magnetic interference [166]. Another advantage over conventional strain gauges is that a single fiber can contain multiple FBGs, reducing instrumentation complexity and additional weight.

The instrumented AREA rotor blade has a length of 1550mm, a linear twist of 10°, asymmetrical NACA 23012 airfoil a chordlength of 100 mm up to 0.6%R that is tapered to 60mm at the blade tip. Four optical fibers were glued in the spanwise direction to the surface of the blade each in one of the four quadrants of the cross-section. The orientation of all sensors was parallel to the x_1 axis. Figure 1.6a shows the instrumented AREA rotor blade in its cantilevered setup.

Süße and Hajek [166] used the kinematic assumption of Euler-Bernoulli to describe the axial strain field $\epsilon_{11}(x_1, x_2, x_3)$ as a function of sectional strains and cross-sectional coordinates x_2 and x_3, neglecting torsion and shear deformations. By introducing the sectional constitutive law with the sectional compliance matrix $\underline{\underline{S}}$ into equation 1.3 the relationship between axial strains ϵ_{11} and the sectional forces is obtained.

$$\epsilon_{11} = \begin{bmatrix} 1 & x_3 & -x_2 \end{bmatrix} \begin{bmatrix} \bar{\epsilon}_1 \\ \kappa_2 \\ \kappa_3 \end{bmatrix} = \begin{bmatrix} 1 & x_3 & -x_2 \end{bmatrix} \begin{bmatrix} S_{11} & S_{15} & S_{16} \\ S_{51} & S_{55} & S_{56} \\ S_{61} & S_{65} & S_{66} \end{bmatrix} \begin{bmatrix} F_1 \\ M_2 \\ M_3 \end{bmatrix} \tag{1.3}$$

By neglecting axial properties, they have simplified the equation to

$$\epsilon_{11} = \begin{bmatrix} x_3 & -x_2 \end{bmatrix} \begin{bmatrix} S_{55} & S_{56} \\ S_{65} & S_{66} \end{bmatrix} \begin{bmatrix} M_2 \\ M_3 \end{bmatrix}. \tag{1.4}$$

The resulting system of linear equations is solved at each radial station for the unknown sectional compliance matrix with at least two linearly independent load cases (j) with at least three sensor positions (i) by using the half-vectorization $\underline{S}$ of the symmetric compliance matrix .

$$\epsilon^{(j)}_{11,(i)} = \underline{\underline{A}}_{(i)} \underline{\underline{S}} \underline{F}^{(j)} \tag{1.5}$$

$$\epsilon^{(j)}_{11,(i)} = \underline{\underline{A}}_{(i)} \underline{\underline{G}}^{(j)} \underline{S} \tag{1.6}$$

The sectional bending stiffness properties K_{55}, K_{56} and K_{66} are finally obtained from the inverse of the compliance matrix $\underline{\underline{K}} = \underline{\underline{S}}^{-1}$.

Because the system of equations was overdetermined with the input of four FBG sensors, Süße and Hajek [166] compared the result of different sensor configurations and a least squares solution to each other and to the predesigned stiffness properties of the AREA rotorblade determined with VABS [127].
Their experimental results of the lead-lag bending stiffness K_{66} and the coupling relation K_{56} are in good agreement with the predicted VABS results along the span of the nonuniform blade. The experimentally determined flap bending stiffness K_{55} is on average 15-20% lower that its predicted values. It is assumed, that epistemic uncertainties of the preVABS description of the AREA rotor blade and aleatory uncertainties such as manufacturing and material uncertainties are responsible for this offset.
It can be concluded, that this strain based method is capable of determining the bending stiffness properties of an asymmetrical and anisotropic rotor blade without assuming partial uniformity.
The advantage of the method is that in addition to the sensor signal, only the position and orientation of the sensors are required, and no further input or correction by a finite element model is necessary. On top of that, the sensor network allows the usage for structural health and load monitoring purposes as well as the identification of the elastic blade movements during rotor operation [166].

Expensive sensors and high instrumentation and bonding efforts prohibit the application for serial production monitoring of each manufactured rotor blade. However, the biggest missing element in this method is the disregard of torsional and shear expressions. For a long slender rotor blade, the shear terms contribute only to a small and often negligible part to the dynamic rotor behavior, whereas the torsional behavior is essential.

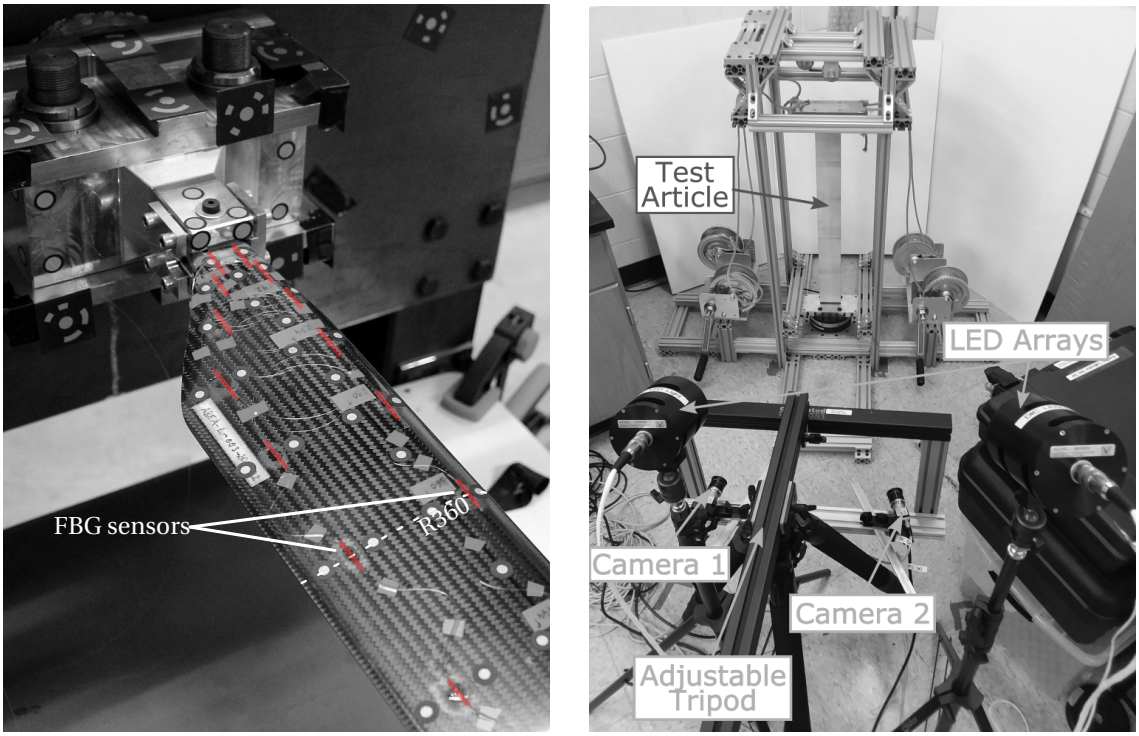

(a) FBG strain measurements of the AREA rotor blade. Adapted from Süße and Hajek [166]

(b) Experimental DIC setup of Sinotte with a vertically mounted beam. Adapted from Sinotte [159].

Figure 1.6

In 2019, Sinotte and Bauchau [161] introduced an experimental approach that recognizes the inconsistency of the Euler-Bernoulli formulation, as it cannot account for an accurate estimate of the strain energy [14]. For instance, it is well known that the torsional behavior of beams with non-circular cross-sections involves warping of their cross-sections [14].
Following the perspective that the nodal displacement over the beams cross-section can be described as the superposition of a rigid section motion and the warping introduced by sectional stress resultants, the following relationship between the strain tensor $\underline{\varepsilon}^T = \{\varepsilon_{11}, 2\varepsilon_{12}, 2\varepsilon_{13}, \varepsilon_{22}, \varepsilon_{33}, 2\varepsilon_{23}\}$ and the applied sectional forces $\underline{F}^T = \{F_x, F_y, F_z, M_x, M_y, M_z\}$ can be expressed by the following equation, assuming that the strain components remain small.

$$\hat{\underline{\varepsilon}} = \left[\underline{\underline{A}}\left(\underline{\underline{Z}}\,\underline{\underline{S}} + \underline{\underline{W}}\,\tilde{K}^T\right) + \underline{\underline{B}}\,\underline{\underline{W}}\right]\underline{F} \tag{1.7}$$

The derivation of this equation can be found in the publications of Han and Bauchau and is explained in more detail in chapter 4. In [14] it is presented for an initially straight beam and is extended for initially curved and twisted beams in [64].

Equation (1.7) provides the governing description the problem in which the inverse of the 6×6 sectional compliance matrix $\underline{\underline{S}}$ is the desired property. In figure 1.6b the experimental setup of Sinotte [159] with a vertically mounted beam is shown, in which the sectional stress resultants $\underline{F}$ are measured with a 6-axis load cell at the blade attachment and transformed to the desired radial stations. During the experiments six independent load cases were applied at the tip with a set of winches, pulleys and hanging weights [159]. The other measured quantities are the plane surface strains $\epsilon_{11,e}$, $\epsilon_{12,e}$ and $\epsilon_{22,e}$, the surface coordinates, which are stored in $\underline{\underline{Z}}$, and the displacements using Digital Image Correlation. The depicted experimental setup shows the two 5 MP cameras on an adjustable tripod. Sinotte decided to capture the specimens surface with multiple spanwise images and to reassembled them later with the use of alphabetic markings along the span. That way, a high spatial resolution of the surface was obtained.
The only remaining unknown component of the equation is the warping displacement under unit loads $\underline{\underline{W}}$. What makes this methodology so unique is, that the warping displacement is evaluated with the help of a sectional finite element model using *SectionBuilder*.

Equation (1.7) is transformed to give a linear system of equations of the form $\underline{\underline{A}}\underline{S} = \underline{b}$ for each strain location (i) and load case (j) which are subsequently vertically stacked. Since the number of required strain measurement locations is multiple times larger than the minimum required set to solve the system of equations, the heavily overdetermined system is solved using Singular Value Decomposition (SVD).

To demonstrate the proposed methodology, different sets of test articles were studies. A prismatic isotropic aluminum and asymmetric anisotropic composite beams with rectangular cross-section as well as composite beams that resemble simplified rotor blades are examined. The latter have 80 mm chord, an asymmetric VR-7 airfoil, consisting of a foam core wrapped with a single $\pm 45°$ plain-weave ply of carbon fiber prepreg with one specimen having an additional characteristic D-spar $\pm 45°$ web. [159]

To capture and quantify the effects of experimental measurement inaccuracies on stiffness properties, a uncertainty quantification study was also conducted using the Taylor Series methodology. The systematic and random errors of the load cell were obtained from calibration. The strain measurements over reference configurations showed an error of two times standard deviation of $\sim 25\ \mu\epsilon$.
For the first study of the isotropic aluminum beam, a close agreement between the calculated expected strains and the DIC measurements was demonstrated. With the exception of the lag shearing stiffness (K_{22}), showed all stiffness coefficients a variations below approximately $< 10\%$ in comparsion to the analytical values. The lag shearing stiffness was significantly higher than the analytical value and showed significant variations along the span due to a low signal to noise ratio,

as the measured shear strain ϵ_{12} was only $2-4$ times larger than the estimated strain measurement noise. For the flap shear stiffness, an almost perfect agreement was visible due to the fact, that it was almost entirely predicted by the numerical warping field.
For the composite blade with and without spar, the results showed generally good agreement between the measured and the predicted value, although the lag shear stiffness showed again difficulties with a large uncertainty term and a maximum underprediction of factor three for the blade without the spar, while the flap shear stiffness showed good agreement presumably from the large influence of the warping correction terms. It is also apparent from agreement of these results that the addition of the spar is not well captured by the numerical prediction, presumably indicating a potential discrepancy that exists between the designed and manufactured blades [160].

In conclusion of the general formulation by Sinotte and Bauchau it can be stated, that their method allows the determination of all the stiffness matrix coefficients without assuming partial uniformity along the span. A large signal to noise ratio of both the strain and load measurement proved however crucial to obtain an accurate stiffness measurement. The results showed generally good agreement between the measured and the predicted values, although the lag shear stiffness showed the largest deviations and fluctuations from the prediction. Yet, it is noted that the shear stiffness coefficients have insignificant effect on the dynamic response of blades and are therefore often neglected in most comprehensive rotor analysis.

In addition to being able to determine the full cross-sectional stiffness properties, this methodology is suitable to be integrated into a production process due to its low instrumentation overhead, because for preparation only a stochastic pattern has to be painted on the rotor blade.
What is still missing is the study of rotor blades with a complete representative internal structure in an experimental setup with low execution and postprocessing efforts.
These promising results motivated me to follow up and expand on this methodology in this thesis and to investigate it for a more complex application of a realistic rotor blade structure.

Other Notable Methods

Dynamic measurements can also be used to estimate the stiffness properties. Based on the known or assumed mass and inertia properties of the rotor blade the stiffness can be calculated from measured non-rotating natural frequencies. These natural frequencies can be determined under different excitations and boundary conditions with laser vibrometers or accelerometers and a subsequent Fourier transormation [159], [166]. The disadvantages of these methods are that they strongly depend on the boundary conditions and the assumptions of the mass distribution and

that the determination of nonuniform properties is difficult.

In another noteworthy methodology, Jung et. al. [77], Schulz et. al. [148] and Hwang et. al. [74] used computer tomography (CT) data of the rotor blade to reconstruct the finite element models to determine the structural beam properties of the blade. The main disadvantage of this methodology is that it is not a direct measurement technique and thus relies on accurate material models in both density and constitutive behavior. Uncertainties in this context are therefore not taken into account and the large amount of post-processing work of this technique should also not go unmentioned.

2 Parametric Finite Element Preprocessor for Composite Rotor Blade Cross-Sections

Geometric and composite definitions of rotor blades can be constructed using Computer-Aided Design (CAD) software, but converting these definitions to a cross-sectional finite element representation can prevent design optimizations due to the associated manual modeling effort. This is one reason why the structural rotor blade models of current predesign methods have often an inaccurate level of detail and miss important structural elements and components of the rotor blade.

This chapter describes the Structural Optimization and Aeroelastic Analysis (*SONATA*) framework, its methodology and its fundamental principles. At its core is a parametric finite element preprocessor for slender fiber composite beam structure *(SONATA-CBM)* that is extended to meet the interfaces requirements of a multidisciplinary rotor-blade design optimization framework such as an automated and parametric setup. It incorporates the structurally relevant components and supports a rapid transition to a commercial CAD system by providing an interface, so that the conversion to a full three-dimensional CAD description of the resulting rotor blade design does not become a long and iterative task once again.
It essentially closes the gap between the one-dimensional beam description and the three-dimensionality of the structure following the approach to separate the problem into a two-dimensional analysis over the beam cross-sections (see figure 2.1). Parts of this chapter have been published by the author in the following references: ERF2018, ERF2019A, COMPSTRUC2020.

Pursuing a common goal as the NASA's Revolutionary Vertical Lift Technology Project (RVLT) to provide validated tools for multidisciplinary design, analysis and optimization (MDAO) of rotorcraft, bringing the components together to the same programming language addresses the need for a low implementation effort at user level so they are flexible and easy to use with *OpenMDAO* [113]. *OpenMDAO* is an open-source computing module for system analysis and multidisciplinary optimization, written in Python to allow the user to break down the structure of complex optimization tasks into a hierarchic manner while managing the numerical methods [59]. *SONATA* has therefore

been written in Python as well, leveraging the powerful functionalities of the Python wrapper for the open-source CAD-Kernel *Opencascade – pythonOCC*[124]
The decision to develop Python modules and interfaces was additionally inspired by the idea of a robust multi-fidelity preliminary rotorcraft design method by Wirth [174] and by NASA's effort to develop a Python module for existing rotorcraft design and analysis tools for the use of *OpenMDAO* referred to as RotorCraft Optimization Tools (*RCOTOOLS*). *RCOTOOLS* currently incorporates interfaces to the NASA Design and Analysis of RotorCraft (*NDARC*) vehicle sizing tool and the Comprehensive Analytical Model of Rotorcraft Aerodynamics and Dynamics II (*CAMRAD II*) [113]. Recently, Silva and Johnson [158] began integrating *IXGEN* into the *RCOTOOLS* module with the intention to develop a system to evaluate aeromechanical problems for rotorcraft configurations with representative rotor and wing structural properties in the conceptual design stage more quickly [140].

The developments and source code of this chapter is available via the *GIT* repositories for SONATA[1] and the open-source structural code *ANAB4*[2].

Figure 2.1 provides an overview of the components and the procedure of *SONATA*. Creating the rotor blade model essentially starts with the initialization and global parameterization of the problem. A common and accessible definition of the rotorblade uses a wireframe created by the distribution of airfoils along the span. The wireframe describes a linear multi-section three-dimensional surface of the blade. The surface can also be created by means of an alternative definition or by importing an existing 3D CAD model [145]. The next step of *SONATA* is the composite topology generation of the internal structure at specified radial stations which is then discretized into a two-dimensional finite element definition before the one-dimensional beam sectional properties, three-dimensional strain, stress and displacement distributions are recovered.

This chapter is subsequently structured according to the steps described above and illustrated in figure 2.1. Three different validation studies conclude the chapter. Structural beam properties are successfully verified for both *VABS* and *ANBA4* using isotropic circular cross-sections showing mesh convergence and composite box beam examples from literature, thereby verifying the parametric approach and implementation of *SONATA* as well as the solver integration. Last but not least, the framework is used to evaluate a fully resolved highly flexible wind turbine blade with initial twist and curvature.

[1] http://gitlab.lrz.de/HTMWTUM/SONATA
[2] https://bitbucket.org/anba_code/anba_v4

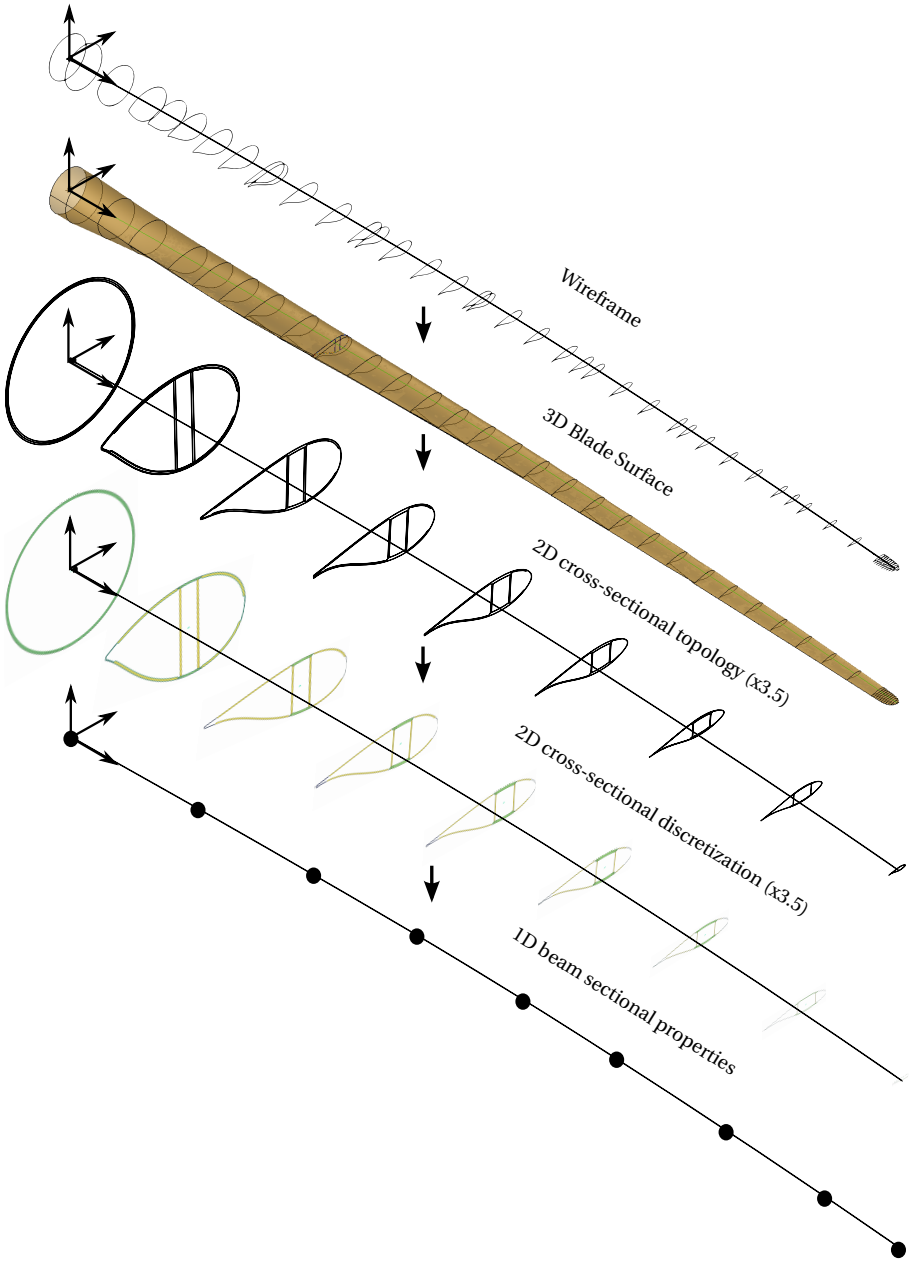

Figure 2.1: General Methodology of the parametric finite element preprocessor for composite rotor blade cross-sections (*SONATA*). The depicted example is a 15 MW wind turbine rotorblade which dataset was provided by NREL [48]. The 2D cross-sectional topologies and discretizations are magnified by a factor of 3.5 for better visualization.

2.1 Initialization and Parameterization

The global right-handed coordinate system is called the blade reference frame with the unit vectors denoted x_r, y_r and z_r in figure 2.2. x_r is pointing in the beam direction. z_r is pointing upwards so that in the case of a counter-clockwise rotating rotor blade, the resulting y_r axis is pointing towards the leading edge.

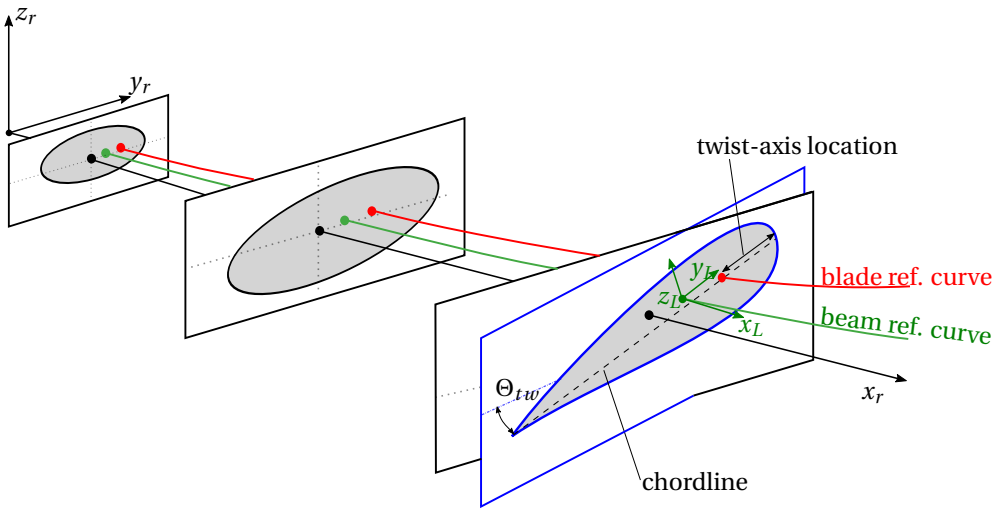

Figure 2.2: SONATA blade and beam definition

The local coordinate systems (CBM frames) denoted with subscript L, are defined for each structural two-dimensional cross-section that is modeled. The stiffness and inertia properties of the beam are evaluated with respect to the local CBM-frame. The unit vector of the local CBM frame x_L is tangent to the arbitrarily initially curved and twisted beam reference curve. The unit vectors y_L and z_L are in the plane normal to the beam reference curve. The user can decide if he wants to rotate the local coordinate system about x_L so that y_L is pointing towards the leading edge parallel to the chordline.

The global one-dimensional beam and two-dimensional cross-sectional analyses are inherently connected. It is therefore important to ensure that coordinates from the two separate analyses are consistent [68]. Yu [179] showed that the effects of an oblique cross-sectional plane may be accounted for, but it has only proven to work with the classical Euler-Bernoulli theory and not with the generalized Timoshenko theory. Therefore, the cross-sectional analysis in this work is performed in a plane normal to the beam reference line. Figure 2.2 depicts the situation of the curvilinear coordinates assuming that the cross-sectional plane is normal to the beam reference line. Yet, the user is free to choose to rotate the curvilinear coordinates along x_L (e.g., so that the coordinates follow a initial twist κ_1 of the rotor blade).

The outer shape of the structure is either predefined by a 3D surface component and imported from a CAD file as *STEP* file format or defined as wireframe through a collection of airfoils or any other arbitrary closed curve. In the latter, the curves are projected along the x_R-axis, translated to the non-dimensional twist-axis location, rotated by the twist angle, Θ_{tw}, around x_R and scaled to the desired size. The grid points of the wireframe are created by a minimal set from the information of the input parameters along the radial x coordinates. SONATA input files are defines using the YAML syntax. For the definition of the outer shape it provides twist, chord, twist-axis location, airfoil definitions and the beam and blade reference curve along the radial non-dimensional grid. When generating the wireframe based on the minimal set of input parameters and not all radial sections are specified with an airfoil, intermediate airfoils are generated by translating coordinate points $p_1(s)$ of airfoil 1 in the direction of vector $v(s) = p_2(s) - p_1(s)$ towards airfoil 2. The magnitude of the translation is the vector's magnitude multiplied by factor k, leaving the following relation:

$$p_3(s) = p_1(s) + k\left[p_2(s) - p_1(s))\right]. \tag{2.1}$$

The resulting wireframe describes a surfaces or loft that is generated by linearly connecting the set of sections as illustrated in figure 2.3c and 2.3d.

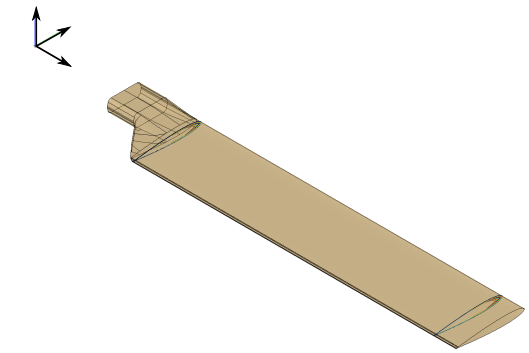

(a) MERIT rotor blade surface [130]

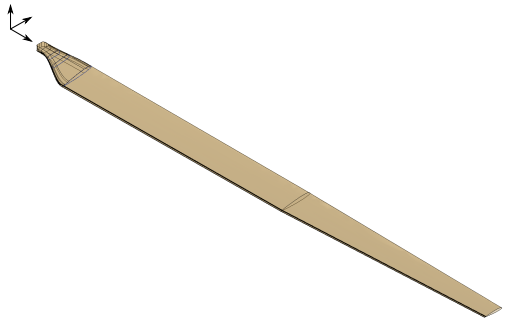

(b) AREA rotor blade surface [128]

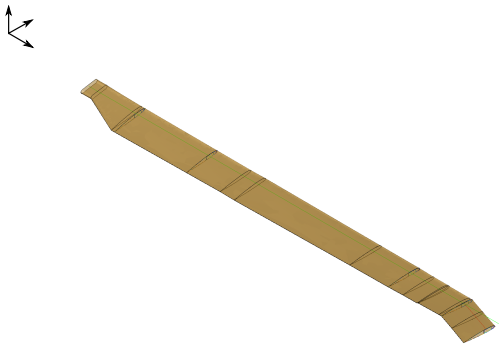

(c) UH-60A rotor blade surface. Adapted from [132]

(d) Generic windturbine blade surface. Adapted from [48]

Figure 2.3

The internal structure can be defined at specific cross-sections of interest. At those locations the two-dimensional finite element model is generated in the y_L-z_L plane normal to the beam's reference curve. Figure 2.2 illustrates, that in the case of an curved beam reference curve, the local cross-section and corresponding coordinate-system doesn't coincide with the global reference frame and thus the surface is intersected with the y_L-z_L plane to obtain a closed curve.

The two-dimensional finite element preprocessor *SONATA-CBM* originates from such an arbitrary closed curve. Besides obtaining it from the description above, it can also be obtained in the form of a coordinate table or a 2D parametric curve from a STEP file input.

2.2 Cross-Section Composite Topology

The method for generating the internal cross-sectional topology was inspired from composite manufacturing processes, where layers are placed on top of each other in negative molds consecutively from the outside to the inside of the blade. The motivation behind it is to avoid complex boundary conditions and constraints in an optimization and to keep the resulting solution in the viable solution space. At the same time, enabling a detailed and realistic representation of the cross-sectional layup with many design freedoms not restricted to predefined topologies.

Each layer is described by its thickness, start and end location, a fiber orientation and an assigned material. After the layup on top of the outer boundary closed curve is completed, webs are introduced and subsequently new closed curved geometries are generate where the layup procedure is repeated. The first segment (labeled Nb. 0) includes the layup attached to the original boundary curve. Following segments are based on the newly generated closed geometries and are ordered subsequently from the leading edge to the trailing edge, separated by webs attached to the innermost layer of the first segment. Remaining cavities can be filled with a core material and additional trim or tuning masses can be inserted afterwards.

At first, the outer boundary curve, represented as counterclockwise set of consecutive B-Splines, is defined in curve coordinates s between zero and one. Multiple connected B-Splines (*BSplineLst*) are used to account for discontinuous features such as corners and edges. The origin is typically located at the trailing-edge (TE). If no origin is specified, it is the point of intersection of the y-axis rotated by Θ_{tw} with the origin curve located farthest to the left ($-y_L$). The curve coordinate system propagates through the layers with an interval tree structure. It allows to efficiently find the intervals/layers that overlap and locate the corresponding coordinate for each layer.

Figure 2.4 illustrates the idea of the interval-tree structure by showing a minimal example for the layup of table 2.1. There are four layers in total. The first (#1) spans the entire range of coordinates from 0 to 1. Note that the last layer (#4) partially overlaps the second (#2) and third (#3).

Layer #	s_{start}	s_{end}
1	0	1
2	0.1	0.9
3	0.2	0.6
4	0.3	0.8

Table 2.1: Minimal layup definition of figure 2.4.

The first plot of figure 2.4 shows the layup as it was defined with assigned colors. The initial closed curve segment boundary is displayed as black bar ranging from zero to one.
The middle plot shows the relevant part of the cumulated boundaries by trimming them into their relevant part. In other words, the colors of the layers whose information and *BSplineLst* are needed to create this layer are shown. For example: to create layer #4 from s_{start}=0.3 to s_{end}=0.8, the B-splines of layer #3 from s=0.3 to s=0.6 and from s=0.6 to s=0.8 of layer #2 are needed. The final segment boundary represents the resulting final interval from 0 to 1 that is created after the last layer. This is particularly important when new internal segments are generated based on the first segment. That is always the case when, after completion of the first segment, webs are introduced into the structure.
The bottom plot shows the same procedure with the inverse direction. This is needed for the later meshing procedure as this propagates in a reversed manner through the layup. Starting at the top layer and propagating to the bottom. The grey bar represent regions on the layer where no predefined nodes are translated from the layer above. Analog to this, the colors correspond to the layer from which mesh information is passed down. More about this in section 2.3. It is important to note that the end coordinate does not have to be larger than the start coordinate so that the layers can be placed in the rear part of the section.

Each layer is generated by the following consecutive steps.

1. Determine the relevant underlying *BSplineLst* between start and end coordinate of the layer using the interval tree data structure.

2. Discretize the *BSplineLst* and perform an parallel offset to return an approximate representation of all points with a given thickness of each layer.

3. Generate a new *BSplineLst* by interpolation and add smooth layer cutoffs to connect the lower and upper *BSplineLst* if necessary.

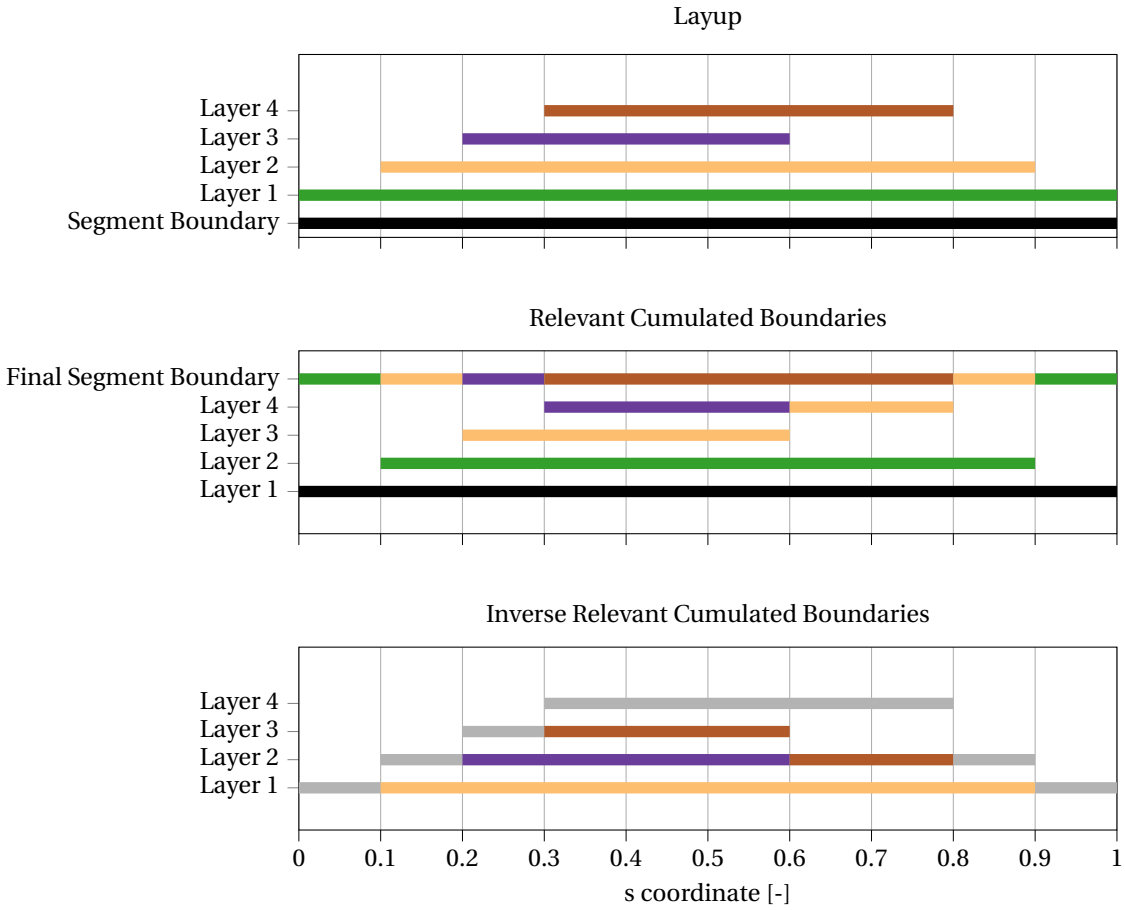

Figure 2.4: Illustration of the resulting cumulated boundaries of the intervaltree structure.

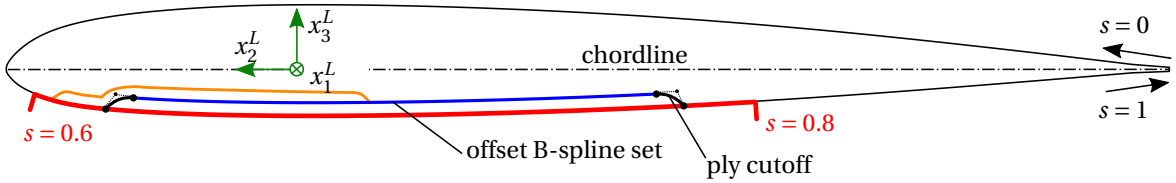

Figure 2.5: Definition of the local reference coordinate system (L) and the s-coordinates along the arc of an outer shape for a beam or blade cross section.

If the newly generated layer is closed and therefore defined from s=0 to s=1, the origin is detected by searching for an orthogonal projection of the origin of the previous layer. If no projection is found it takes the closest neighbor of the discrete offset points. The resulting *BSplineLst* of the layer is subsequently reordered accordingly. The other case is that the layer ends at an arbitrary location, so a connection must be established between the new offset *BSplineLst* and the original *BSplineLst*. Different layer cutoffs were investigated and implemented to connect the lower and upper *BSplineLst* including a stepped, linear, round and a S-shaped termination. The round cutoff was selected as

default for all further studies because it best represents the manufacturing process and smoothing characteristic when multiple plies are stacked on top of each other in a scarfed region. In most manufacturing processes, the edges of composite plies will be rounded under the influence of pressure and temperature, which is why a shafted laminate made of several plies will not have a sharp step structure, but a smoothed transition (see figure 2.5).
In this case, a quadratic Bézier-Spline describes the cutoff with three control points. The first and last control points are the endpoints with one at the lower spline and one at the trimmed upper spline. The cutoff depth is a function of layer thickness. The intermediate control point responsible for the curvature is extended in the tangential direction of the upper spline by 50% of the layer thickness ($0.5t\underline{\hat{v}}$, with the thickness t and the normalized tagential vector $\underline{\hat{v}}$).

The following methodology is shown with the example of a generic UH-60A composite rotor blade with twist, planform, airfoil and chordline information from Davis [43] as described in recent publications ERF2018, ERF2019 and shown in figure 2.3c.
Figure 2.6 represents a generic example of a composite blade cross section. It demonstrate the topology capabilities of SONATA and accounts for the most common topology requirements for rotorcraft blades, including skin layers, erosion protection, a C-spar with filled cavities and an added circular trim mass, a box beam, honeycomb core and trailing edge reinforcements. The input parameters are summarized in table 2.2 and 2.3.

s_{start}	s_{end}
web 1	
0.43	0.57
web 2	
0.32	0.68

trim mass	
s [-]	0.5018
t [m]	7.5×10^{-3}
∅ [m]	9.5×10^{-3}
mat. ID	14

Table 2.2: Web and trim mass definition of figure 2.6 and 2.7

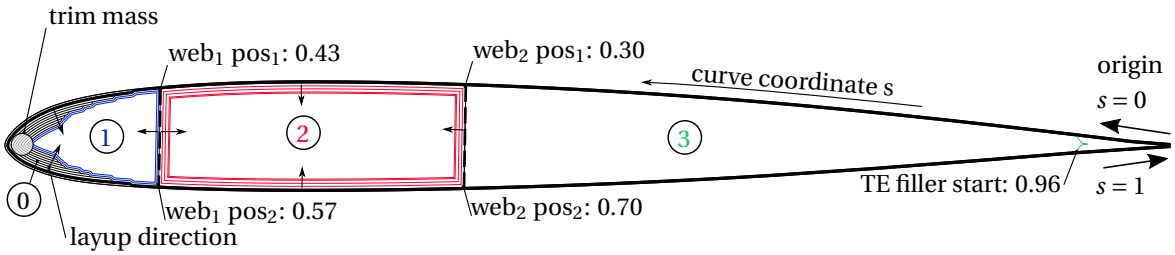

Figure 2.6: Topology definition of a generic composite UH-60A rotor blade cross section.

The first set of layers are grouped into Segment 0. The first layer generated is a steel erosion protection strip that ranges from coordinate 0.44 to 0.56 with a thickness of 0.82mm. Because of the isotropic material used, the orientation can be neglected for this layer. The material ID represents a reference index of an associated material database. The next 4 layers define the skin of the rotor blade placed in both 0° and ±45° orientation on top of each other. The layers Spar 1 to Spar 7

s_{start}	s_{end}	thickness [m]	orientation Θ_3 [°]	mat. ID	name
Segment 0					
0.44	0.56	0.82×10^{-3}	0	7	Erosion Strip
0.00	1.00	0.25×10^{-3}	0	8	Overwrap Ply 1
0.00	1.00	0.25×10^{-3}	±45	8	Overwrap Ply 2
0.00	1.00	0.25×10^{-3}	±45	8	Overwrap Ply 3
0.00	1.00	0.25×10^{-3}	0	8	Overwrap Ply 4
0.45	0.55	1.00×10^{-3}	0	2	Spar 1
⋮	⋮	⋮	⋮	⋮	⋮
0.48	0.52	1.00×10^{-3}	0	2	Spar 7
Segment 1 (filler material: 3)					
0.00	1.00	0.80×10^{-3}	45	2	Spar 8
0.00	1.00	0.80×10^{-3}	-45	2	Spar 9
Segment 2					
0.00	1.00	1.35×10^{-3}	0	9	Spar Cap Ply 1
0.00	1.00	1.35×10^{-3}	45	9	Spar Cap Ply 2
0.00	1.00	1.45×10^{-3}	-45	9	Spar Cap Ply 3
0.00	1.00	0.50×10^{-3}	90	9	Spar Cap Ply 4
Segment 3 (filler material: 11)					
0.96	0.04	0.8×10^{-3}	45	8	TE Filler

Table 2.3: Layup definition of figure 2.6 and 2.7

are unidirectional carbon fiber composite layers that generate a C-spar with a ply drop-off in the leading edge region of the cross-section.
Once the first set of layers (Segment 0) has been created, webs are introduced to the structure. They are defined in this example as a straight line between two positions. The first web ranges from coordinate 0.43 to 0.57 while the second is placed behind from 0.30 to 0.70.
The three newly generated closed curved geometries are used to repeat the layup procedure. During the manufacturing process this translates to a process of wrapping plies around a core. A core material is assigned to Segment 1 and 3 that fills up the remaining cavity. Segment 2 consists of four carbon fiber layers of different orientation from 0 to 1 to generate a hollow box spar.
After the layup is defined a trim mass can be placed on top of the existing layers and will be integrated into the structure during the discretization. Table 2.2 shows the current parameterization of the trim mass. In this case, the curve coordinate s on the outer boundary curve is used together with a normal distance to define the position of the center of the circle with the specified diameter $\varnothing$. Some rotor blades have triangular or semicircular trim masses to move the weight even closer to the leading edge to influence the center of gravity even more efficiently. Although it is not yet implemented in the parameterization, the shape of the trim mass, which will be mapped into the structure later during meshing, can be chosen arbitrarily.

Research at the National Renewable Energy Laboratory (NREL) by Mendoza et al. [110] extended the functionality to include a parametric curvature variable of the shear web by defining it as a quadratic Bézier spline. While the first and the last control point remain fixed on the layup of segment 0, the control point in the middle is changed by the input value curves the web. They implemented the addition in order to study innovative inflatable blade concepts for wind turbine blades.

2.3 Discretization

Once the cross-sectional topology has been generated, while respecting the layup definitions, the finite element discretization of the mesh follows in a reversed order – from the inside to the outside. Each layer is meshed by orthogonal projections with corner style differentiation. Figure 2.8 shows the first six cornerstyles that are currently implemented while figure 2.7 shows the final result of the described procedure.

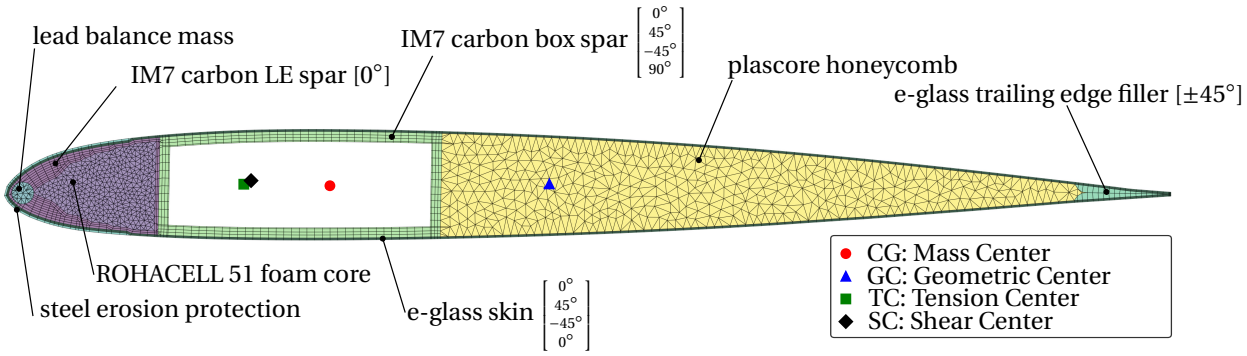

Figure 2.7: SONATA-CBM discretization of a generic composite UH-60A rotor blade cross-section in reference to [140] to illustrate the modeling capabilities.

As figure 2.5 illustrates, each layer is described by two *BSplineLst*, the inner $a_{BSplineLst}$ and outer $b_{BSplineLst}$. The nodes placed on them are called accordingly a_{nodes} and b_{nodes}. The following procedure is applied to each layer, starting at the innermost, and moving outwards.

1. Based on the inverse relevant cumulated boundaries of the intervaltree structure of the layup (see figure 2.4) the existing a_{nodes} are determined. If sections on the a_{bsplines} are found with no preexisting nodes (grey), new nodes are generated and distributed equidistantly on each B-Spline of the *BSplineLst*, thus respecting the corners of it. The equidistant spacing of the nodes is defined by a global length measure (l). The user can control the width and resolution quality of the elements by this length measure with the resolution parameter (res). The resolution parameter describes approximately the number of points on the original

curve of segment zero (L_0). This results in the following inverse proportional relationship: $l = L_0/\text{res}$.

2. Orthogonal projections of each a_{node} onto the $b_{BSplineLst}$ are created. If two or more projections are found within the default tolerance of 1.01 times the layer thickness, angle of the potential corner α is determined and the number of potential b_{bsplines} corners between them is identified.

3. Based on a critical angle α_{crit} and the number of exterior corners the corner-style and as a consequence the meshing procedure is determined. In figure 2.8 the first 6 different corner styles are shown.

4. After all nodes are placed on both sets of B-splines, they are connected to form cells with associated material and ply angles, producing quadrilateral cells as the common structural grid. The ply cutoff generates triangular cells.

5. In subsequent steps sharp cells, large aspect-ratio cells and cell angles are modified to improve mesh quality.

Cornerstyle 0 represents the case when two or more orthogonal projections are found but no exterior corner is present. The corresponding b_{node} is defined by the intersection of the bisecting vector between the first and last orthogonal projection point.
Cornersytle 1 is self-explanatory. The exterior corner on $b_{BSplineLst}$ represents the corresponding b_{node} to the identified corner node.
Cornerstyle 2, determines the desired b_{node} by using the mid point between the two orthogonal projected points to create a straight line. The intersection with the $b_{BSplineLst}$ defines the remaining b_{node}.
Analog to Cornerstyle 1, Cornerstyle 3 is defined by using the exterior corner as the missing b_{node} to form a quadrilateral cell.
Cornerstyle 4 and 5 use the multiple exterior corners to form quadrilateral cells. Cornerstyle 4 creates the missing node analog to Cornerstyle 2 by using the mid-point projection.

If the angle α of one corner is below α_{crit} (default 50°) the sharp corner is improved by placing equidistant nodes (middle nodes) on the connecting line between the two corner nodes (see figure 2.9). Similar orthogonal projections create front and back nodes to define new cells.

Since the mesh propagates from the inside to the outside, there is an inevitable elongation of the elements in areas of strong curvature, which increases from layer to layer. If the aspect ratio reaches

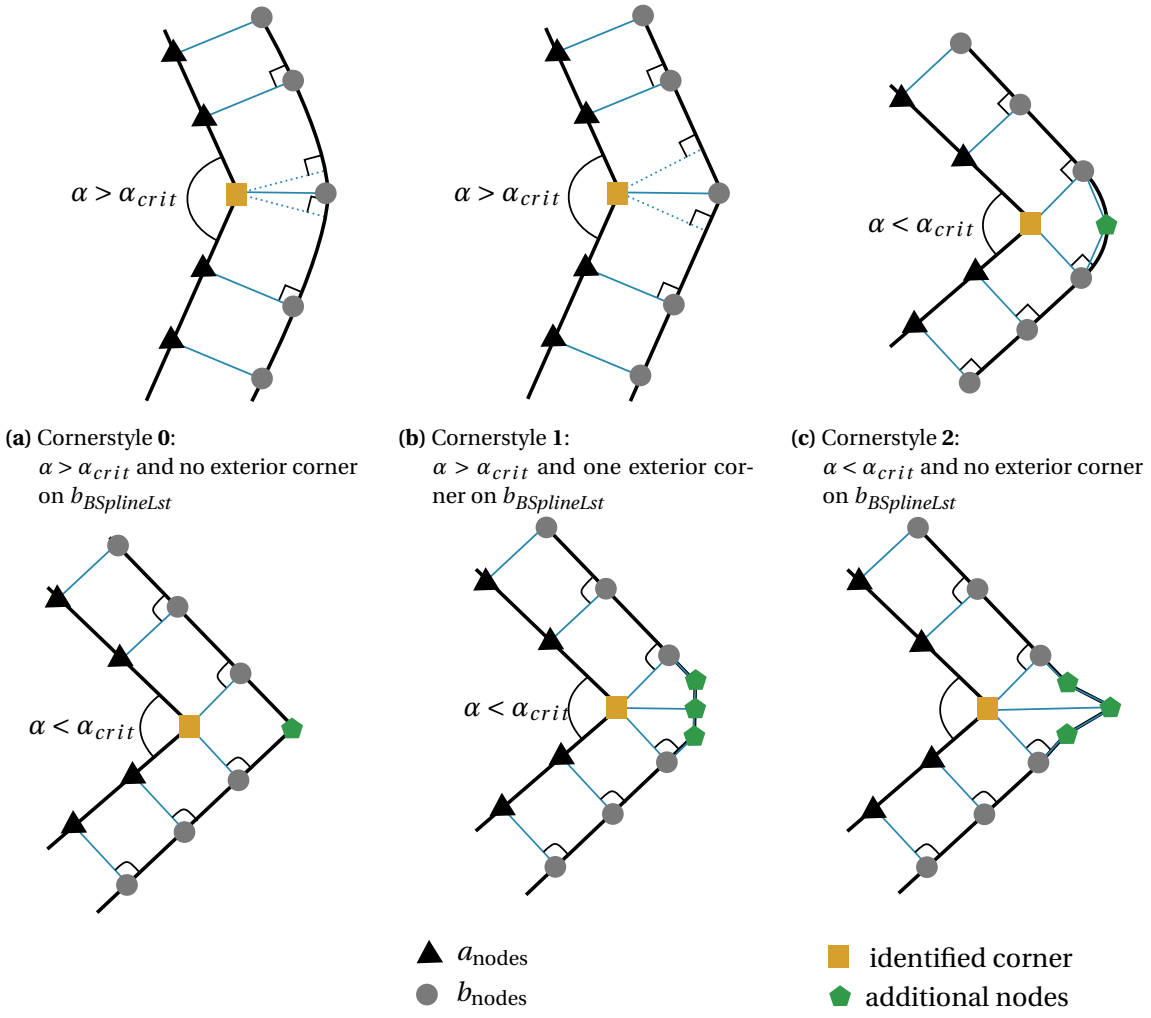

(a) Cornerstyle **0**: $\alpha > \alpha_{crit}$ and no exterior corner on $b_{BSplineLst}$

(b) Cornerstyle **1**: $\alpha > \alpha_{crit}$ and one exterior corner on $b_{BSplineLst}$

(c) Cornerstyle **2**: $\alpha < \alpha_{crit}$ and no exterior corner on $b_{BSplineLst}$

(d) Cornerstyle **3**: $\alpha < \alpha_{crit}$ and one exterior corner on $b_{BSplineLst}$

(e) Cornerstyle **4**: $\alpha < \alpha_{crit}$ and two exterior corners on $b_{BSplineLst}$

(f) Cornerstyle **5**: $\alpha < \alpha_{crit}$ and three exterior corners on $b_{BSplineLst}$

Figure 2.8: Cornerstyles 0 to 5 between two sets of B-Splines, the inner $a_{\text{BSplineLst}}$ with the a_{nodes} and the outer $b_{\text{BSplineLst}}$ with the b_{nodes}.

the default limit of 1.8, the cell is broken up into three triangular cells.
The same effect happens in concave region but with the opposite effect to decrease the aspect ratio and causes the cell size to decrease. Therefore, when the node distant reaches a certain threshold, the nodes of close vicinity are merged.

As soon as every layer of the segment is meshed, the remaining cavities are triangulated with an area constraint. It uses the Triangle module, which is a python wrapper around Jonathan Richard Shewchuks [156] two-dimensional mesh generator and delaunay triangulator library. The starting

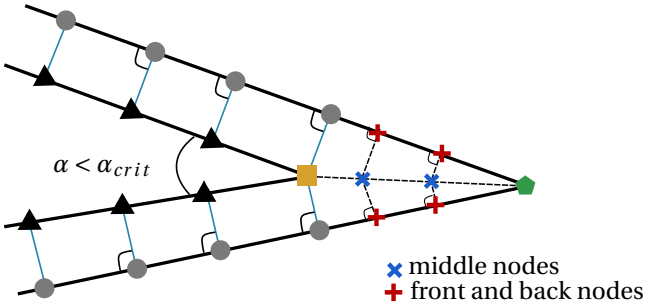

Figure 2.9: Sharp corner modification

point and boundary for the triangulation are all nodes that are on the innermost boundary of the generated topology.

After the mesh has been generated for every segment, the cells are consolidated on web interfaces to make sure that no hanging nodes remain in the mesh. A node matching matrix $\underline{\underline{NM}}$ is created, based and sorted on the individual node to node distances of the layers left and right of the web. Remaining cells with hanging nodes are split. Identified quad cells, that are intersected by the hanging nodes, are split into a triangle and a quad and an identified triangle cell into two triangles.

An optional and final step integrates geometrical shapes in the existing mesh. As described, *SONATA* currently supports the use of circular trim masses which can be modified to other arbitrary geometries. The corresponding algorithm to map existing nodes onto the contour line of a specified shape is schematically illustrated in Figure 2.10a.
In preparation, all cells that are intersected by the contour, or are positioned completely inside, are identified and marked according to the number of nodes located inside the contour. During step 1, the inner nodes of each cell marked with 1 (i.e., one node of that cell is inside the shape) is moved along the cell edge with the shortest distance to the intersecting curve. The second step moves the remaining inner nodes of cells marked 2 along the shortest edge direction onto the intersecting curve. Finally, step 3 moves the outer nodes of cells marked with 3 along the edge direction onto the intersecting curve. Once the process in completed, inner cells marked with 3 and 4 are deleted. A new unstructured mesh is created by using the boundary nodes as starting point for the triangulation inside the shape and allocated them the defined material properties.

Following the *VABS* layup convention [178], three coordinate systems are present within the definition of each element. The local beam coordinate system (x_l, y_l, z_l) as defined in figure 2.2 at which the beam properties are evaluated.
The intermediate ply coordinate system (x_p, y_p, z_p) as illustrated in figure 2.11 is formed by rotating

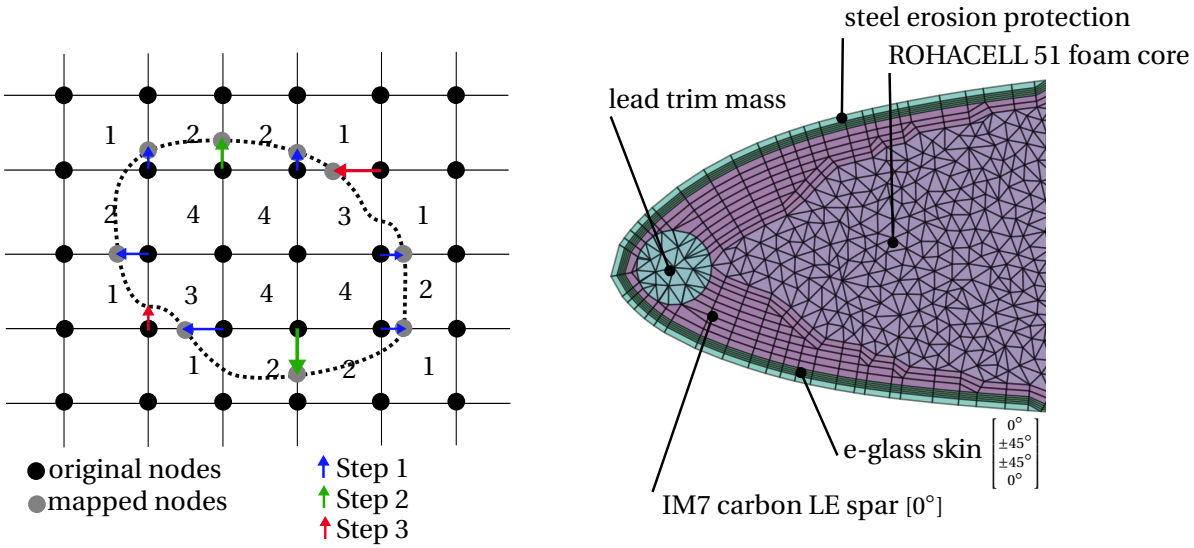

(a) Schematic representation of the algorithm

(b) Leading edge region of figure 2.7 showing the scarfed ply drops of the C-Spar and the integration of a circular trim mass into the existing mesh.

Figure 2.10: Schematic representation and application of the mapping algorithm to embed arbitrary curves into an existing mesh.

the cbm coordinate system (x_l, y_l, z_l) about x_l by the amount of θ_{11} so that y_p is parallel to the underlying layer. The ply angle for triangulated unstructured components remain zero.
The material coordinate system (x_m, y_m, z_m) is defined by rotating the ply coordinate system by the amount of θ_3 about z_p. The material or fiber orientation angle θ_3 is defined by the layup table (see table 2.3) between -90° and 90°.

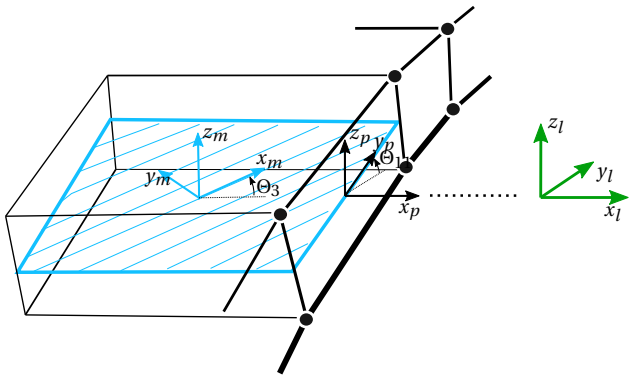

Figure 2.11: Local coordinate system definition adapted from [178]

Each cell that is created in the discretization process is associated with a material, which elastic constants are always expressed in material coordinates. It can either be isotropic with as few as two

elastic constants, orthotropic with 9 independent elastic constants or general anisotropic with as many as 21 elastic constants. The mass density ρ, coefficients of thermal expansion and strength characteristics complete the material description. Strength characteristics are of particular relevance when failure criteria are applied to subsequent analysis.

SONATA is further capable of splitting quadrilateral cells into two triangular cells. This is especially useful for the *ANBA4* solver that consistently requires either quadrilateral or triangular elements but does not support the combination of those.

2.4 Applications

With its generic architecture, the application of *SONATA*, although specifically designed for this purpose, is not limited to helicopter rotor blades. Rather, it allows a much wider range of applications for fiber composite beams. As long as the cross-section is closed, an almost unlimited variety of composite structures can be realized. By small changes in the software architecture, the methodology can be extended to open cross sections in the future.
In figure 2.12 a few application examples are shown. It starts with a rectangular box beam, the simplest cross sections used for validation and mesh convergence studies. The second cross-section in figure 2.12b shows a truly generic example, which illustrates the possible curvature of a web. Furthermore, the round contour was placed in the triangulated area. In this example it is also clear that the cell height always corresponds to the layer thickness. If very thick layers are used to create the topology, it often results in very stretched cells. In the area of the greatest curvature of these layers, the cells are divided based on the aspect ratio of the cell edges, to prevent further growth or shrinkage as the discretization algorithm propagates through the layup. Figure 2.12c shows a symmetric helicopter rotor blade that uses a very distinctly pronounced C shaped spar in combination with a reversed D shear web. The skin and the shear web are composed of 3 layers $\pm 45°$ twill weave carbon fiber reinforced plastic. The spar of unidirectional material in axial direction shows the propagation and smoothing of the ply cutoff. In this example, the quadrilateral elements of the layup were split into triangular elements to ensure a common element type across the mesh.
The last example, shows the full potential of the methodology, by incorporating the most common topology requirements from rotorcraft or wind turbine blades. It essentially combines the topology features of the generic composite UH-60A rotor blade cross-section of figure 2.7 in the front with shear webs and spar-caps similar to the ones found in wind-turbine blade architectures. In this example, the rear shear webs contain a triangulated area that is created by two webs front and aft of the yellow triangulated cavity.

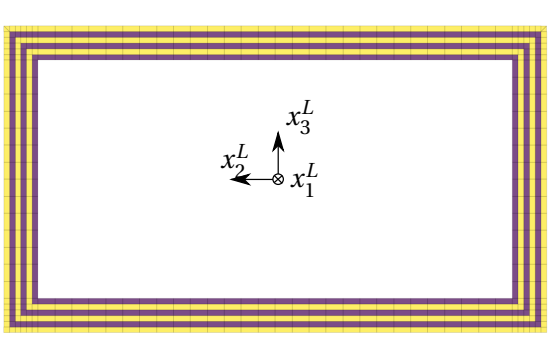

(a) Box beam cross-section with 6 layers

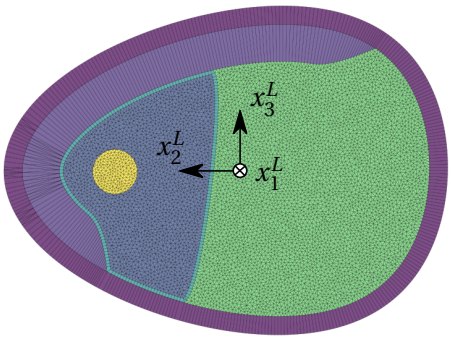

(b) Generic cross-section with a curved web (implemented by Feil [48])

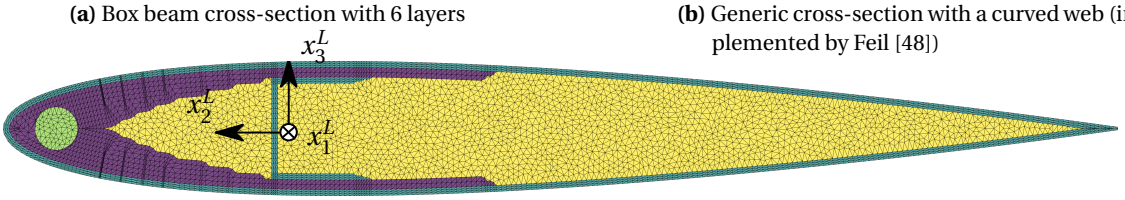

(c) Generic C-spar rotor blade cross-section with shear web and trim mass

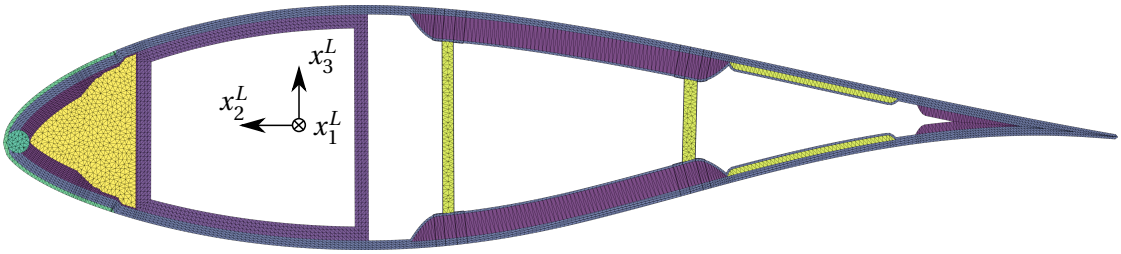

(d) Generic windturbine rotor blade cross-section with multiple shear webs, spar caps, trailing edge filler, etc. Adapted from [48]

Figure 2.12: Application examples of SONATA

Because every parameter of the described procedure can serve as design variable in later optimizations or numerical studies, it is often helpful to develop a surrogate model of the selected topology architecture. Bortolotti and Feil at the National Renewable Energy Laboratory (NREL) in Boulder, Colorado therefore developed a surrogate format that groups and handles the complex architecture and reduces a wind-turbine specific architecture to fewer design variables that can be defined globally along the radius.

2.4.1 Beam Sectional Properties

SONATA has been implemented to either use the commercial solver *VABS* or the open-source solver *ANBA4* [48], [115] to solve the two-dimensional local deformation field in a cross-sectional analysis to reduce the three-dimensional problem to a nonlinear one-dimensional beam analysis.
VABS and *ANBA4* use the finite element mesh of each cross-section, with all details of its geome-

try and materials, as inputs to calculate the cross-sectional properties of the beam, that includes the sectional stiffness properties and the inertia properties. These properties are required for performing a one-dimensional beam analysis to predict the global behavior of the slender structural component. From sectional loads or on the basis of the global behavior of the beam the three-dimensional displacement, strain and stress distribution within the structure can be recovered in both the local cross-sectional frame and the material frame [178]. Details about the recovered beam properties, postprocessing functionalities and the result evaluation within the *SONATA* framework are given in this section. Studies in this work were conducted with *VABS* version 3.4 [178] and *ANBA4* (i.e, ANBA version 4.0).

The sectional properties of the beam are defined in the local CBM coordinate system denoted with subscript L, which is attached to the beam reference curve, as illustrated in figure 2.2. Axis $\underline{x_L}$ is tangent to the curve, and $\underline{y_L}$ and $\underline{z_L}$ defined the cross-sectional plane. The geometry of the beam is defined by the beam reference curve.
The symmetric 6×6 sectional stiffness matrix, $\underline{\underline{K}}$, relates the sectional strains $\underline{\epsilon_c}^T = (\epsilon_1, \epsilon_2, \epsilon_3, \kappa_1, \kappa_2, \kappa_3)$ with the sectional axial strain ϵ_1, transverse shearing strains, ϵ_2 and ϵ_3, twisting rate κ_1 and two bending curvatures, κ_2 and κ_3 to the stress resultant vector $\underline{F}^T = (F_1, F_2, F_3, M_1, M_2, M_3)$ with the axial force F_1, transverse shear forces, F_2 and F_3, twisting moment M_1 and the two bending moments M_2 and M_3. The three forces are the resultants of the stress distributions across the cross section of the beam, while the three moments are evaluated with respect to the reference axis of the beam. The inverse of the sectional stiffness matrix, i.e. $\underline{\underline{S}} = \underline{\underline{K}}^{-1}$, is the symmetric sectional compliance matrix. [11]

$$\begin{pmatrix} F_1 \\ F_2 \\ F_3 \\ M_1 \\ M_2 \\ M_3 \end{pmatrix} = \begin{bmatrix} K_{11} & K_{12} & K_{13} & K_{14} & K_{15} & K_{16} \\ K_{12} & K_{22} & K_{23} & K_{24} & k_{25} & K_{26} \\ K_{13} & K_{23} & K_{33} & k_{34} & K_{35} & K_{36} \\ K_{14} & K_{24} & K_{34} & K_{44} & K_{45} & K_{46} \\ K_{15} & K_{25} & K_{35} & k_{45} & K_{55} & K_{56} \\ K_{16} & K_{26} & K_{36} & K_{46} & K_{56} & K_{66} \end{bmatrix} \begin{pmatrix} \epsilon_1 \\ \epsilon_2 \\ \epsilon_3 \\ \kappa_1 \\ \kappa_2 \\ \kappa_3 \end{pmatrix}; \quad \underline{F} = \underline{\underline{K}}\,\underline{\epsilon_c} \tag{2.2}$$

If the cross-sectional properties are to evaluated at a different location and coordinate systems (p) other than the beam reference frame from figure 2.2. It can be transformed with a translation and rotation of the second order tensors by applying the motion tensor $\underline{\underline{C}}_p$. [159].

$$\underline{\underline{K}}_p = \underline{\underline{C}}_p^T \underline{\underline{K}}\,\underline{\underline{C}}_p; \quad \text{with} \quad \underline{\underline{C}}_p = \begin{bmatrix} \underline{\underline{R}}_\alpha & \tilde{r}_p \underline{\underline{R}}_\alpha \\ 0 & \underline{\underline{R}}_\alpha \end{bmatrix} \tag{2.3}$$

The motion tensor is composed of the rotation matrix $\underline{\underline{R}}_\alpha$ and the skew-symmetric representation of the two-dimensional position vector $\tilde{r}_p$.

$$\underline{\underline{R}}_\alpha = \begin{bmatrix} 1 & 0 & 0 \\ 0 & \cos(\alpha) & -\sin(\alpha) \\ 0 & \sin(\alpha) & \cos(\alpha) \end{bmatrix}, \qquad \tilde{r}_p = \begin{bmatrix} 0 & -z_p & y_p \\ z_p & 0 & 0 \\ -y_p & 0 & 0 \end{bmatrix} \tag{2.4}$$

It is of frequent interest to the engineer that in addition to the stiffness matrix of the cross section, beam characteristics such as the tension center, the principal axes of bending, the shear center location and the principal axes of shear are recovered.
The symmetric 6×6 sectional stiffness matrix contains this additional information. The so-called tension center or centroid of the cross section is the location where an applied axial load in the direction $\underline{x}_l$ induces no bending moment ($K_{15} = K_{16} = 0$) [159]. It's location with respect to the beam reference coordinate system is determined from the following components of the sectional stiffness matrix $\underline{\underline{K}}$:

$$x_{t2} = -\frac{K_{16}}{K_{11}}, \quad x_{t3} = \frac{K_{15}}{K_{11}} \tag{2.5}$$

By definition, the principal axes of bending are such that the bending coupling relation $K_{56} = 0$ [13]. This results in equation (2.6) for the alignment of the principal bending axes.

$$\alpha_{pb} = \frac{1}{2}\tan^{-1}\left(\frac{-2K_{56}}{K_{66} - K_{55}}\right) \tag{2.6}$$

If the stiffness matrix is now evaluated in a coordinate system at the location of the tension center and with its orientation with respect to the bending principal axes, the terms K_{16}, K_{15} and K_{56} all become zero and the corresponding principal stiffnesses in the transformed frame reach a maximum and a minimum, respectively.

The torsional deformation generated by the transverse shear forces F_2 and F_3 vanishes, when the transverse loads are applied at the shear center. Or in other terms, if the sectional stiffness matrix is evaluated at the shear center, the coupling relations between transverse shear and torsion must become zero ($K_{24} = K_{34} = 0$). It's location is defined as:

$$x_{s2} = -\frac{K_{22}K_{34} - K_{23}K_{24}}{K_{22}K_{33} - K_{23}^2}, \quad x_{s3} = \frac{K_{23}K_{34} - K_{33}K_{24}}{K_{22}K_{33} - K_{23}^2}. \tag{2.7}$$

Analog to the principal axes of bending, the principal axes of shear are defined such that the coupling relation K_{23} vanishes under the following rotation of the coordinate system

$$\alpha_{ps} = \frac{1}{2}\tan^{-1}\left(\frac{-2K_{23}}{K_{22} - K_{33}}\right). \tag{2.8}$$

At a coordinate system, located at the shear center with its orientation with respect to the principal axes of shear, the terms K_{23}, K_{24} and K_{34} all become zero and the corresponding principal shear stiffnesses reach again a maximum and a minimum.[159]

For a complete characterization of a beam cross-section, the mass and inertia properties are required in conjunction with the stiffness properties. The relationship between the sectional linear velocities (v_1, v_2, v_3) and angular velocities (w_1, w_2, w_3) to the sectional linear and angular momentum vector $\underline{P}^T = \{p_1, p_2, p_3, h_1, h_2, h_3\}$ is described with respect to the beam reference coordinate system by the symmetric 6×6 sectional mass matrix $\underline{\underline{M}}$ with the following form: [11]

$$\begin{pmatrix} p_1 \\ p_2 \\ p_3 \\ h_1 \\ h_2 \\ h_3 \end{pmatrix} = \begin{bmatrix} m_{00} & 0 & 0 & 0 & m_{00}x_{3m} & -m_{00}x_{2m} \\ 0 & m_{00} & 0 & -m_{00}x_{3m} & 0 & 0 \\ 0 & 0 & m_{00} & m_{00}x_{2m} & 0 & 0 \\ 0 & -m_{00}x_{3m} & m_{00}x_{2m} & m_{11} & 0 & 0 \\ m_{00}x_{3m} & 0 & 0 & 0 & m_{22} & -m_{23} \\ -m_{00}x_{2m} & 0 & 0 & 0 & -m_{23} & m_{33} \end{bmatrix} \begin{pmatrix} v_1 \\ v_2 \\ v_3 \\ w_1 \\ w_2 \\ w_3 \end{pmatrix}; \quad \underline{P} = \underline{\underline{M}}\,\underline{V} \tag{2.9}$$

The entries are described by the surface integral over the cross-section with the distinctive material density ρ. m_{00} is the sectional mass per unit span. x_{2m} and x_{3m} describe the location of the sectional center of mass. m_{22} and m_{33} are the sectional mass moments of inertia per unit span about the y_l and z_l unit vectors. m_{23} is the cross-product of inertia and $m_{11} = m_{22} + m_{33}$ the polar moment of inertia per unit span.

$$\begin{aligned} m_{00} &= \int_{\mathcal{A}} \rho \, d\mathcal{A}, & m_{22} &= \int_{\mathcal{A}} \rho x_2^2 \, d\mathcal{A}, \\ m_{00}x_{2m} &= \int_{\mathcal{A}} \rho x_2 \, d\mathcal{A}, & m_{33} &= \int_{\mathcal{A}} \rho x_3^2 \, d\mathcal{A}, \\ m_{00}x_{3m} &= \int_{\mathcal{A}} \rho x_3 \, d\mathcal{A} & m_{23} &= \int_{\mathcal{A}} \rho x_2 x_3 \, d\mathcal{A} \end{aligned} \tag{2.10}$$

2.4.2 3D Strain, Stress and Displacement Analysis

The classical application in a multidisciplinary rotor blade design, analysis, or optimization is to perform a modal analysis or aeroelastic analysis in the time domain after determining the beam properties of the rotor blade. In the latter, for example, load cases and flight conditions are calculated and, for this purpose, the vibration behavior, elastic blade deformation and internal forces are determined. The one-dimensional sectional forces along the beam $\underline{F}(x_l)$ are the input values for

the evaluation of the three-dimensional strain, stress and deformation states in the cross section. Figure 2.13 shows the recovered axial strain field $\epsilon_{11,L}$ of the generic UH-60A rotor blade under a pure flap bending moment of $M_2 = 1000$ Nm. Under the same load case, the in-plane warping displacement of the cross-section is shown. To illustrate the effects for this example, a magnification factor of 100 is used. Besides recovering the warping displacements of the cross-section, the warping derivatives are recovered as well when using *ANBA4*.

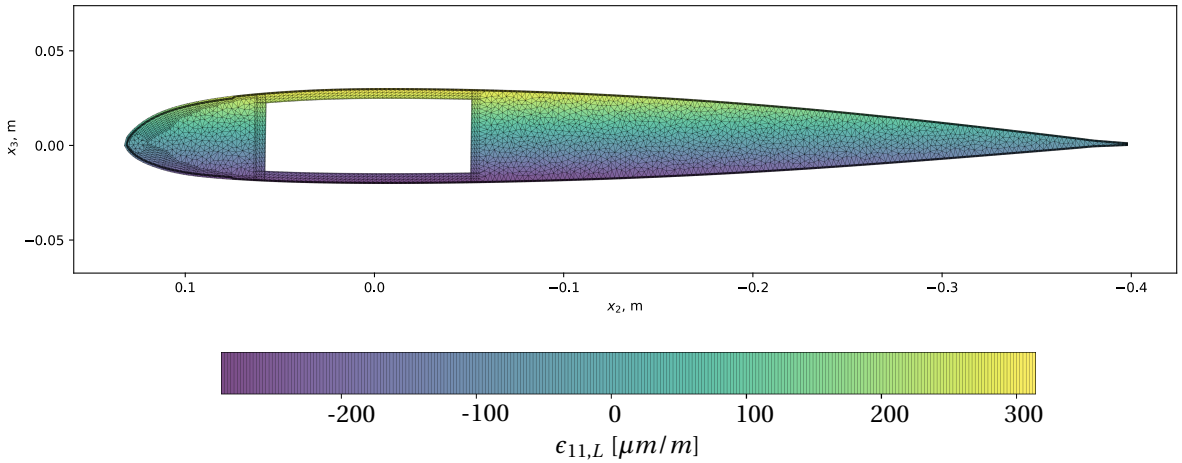

Figure 2.13: Axial strain field ($\epsilon_{11,L}$) of the generic UH-60A rotor blade under pure flap bending moment $M_2 = 1000$ Nm.

Defining the strength of a material in conjunction with its elastic properties makes it possible for failure criteria to predict its safety factor (SF) as well as possible failure modes. For this purpose, already existing composite modules by João Paulo Bernhard [20] were adapted and implemented. The safety factor and the failure mode can currently be calculated according to the layer-wise two-dimensional maximum-stress, maximum-strain, Tsai-Wu and Hashin criterion for composite materials and according to the von Mises yield criterion for isotropic metallic components at which failure of the component occurs when the strain energy exceeds a limit value.

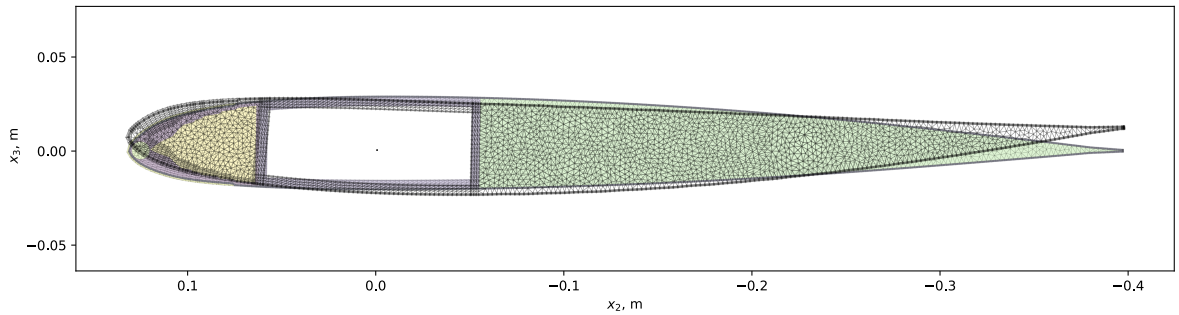

Figure 2.14: In-plane warping displacement of the generic UH-60A Rotor Blade under pure flap bending moment $M_2 = 1000$ Nm. The warping displacement is magnified by a factor of 100 for better illustration.

2.5 Validation

Parts of this section were developed as part of a collaboration between the National Renewable Energy Laboratory (NREL), the Politecnico di Milano, Italy and the Institute of Helicopter Technology at TUM with the goal to verify and validated both *SONATA* and *ANBA4*. Partial results have been published in 2020 in the Journal of Composite Structures COMPSTRUC2020. A secondary objective of this section is to study the mesh convergence of *SONATA*, even though it was performed by Morandini [115] separately for *ANBA4*.

In the following, results from *SONATA*, using both *VABS* and *ANBA4*, are compared to other well-investigated approaches from literature based on *VABS* and *NABSA* data for the very same test cases. *NABSA* stands for Nonhomogeneous Anisotropic Beam Section Analysis, which is a two-dimensional finite element program developed by Bauchau and is based on the work Giavotto et al. [56]. Current validation objectives are to demonstrate the accuracy of the parametric processing, topology, and meshing features within *SONATA*, and its interfaces to *VABS* and *ANBA4*. While *VABS* is a commercial off-the-shelf solution, the following comparisons of *ANBA4* results with both current VABS results and previous studies from literature serve to gain confidence in using the current version of *ANBA4* as a valuable open-source option. All examples make use of linear triangular elements.

2.5.1 Isotropic Circular Cross Section

In the first study, a simple circular tube made of aluminum which has an outer radius of $R = 0.3\,\text{m}$, an inner radius of $R_i = 0.1$ m, with the Young's modulus of E=73 GPa, Poison's ratio of $\nu = 0.33$ and the density of $\rho = 2800\,\text{kg/m}^3$ is used. This benchmark example was also used by Chen [40] and Hu [73] during the validation and assessment of *PreVABS*, *VABS-IDE* and *VABS-GUI*, which are all structural two-dimensional finite element preprocessors specifically designed for the use with *VABS*. This specific study was supported by Cole Saunders [144] during his term project.
A mesh convergence study is performed by refining the mesh with *SONATA* by increasing the number of layers and the mesh resolution parameter, which is globally responsible for the width of the cells. Attention is paid, that the aspect ratio of the cells are well-balanced. Starting with only one layer to model the complete thickness of the circular tube with as little as 34 elements, the study refined the resolution up to 40 layers and 8040 elements. Figure 2.15 shows the case of 4 and 8 layers that resulted in 136 and 536 linear quadrilateral elements with 4 nodes respectively. Depending on the resolution, the outer circle curve becomes a more or less good approximation of the perfect circle. This leads to the fact that in each case the effective circle area and thus also

the stiffnesses are lower compared to the analytical solution.

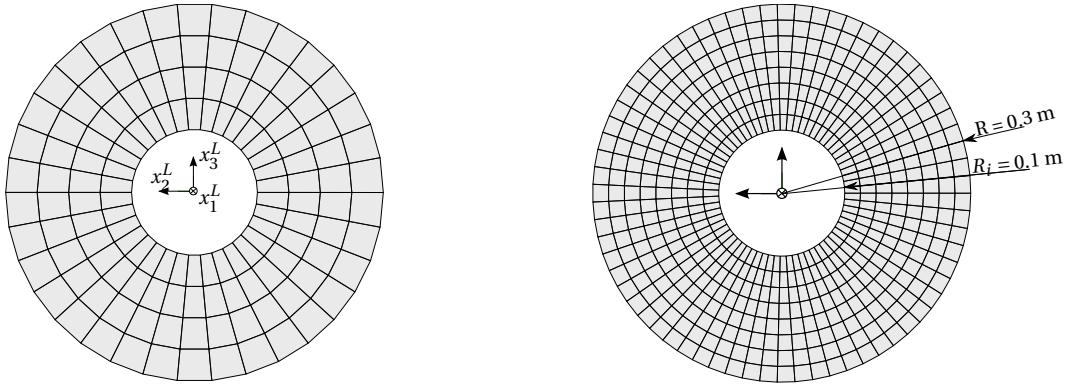

(a) 4 layers and 136 linear quadrilateral elements with 4 nodes each

(b) 8 layers and 536 linear quadrilateral elements with 4 nodes each

Figure 2.15: Isotropic circular cross-sectional dimensions and discretization

The results are shown in table 2.4 and the corresponding figure 2.16 showing the relative error compared to the analytical solution K_a and to the other two-dimensional finite element preprocessors *VABS-IDE, VABS-GUI* and *PreVABS* [39]. While *SONATA* and *PreVABS* follow a similar approach to create a structured mesh using layer information and the projection of nodes orthogonal to the layers, the *VABS-IDE* and *VABS-GUI* discretization resulted in a unstructured triangulated representation of the cross-section. Note, that in the example the *PreVabs* mesh uses 8 node second order quadrilateral elements, which is a possible explanation of a lower relative error at the same number of elements compared to the *SONATA*/*VABS* results.

Preprocessor	**Nb. of Elements**	**Stiffness Coefficients** K_{11} [N]	K_{22} [N]	K_{33} [N]	K_{44} [Nm^2]	K_{55} [Nm^2]	K_{66} [Nm^2]
Analytical Results		1.835E+10	-	-	3.449E+08	4.587E+08	4.587E+08
VABS-IDE [73]	159	1.835E+10	4.835E+09	4.832E+09	3.414E+08	4.585E+08	4.585E+08
	553	1.835E+10	4.726E+09	4.727E+09	3.439E+08	4.581E+08	4.581E+08
	2179	1.834E+10	4.716E+09	4.727E+09	3.496E+08	4.568E+08	4.586E+08
VABS-GUI [73]	161	1.834E+10	4.682E+09	4.682E+09	3.515E+08	4.586E+08	4.586E+08
	577	1.834E+10	4.695E+09	4.695E+08	3.515E+08	4.586E+08	4.586E+08
	2177	1.834E+10	4.683E+09	4.683E+09	3.515E+08	4.586E+08	4.586E+08
PreVABS [40]	1216	1.834E+10	4.682E+09	4.682E+09	3.515E+08	4.586E+08	4.586E+08
SONATA/VABS	34	1.824e+10	4.772e+09	4.772e+09	3.410e+08	4.592e+08	4.592e+08
	68	1.824e+10	4.721e+09	4.721e+09	3.410e+08	4.552e+08	4.552e+08
	136	1.824e+10	4.680e+09	4.680e+09	3.410e+08	4.541e+08	4.541e+08
	536	1.832e+10	4.682e+09	4.682e+09	3.439e+08	4.575e+08	4.575e+08
	840	1.833e+10	4.682e+09	4.682e+09	3.442e+08	4.579e+08	4.579e+08
	2340	1.834e+10	4.681e+09	4.681e+09	3.445e+08	4.583e+08	4.583e+08
	8040	1.834e+10	4.681e+09	4.681e+09	3.448e+08	4.585e+08	4.585e+08

Table 2.4: Stiffness of an isotropic cylindrical aluminum cross-section discretized with different two dimensional finite element preprocessors and calculated with *VABS*

Figure 2.16 shows that all solutions are well with a 1.5% range of the analytical values. As expected,

the relative error of *SONATA*/ *VABS* is reduced with increasing mesh resolution showing a satisfactory converging behavior. This cannot be claimed about the results of *VABS-IDE*. However, no specific reasons for this behavior are known.

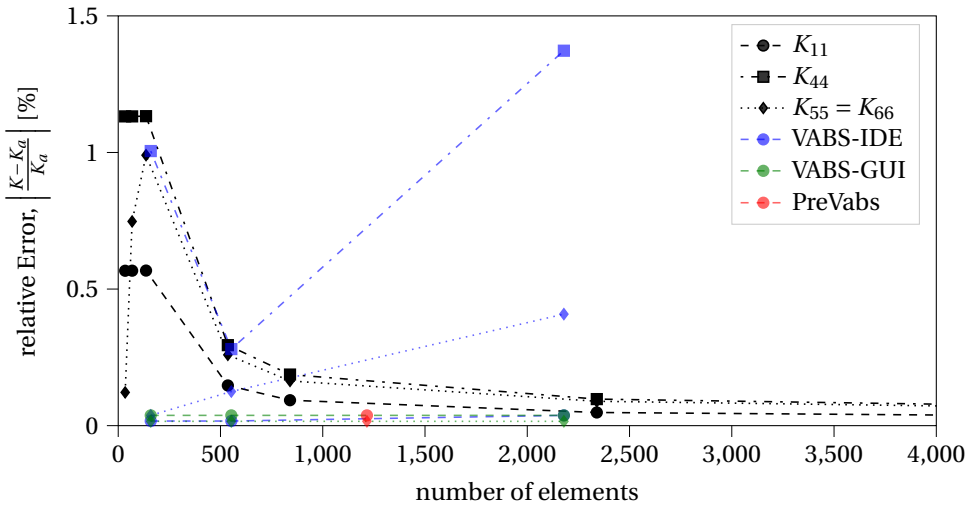

Figure 2.16: Mesh convergence of *SONATA*/ *VABS* in comparison to *VABS-IDE* [73] and VABS-GUI [73] and *PreVABS* [40]

It can be concluded, that for the first test case of the hollow cylinder with an isotropic material, the calculated results are very good compared to the published and analytical data and reached convergence with increasing resolution. The user of *SONATA* should weigh the accuracy and runtime requirements for modeling and, if necessary, do a specific mesh convergence study for the use cases.

2.5.2 Composite Box Beam

In this study, a composite box beam with three different circumferentially uniform stiffness (CUS) layup configurations, $[0°]_6$, $[-15°]_6$, and $[-30°, 0°]_3$ is considered. This is another well examined benchmark testcase with many references in literature. The fiber-orientation angles denoted in this work are in accordance with the coordinate system shown in figure 2.11. Box beam geometry properties are shown in table 2.5 and material properties in table 2.6. According to the reference case from literature [135], layup $[-15°]_6$ has a different Poisson's ratio of $\nu_{12} = 0.42$. The box beams (see Fig. 2.17) were analyzed using approximately 200 equidistant points along the outer shape, resulting in a total of 1,481 nodes and 2,536 three node triangular elements.

Table 2.7 shows the results with a $[0°]_6$ layup. Off-diagonal terms are negligible for this symmetric case. The first two columns show literature [135] results using *NABSA* and *VABS*, while the latter

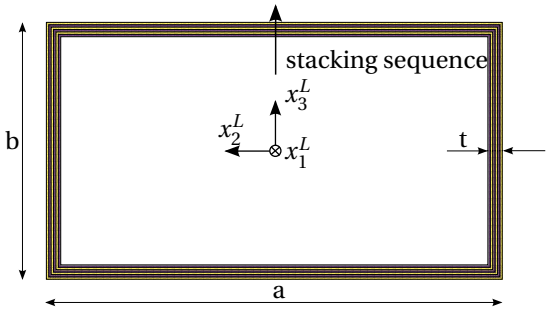

Figure 2.17: Box beam cross-sectional geometry, topology and discretized mesh

Description	Value [mm]
Width, a	24.2
Height, b	13.6
Length, L	764
Ply thickness, t_{ply}	0.127
Wall thickness (6 plies), t	0.762

Table 2.5: Box beam geometrical properties

Young's modulus [GPa]		Shear modulus [GPa]		Poisson's ratio	
E_1	142.0	$G_{12} = G_{13}$	6.0	$\nu_{12} = \nu_{13}$	0.3
$E_2 = E_3$	9.79	G_{23}	4.8	ν_{23}	0.34

Table 2.6: AS4/3501-6 Graphite/Epoxy Composite Material Properties adapted from [135] [15]

two columns show the results from SONATA, using either VABS or ANBA4 as a structural solver. Table 2.7 shows that the stiffness values derived through *SONATA* between *VABS* and *ANBA4* are identical, and the comparison of those to *NABSA* and *VABS* from previous work successfully verifies the accuracy of the *SONATA* framework. Minor differences were insignificant and can at least in part be attributed to inaccuracies in input parameters and to a minor extend to the parametric topology and mesh generation in *SONATA*.

Stiffness	*NABSA* [135]	*VABS* [135]	*SONATA*/*VABS*	*SONATA*/*ANBA4*
K_{11}, N	7.8765 E+06	7.8765 E+06	7.8603 E+06	7.8603 E+06
K_{22}, N	1.9758 E+05	1.9803 E+05	1.9764 E+05	1.9764 E+05
K_{33}, N	8.4550 E+04	8.4995 E+04	8.4745 E+04	8.4745 E+04
K_{44}, Nm^2	2.3400 E+01	2.3500 E+01	2.3471 E+01	2.3471 E+01
K_{55}, Nm^2	2.4900 E+02	2.4900 E+02	2.4951 E+08	2.4951 E+02
K_{66}, Nm^2	6.1700 E+02	6.1700 E+02	6.1619 E+08	6.1619 E+02

Table 2.7: Stiffness of a prismatic box beam with a $[0°]_6$ layup

Table 2.8 shows results with all plies being identically oriented in a $[-15°]_6$ layup and Table 2.9 in a $[-30°, 0°]_3$ layup. Both examples result in additional extension-torsion, K_{14}, and shear-bending, K_{25} and K_{36}, coupling terms. The *SONATA*/*VABS* and *SONATA*/*ANBA4* results were again identical and both showed excellent agreement with the literature. Even though VABS results from literature for the $[-30°, 0°]_3$ layup are available [135], they were excluded for this work because they were computed using an older version of *VABS*. Since *VABS* version 3.2, the energy transformation equations into the generalized Timoshenko stiffness matrix were redefined, thereby solving two

previous inconsistencies that impacted the predicted generalized Timoshenko stiffness matrix. Those changes can measurably impact stiffness results, such as in a box beam layup with nonzero material orientation angles. This was explained in detail by Ho et al. [68].

Stiffness	*NABSA* [177], [180]	*VABS* [177]	*SONATA*/*VABS*	*SONATA*/*ANBA4*
K_{11}, N	6.3947 E+06	6.3947 E+06	6.3636 E+06	6.3636 E+06
K_{14}, Nm	1.2139 E+04	1.2139 E+04	1.2030 E+04	1.2030 E+04
K_{22}, N	4.0157 E+05	4.0170 E+05	3.9458 E+05	3.9458 E+05
K_{25}, Nm	-5.8787 E+03	-5.8787 E+03	-5.8417 E+03	-5.8417 E+03
K_{33}, N	1.7533 E+05	1.7546 E+05	1.7543 E+05	1.7543 E+05
K_{36}, Nm	-6.3692 E+03	-6.3692 E+03	-6.3106 E+03	-6.3106 E+03
K_{44}, Nm^2	4.8200 E+01	4.8200 E+01	4.8412 E+01	4.8412 E+01
K_{55}, Nm^2	1.9000 E+02	1.9000 E+02	1.9426 E+02	1.9426 E+02
K_{66}, Nm^2	4.9500 E+02	4.9500 E+02	4.9453 E+02	4.9453 E+02

Table 2.8: Stiffness of a prismatic box beam with a $[-15°]_6$ layup

Stiffness	*NABSA* [135]	*SONATA*/*VABS*	*SONATA*/*ANBA4*
K_{11}, N	5.5625 E+06	5.5400 E+06	5.5400 E+06
K_{14}, Nm	5.8889 E+03	5.8832 E+03	5.8832 E+03
K_{22}, N	4.3655 E+05	4.3695 E+05	4.3695 E+05
K_{25}, Nm	-2.9840 E+03	-2.9803 E+03	-2.9803 E+03
K_{33}, N	1.8868 E+05	1.8898 E+05	1.8898 E+05
K_{36}, Nm	-3.1422 E+03	-3.1432 E+03	-3.1432 E+03
K_{44}, Nm^2	5.0800 E+01	5.0867 E+01	5.0867 E+01
K_{55}, Nm^2	1.7600 E+02	1.7622 E+02	1.7622 E+02
K_{66}, Nm^2	4.3600 E+02	4.3584 E+02	4.3584 E+02

Table 2.9: Stiffness of a prismatic box beam with a $[-30°, 0°]_3$ layup

2.5.3 Wind Turbine Numerical Analysis

This section analyzes the recently published 15-MW reference wind turbine blade [51]. The publicly available datasets were provided by Feil and Bortolotti of NREL [48]. The example demonstrates the capabilities of *SONATA* and was assessed in an appropriate context to further validate the use of *ANBA4* in comparison to *VABS* with and without the consideration of initial twist and curvature in the solution procedure.

The blade has a total length of 117 m, a circular blade root with a diameter of 5.2 m and a maximum blade chord of 5.77 m at the radial station $r/R = 0.272$ [48]. The total mass integrates to approximately 68 tons.

The blade 3D geometry and nine exemplary cross sections were previously illustrated in figure 2.1. Its internal structure consists of unidirectional and triaxial glass-composite materials, carbon-composite spar caps, and additional layers of foam and gelcoat [48]. At 28 radial sections the topology and finite element mesh was created in the process. In this context a surrogate description of the topology by Feil and Bortolotti is used to reduce the wind-turbine specific architecture to fewer design variables globally along the span.
This abstraction level contains, instead of a layer-by-layer definition, the description of more comprehensive structural components such as the skin, spar-caps, leading and trailing edge reinforcements, webs and multiple filler and sandwich definitions. However, note that all components translate in the end to the same topology definition and meshing procedure as previously described and shown in figure 2.12d.

Figure 2.20 shows the fully resolved sectional stiffness properties of the blade along the span in the form of the symmetrical stiffness matrix K.
Figure 2.19 furthermore presents the inertia properties, including the section mass, m_{00}, the mass moment of inertia, m_{22}, about the x_2 axis, the mass moment of inertia, m_{33}, about the x_3 axis, and the product of inertia, m_{23}, as well as the mass center, x_{m2}, the tension center, x_{t2}, and the shear center, x_{s2}, locations as described in this section.
The identical discretization was used for three different sectional analysis. While the first study was performed with *VABS* taking into account the correct curvatures and twists of the beam reference curve, these are neglected in the second study $VABS_{\mathrm{R}}$. The third and final analysis with *ANBA4* does not consider these effects at this time, and is therefore well suited for a code-to-code comparison to $VABS_{\mathrm{R}}$.

Figure 2.18a shows the beam reference curve of the 15-MW reference wind turbine in flap-wise direction. Note that in this case, no chordwise initial pre-bend is present. Similar to the composite topology the beam reference curve is internally represented as *BSplineLst* which is created from the users discrete input of beam reference curve coordinate points. A curve is then constructed whose shape closely follows this sequence of control points or knots. The current implementation describes a so called interpolating curve that passes through each control point. Discontinuities in the data set are separated by an angular deflection tolerance dividing the piecewise polynomial or rational B-spline curves in a multiple contiguous set (*BSplineLst*). [143]
This discrete description leads in this example to the fact that the beam reference curve's curvature in flap direction κ_2 shown in figure 2.18b fluctuates more than probably intended by the user. The figure also illustrates the initial twist κ_1 and the initial curvature in chord-wise direction κ_3. Within the assumption of neglecting the described initial twist and curvature, results in figure 2.20 and 2.19 show that – besides being verified through box beam examples (see Section 2.5.2) – the verification

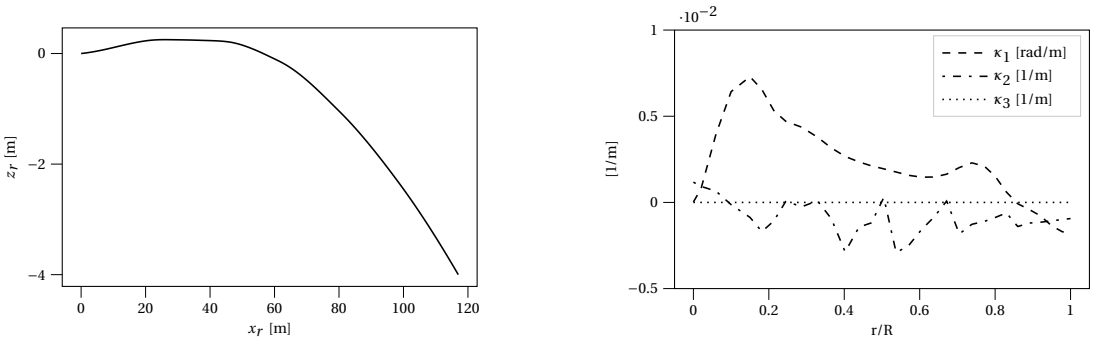

(a) Beam reference axis of the 15 MW reference wind-turbine blade

(b) curvature of the 15 MW reference wind-turbine blade

Figure 2.18

of *ANBA4* was once more successfully established when applied to a fully resolved wind turbine blade.

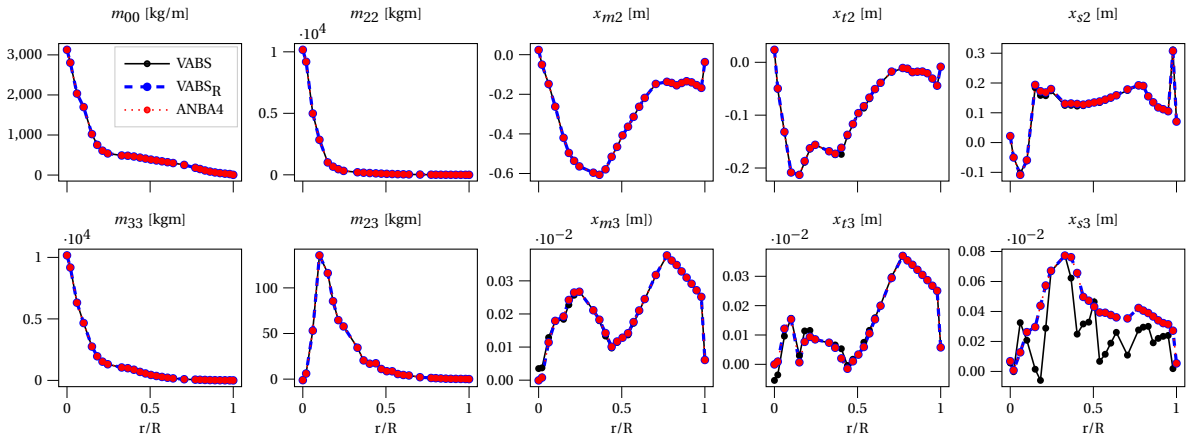

Figure 2.19: Verification of inertia properties, tension-center (x_{t2}, x_{t3}) and shear-center (x_{s2}, x_{s3}) location between *VABS*, *VABS*$_R$ (excludes effects from initial twist and curvature) and *ANBA4* along the nondimensional blade spam, r/R, for the 15-MW reference wind-turbine blade

The wind turbine blade incorporates axial-bend, K_{15} and K_{16}, and bend-bend, K_{56}, coupling terms. Because the fiber orientation of all components is 0° (oriented in an axial direction), bend-twist coupling (K_{45} and K_{46}) originates solely from initial twist and curvature; see *VABS* results in figure 2.20. Small discontinuities in the *VABS* results (e.g., K_{24} or x_{s3}) result from the aforementioned fluctuating curvature κ_2. The shear-center location is determined from the described equations, therefore the same effect fluctuating characteristics are visible. *ANBA4* can be seen as an applicable and open-source solver within *SONATA* for the analysis of slender composite structures such as rotor blades. However, special attention is necessary when the problem consists of a beam with initial twist and curvature.

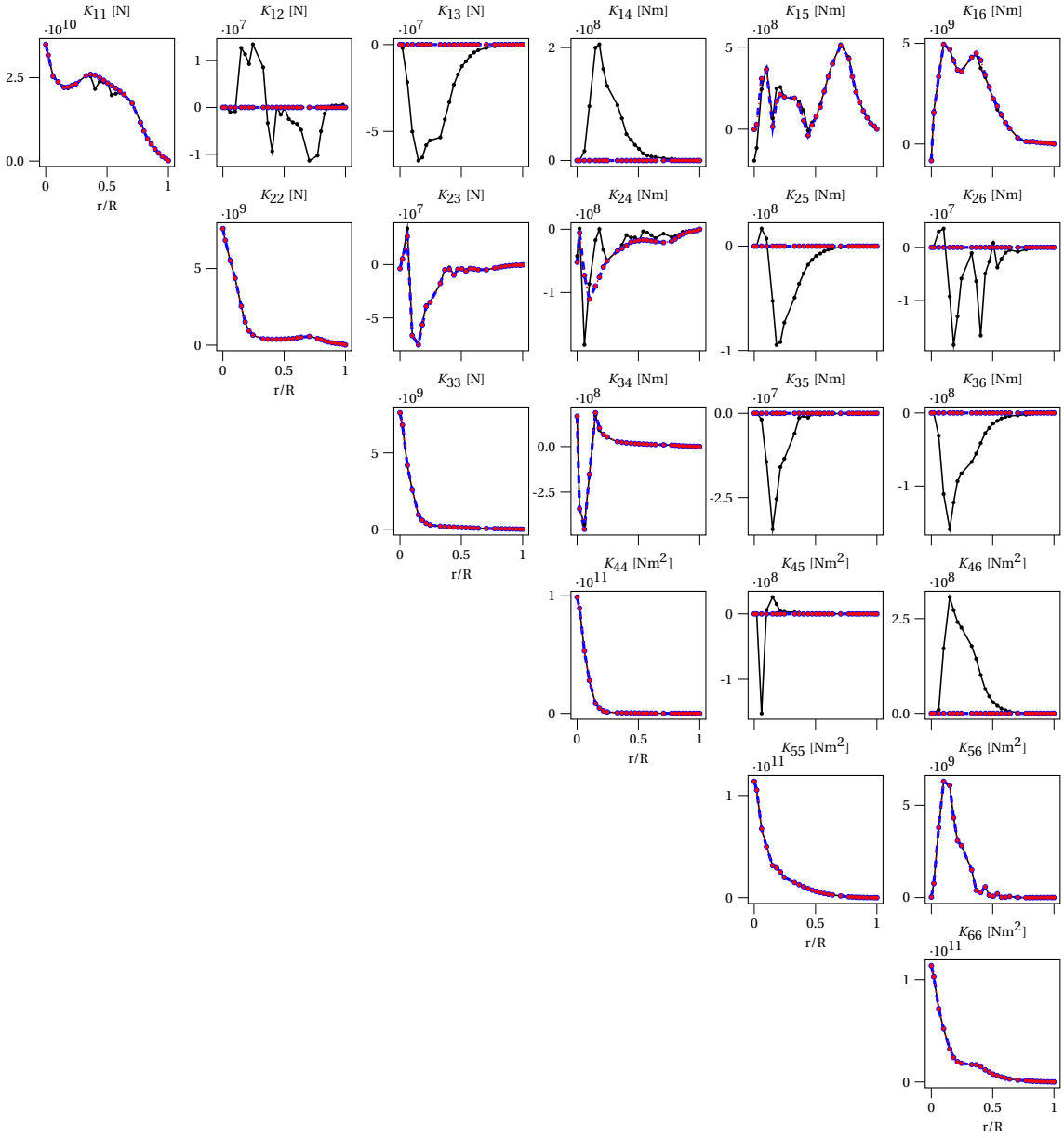

Figure 2.20: Stiffness matrix verification between *VABS*, *VABS*$_{\mathrm{R}}$ (excludes effects from initial twist and curvature) and *ANBA4* along the nondimensional blade spam, r/R, for the 15-MW reference wind-turbine blade

3 Propagation of Material and Manufacturing Uncertainties

The objective of this chapter is to reaffirm the research hypothesis that improvements of numerical and experimental structural beam analysis methods are necessary for the development of helicopter rotor blades to be used in multidisciplinary optimizations under consideration of uncertainties. The hypothesis was formulated and inspired on the basis of previous studies from Li [94], Murugan [118] and Sinotte [159], in particular. Li [94] stated, that the under-representation of uncertainties is a significant reason why the industry in not yet comfortable to use multidisciplinary design optimization methods. By studying the propagation of material and manufacturing uncertainties of a rotor blade on the beam-properties, the rotating-natural frequencies, the aeroelastic response and vibratory loads in hover and forward flight it gives answers to the question if optimization potentials eaten up by the structural uncertainties. At the same time, should the modeled material and manufacturing uncertainties have no effect on the rotor dynamics and vibration loads, more accurate numerical and experimental methods to determine the beam properties would be obsolete.

To answer these questions in this chapter, Monte Carlo Simulations (MCS) are used as a technical numerical tool. In this context, the MCS consists of three main components. In the first step, a set of n_s random data points are extracted based on assumed randomness distributions. If the underlying deterministic computational model is computationally inexpensive a plentiful number of random samples can be drawn and evaluated for the subsequent analysis. However, due to its stratification properties, a Latin hypercube sampling (LHS) method can be used to recover uncertainty information with relatively small sample sizes. Due to the increased computational requirements of each individual function evaluation of the following investigations LHS is used.
In this method, the domain of each individual random variable is divided into discrete subdomains, from which a random value is then selected and subsequently randomly paired to form n_s input data points. [165]

The second step is to execute the deterministic simulation model to get the corresponding system

output response that is evaluated in the last step.
Figure 3.1 depicts the flowchart of the Monte Carlo Simulations and its underlying model evaluation process. The objective of this study is to evaluate the effect of aleatory material and manufacturing uncertainties using a high fidelity composite helicopter rotor blade structural model, and how they affect the overall helicopter rotor behavior. This study is divided into two independent analysis to study the material and manufacturing uncertainties separately. This allows to gain insight into the mechanisms and the propagation of uncertainties to the rotor's dynamic behavior.

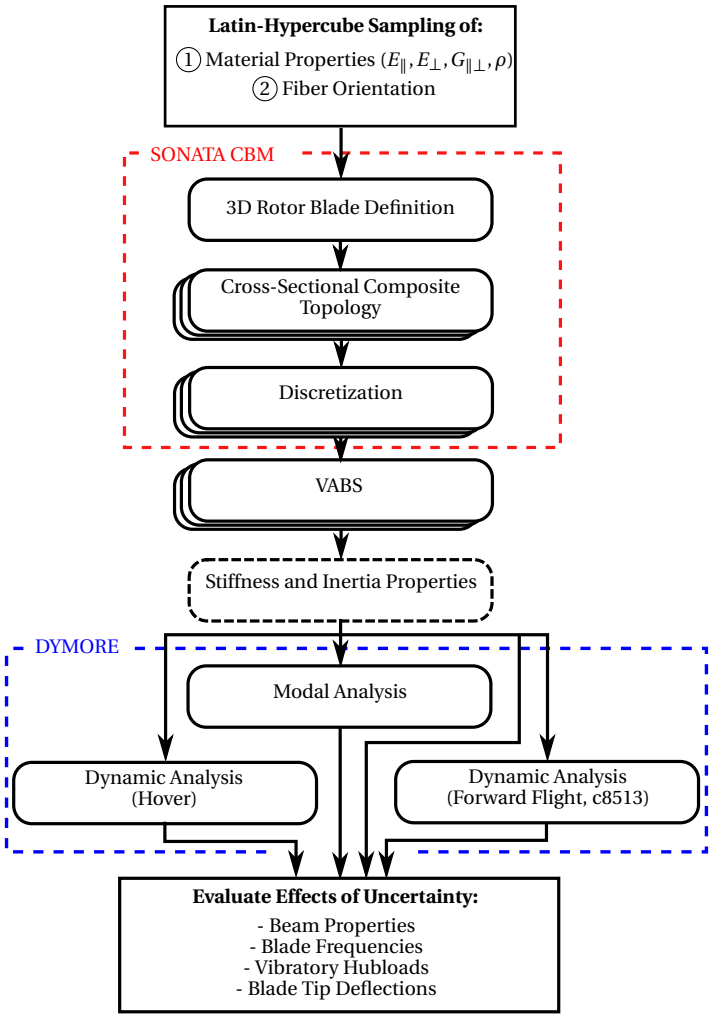

Figure 3.1: Monte-Carlo Simulation flowchart

In the first analysis the material uncertainties are studied. Studies have shown that the mechanical properties of composites show a considerable variance due to uncertainties associated with fiber and matrix material properties, fiber volume fractions, fiber orientation and undulation, intralaminar voids, etc. [121].
The second analysis of this study, the uncertainties in fiber orientation is studied. Until now, the

rotor-blade manufacturing process is still hand layup and a distortion of ply angles is possible, but also because placing composite textile into a three-dimensional mold will inevitably result in a fiber angle distortion. While the latter can be extracted and accounted for in a drape analysis, this is typically not performed before deriving all individual plies in a composite CAD tool later in the design process.

The deterministic simulation model which is executed for each sample consists of all the components in figure 3.1 with rounded corners. It starts with the general methodology of *SONATA* also shown in figure 2.1 that begins with the procedure to create a three-dimensional description of the rotor-blade surface before the composite topology generation of the internal structure is created at specific radial stations which is then discretized into a two-dimensional finite element mesh before the one-dimensional beam sectional properties in the form of the 6x6 stiffness and mass matrix are passed to a flexible multibody representation of the UH-60A helicopter rotor which is modeled using *Dymore*. The results of a analysis in hover and forward flight conditions as well as a modal analysis are examined in the subsequent stochastic evaluation.

This chapter briefly describes the UH-60A flexible multibody system analysis setup and the choosen rotor blade description before dividing the results according to the separate analysis. Note that parts of this chapter were published in ERF2019A and ERF2019B at the European Rotorcraft Forum 2019, Warsaw.

3.1 UH-60A Flexible Multibody System Analysis

The helicopter rotor model is simulated using *Dymore* [12], a software for simulation of flexible multibody systems which features one and two dimensional finite element representations and helicopter specific aerodynamic models developed by Professor Olivier Bauchau and colleagues at the Georgia Institute of Technology. The finite element based flexible multibody dynamics formulation has become the norm for the complex, nonlinear problem of rotorcraft dynamics analysis. [10]. In the past *Dymore* was used in the context of wind turbine simulation [90], [104], [164], structural analysis of tilt-rotors and active flaps [123], [155], [157] as well as helicopter structural optimization, morphing and adaptive structures [8], [32], [34], [60], [84], [94], [114], [138].

To refer to a validated model, a rotor model from Rex [137] similar to the UH-60A main rotor was used in the present analysis. In this context, non-linear partial differential equations describe the governing equations for the beam structures of the rotor blades and the rotor shaft though the *Geometrically Exact Beam Theory (GEBT)* [10] that accounts for arbitrarily large displacements and

rotations yet small strain components. The approximate numerical solution of the beam equations is obtained by dividing the rotor blade into 14 finite elements of order one using linear shape functions with two corresponding nodes [10].
Except for the pitch links and the servos that include lengthwise stiffnesses, the control linkage and the rotor hub are represented by rigid bodies. The nonlinear characteristic of the lag-damper is included as well. Aerodynamic collocation points are distributed along the radial span and 2D steady airfoil polars [72] depending on Mach number are used to represent the rotor blade aerodynamic forces and section pitch moment. The *Peters-He* model (12 modes), is used to account for the rotor inflow dynamics. The rotor model is described in detail in ref. [137]. In this work, the rotor is operated in a wind tunnel setup. Which means that the fuselage, empennage and tail rotor are not included into the simulation framework. However, the rotor can be trimmed towards free flight conditions using the inverse Jacobian matrix of inputs and trim targets for the estimate of the control settings [137].
The considered flight states are a low speed horizontal forward flight corresponding to the airloads flight test counter C8513 [28] and a symmetric hover case at the altitude and blade loading of the airloads counter C8513 shown in table 3.1. In order to validate the structural dynamics of the baseline rotor and thus implicitly the structural properties, the eigenvalues and natural frequencies were compared by Rex [137] with experimental results from reference [62]. In the first validation study, the static, non-rotating experimental setup of a shaker-excited suspended rotor blade [62] was simulated using *Dymore*. For this independent study, the number of finite elements of the rotor blade were increased from 14 to 40. The results show that the natural frequencies and the natural modes match reasonably well, which is an indication of the dynamic similarities of the reference blade [62].
Evaluating the rotor natural frequencies formed the second part in the validation chain by comparing the fan-plot calculations against reference simulations performed by *RCAS*, *CAMRAD II* and *DYMORE* [69], [162]. Again, the general agreement of the eigenfrequencies over rotational speed suggesting the correct rotor kinematics and blade properties. The influence of the different stiffness of the pitch link was also emphasized by Rex [137]
As the subsequent logical validation step, the aerodynamics were added to the setup by comparing the rotor in hover out of ground conditions and trimmed forward flight conditions to the full scale test campaign in the 80 x 120 ft wind tunnel at NASA Ames [119] and flight test data. In summary, it can be concluded that the validity of the UH-60A simulation model used in this study has been demonstrated against available experimental data [137]

The communication between the beam stuctural model of SONATA and the multibody dynamics simulation model with *Dymore* is realized by using *OpenMDAO* [59]. *Dymore*[12] is included into the framework as an *Explicit Component*. This is realized by wrapping the C written code *Dymore* to Python using *SWIG* making specific functions, properties and parameters of the model accessi-

flight states:	**hover**	**low speed flight (C8513)**
advance ratio, μ	0.0	0.149
C_W/σ	0.0792	0.0792
rotor speed, N_r, [RPM]	258	258
density, ρ, [kg/m^3]	1.13	1.13

Table 3.1: Considered flight states

ble from an outside python controller. More details on the connection between *OpenMDAO* and *Dymore* are described in [132], [137]. In general, all model properties which are represented by a table in *Dymore*, like the rotor angular velocity, actuator displacement, etc can be modified. In particular, beam properties, the flight velocity and auto pilot characteristics can be updated in the model during execution because the calculation in time domain as well as in frequency domain is controlled from the python module. Likewise, sensor states can be observed and evaluated during execution and the values are returned to *OpenMDAO*. This allows for example to select the model properties and time step width for each step individually.
In order to run multiple hover and forward flight simulations in this study with different rotor blade structural properties a fast convergence of the rotor behavior is desired. The initial start solution of the simulation contains the steady-state rotor condition with reference beam properties. Based on this, the beam properties of each sample are inserted step by step using linear interpolation over the period of one second to accelerate the convergence towards a periodic steady state of the rotor and reduce computational expenses. The periodic response is extracted by simulating approximately 13 rotor revolutions until the differences between two rotor revolutions are sufficiently small.

3.2 Generic UH-60A Composite Blade

This section describes the test article of this study. Since the results of this Monte Carlo study are only meaningful if the baseline rotor blade of the simulation has a realistic internal fiber composite structure, which would be present in a modern rotor blade. It is equally important that the rotor dynamic properties of this generic rotor correspond to a reasonable design. This requires that the natural frequencies of the baseline design are carefully placed so that they have a sufficient distance to the rotor harmonics at nominal rotor speed.
Therefore, it was decided to develop a new generic fiber composite design of the classic UH-60A rotor blade. The original outer geometry of the rotor blade remained untouched, generated from the dataset of Davis [43] as illustrated in figure 3.2.

As described in the previous chapter, the wireframe that defines the outer shape of the rotor blade is defined by a collection of airfoils that are projected along x_r, after translating them to the non-dimensional pitch-axis location, rotating them about the twist angle around x_r, scaling them to the desired chord length and moving them onto the blade reference curve.
Because both the rotor blade reference curve and the beam reference curve can be arbitrarily curved and twisted, secondary local coordinate systems are defined for each structural two-dimensional composite cross-section that is modeled. In this particular case, curvilinear coordinates are chosen in accordance with the reference data. While the unit vector of the local x_l remains tangent to the beam reference curve. The unit vector y_l is chosen to point toward the leading edge of each section. Thus, following the initial twist of the rotor blade. Note, that in this particular case the beam reference curve is parallel to x_r of the reference frame.
Figure 3.2 also shows the five discrete radial locations, at which the inner composite structure is modeled and discretized with SONATA. Subsequently, the beam sectional properties are calculated with VABS at each cross-section and are passed to the beam definition of Dymore. The blade attachment and root are not specified in the context of this study. Yet to provide a complete description of the blade, the structural mass and stiffness properties of the original UH-60A [43] are used up to the first cross-section at 0.25R.

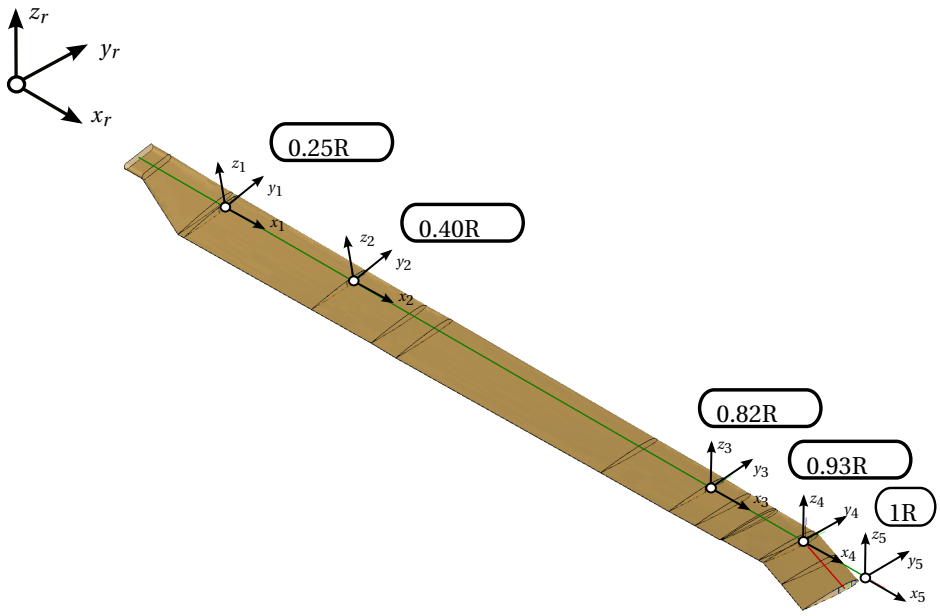

Figure 3.2: Surface of the UH-60A rotor blade, generated from the dataset of Davis [43]. Specific cross-sections are distributed at 0.25R, 0.4R, 0.82R, 0.93R and R

In figure 3.3 the structural cross-section of $0.4R$ is shown. The architecture of this cross-section is representative for the remaining four sections. The rotor-blade has a 1 mm thick skin of four

layers e-glass with both 0° and ±45° fiber orientation. A nickel erosion protection strip of 0.82 mm thickness protects the leading edge of the blade against rain and sand. While the blade skin its ±45° layers serves mechanically mainly for the transfer of torsional forces, the spar inside the cross-section is responsible for the transfer of the centrifugal loads and allowing a defined flapping and lagging movement. For this study a design was chosen that combines a distinctive C-spar of unidirectional high-tensile strength (HT) carbon in the leading edge region with a box spar. The c-spar was chosen to provide the possibility to embed an additional trim mass into the structure and move the mass center closer the pitch-axis. The box-spar was chosen to provide a great flexibility for the mechanical properties of the design. The material was chosen to be an intermediate modulus carbon fiber epoxy composite with a fiber volume content (FVC) of 60%. The layup was therefore set to provide 4 layers of different fiber orientations in all major directions [0°, 45°, −45°, 90°] with baseline thicknesses of [1.35 mm, 1.35 mm, 1.35 mm, 0.5 mm]. The cavity in the rear part of the cross-section is filled with a HexWeb 5.2-1/4-25 aluminum honeycomb material [150] and the front part is filled with a Rohacell IG-F 51 foam. The structurally integrated front cavity is used to place tuning masses into the structure by replacing the foam core with a tungsten-epoxy granulate at radial station 0.25R and 0.93R to make sure that the eigenfrequencies of the rotor do not cross multiples of the rotor-harmonic at nominal rotational speed and that the rearward mass of the swept tip is balanced. The only other difference of the other sections compared to the illustration of figure 3.3 (SC-1095), besides small changes in chord-length, is the airfoil-shape SC-1094R8 between 0.5R and 0.82R.

In figure 3.4 and figure 3.5 the stiffness and inertial properties of the described rotor blades are shown. They are baseline values for the MCS and are compared against the original UH-60A properties from Davis [43].

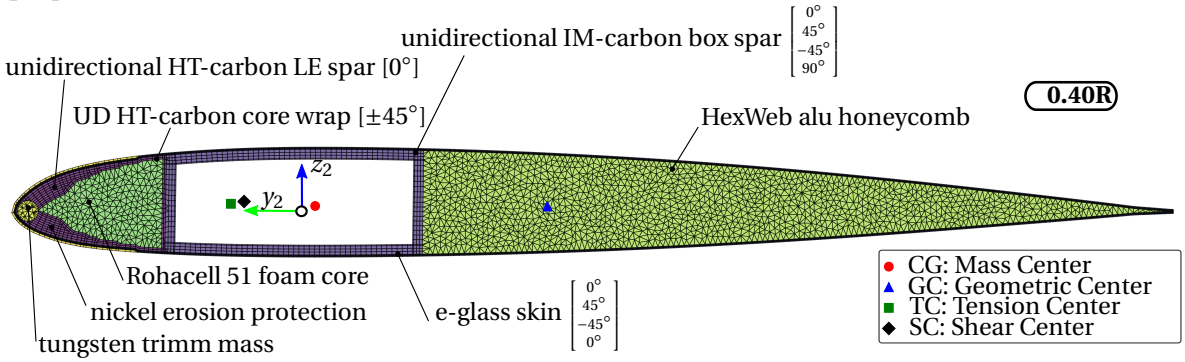

Figure 3.3: Composite rotor-blade cross-section at 0.4R

The peaks in the mass per unit length m_{00} indicate the location of the tuning masses at 0.25R and 0.93R. The same applies to the center of mass location in chordwise direction x_{m2}, moving the center of mass towards the leading edge. The large gradient at the end of the mass-properties can

be explained by the swept blade tip, which moves the cross-section backward relative to the beam reference coordinate system. While, mass distribution and center of gravity location are relatively similar to the reference UH-60A properties, the new composite design drastically reduces the mass moment of inertia about the y-axis.

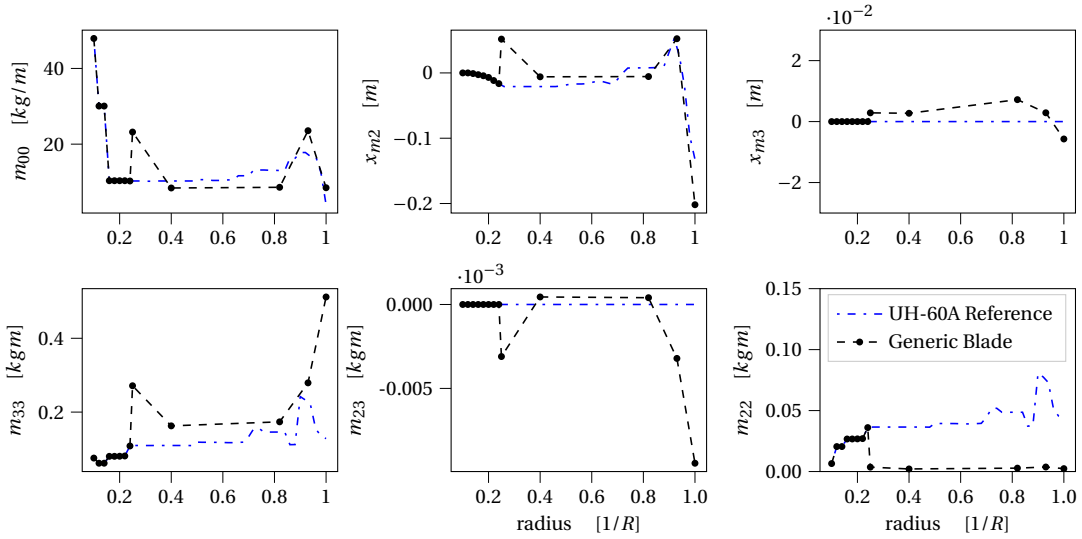

Figure 3.4: Baseline beam inertial properties

In figure 3.5 the diagonals of the stiffness matrix are illustrated. The axial stiffness K_{11} The torsional stiffness K_{44}, flap-stiffness K_{55} and lag-stiffness K_{66} are all increased compared to the UH-60A reference blade. The peak stiffnesses of K_{44} and K_{66} at the tip are a result of the offset from the reference axis.
The fan diagram of figure 3.6 shows the corresponding eigenfrequencies of the rotor versus rotational speed. For the modal analysis no aerodynamic forces were considered, the pitchlinks and the rotor-controls were also assumed to be rigid. The fundamental lag (1st mode), the first three flap (2nd, 3rd, 6th) and the torsional (4th mode) frequency are relatively similar to the original UH-60A. Particularly the fourth flap frequency (7th mode) is increased due to the higher stiffnesses of the current design.

A dynamically balanced design of the initial baseline configuration is important. Previous studies by Murugan et. al. [118] have already shown that otherwise small variations from the baseline design can have a large impact on the dynamic response of the rotor. This would massively distort the results and validity of this study.
The fan diagram of figure 3.6 shows the similarity of the eigenfrequencies compared to the original UH-60A reference design. The first two modes are mainly rigid-body modes, which are primarily defined by the flapping and lead-lag hinge offset of the articulated rotor. In the range of the fifth rotor harmonic 5Ω the usually distinctive modes (3rd flapping, 2nd lead-lag and 1st torsion) couple

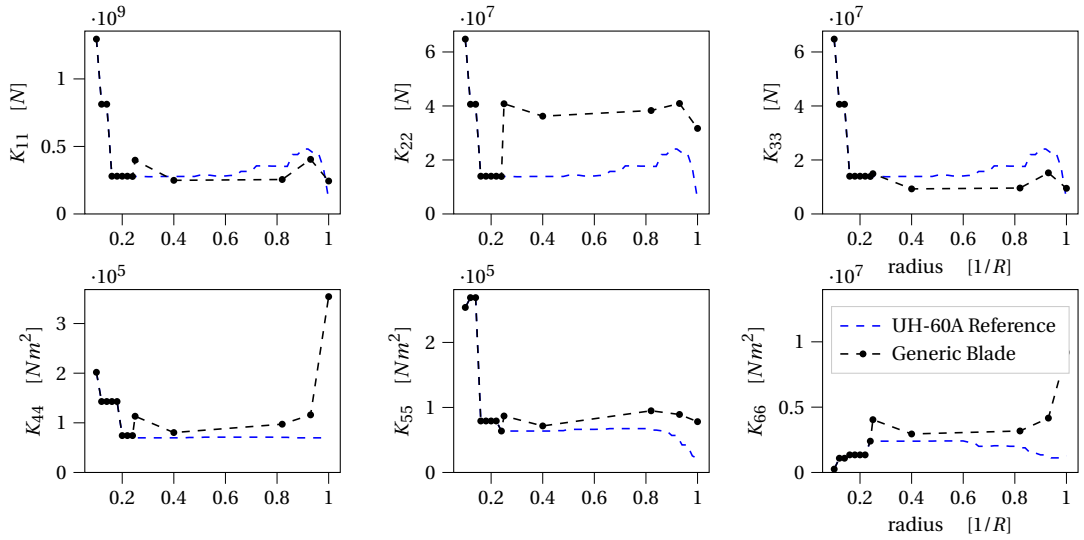

Figure 3.5: Baseline beam stiffness properties

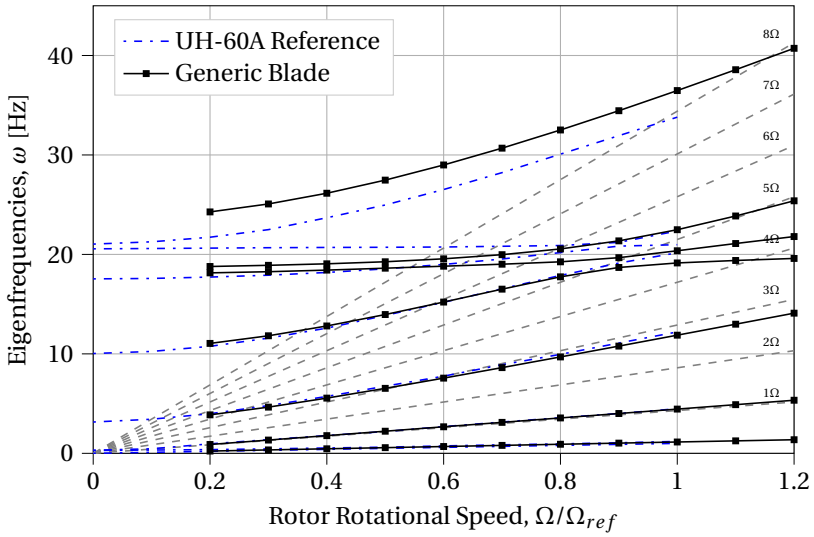

Figure 3.6: Baseline rotor fan diagram, reference UH-60A data obtained from ref. [29]

with each other. Nevertheless, care was taken in the design to ensure that the distance to the nearest rotor harmonic of each mode is at least equal to or greater than the original reference rotor blade.

3.3 Monte-Carlo Simulation

The objective of this study is to evaluate the effect of aleatory material and manufacturing uncertainties, and how they affect the overall helicopter rotor behavior. A Monte-Carlo approach is

chosen for this study (highlighted in figure 3.1). In the first analysis the material uncertainties are studied. Studies have shown that the mechanical properties of composites show a considerable variance due to uncertainties associated with fiber and matrix material properties, fiber volume fractions, fiber orientation and undulation, intralaminar voids, etc. [121].

The baseline elastic properties of the fiber composite materials of the rotor-blade are derived from a semi-empiric Puck approach [149] using basic reference values for HT- and IM-carbon fiber and epoxy matrix material with a fiber volume content (FVC) of 60%. The unidirectional HT-carbon composite is used for the C-spar (in the following referred as "material 1"). The unidirectional IM-carbon composite is used for the box-spar (in the following referred as "material 3"). Latin-Hypercube sampling (LHS) is used to generate a near-random normal distribution of material-properties $E_{\parallel}, E_{\perp}, G_{\parallel\perp}$ and ρ. The mean (μ) and the coefficient of variation (COV) of the material properties are listed in table 3.2. The COV is the normalized measure of dispersion of a probability distribution. It is defined as the ratio of the standard deviation (SD, σ) to the mean of the distribution.

Material properties	**Mean**	**COV**
$E_{1\parallel}$	139.36 GPa	7 %
$E_{1\perp}$	12.62 GPa	4 %
$G_{1\parallel\perp}$	5.89 GPa	12 %
ρ_1	1.536 g/cm^3	5 %
$E_{3\parallel}$	177.76 GPa	7 %
$E_{3\perp}$	12.62 GPa	4 %
$G_{3\parallel\perp}$	5.89 GPa	12 %
ρ_3	1.572 g/cm^3	5 %

Table 3.2: Uncertainties in material properties taken from [121] based on a COV of 5% in microlevel composite properties.

Fiber orientation	**Mean**	**SD**
$\theta_{3,\text{bs1}}$	0 °	5 °
$\theta_{3,\text{bs2}}$	45 °	5 °
$\theta_{3,\text{bs3}}$	-45 °	5 °
$\theta_{3,\text{bs4}}$	90 °	5 °

Table 3.3: Assumed fiber orientation uncertainties

Similar to ref. [118], the COVs assumed in this study are taken from reference [121]. Onkar et. al. describe the effect of a COV of 5% in microlevel composite properties such as elastic properties of the fiber E_f, ν_f and matrix phase E_m, ν_m and FVC, changing the macrolevel effective material properties for different composite systems. The COV in $E_{\parallel}$ was found to be approximately 7% for all types of composite systems, whereas the shear-modulus $G_{\parallel\perp}$ showed a larger variation of 12%. The material density is herein assumed to be normally distributed with a COV of 5% for this study. Drawing 1000 random samples from the distribution, figure 3.7 shows the statistical distribution of the material 3 properties. The maximum likelihood estimation shows standard deviations close to the prescribed COVs for both materials.

In the second analysis of this study the uncertainties in fiber orientation θ_3 of the four box spar layers is studied. Until now, the rotor-blade manufacturing process is still hand layup and a distor-

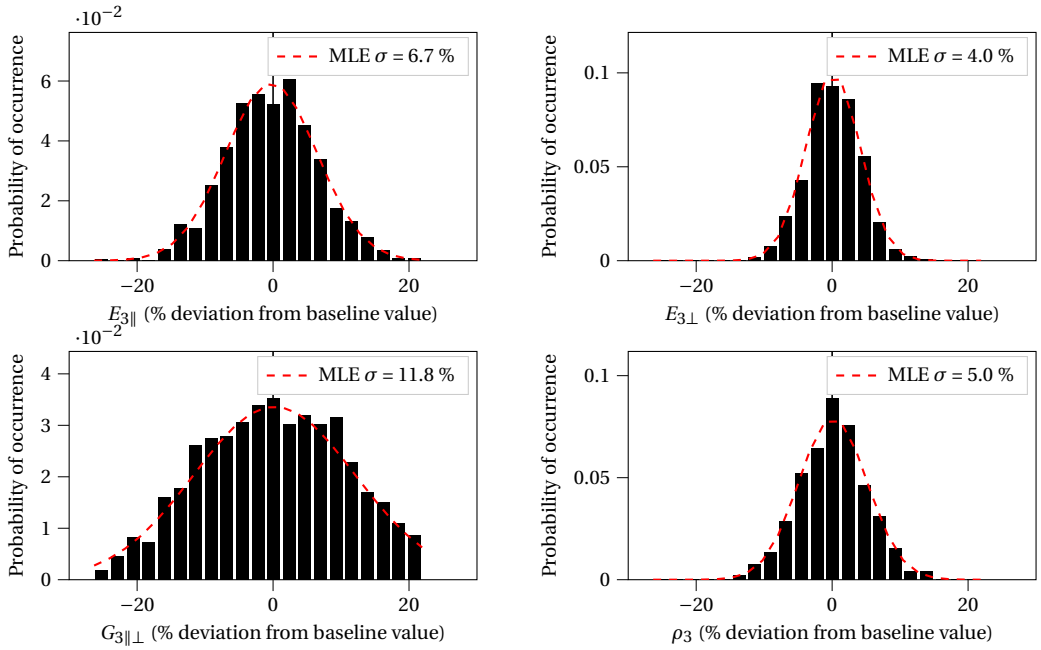

Figure 3.7: Probability distribution of properties of the IM-carbon composite (material 3)

tion of ply layup angles is possible during the manufacturing process but also due to the inevitable distortion during placing textiles in a general three-dimensional mold. For this separate analysis a SD of 5 degree is assumed. Table 3.3 shows the design variables. Equal to the first study, 1000 LHS samples are generated for the Monte-Carlo Simulation.

After a sample is drawn from the distribution, the rotor blade structural analysis is performed including the cross-section topology generation (described in figure 3.2), followed by the discretization and calculation of stiffness and inertia properties with *VABS*. The resulting beam-properties are evaluated together with the results from the modal, hover and forward flight analysis.

3.3.1 Propagation of Material Uncertainties

The resulting cross-sectional beam property distribution of the material uncertainty Monte-Carlo Simulation are discussed first. To demonstrate the sufficiency of the number of samples the convergence of SD of torsional- (K_{44}) and flap (K_{55}) stiffness at radial station 0.4R are shown in figure 3.8. In figure 3.9 and figure 3.10 the mean inertial properties and diagonals of the stiffness matrix are shown together with a $\pm 2\sigma$ confidence interval showing the variance of the different entries. The largest influence of uncertainty exists for the center of gravity in chordwise direction X_{m2} with a COV of 10.2% at 0.25R, while the mass per unit span m_{00} is only affected with a COV of 1.4%. The

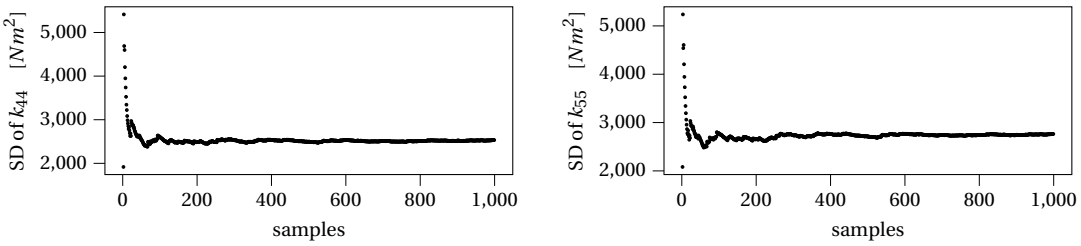

Figure 3.8: Convergence of the SD of torsional- K_{44} and flap stiffness K_{55} for the material uncertainty analysis

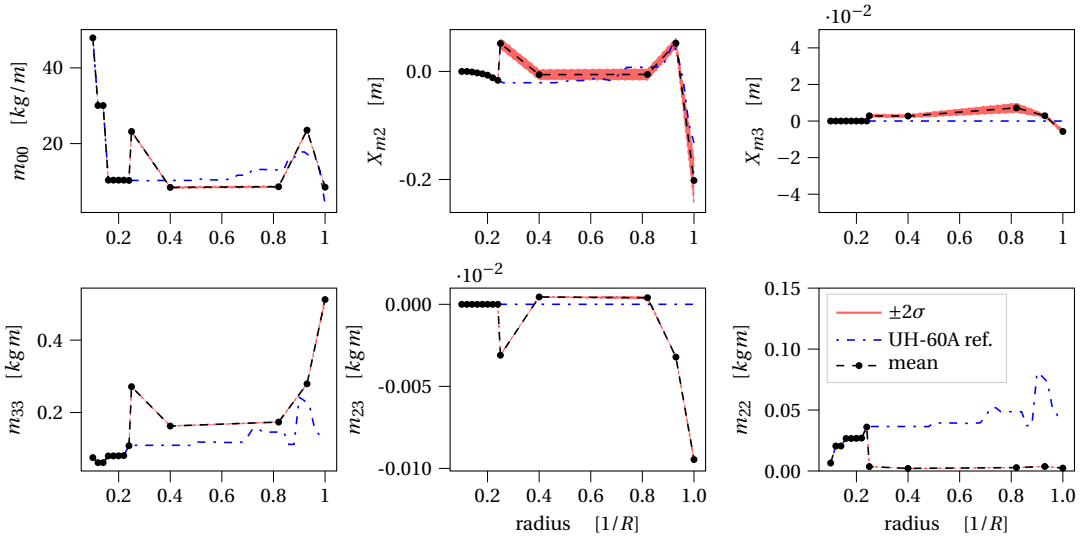

Figure 3.9: Beam inertial properties and $\pm 2\sigma$ confidence interval for the material uncertainty analysis

mass moment of inertia m_{22} (COV of 2.1%) and m_{33} (COV of 0.3%) are also just slightly influenced.

The axial, torsional, and flap stiffness show COVs of 3.0, 3.2 and 3.9% at 0.4R, respectively. The lag stiffness K_{66} shows the lowest impact by the introduced uncertainties with a COV of 1.6%. Figure 3.11 shows the histogram of the classical 4x4 stiffness matrix for radial station 0.4R. Note that for the Gaussian distributed input, most of the results are also represented by a Gaussian normal distribution. It is shown that in particular the torsional coupling relations K_{14}, K_{45}, K_{45} of this cross-section are barely influenced by the added uncertainty. At the same time the flap-lag coupling relation K_{56} shows the largest sensitivity with a COV of 8.2%.

All five cross-sections of this blade have the same layout, therefore not only the properties along the span stay relatively constant, but also the influence of uncertainties. However, when comparing the histograms of 0.4R (figure 3.11) and 1R (figure 3.12), it is noticed that the torsional coupling terms become much more sensitive at the swept blade tip, increasing the COV from $< 1\%$ to $\approx 5\%$.

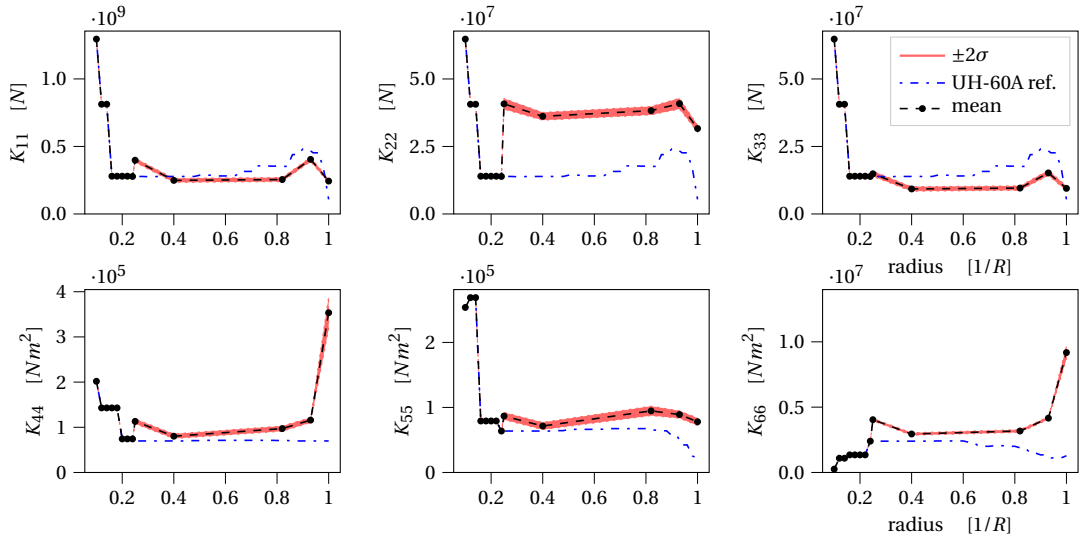

Figure 3.10: Beam stiffness properties and $\pm 2\sigma$ confidence interval for the material uncertainty analysis

As the next logical analysis, the effect of material uncertainties on the rotating natural frequencies of the rotor are evaluated. The placement of natural frequencies of the rotor is an important design aspect to reduce the dynamic loads at the rotor hub and propagation of vibration into the fuselage. A well tuned rotor will also help to reduce fatigue of components in the rotating frame. Usually, this is done by the targeted introduction of additional tuning masses into the structure (as it was done for this rotor blade) in such a way that the natural frequencies are a safe distance away from the rotor harmonics. A rule of thumb states that distance to be approximately 0.2/rev [171]. A rotor particularly transfers the frequencies that are integer multiples of the number of blades and their neighbors from the rotating to the fixed frame. In this case, for a four bladed rotor the frequencies at 3Ω, 4Ω and 5Ω as well as 7Ω, 8Ω and 9Ω are important to keep a save distance from.
In figure 3.13 the mean rotating natural frequencies are shown from 20% to 120% rotor rotational speed together with a $\pm 2\sigma$ confidence interval. Because the UH-60A rotor has a distinctive flap and lag elastomeric hinge, the first two frequencies represent the rigid body lag and flap modes. The impact of uncertainty varies with each mode. Higher modes are affected to a larger extend because the structural elasticity becomes dominant compared to the effect of centrifugal stiffening at the lower modes. This is also the reason why the 7th mode (4th flap mode) shows a larger influence at lower rotational speeds.
In the next sections, it is discussed how the dispersion in eigenfrequencies affect the dynamic response and the 4/rev vibratory hubloads of the rotor.

The uncertainty of the elastic tip deflections in hover can give an indication for the probability and the magnitude of miss-alignment that would need to be counteracted by a blade tracking procedure. Note however, that the 4 blades of the rotor are identical for this study and no blade

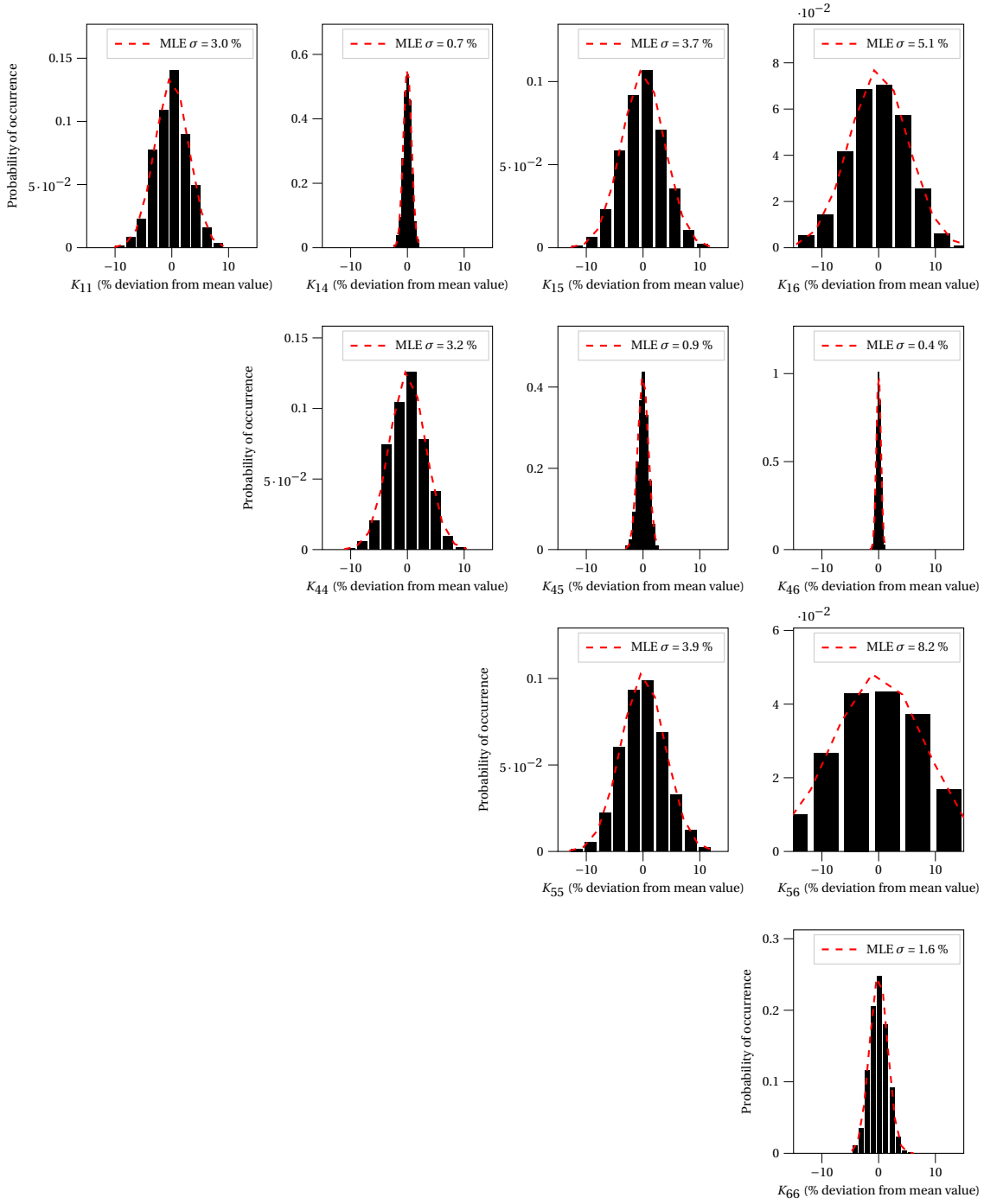

Figure 3.11: Histogram of the classical stiffness matrix at 0.4R (material uncertainty analysis)

dissimilarity is considered.

In figure 3.14 the histograms of the elastic flap, lag and torsion response in hover are shown. The response is the relative measure of the tip to the blade attachment and is not superimposed with the flap, lag and torsion response of the elastomeric bearing. The flap, lag and torsion response

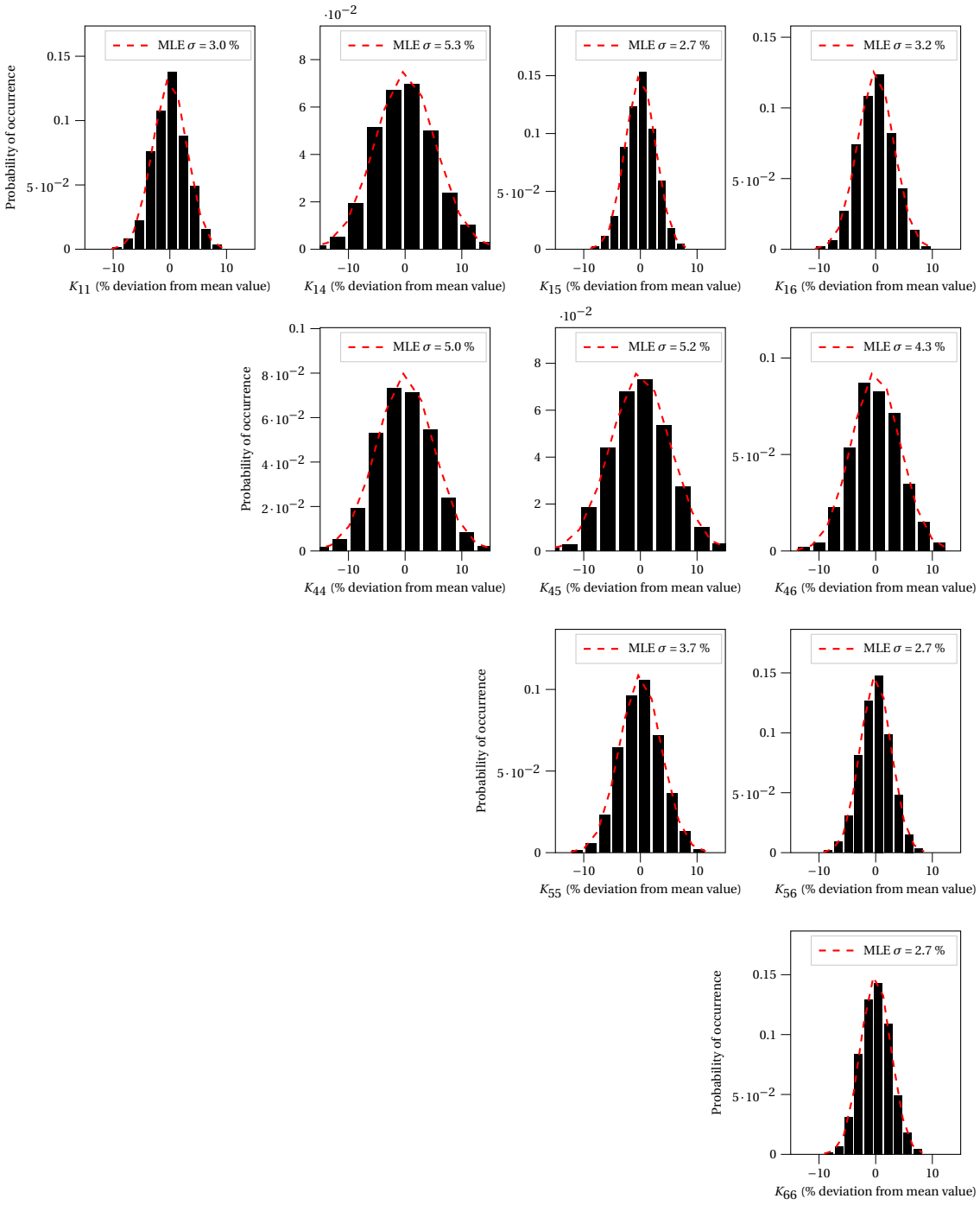

Figure 3.12: Histogram of the classical stiffness matrix at 1R (material uncertainty analysis)

distributions have a COV of 6.2%, 5.6% and 3.9% respectively.

In this section the elastic blade tip response (flap, lag and torsion) is evaluated over azimuth position for the forward flight state. Additionally, the 4/rev vibratory hub forces and hub moments are

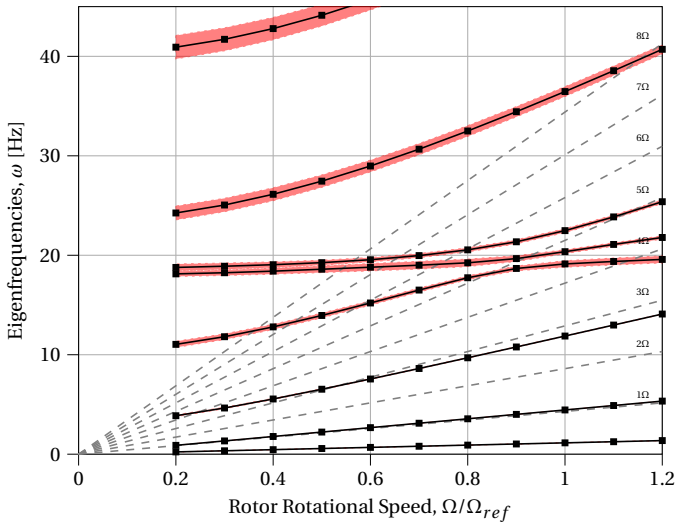

Figure 3.13: Mean eigenfrequencies with $\pm 2\sigma$ confidence interval versus rotational speed for the material uncertainty analysis

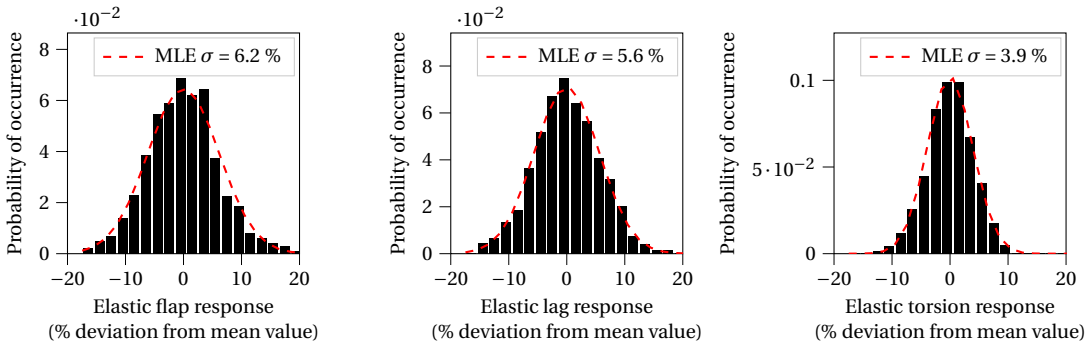

Figure 3.14: Histograms of the elastic flap, lag and torsion response in hover for the material uncertainty analysis

studied.

The flight state considered for this study is a low speed horizontal forward flight corresponding to the airloads flight test counter 8513 listed in table 3.1 with a advance ration of $\mu \approx 0.15$ and a blade loading of $C_w/\sigma = 0.0792$ [28].

Similar to the elastic blade tip response in hover, its behavior is studied during the forward flight state, shown in figure 3.15. However in this case, the blade tip response varies along the azimuth position of the blade. The mean values and the $\pm 2\sigma$ confidence interval are shown. The amplitudes of the torsion response shows a deviation of approximately 0.5 degree. The uncertainty of amplitude in the 5/rev periodic response of the torsional response, will potentially have also an impact on the hub vibration levels. The flap response is less than the observed torsional response. As mentioned before, the rotor particularly transfers the frequencies that are integer multiples of the number of blades and their neighbors from the rotating to the fixed frame, so that frequencies

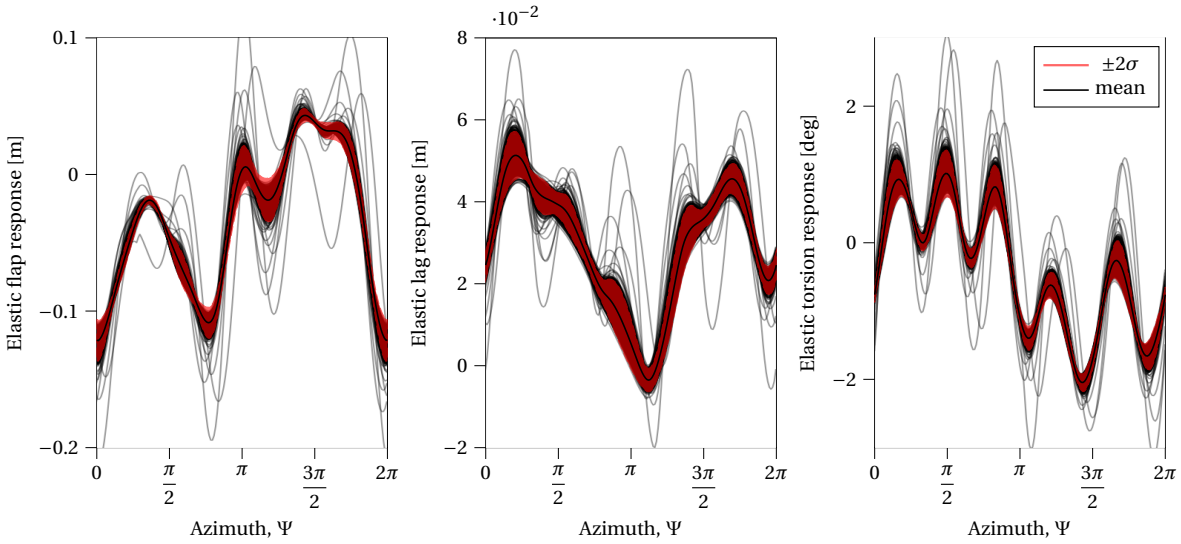

Figure 3.15: Elastic flap, lag and torsion response in forward flight with $\pm 2\sigma$ confidence interval for the material uncertainty analysis

of 3Ω, 4Ω and 5Ω will transform to 4/rev frequencies in the fixed frame. In figure 3.16 the effect onto the 4/rev vibratory hubloads is evaluated. The six components are the longitudinal shear (F_x), lateral shear (F_y) and vertical force (F_z) as well as rolling moment (M_x), pitching moment (M_y) and torque (M_z). These components are obtained by performing a fast Fourier transform (FFT) of the time signal. The 4/rev forces are normalized by the rotor steady thrust (T). The 4/rev moments are normalized by the rotor steady torque (Q). The first interesting observation is that the histogram does not show a Gaussian normal distributions. The second observation is that the F_x, F_y and M_y show the larges deviation with a COV of 24, 18.7 and 19.6% respectively. The vertical components show a COV of 10% while the rolling moment M_x has the smallest COV of 7.1%.

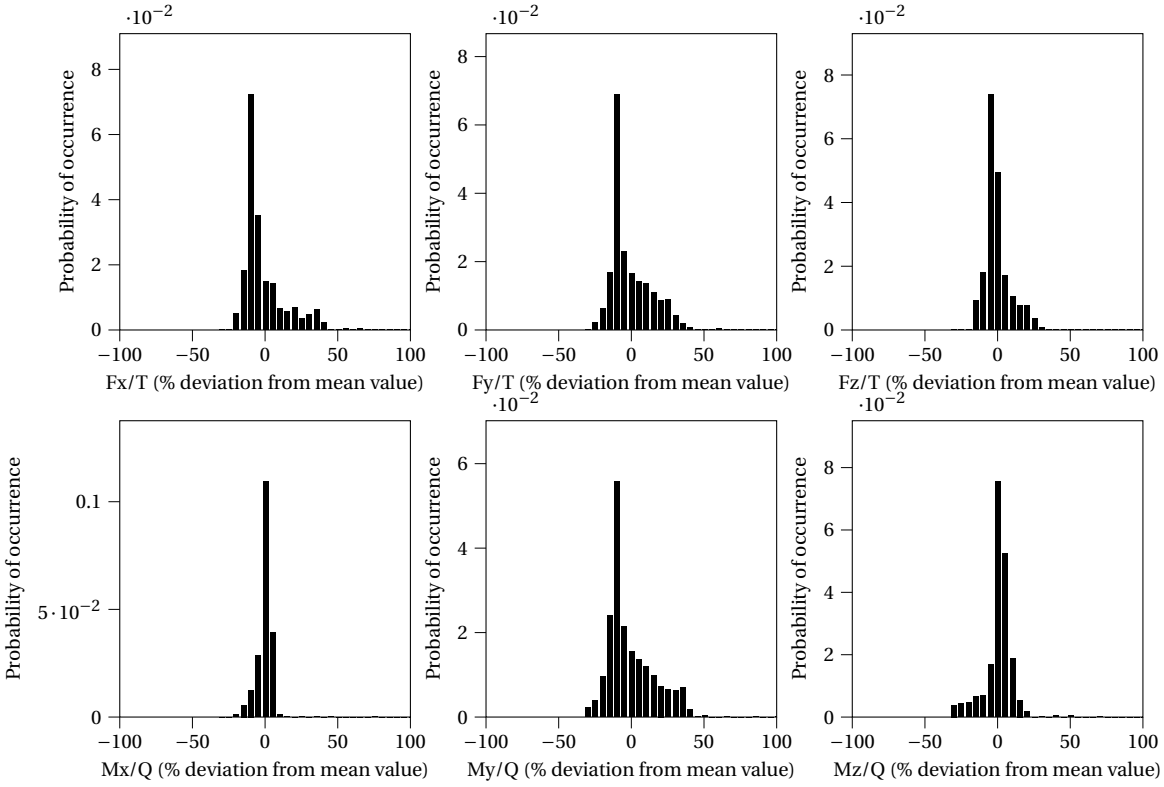

Figure 3.16: Histogram of 4/rev vibratory hubforces and moments in forward flight for the material uncertainty analysis

3.3.2 Propagation of Manufacturing Uncertainties

Following the first analysis of material uncertainties, this section evaluates the effects of fiber orientation uncertainties based on the LHS Monte-Carlo Simulation with 1000 random samples. Unlike the first analysis, the parameters of this MCS do not affect the mass or inertial properties of the blade in any way. The diagonals of the beam stiffness properties show the effect of fiber orientation is in the same magnitude as the effect of material uncertainty with a COV of 2.8, 4.1, 4.1 and 0.4% for the K_{11}, K_{44}, K_{55} and K_{66} respectively. The coupling relations of the cross-section at 0.4R in figure 3.17 and 1R in figure 3.18 demonstrate the substantial effect to the twist-axial K_{14}, twist-flap K_{45}, twist-lag K_{46} coupling relations. Compared to the material uncertainty study, those terms are increased from a COV <1% to a COV of approximately 30% at 0.4R. At the same time, the effect to lag-stiffness K_{66}, and flap-lag coupling relation K_{56} is relatively small.
The uncertainty in fiber orientation will disturb the symmetric layup of the box-spar that enhances those coupling relations. This effect is amplified at radial station 1R because of the coordinate-system's location. In figure 3.19 the mean rotating natural frequencies are illustrated together with a $\pm 2\sigma$ confidence interval. The mean torsional frequency (4th mode) is lower compared to the baseline case and the analysis of material uncertainties. The beam properties anticipated that the $\pm 2\sigma$ confidence interval of the torsional mode will also be larger. Note that the -2σ boundary of this mode is very close to the 4/rev rotor harmonic. This shift of torsional frequencies towards the 4/rev is expected to affect the dynamic behavior and the resulting vibratory hubforces and moments adversely.
This behavior can be explained by the fact that the baseline configuration represents the mechanically stiffest solution. The 0° layers contribute to the highest longitudinal and bending stiffness and the 45° layers have the highest shear stiffness. Any change from the ideal configuration inevitably leads to a decrease in stiffness. It is therefore to be expected that the natural frequency spectrum of the MCS is below the reference configuration, as the inertial terms don't vary in this study. Similar to the first analysis, the impact of uncertainty varies with each mode. Generally, higher modes are affected to a larger extend because the ratio of structural elasticity to centrifugal stiffening increases.

For the symmetric hover flight state, the fiber orientation uncertainty has the consequence that both the flap and torsion response are affected substantially. Figure 3.20 shows for this purpose the histogram of the elastic flap, lag and torsion response. The response is the relative tip displacement measure to the blade attachment. The flap response has a COV of 61.6%, the torsion response has a COV of 63.5% while the lag response stays relatively uninfluenced.

The elastic tip response during forward flight is also shown for fiber orientation uncertainty in

figure 3.21. Compared to the tip response of the study of material uncertainty, the torsional response of this analysis shows larger mean amplitudes. The most significant impact is the large $\pm 2\sigma$ confidence interval that has a magnitude of around 5 degree for the torsional response. Note that for all responses, the higher harmonic fraction of the signal becomes much more visible.
Figure 3.22 shows the 4/rev vibratory hubforces and moments in forward-flight. The increased vibratory loads were anticipated from the previous evaluations. Again, non Gaussian distributions result from the introduced uncertainty. All fractions of the vibratory hubloads show an increased distribution. The largest variation is registered at the vertical force and torque components with a COV of 80% and peak values up to 400%.

3.4 Discussion

The variations resulting from the manufacturing tolerances and deviations in the material properties are of such magnitude that they cause the rotor system performance to change significantly and that despite uncertainties in the operational loads or flight states are not even considered yet. Also note, that the assumption of this study is that one random sample from the material or fiber orientation distribution is applied to the all five cross-sections with the same value. Hence the material properties and fiber orientation are constant over the span of the rotor blade. In reality however, some parameters presumably vary along the span of the blade and therefore the effects might counteract each other to some extend and change the effect on the rotor blade properties and dynamic behavior.
Similarly, all four rotor-blades are assumed to be equal for each sampled case. No blade dissimilarity is assumed for this study. In reality, blade dissimilarity is counteracted to some extend by a tracking and balancing the blades of a rotor. In the future, blade dissimilarity could be investigated with its effect to rotor behavior and tracking and balancing efforts. To conclude, it is clearly essential to take uncertainties into account from the beginning of the multidisciplinary rotor blade system design, especially when an optimal solution is desired [165]. As it was previously stated for the rotating natural frequencies of the rotor, traditional design processes account for uncertainties by imposing constraints such as empirical and predefined safety factors. This is however primarily based on past experiences, which may not be available, be inappropriate or outdated for new rotor designs [165].
The results of this study emphasize and motivate the need for a uncertainty-based design processes that introduce uncertainties systematically to improve the robustness (decrease the sensitivity of the system performance to variations), increase reliability and reduce the likelihood of functional failure under potentially critical conditions and exploit the full potential of fiber composite rotor blades in a multidisciplinary design optimization. [165]

This study also stresses the importance of knowledge of the structural rotor blade beam characteristics.
The engineer needs to have tools at hand that can predict the beam properties with sufficient accuracy and, if desired, can be used for such uncertainty-based design processes. It is important that all the structurally relevant components can be represented in the structural model. We are talking about structural models that are suitable for an uncertainty-based preliminary design process, which usually calls for adequate computational resources and automated structural preprocessing. In the near and mid-term future, a 1D nonlinear beam model and a 2D cross-sectional analysis will most likely still be used in this context due to the modeling effort and computational resources.

The second tool engineers need is an experimental procedure to determine the beam stiffness properties, including the off-diagonal coupling relations, of the actual manufactured rotor blades at an accuracy at least sufficient to ensure that the remaining uncertainties no longer have a significant effect on the dynamic rotor behavior. This problem describes the next major objective of this work, examined in the following chapter, as current methods often use simplified beam models and measure average stiffness's over large regions of the blade while neglecting essential coupling-relations.

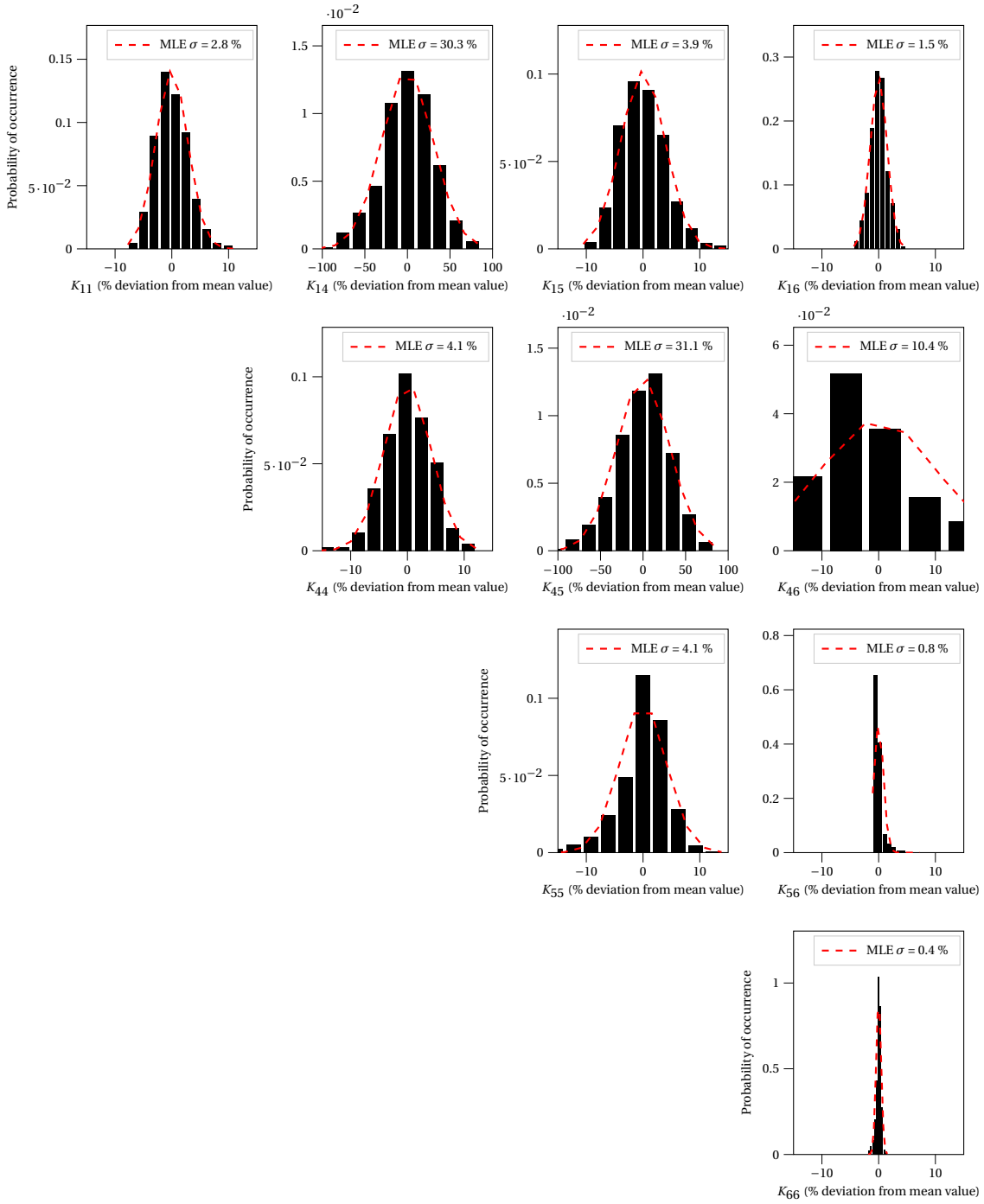

Figure 3.17: Histogram of the classical stiffness matrix at 0.4R (fiber orientation uncertainty analysis)

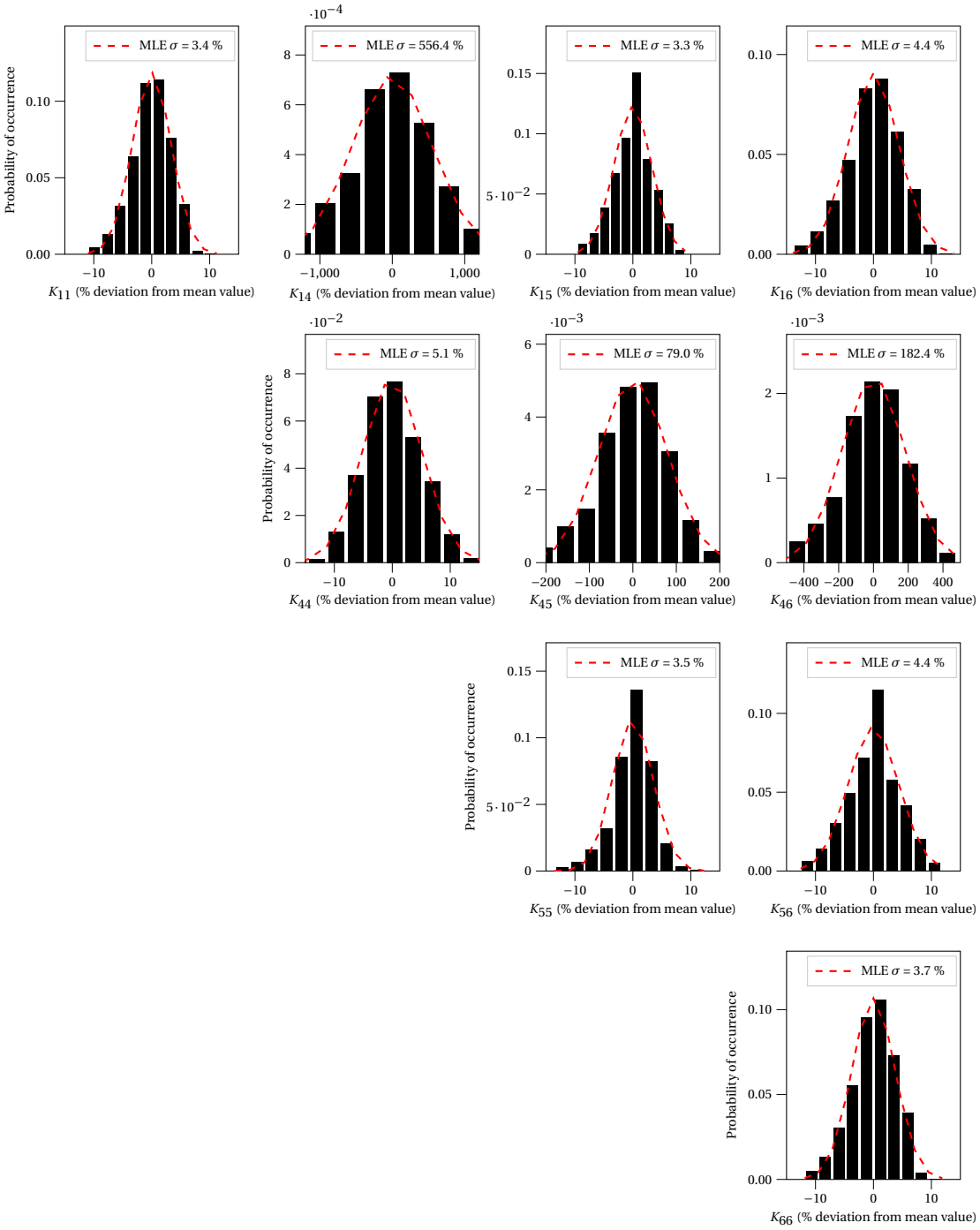

Figure 3.18: Histogram of the classical stiffness matrix at 1R (fiber orientation uncertainty analysis)

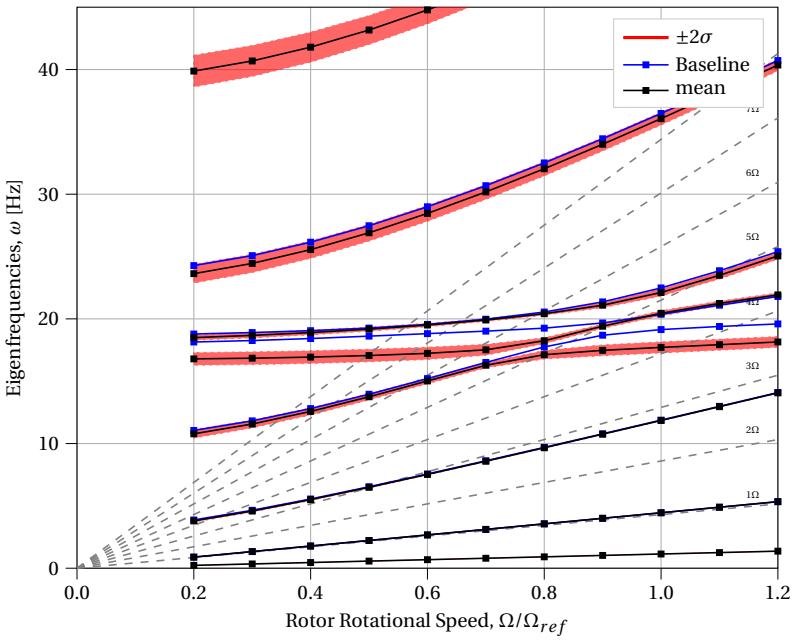

Figure 3.19: Mean natural frequencies with $\pm 2\sigma$ confidence interval versus rotational speed (fiber orientation uncertainty analysis)

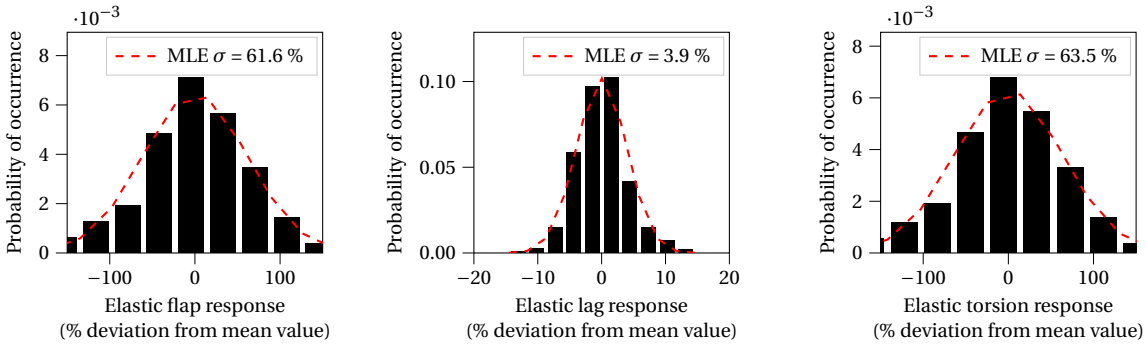

Figure 3.20: Histograms of the elastic flap, lag and torsion response in hover (fiber orientation uncertainty analysis)

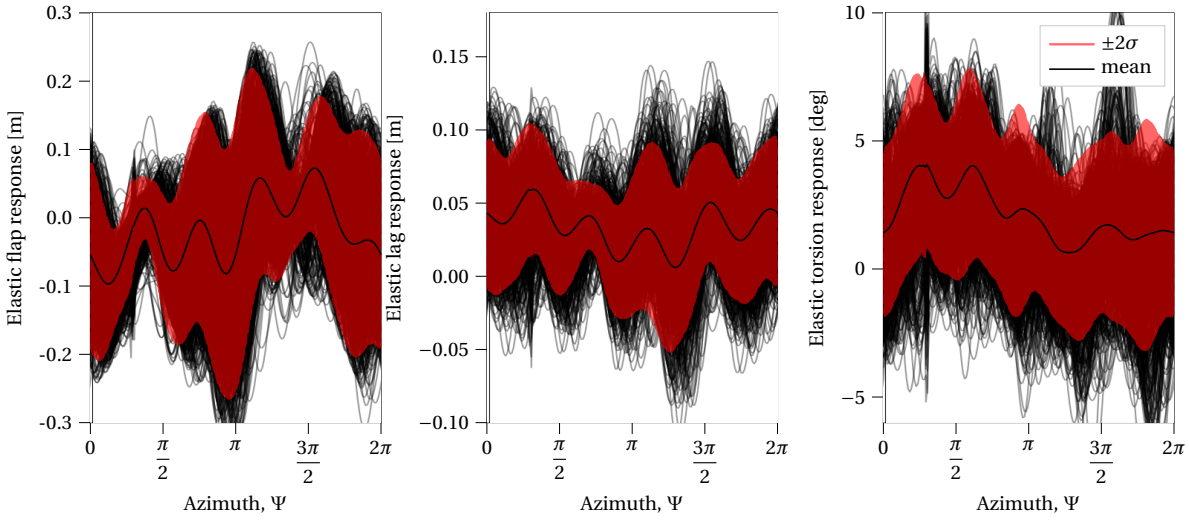

Figure 3.21: Elastic flap, lag and torsion response in forward flight with $\pm 2\sigma$ confidence interval (fiber orientation uncertainty analysis)

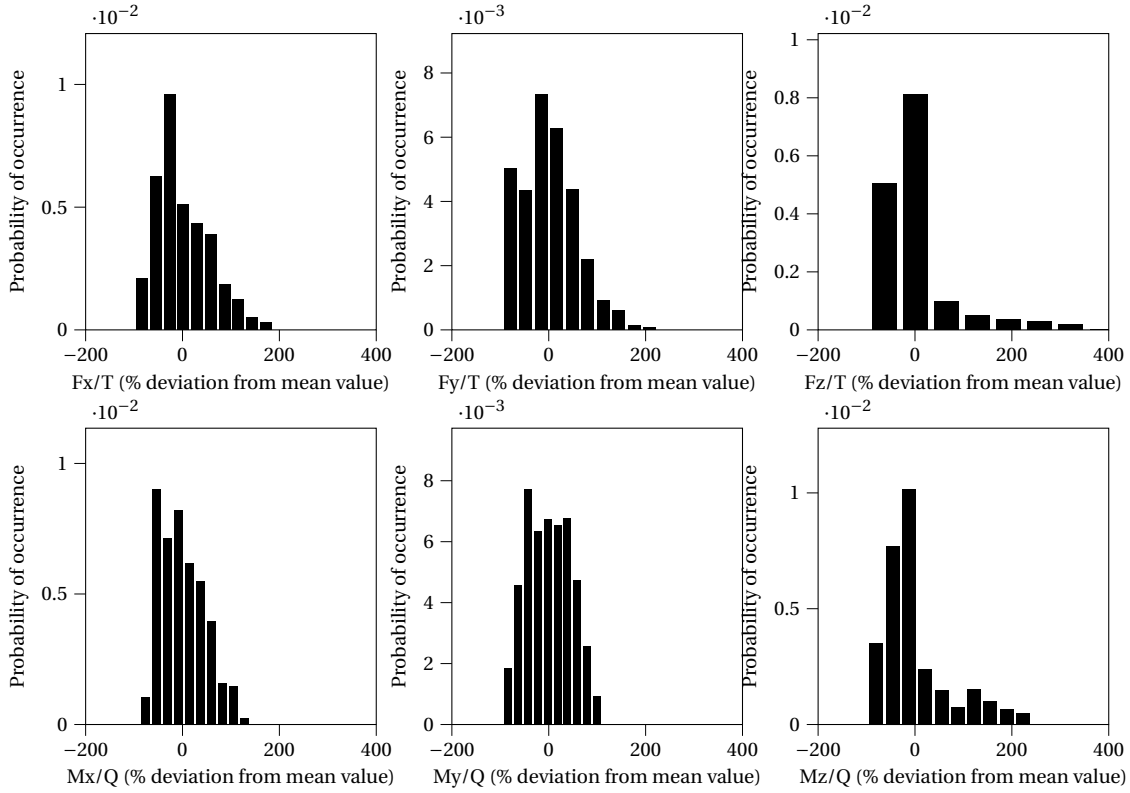

Figure 3.22: Histogram of 4/rev vibratory hubforces and moments in forward flight (fiber orientation uncertainty analysis)

4 Hybrid Experimental Measurement of Sectional Stiffness Properties

The objective of this chapter is to refine a method to experimentally determine the sectional stiffness properties of modern fiber composite rotor blades, which is a prerequisite for the prediction of the dynamic behavior.
The herein presented specimen of the methodology is the first rotor blade specifically developed for the Munich Experimental Rotor Investigation Testbed (MERIT) [66], [67], a rotor test bench designed for universal rotor and propeller aerodynamic and structural dynamic investigations, whose robust design allows for highly dynamic load applications such as Mach-scaled dynamic stall experiments.
Parts of this chapter were previously published in ERF2021A. In addition, two student theses contributed to this chapter, see GAUGELH.2020 (experimental design, setup and execution) and ROTH2020 (concept and design of a balancing device for rotor blades).

The beam behavior is characterized by the symmetric 6×6 sectional stiffness matrix $\underline{\underline{K}}$ along the span leaving 21 desired properties for each radial station. This study hereby follows the novel approach first introduced by Sinotte and Bauchau [159]–[161].
While most classical experimental techniques rely on measuring the beam displacements or rotations using simplified beam models, neglecting coupling effects and averaging regions of interest, this hybrid method relies on the measurement of the strain field and combines it with a numerically determined warping field. The strain field is measured using Digital Image Correlation (DIC)- a contact-free, optical 3D deformation measurement method in order to analyze and calculate deformations. The surface structure of the specimen is recognized in digital camera images, and coordinates are assigned to image pixels. During the deformation of the specimen, images are taken and compared to the undeformed state in order to calculate the displacement and deformation of the object. In this case, the homogeneous surface of the rotor blade has few characteristic features, so the surface was pretreated with a stochastic color pattern.

4.1 Governing Equations

Based on the central solution of the nonlinear three-dimensional beam theory by Han and Bauchau [14], [63], the nodal displacement $\underline{\hat{u}}$ is described as the superposition of a rigid-section motion and the nodal warping introduced by sectional stress resultants $\underline{F}^T = \{F_x, F_y, F_z, M_x, M_y, M_z\}$.

$$\underline{\hat{u}}(\bar{\alpha}_1) = \underline{\underline{Z}}\,\underline{\mathcal{U}}(\alpha_1) + \underline{\underline{W}}\,\underline{F}(\alpha_1) \tag{4.1}$$

with

$$\underline{\underline{Z}} = \begin{bmatrix} \underline{\underline{z}} \\ \underline{\underline{0}} \end{bmatrix}; \quad \underline{\underline{z}} = \begin{bmatrix} 1 & 0 & 0 & 0 & \bar{\alpha_3} & -\bar{\alpha_2} \\ 0 & 1 & 0 & -\bar{\alpha_3} & 0 & 0 \\ 0 & 0 & 1 & \bar{\alpha_2} & 0 & 0 \end{bmatrix} \tag{4.2}$$

The first term of equation (4.1) describes the rigid-section motion at a specific point of the cross-section by multiplying the nodal location matrix $\underline{\underline{Z}}$ with the average sectional displacement $\underline{\mathcal{U}}$. The second term multiplies the nodal warping displacement under unit loads $\underline{\underline{W}}$ with the sectional stress resultant. The notation $\hat{(.)}$ indicates nodal quantities of the discretized model.
Based on the general theory of three-dimensional elasticity, their approach makes the assumptions that the cross-sectional strains associated with the rigid-section motion and the warping displacements always remain small [63]. With these assumptions, the solutions provided are the exact representation of the three-dimensional elasticity problem for beams subjected to arbitrarily large motions [63]. Given that, the strain tensor $\underline{\varepsilon}^T = \{\varepsilon_{11}, 2\varepsilon_{12}, 2\varepsilon_{13}, \varepsilon_{22}, \varepsilon_{33}, 2\varepsilon_{23}\}$ is described by the following strain-displacement relation in matrix notation with the differential operators $\underline{\underline{A}}$ and $\underline{\underline{B}}$. $(.)'$ denotes the spatial derivative with respect to the spanwise variable α_1.

$$\begin{aligned} \varepsilon_{11} &= \frac{\partial u_1}{\partial \alpha_1}, & \varepsilon_{22} &= \frac{\partial u_2}{\partial \alpha_2}, & \varepsilon_{33} &= \frac{\partial u_3}{\partial \alpha_3}, \\ 2\varepsilon_{12} &= \frac{\partial u_1}{\partial \alpha_2} + \frac{\partial u_2}{\partial \alpha_1}, & 2\varepsilon_{13} &= \frac{\partial u_1}{\partial \alpha_3} + \frac{\partial u_3}{\partial \alpha_1}, & 2\varepsilon_{23} &= \frac{\partial u_2}{\partial \alpha_3} + \frac{\partial u_3}{\partial \alpha_2}, \end{aligned} \tag{4.3}$$

$$\underline{\varepsilon} = \underline{\underline{A}}\,\underline{u}' + \underline{\underline{B}}\,\underline{u} \tag{4.4}$$

By spatially differentiating the nodal displacement with respect to the spanwise coordinate $(\bar{\alpha}_1)$,

the following equation is derived.

$$\underline{\hat{u}}'(\bar{\alpha}_1) = \frac{\partial \underline{\hat{u}}}{\alpha_1} = \underline{\underline{Z}}\,\underline{\mathcal{U}}'(\bar{\alpha}_1) + \underline{\underline{W}}\,\underline{F}'(\bar{\alpha}_1) \tag{4.5}$$

Together with the description of the sectional constitutive law $\underline{\varepsilon}_c = \underline{\mathcal{U}}'(\bar{\alpha}_1) + \underline{\mathcal{U}}(\bar{\alpha}_1) = \underline{\underline{S}}\,\underline{F}$ and the stress resultant equilibrium equation $\underline{F}' = \tilde{\mathcal{K}}^T \underline{F}$ it can be introduced into equation (4.4) along with (4.1) giving the description of the three-dimensional strain tensor. Because rigid-body displacements create no strains, the last term vanishes to zero.

$$\begin{aligned}
\underline{\hat{\varepsilon}} &= \underline{\underline{A}}\,\underline{u}' + \underline{\underline{B}}\,\underline{u} \qquad (4.6)\\
&= \underline{\underline{A}}\left[\underline{\underline{Z}}\left(\underline{\underline{S}}\,\underline{F} - \tilde{\mathcal{K}}\underline{\mathcal{U}}\right) + \underline{\underline{W}}\tilde{\mathcal{K}}^T\underline{F}\right] + \underline{\underline{B}}\left[\underline{\underline{Z}}\,\underline{\mathcal{U}}(\bar{\alpha}_1) + \bar{\underline{\underline{W}}}\,\underline{F}(\bar{\alpha}_1)\right]\\
&= \left[\underline{\underline{A}}\left(\underline{\underline{Z}}\,\underline{\underline{S}} + \underline{\underline{W}}\tilde{\mathcal{K}}^T\right) + \underline{\underline{B}}\,\underline{\underline{W}}\right]\underline{F} + \underbrace{\left[\underline{\underline{B}}\,\underline{\underline{Z}} - \tilde{\mathcal{K}}\right]\underline{\mathcal{U}}}_{=0;\ \text{rigid-body disp.}}
\end{aligned}$$

$$\underline{\hat{\varepsilon}} = \left[\underline{\underline{A}}\left(\underline{\underline{Z}}\,\underline{\underline{S}} + \underline{\underline{W}}\tilde{K}^T\right) + \underline{\underline{B}}\,\underline{\underline{W}}\right]\underline{F} \tag{4.7}$$

As described in chapter 2, the orientation of the cross-section will change along the span for initially curved and twisted beams. $\tilde{\mathcal{K}}$ depicts the 6×6 nondimensional curvature tensor for an initially curved or twisted beam with the twist rate κ_1, and the curvature κ_2, κ_3 about the y_l and z_l axis respectively.

$$\tilde{\mathcal{K}}^* = \begin{bmatrix}
0 & -\kappa_3 & \kappa_2 & 0 & 0 & 0\\
\kappa_3 & 0 & -\kappa_1 & 0 & 0 & -1\\
-\kappa_2 & \kappa_1 & 0 & 0 & 1 & 0\\
0 & 0 & 0 & 0 & -\kappa_3 & \kappa_2\\
0 & 0 & 0 & \kappa_3 & 0 & -\kappa_1\\
0 & 0 & 0 & -\kappa_2 & \kappa_1 & 0
\end{bmatrix} \tag{4.8}$$

Equation (4.7) provides the governing description of our problem. The inverse of the sectional compliance matrix $\underline{\underline{K}} = \underline{\underline{S}}^{-1}$ is the desired property. In our experimental setup, we can measure the sectional stress resultants $\underline{F}$ with a 6-axis load cell at the root-attachment of the blade and transform the loads to the desired spanwise location by using the free-body diagram. The second measured quantity are the plane surface strains $\varepsilon_{11,e}, \varepsilon_{12,e}$ and $\varepsilon_{22,e}$. The strains are always calculated in material, i.e. in local coordinates moving with the specimen while the $\underline{e}_3$-axis is in the

thickness direction. To ensure a common orientation of the strains, the strain rotation matrix $\underline{\underline{R}}_e$ is introduced to the equation. The full strain tensor can be derived with the knowledge of the material constitutive behavior but it is not needed, since the last three terms of the equation reduce to zero. The strain ε_{13} is obtained through $\underline{\underline{R}}_e$ for values of $\theta \neq 0$.

$$\begin{aligned} \underline{\underline{R}}_e \hat{\underline{\varepsilon}}_e &= \left[\underline{\underline{A}}\left(\underline{\underline{Z}}\,\underline{\underline{S}} + \underline{\underline{W}}\tilde{\mathcal{K}}^T\right) + \underline{\underline{B}}\,\underline{\underline{W}}\right]\underline{F} \\ \hat{\underline{\varepsilon}}_e &= \underline{\underline{R}}_e^{-1}\left[\underline{\underline{A}}\left(\underline{\underline{Z}}\,\underline{\underline{S}} + \underline{\underline{W}}\tilde{\mathcal{K}}^T\right) + \underline{\underline{B}}_L\,\underline{\underline{W}}\right]\underline{F} \end{aligned} \tag{4.9}$$

with the strain-rotation matrix defined as

$$\underline{\underline{R}}_e = \begin{bmatrix} 1 & 0 & 0 & 0 & 0 & 0 \\ 0 & \cos\theta & -\sin\theta & 0 & 0 & 0 \\ 0 & \sin\theta & \cos\theta & 0 & 0 & 0 \\ 0 & 0 & 0 & \cos^2\theta & \sin^2\theta & -\sin 2\theta \\ 0 & 0 & 0 & \sin^2\theta & \cos^2\theta & \sin 2\theta \\ 0 & 0 & 0 & \frac{1}{2}\sin 2\theta & -\frac{1}{2}\sin 2\theta & \cos 2\theta \end{bmatrix} \tag{4.10}$$

The hybrid approach is based on the fact that the warping displacement under unit loads $\underline{\underline{W}}$ is evaluated with the help of a sectional finite element model SONATA and ANBA4.
After mapping and interpolating the experimental strain data to the closest nodal location denoting $(.)_i$, at which the warping displacement is evaluated, the governing equation describes an overdetermined system of equations with independent load-cases denoted $(.)_j$.

$$\begin{aligned} \underline{\varepsilon}_{e,i}^{(j)} &= \underbrace{\underline{\underline{R}}_{e,i}^{-1}\underline{\underline{A}}_i\underline{\underline{Z}}_i}_{\underline{\underline{U}}_i}\underline{\underline{S}}\,\underline{F}^{(j)} + \underbrace{\underline{\underline{R}}_{e,i}^{-1}\left(\underline{\underline{A}}\,\underline{\underline{W}}\tilde{K}^T + \underline{\underline{B}}\,\underline{\underline{W}}\right)}_{\underline{\underline{V}}_i}\underline{F}^{(j)} \\ \underline{\varepsilon}_{e,i}^{(j)} &= \underline{\underline{U}}_i\underline{\underline{S}}\,\underline{F}^{(j)} + \underline{\underline{V}}_i\underline{F}^{(j)} \end{aligned} \tag{4.11}$$

The system is solved by using the half-vectorization of the symmetric compliance matrix leaving the 21 unknowns. The 6×21 matrix $\underline{\underline{G}}$ is defined with the duplication matrix $\underline{\underline{\underline{D}}}_n$ $\mathrm{vech}(\underline{\underline{S}}) = \mathrm{vec}(\underline{\underline{S}})$ as:

$$\underline{\underline{S}}\,\underline{F}^{(j)} = \underline{\underline{G}}^{(j)} \cdot \mathrm{vech}(\underline{\underline{S}}) = \underline{\underline{G}}^{(j)}\,\underline{S} \tag{4.12}$$

$$\underline{\underline{G}}^{(j)} = \left(\underline{\underline{I}} \otimes \underline{F}^{(j)}\right)\underline{\underline{\underline{D}}}_n \tag{4.13}$$

$$\underline{\underline{U}}_i \underline{\underline{G}}^{(j)} \underline{S} = \underline{\varepsilon}_{\epsilon,i}^{(j)} - \underline{\underline{V}}_i \underline{F}^{(j)} \tag{4.14}$$
$$\underline{\underline{\mathbb{A}}}\,\underline{S} = \underline{b}$$

The heavily over-determined system of linear equations is solved by minimizing the Euclidean 2-norm of $\|b - \mathbb{A}\underline{S}\|_2$.

The Singular Value Decomposition (SVD) is a suitable method to solve this problem. An exact rank 21 truncated SVD is substituted for $\underline{\underline{\mathbb{A}}} = \underline{\underline{\tilde{U}}}\,\underline{\underline{\tilde{\Sigma}}}\,\underline{\underline{\tilde{V}}}^T$, in order to obtain the left Moore-Penrose pseudo-inverse $\mathbb{A}^\dagger$. Determining the pseudo-inverse $\mathbb{A}^\dagger$ from the unitary matrices $\underline{\underline{\tilde{U}}}$ and $\underline{\underline{\tilde{V}}}$ and the diagonal matrix $\underline{\underline{\tilde{\Sigma}}}$ is computationally efficient.[30]

$$\underline{\underline{\mathbb{A}}}^\dagger = \underline{\underline{\tilde{V}}}\,\underline{\underline{\tilde{\Sigma}}}^{-1}\underline{\underline{\tilde{U}}}^T \qquad \Rightarrow \qquad \underline{\underline{\mathbb{A}}}^\dagger\underline{\underline{\mathbb{A}}} = \underline{\underline{I}}_{21\times 21} \tag{4.15}$$

The Eckart-Young-Mirsky theorem [45] proofs that $\underline{\underline{\mathbb{A}}}^\dagger$ is the best approximation of $\underline{\underline{\mathbb{A}}}$ by a rank 21 matrix, minimizing $\|b - \mathbb{A}\underline{S}\|_2$. It follows, that $\underline{S}$ becomes:

$$\underline{\underline{\mathbb{A}}}^\dagger\underline{\underline{\mathbb{A}}}\,\underline{\tilde{S}} = \underline{\underline{\mathbb{A}}}^\dagger\underline{b} \qquad \Rightarrow \qquad \underline{S} = \underline{\underline{\tilde{V}}}\,\underline{\underline{\tilde{\Sigma}}}^{-1}\underline{\underline{\tilde{U}}}^T\underline{b}. \tag{4.16}$$

Finally, the sectional stiffness matrix $\underline{\underline{K}}$ is obtained from the inverse of the sectional compliance matrix $\underline{\underline{S}}$.

$$\underline{\underline{K}} = \underline{\underline{S}}^{-1} = \left[\begin{array}{cccccc} K_{11} & K_{12} & K_{13} & K_{14} & K_{15} & K_{16} \\ K_{12} & K_{22} & K_{23} & K_{24} & K_{25} & K_{26} \\ K_{13} & K_{23} & K_{33} & K_{34} & K_{35} & K_{36} \\ K_{14} & K_{24} & K_{34} & K_{44} & K_{45} & K_{46} \\ \hline K_{15} & K_{25} & K_{35} & K_{45} & K_{55} & K_{56} \\ K_{16} & K_{26} & K_{36} & K_{46} & K_{56} & K_{66} \end{array}\right] \tag{4.17}$$

4.2 Digital Image Correlation

The strain field is measured using Digital Image Correlation (DIC) - a contact-free, optical 3D deformation measurement method in order to analyze and calculate deformations. The surface structure of the specimen is recognized in digital camera images, and coordinates are assigned to image pixels. During the deformation of the specimen, images are taken and compared to the undeformed state in order to calculate the displacement and deformation of the object. In the case of a 3D measurement set-up, two cameras (stereo set-up) are used, which are calibrated prior to the measurement. The specimen is located in the calibrated 3D volume. The experimental setup with *GOM ARAMIS* cameras and the subsequent postprocessing with the software *GOM Correlate 2020* is described in detail in section 4.5 und 4.6. [57]
In the case, that the test specimen has only few characteristic features, e.g. in the case of homogeneous surfaces, it is pretreated with a stochastic color pattern.

4.2.1 Principle

The principle of Digital Image Correlation is to clearly identify areas of a image with sufficient information. This allows the software to identify the same zones in further images if they do not differ too much from their original shape. From this unique, homologous identification of image points, 3D coordinates can be derived through triangulation. Subsequently, quantities such as displacements, velocities, accelerations or strains can be calculated from the 3D coordinates.
For the collection of image information, reference point markers as shown in figure 4.1a can be used. For identification, the contrast gradient from white to black and the location of the markers with respect to each other is used. The software can identify the location of the high gray value gradient from black to white and then fits an ellipse into this unique gray value transition. The center of the ellipse determines the measuring point.[57]
The second possibility to uniquely identify individual image areas as shown if figure 4.1b, is to use stochastic image information. There are several approaches to identify deforming image regions. However, the basic assumption is that there is a causal relationship between the initial state and the deformed state. The correlation function provides a measure of the similarity between two signals f and g, $f(x,y) \overset{!}{\longleftrightarrow} g(x,y)$. The identification of facets (a subset of pixels) in several images is called facet matching.

$$c\left(\Delta x, \Delta y\right) = \frac{\langle f\left(x,y\right), g\left(x+\Delta x, y+\Delta y\right)\rangle}{|f\left(x,y\right)| \cdot |g\left(x,y\right)|} \tag{4.18}$$

By distributing random image information through a stochastic color pattern, it is ensured that a facet can be identified as uniquely as possible in its immediate surroundings. The probability of

a random pattern occurring more than once in such an environment is low. For example, with a facet size of 19 by 19 pixels and 256 gray values, the number of variations is $256^{(19\times19)}$. The ideal facet has a pattern that is as pronounced and as evenly distributed as possible and has a texture with about three to four contrast points. A pattern quality measure is implemented within the software and gives a numerical value of the stochastic pattern within the facet. A value of > 4 is considered sufficient. A variation in facet-size can increase or reduce the stochastic information and can be adjusted accordingly. Each of these facets represents its center point, which is used as an identification point equivalent to the ellipse center point in the reference point marks. [57]

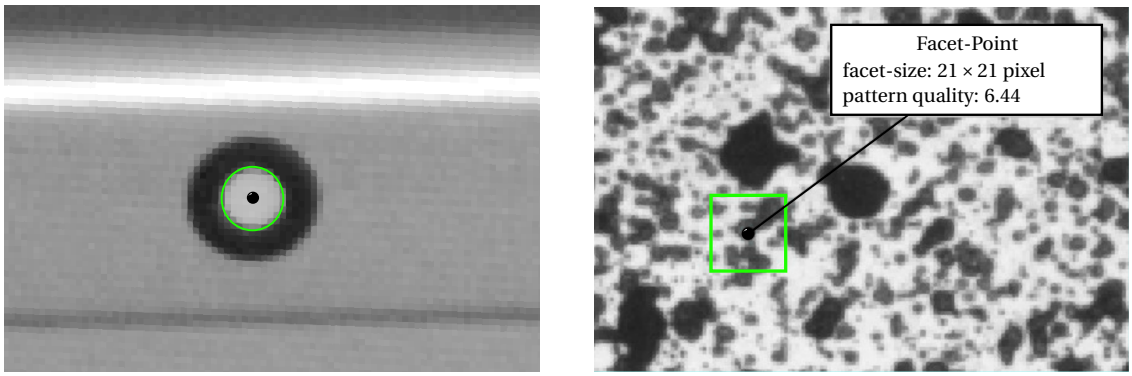

(a) Reference point maker on a homogeneous aluminum surface with the fitted ellipse and its center

(b) Facet point component on a stochastic color pattern with a size of 21 × 21 pixels

Figure 4.1

The calculated image point coordinates are used to calculate 3D points on a surface by the principle of triangulation. When the cameras identify two signals emanating from one point, based on the camera calibration, angle measurements can be used to uniquely determine its location. To obtain correct measurement data, the cameras must be calibrated. The software uses captured camera images of a precisely measured calibration object to determine geometric parameters, e.g. position and orientation of each camera as well as the imaging properties of the camera lenses and chips. The *intersection deviation* is the value of validity of the sensor calibration [57].
The software takes an image point from the left camera picture (primary camera) $\underline{x}_L$ and searches for the same image point in the right camera picture $\underline{x}_R$. If the points $\underline{x}_L$ and $\underline{x}_R$ are known, their projection lines from the camera image plane are also defined. If the two image points correspond to the same 3D point, the projection lines must intersect precisely at $\underline{x}$. The differences between the calculated 3D-coordinate point and the theoretical intersection of projection lines is the intersection deviation. A value below < 0.03 pixel is considered to be adequate. [57]

4.2.2 Strain Calculation

Strain is a normalized measure of deformation which characterizes the change of distance and angles between particles. The motion of a particle or image point is described by the evolution of its spatial coordinates or its position vectors over time. The primary measure of deformation is specified by the material deformation gradient tensor $\underline{\underline{F}}$ that contains the information of relative motion in the differential neighborhood [120]. The fundamental equation of deformation is

$$d\underline{x} = \frac{\partial \underline{x}(\underline{X}, t)}{\partial \underline{X}} \cdot d\underline{X} = \underline{\underline{F}}(\underline{X}, t) \cdot d\underline{X}. \tag{4.19}$$

The measuring system provides image points on a surface. This means that initially only strains on the surface, or more precisely in the current, surface-tangential reference plane can be determined. To compute a 2D deformation gradient tensor $\underline{\underline{F}}$ from a set of image points the following procedure is used by *GOM Correlate* [57]: The topology of the point distribution in the measurement image is triangulated. The points used for the strain calculation are projected onto a local compensation plane. The plane is determined by averaging the surface normals of the local triangles involved. The motion and deformation of an element consisting of i points p_i is described as a function of rigid body translation $\underline{u}$ and $\underline{\underline{F}}$ as follows.

$$\underline{p}_i' = \underline{u} + \underline{\underline{F}}\,\underline{p}_i \tag{4.20}$$

Theoretically, a triangle is sufficient for calculating the six unknowns of this equation. However, in order to obtain a better support of the individual punctual measured values, the software takes into account further neighboring points leaving an overdetermined system of equations which is solved by iterative minimization [57].
Because the resulting deformation gradient tensor $\underline{\underline{F}}$ is not a suitable measure of deformation for engineering purposes, the right polar decomposition of $\underline{\underline{F}}$ splits the second order tensor into the material stretch tensor $\underline{\underline{U}}$, a unique positive-definite symmetrical second order tensor, and an unique orthogonal second order rotation tensor $\underline{\underline{Q}}$ such that:

$$\begin{aligned} \underline{\underline{U}} &= \sqrt{\underline{\underline{F}}^T \underline{\underline{F}}} \\ \underline{\underline{Q}} &= \underline{\underline{F}}\,\underline{\underline{U}}^{-1} \end{aligned} \tag{4.21}$$

By definition the symmetric stretch tensor contains the surface strain measurements:

$$\underline{\underline{U}} = \begin{bmatrix} \varepsilon_{11} + 1 & \varepsilon_{12} \\ \varepsilon_{21} & \varepsilon_{22} + 1 \end{bmatrix} \tag{4.22}$$

4.3 Design and Manufacturing of MERIT Rotor Blades

In general, the helicopters operational limitations such as vibrations, aeroelastic stability, maximum control loads and fatigue limitations are all affected by the onset of transient flow separation such as dynamic stall [91]. Therefore, the accurate prediction of unsteady airloads can be beneficial in the successful design of an advanced rotorcraft.
Within a helicopter rotor flowfield, the rotor blades encounter numerous unsteady aerodynamic effects from various sources. The first and most obvious source of unsteadiness is encountered through a continuous change in angle of attack over time. It is a combination of the pilots controlled collective and cyclic blade pitch, the dynamic motion and elastic bending of the rotor blades and the local variation in inflow velocity. On top of that, gusts and a complex three dimensional vortex wake system complicate the unsteady environment even more. Understanding and modeling the resulting aerodynamic response of the rotor blades is still one of the major challenges in helicopter design [91], [92].
The problem of dynamic stall is found to occur on the rotor at high speed forward flight where the advancing rotor blade operates close to its shock induced separation boundary or during maneuvers with high load factors where the retreating blade operates at much lower speeds but at very large angles of attack [27], [92].
Many 2D experimental tests have shown very distinctive features of dynamic stall that are significantly different from the static stall mechanisms - see, for example, McCroskey [106]–[108]. One characteristic feature of dynamic stall is a distinctive vortex disturbance that is created near the leading edge region and is swept over the airfoil chord. Along with the vortex moves a pressure change on the upper surface of the airfoil that increases lift and nose-down pitching moment well in excess of the static values [91]. Consequential is a considerable hysteresis in the force and pitching moment behavior. The characteristic airloads induced by the vortex may not only lead to large torsional loads on the blade sections but also to reduced or negative pitch damping. This can be responsible for dynamic instabilities, known as stall flutter [92]. While the increase of maximum lift is advantageous for helicopter performance and the operational flight envelope, the large nose-down pitching moments and instabilities generally define the performance limits of a helicopter rotor [92]. To define the rotor operating envelope, it is necessary to be able to confidently predict the large unsteady and vibratory loads generated by this dynamic stall phenomenon in order to foresee the consequences on the dynamic response of the rotor system.

As a baseline rotor for dynamic-stall experiments, the blades have no twist, a rectangular planform, naca0012 airfoil, 130mm chord and a radius of 900mm. This simplicity allows an easier reproducibility and comparability with other experiments and numerical investigations. Many of these

requirements have been defined by MERIT and it's intended purpose. These and other requirements are briefly described below. The hub of the MERIT test bench is illustrated in figure 4.2

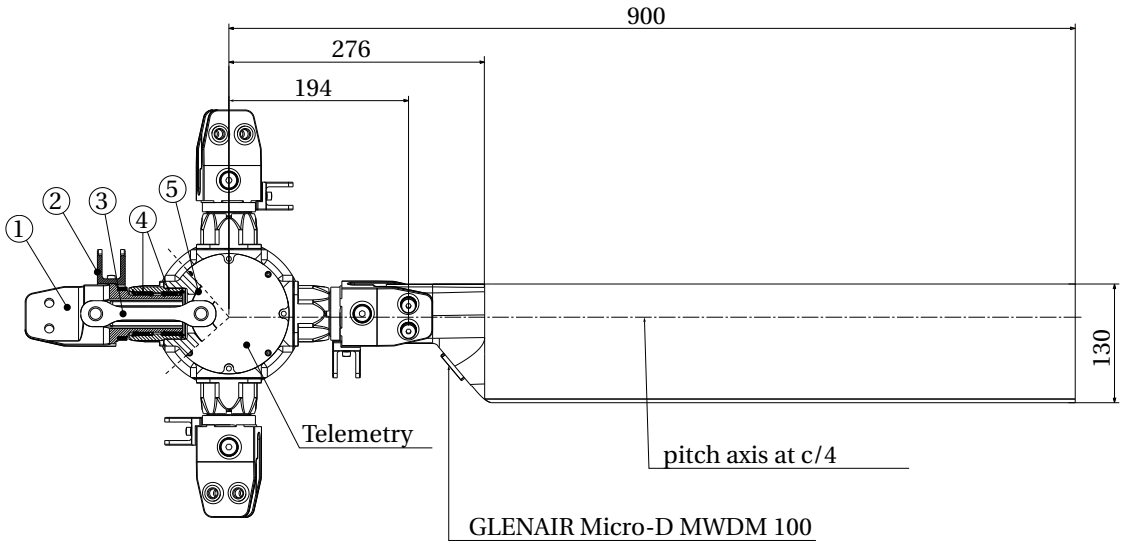

Figure 4.2: MERIT rotor hub and blade dimensions

which is a hingeless design: The blade clamps (1) have a preset pitch of 10° and are supported by two needle bearings each (4) to allow for pitch changes on each blade, while the flap and lead-lag motion is mainly accommodated by the blade's elastic behavior. The pitch-links are attached at (2) to the blade-clamps. Torsionally soft sheet metal tension-torsion straps (3) transfer the high centrifugal loads to the centerpiece (5). The relatively stiff hub design gives the test-bench a powerful response to control inputs and reduced blade movements. A telemetry unit by *MANNER Sensortelemetrie GmbH* is mounted onto to top of the centerpiece that can currently process 32 analog signals.

4.3.1 Blade Attachment

The blade attachment is designed as a bearing laminate. In this case, no loops are wrapped around a bolt, but a simple ply pack is stacked on top of each other, into which bushings are subsequently drilled. This technique is preferred when thicker laminates are involved, which are highly loaded and where large ply areas are available [149]. In this case, the laminate and the bolt connection must be designed for bearing laminate failure. This type of failure can be described as good-natured, since the hole merely deforms and does not fail abruptly as separation. It occurs slowly, since the fiber composite redistributes stress peaks through inter-fiber fractures and delamination. The failure announces itself in time [88], [105], [149], [170].
Important parameters for the strength of the blade attachment are the distances of the holes to

the sides of the laminate. The dimensions shown in figure 4.3 are decisive for the subsequent strength of the connection. The attachment is designed around two high strength steel bolts with a

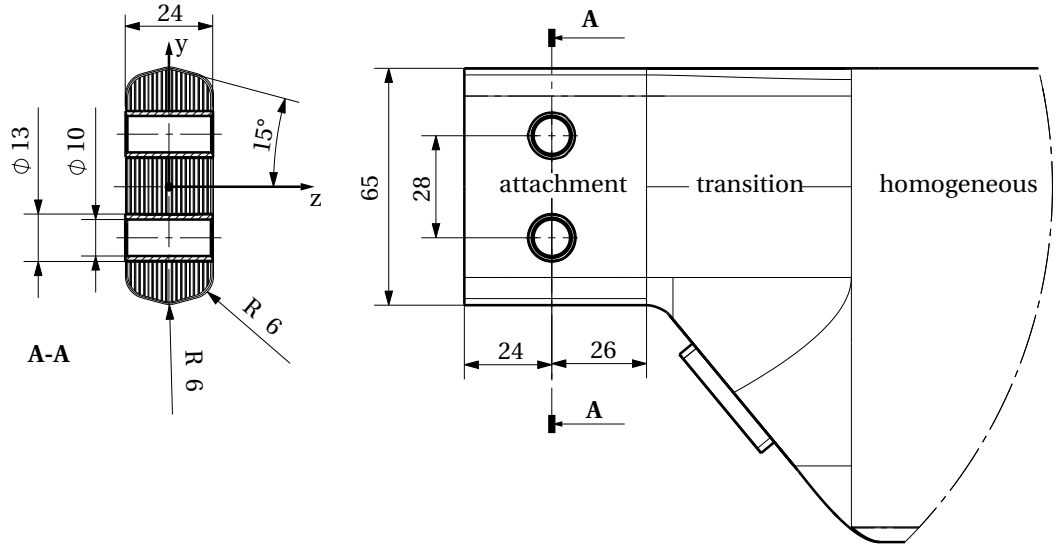

Figure 4.3: MERIT blade attachment and layup cross-section at R194

diameter of ∅10 mm, while ∅13 mm glued-in bushings guide the bolts. This is to prevent damage to the holes in the laminate due to frequent assembly. A glued-in bushing also smoothes out the surface pressure. In addition, the adhesive heals the microscopic interfiber fractures produced during drilling, while sealing it against moisture penetration and insulating it to prevent contact corrosion between the metallic connecting elements and the fiber composite.
The bushings are made of aerospace grade Böhler N352 stainless steel, a martensitic chromium steel with nickel addition, resistant to the effects of seawater and acids [25].
The blade attachment has a thickness of 24 mm. A lateral inclination of 15° ensures better demoldability, while the radii of the cross-section provide better drapability during the manufacturing process.

In general, the following layer thickness ratios are well suited for such a bearing laminate: 50% fraction of 0° layers, 45% fraction of ±45°-layers and 5% fraction of 90° layers [149]. The ply structure is symmetrical to prevent undesirable normal force, bending or torsional couplings. In addition, the differences in fiber angle between adjacent plies is designed as small as possible, as this reduces the interlaminar shear stresses in the laminate. It should also be noted that only a maximum of three plies are adjacent to each other in the same fiber direction. This reduces crack growth in the matrix of the fiber composite and thus increases the damage tolerance of the laminate. Other requirements for the laminate include that the adjacent plies should differ by less than 60°, as this reduces interlaminar stresses and residual stresses during the curing process.
Since the blade attachment has the thickest laminate, and the ply structure in the rotor blade

changes over the radius, the plies in the transition area must be scarfed. This also results in further important requirements for the blade and laminate design that must be taken into account.

Two different composite materials are used for the blade. The first composite material SGL Carbon - SIGRAPREG® C U600-0/SD-E501/33% (C_{UD}) is an Unidirectional (UD) epoxy/carbon fiber prepreg with a fiber areal weight of 600 g/m^2. This material combines a High tenacity (HT) carbon fiber with a epoxy resin (E501) with 33% weight fraction, designed for low curing temperatures of 80°C - 160°C with relatively short curing times. This makes this prepreg system particularly suitable for applications where only low temperatures are possible for curing [151]. For our application a low curing temperature is crucial to reduce thermal stresses and to protect the metrology that can be integrated into the blade structure before curing.
The second material (C_{TW}) combines the same epoxy resin (fractional weight of 45%) with a 200 g/m^2 2x2 twill weave HT carbon fiber [152]. The twill weave is chosen for its improved drapability and reduced fiber ondulation compared to a plain weave.
After consultation with the material supplier, both materials are considered to be the exact same as it was used for the design and manufacturing of the AREA rotorblades [128], [166]. Although there are materials with superior strength characteristics, this material was selected for use in MERIT rotor blades based on existing experience with handling and curing cycles.

One half of the resulting symmetric layup is listed in table 4.1 and also illustrated in figure 4.3. It should be noted here that the sequence number in the left column indicates the insertion sequence in the production process.

The first three layers compose the blade skin (sk) that stretch over the entire blade and which is mainly responsible for the torsional stiffness, which is why the twill-fabric C_{TW} is used here at ±45° to the longitudinal axis of the blade. This allows the fibers to be aligned along the principal stresses under torsion [88]. As the exterior part of the structure, the thinner woven fabric has a high impact resistance to be robust enough to withstand minor accidental impacts during handling and ensures a high surface quality.
To increase the electromagnetic compatibility (EMC) of integrated metrology, Aaronia-Shield® [1], a high performance silver/polyamide blend (20%/80%) net with a very low areal weight, can be placed optionally in between sk1 and sk2.

The unidirectional layers for the spar (sp) range from the attachment to the tip of the blade. The spar plies are evenly distributed in the blade attachment area and have several layers of C_{TW} fabric separating them as transition (tr) plies. The transition plies are scarfed and disappear in the homogeneous section of the blade.

seq.	name	material	orientation	thickness
1	sk1	C_{TW}	± 45°	0.24
2	emc	Aaronia-Shield	0°	0.10
3	sk2	C_{TW}	± 45°	0.24
4	sk3	C_{TW}	± 45°	0.24
5	sp1	C_{UD}	0°	0.56
6	tr1	C_{TW}	± 45°	0.24
7	tr2	C_{TW}	0°/90°	0.24
8	tr3	C_{TW}	± 45°	0.24
9	sp2	C_{UD}	0°	0.56
10	tr4	C_{TW}	± 45°	0.24
11	tr5	C_{TW}	0°/90°	0.24
12	tr6	C_{TW}	± 45°	0.24
13	sp3	C_{UD}	0°	0.56
14	tr7	C_{TW}	± 45°	0.24
15	tr8	C_{TW}	0°/90°	0.24
16	tr9	C_{TW}	± 45°	0.24
17	sp4	C_{UD}	0°	0.56
18	tr10	C_{TW}	± 45°	0.24
19	tr11	C_{TW}	± 45°	0.24
20	tr12	C_{TW}	± 45°	0.24
21	sp5	C_{UD}	0°	0.56
22	tr13	C_{TW}	± 45°	0.24
23	tr14	C_{TW}	± 45°	0.24
24	sp6	C_{UD}	0°	0.56
25	tr15	C_{TW}	± 45°	0.24
26	tr16	C_{TW}	± 45°	0.24
27	tr17	C_{TW}	± 45°	0.24
28	sp7	C_{UD}	0°	0.56
29	tr18	C_{TW}	± 45°	0.24
30	tr19	C_{TW}	0°/90°	0.24
31	tr20	C_{TW}	± 45°	0.24
32	sp8	C_{UD}	0°	0.56
33	tr21	C_{TW}	± 45°	0.24
34	tr22	C_{TW}	0°/90°	0.24
35	tr23	C_{TW}	± 45°	0.24
36	sp9	C_{UD}	0°	0.56
37	tr24	C_{TW}	± 45°	0.24
38	tr25	C_{TW}	0°/90°	0.24
39	tr26	C_{TW}	± 45°	0.24
- - - - - - - - - - - -	**symmetry plane**			- - - - - - - - - - - -

Table 4.1: Blade attachment layup table: sk: skin, tr: transition, sp: spar

For this work, static test results are available from a study for bearing laminates [102], [170]. In this study, the same materials are used with the same proportions of plies, a similar ply structure and edge distances. The resulting equivalent strengths are used to determine the strength margins for the blade attachment under operational loads.

4.3.2 Homogeneous Section

The homogeneous blade area is the aerodynamically effective area that provides the necessary lift and thrust and transmits it to the hub. It ranges from R276 to the tip at R900. The airfoil of the rotor blade is a NACA-0012, a symmetrical airfoil with a maximum thickness of 12% at 30% chord. The airfoil was selected because it is a frequent test case in computational fluid dynamics. In figure 4.4 the airfoil and the cross-sections of the homogeneous section is illustrated. In the figure it can be seen that the coordinate system of the rotor blade is at 25% chord. The cross-section is characteristic for fiber composite rotor blades with small chord. It consists essentially of the skin, spar, core, trim weight, and a trailing edge tab. One of the most important requirements for the cross-section is that the center of gravity be at or slightly ahead of 25% chord [88]. This helps to keep control and torsional forces low and avoid aeroelastic instabilities.

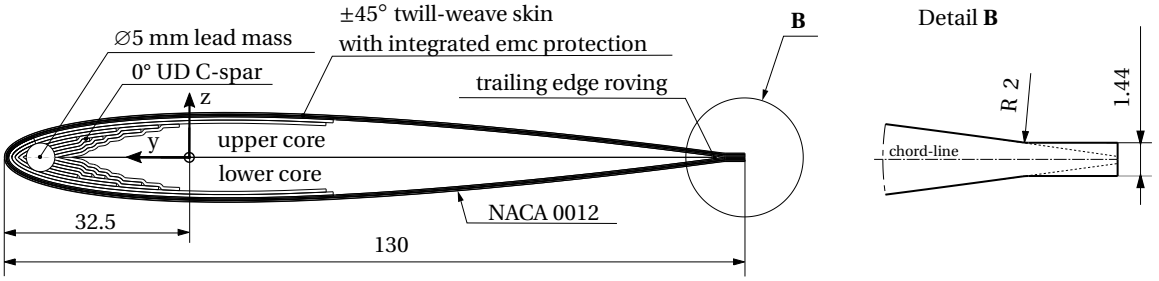

Figure 4.4: Homogeneous section composite layup with a NACA-0012 airfoil with modified tab

Due to a two-part manufacturing process, a trailing edge tab not only increases the shear stiffness of the between the two halves of the skin, but also considerably simplifies the manufacturing process creating a secure bond of the blade. Note that, the tab has an influence on the aerodynamic profile drag and the pitch moment. An enlarged section of the trailing edge is shown in figure 4.4 in detail B. The thickness of the tab of 1.44 mm corresponds to six times the thickness of the C_{TW} fabric. The tab is intersected with the original NACA 0012 airfoil and rounded with a radius of 2 mm.

The cross-section shown in figure 4.4 has a C-shaped spar construction. The spar carries primarily the flapping and lead-lag bending moments as well as the centrifugal forces and is made of unidirectional fibers in the direction of the blade's axis. The advantage of the C-shaped spar is that the center of gravity as well as the shear center are located at the front of the cross section [88] while the manufacturing remains simple. The layup is summarized in table 4.2.

As already mentioned, the center of gravity of the airfoil cross sections must be at or slightly ahead of 25% chord. The center of gravity of a cross section shown in figure 4.4, without the trim mass, is well behind it. To move the center of gravity of the cross-section forward, a balance weight is used

seq.	name	material	orientation	thickness
1	sk1	C_{TW}	± 45°	0.24
2	emc	Aaronia-Shield	0°	0.10
3	sk2	C_{TW}	± 45°	0.24
4	sk3	C_{TW}	± 45°	0.24
5	sp1	C_{UD}	0°	0.56
9	sp2	C_{UD}	0°	0.56
13	sp3	C_{UD}	0°	0.56
17	sp4	C_{UD}	0°	0.56
21	sp5	C_{UD}	0°	0.56
24	sp6	C_{UD}	0°	0.56
28	sp7	C_{UD}	0°	0.56
32	sp8	C_{UD}	0°	0.56
36	sp9	C_{UD}	0°	0.56
- - - - - - - - - - - - **symmetry plane** - - - - - - - - - - - -				

Table 4.2: Layup of the homogeneous section: skin (sk), spar (sp)

near the leading edge. For this purpose a ∅ 5 mm Pb97Sb3 trim is integrated after the first two spar layers, to give more space for pressure sensors and other metrology to be integrated near the leading edge of the blade. The leas alloy has 3% antimony to increase the mechanical properties compared to pure lead. The material's low modulus of elasticity and sufficient elongation at break makes it insensitive to the blade movements and deformations that occur during operation.

The largest component of the homogeneous section is the *Rohacell® 51 RIMA* low density filler material, a closed-cell polymethacrylimide (PMI) rigid foam specially designed to ensure a minimum uptake of resin that is dimensional stable up to temperatures of 200 °C [47].
During the manufacturing process, this core has the task of positioning the still uncured components of the rotor blade [88]. During the curing process, the core is responsible for applying the necessary pressure to the laminate. Therefore, a certain pressing oversize is taken into account in the design of the core [105]. In the cured state, the core ensures on the one hand the stability of the sheet skin to prevent buckling, and on the other hand it protects the sheet skin against further damage caused by punctual pressure loads [88]. In order for the cross-section to remain stable under torsion, the core is compression resistant.
The core is machined into two parts in order to create the possibility to integrate the cables for measurement equipment and to route them between the cores near the neutral axis of the cross-section.

At the trailing edge, a good bond between the two halves is provided by the tab. Nevertheless, an additional trailing edge roving is inserted between the core and the tab to prevent the skin from collapsing during curing.

The section exposed to the highest loads and strains which defines and ensures the dynamic and flight mechanical properties of the rotor is the transition region. When designing the outer geometry of the transition area, special care is taken to create a smooth and fluid transition. Edges and corners are avoided in order to obtain a shape that is suitable for a force-flow-compatible design including a careful scarfing of the laminate. Thickness changes are gradual in order to avoid stress concentrations in the laminate while attention is paid to the symmetry of the residual laminate [44]. Figure 4.3 and 4.5 show the transition area of the rotor blade.
The aerodynamic design was a minor objective. Nevertheless, an aerodynamically favorable shape is created by large radii at the leading edge and a trailing edge that is pronounced towards the end. The trailing edge tab is extrapolated from the homogeneous area to the transition area.
A significant aspect is the integration of a Glenair® Micro-D connector that can be specified with either 100 electrical pins or up to 8 fiber optical termini. Stainless steel blind rivet nuts with thread-size M3 are riveted into the holes of the connector. An attached thin aluminum retainer sheet thereby provides an additional form-fit of the connector assembly with the cured laminate.

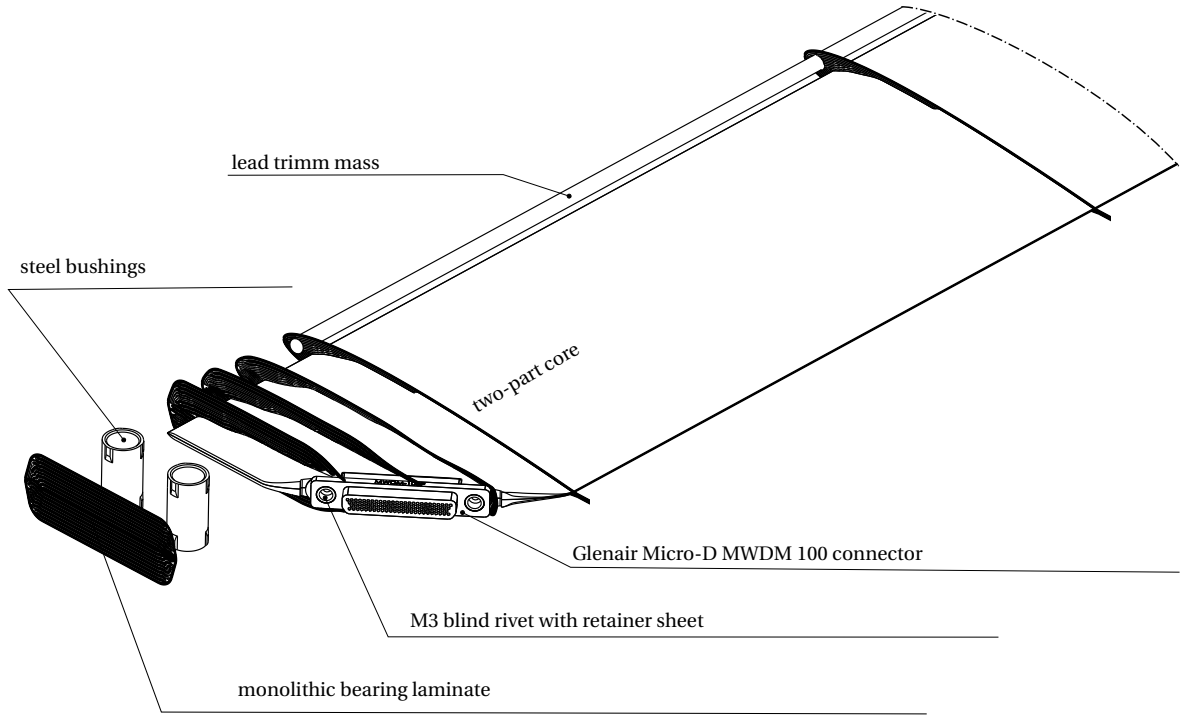

Figure 4.5: 3D section view of the composite layup

4.3.3 Balance Chamber

Each rotor blade and the rotor head itself are subject to certain manufacturing tolerances. These lead to differences in blade weight and center of gravity position and mass distribution of each blade, so that the overall center of gravity of the rotor also has a small radial distance from the axis of rotation. With a rotor diameter of ∅ 1.80 m, the MERIT test rig has small dimensions, but is to be operated at blade tip speeds of up to 220 m/s. The resulting high rotational speeds imply very low unbalance tolerances.
To keep the eccentricity of the rotating rotor as low as possible, all rotor blades are to be balanced. For this purpose, additional masses are introduced into the rotor blade in order to generate the same static moment on all rotor blades. A balancing chamber for these additional masses is therefore designed in the blade tip.
The degree of permissible residual unbalance is described in the standard ISO 21940-11 (procedures and tolerances for rotors with rigid behaviour) [109] for various machines [87]. This standard specifies the allowed residual unbalance as a function of rotational frequency. For helicopter rotors, a quality level of Q2.5 is selected, which translates in this case into an permissible residual unbalance of 20 g·mm for a single blade [87].
To compensate for the unbalance, a balancing chamber is installed on the pitch axis, at the blade tip of each rotor blade, as shown in figure 4.6. It can be filled with balancing weights made of brass and tungsten, which are pressed against a tapped grub screw by a compression spring. The chamber itself is machined out of titanium and is glued with the help of adhesive grooves into the quasi-isotropic monolithic structure of the blade tip using Scotch-Weld® 9323 B/A adhesive. The grooves have the task of ensuring the correct thickness of the adhesive and centering it within the drilled hole. The monolithic structure of the blade tip consists of C_{TW} fabric plies in alternating orientation which are scarfed towards the core of the homogeneous section.
To prevent loosening of the screw due to vibration a stainless steel HELICOIL® Plus Screwlock thread insert is used in combination with a threadlocking adhesive. The balance cell is sealed with a movement detection paint to enable a visual inspection of a possible loosening. This simple design solution features a flat rotor blade end, thereby reducing the adverse aerodynamic effects.
The volume is large enough to reduce the static moment of the blade by about 2% [142], [87]. The available weights are listed in table 4.3. The smallest weight causes with a 900 mm lever arms a

material	length [mm]	mass [g]
tungsten	8	1.6
brass	0.5; 1; 2; 4	0.047 - 0.37

Table 4.3: Balance weights ∅ 3.7 mm

change of about 42 g·mm. Thus, to ensure a finer adjustment of the center of gravity, it is possible

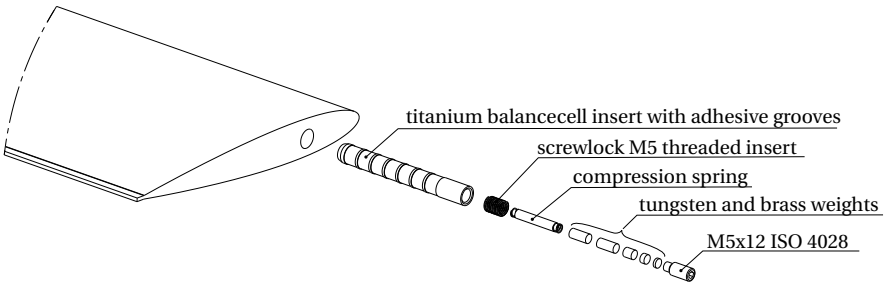

Figure 4.6: Exploded view of the balance chamber

to move the balancing weights by turning the grub screw for fine tuning without disassembly. Since in this case the balancing weights can only be placed on the pitch axis locations, this means that in a two-blade arrangement, balancing in chordwise direction cannot be realized. It is assumed that the deviations in this respect are smaller and less relevant and can be balanced by adding washers at the front or aft blade attachment bolt.

4.3.4 Manufacturing

Manufacturing the rotor blades is a two stage process that allows the integration of metrology onto cured lower and upper shells and can be reduced to a single stage press molding process. The first stages cures the skin and two spar layers (up to sequence 9 of table 4.1) in an autoclave curing process leaving shells to be instrumented. During the second stage the remaining layup with all components is cured by compressing the warmed up molds and laminate.
The mold was designed to meet the requirements of both an autoclave vacuum process and press molding. Its functional design is illustrated in figure 4.8 and is briefly described below:

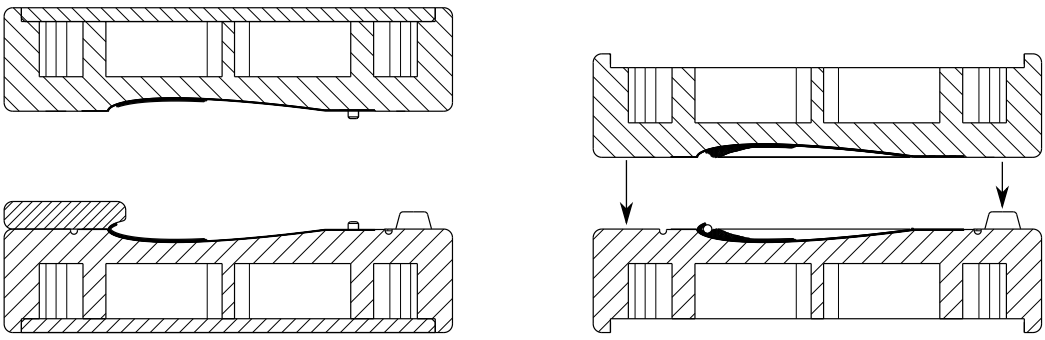

(a) Cure Cycle 1: vacuum autoclave

(b) Cure Cycle 2: press moulding

Figure 4.7

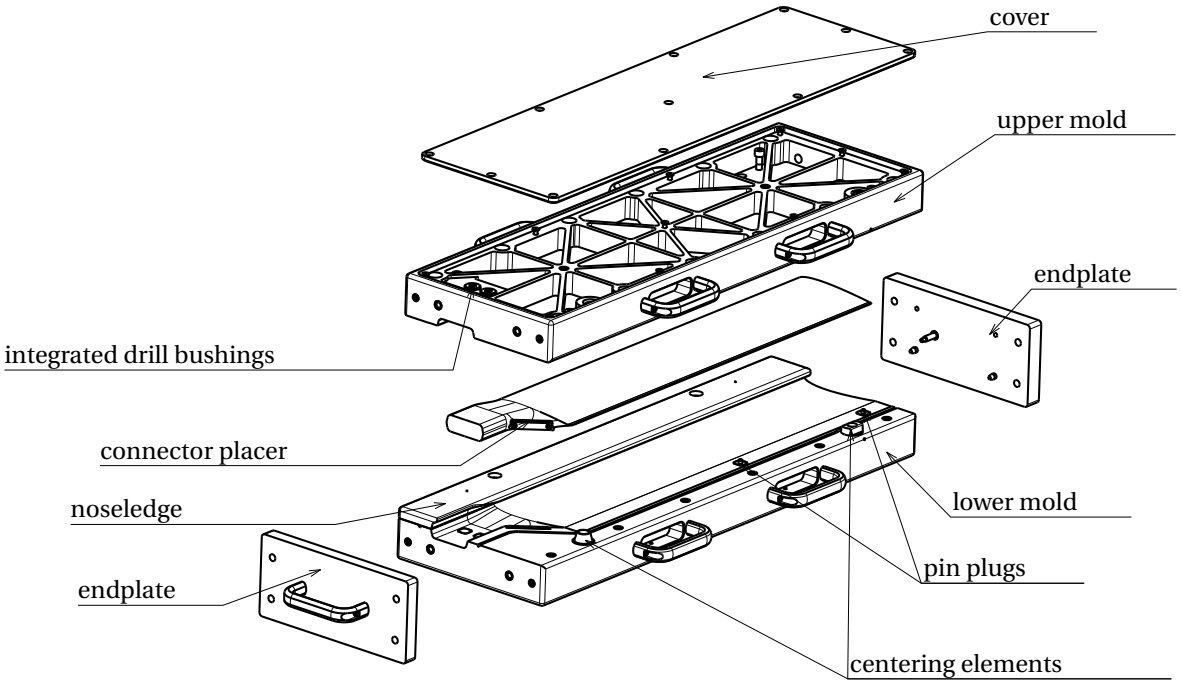

Figure 4.8: MERIT blade mold assembly

Mold Design

The mold consists of a mold top and a bottom machined out of an EN AW 7021 precision cast aluminum plate with high dimensional stability and low residual stresses. A rip structure creates a stiff but lightweight design that offers good heat transfer during oven heating while at the same time enables easy handling.
Because vacuum bags are regularly applied for the first cure cycle in the autoclave and vacuum compacting the thick layup, round edges are all around to prevent ruptures of the bagging as a lid is covering the rip structure. A noseledge is attached during the first curing cycle to create an overlap of the lower and upper shell at the leading edge.
The manufacturing edge of part is extended at the leading and trailing edge, at the tip and at the blade attachment allowing a homogeneous laminate. The excess material at the trailing edge allows to integrate two centering holes into the cured shells for further positioning by placing removable pin plugs into the mold. Scribelines indicate the final edge of part. At the blade attachment similar centering spike plugs are used leaving a centering bore in the blade that assists the precise position of the hole during drilling. Note that the molds also function as drilling jig after the blade is cured using integrated drill bushings that lay beneath the removable spike plugs.
Twelve high strength M10 screws compress the two halves, while a conical and a half-cylindrical centering element ensures precise positioning. The connector placer helps to position the con-

nector during the process. HELICOIL® steel thread inserts improve the durability during repeated press cycles. End plates close the mold at both ends of the mold while a channel traps excess resin. Thermocouples can be placed just underneath the surface of the part to monitor the temperature during curing in the middle, at the blade attachment and at the tip.

To obtain a high surface quality, the mold was sanded and polished before sealing it and applying release agent. All parts of the mold that possibly come in contact with resin are pretreated with the release agent LOCTITE ® FREKOTE 770-NC.

Cure Cycle 1

In preparation, the plies were cut and labeled according to table 4.1 using a digital cutting system. The final contours are derived by draping simulation with CATIA V5 Composite Design.
The serial number *S/N: MERIT-A-001-2020-07* (A: revision, 001: sequential number, 2020-07: manufacturing year and month) is laser-printed on a regular piece of paper and placed into the upper mold.

The skin layers and the optional emc-protection are the first plies to be placed into the molds, wrapping them around pin plugs at the trailing edge. Note that the third skin layer (sk3) is split into a front and aft part, while the latter being applied during the second cycle to ensure a solid bond of the trailing edge tab. The layup for the first cycle is completed with the first two spar layers (sp1, sp2) and the transition plies up to sequence 9. This shell thickness was selected to ensure enough space for the integration of pressure sensors. As a result, the trim mass was placed slightly to the rear. An overlap region at the leading-edge is created by extending the lower plies and trimming the upper plies as shown in figure 4.7a.
When laminating the plies, attention is paid, that all layers are placed without distortion and are well compacted by massaging or rolling out. The stack-up is completed by covering it with peel ply, perforated release film and breather fabric before sealing it into a vacuum bag. The shells are cured under vacuum condition (minimum of -0.7 bar) at 90°C (with a 1°C/min heat-up rate) at 4 bar autoclave pressure for 6 hours. The prepared lower mold and the cured shell are shown in figure 4.9a and 4.9b.

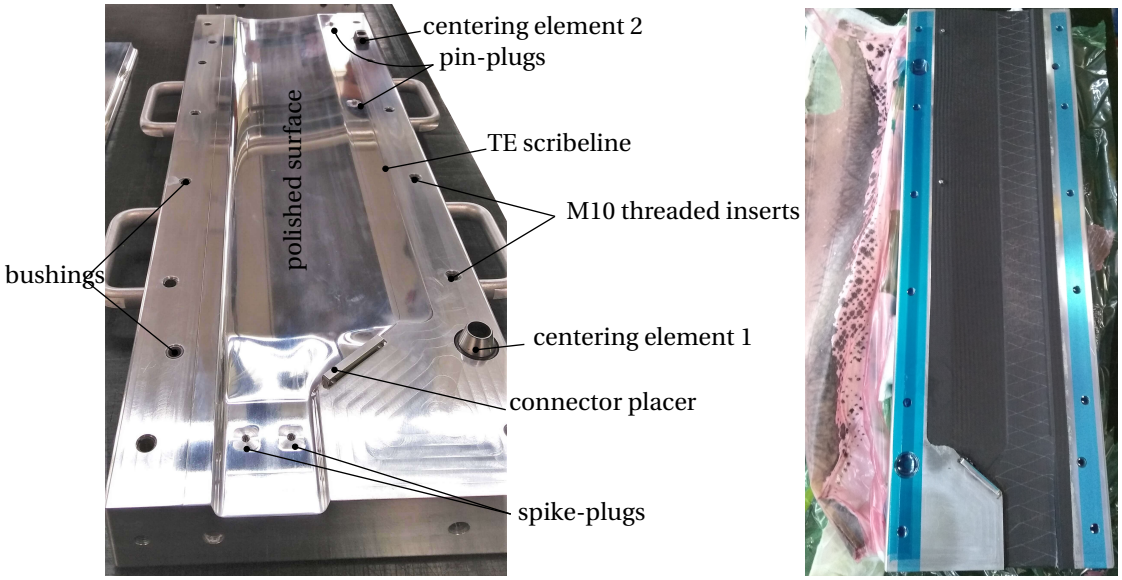

(a) lower mold **(b)** cured shells

Figure 4.9

Cure Cycle 2

In preparation of the second cycle, excess material, particularly at the leading edge overlap, is removed and both shells are matched to each other. At this point metrology can be installed onto the shells, which is not described as part of this work. A stainless steel blind rivet nut together with a slim 0.5mm aluminum retainer sheet is riveted onto the connector. A dummy replaces either the electrical *Glenair® MWDM 2L-100p-6e5-18* Micro-D or the fiber optical Micro-D connector if the blades are not instrumented. The connector is placed into the connector-placer and sealed against an unwanted resin entry.
The trimm mass is cut to 600 mm length and ground to an exact weight of 128 g which has the additional effect of enlarging the surface area improving the later cohesion.
The thoroughly cleaned shells are placed into the molds and the remaining plies are stacked according to table 4.1. Note that besides the blade root, the tip consists of a quasi-isotropic monolithic section with alternating ±45°, 0/90° C_{TW} plies and is not specifically listed in table 4.1.
Especially for the spar layers and the tip plies, it can be helpful to measure the layers from the trailing edge and compare them with the drawing. Every 10 layers, the thick stack-up is compacted for at least 10 minutes in a vacuum bag with a perforated release film and breather fabric to avoid air voids. Once all layers are laid, the trim mass is carefully placed in the groove of the spar layers and the space to the leading edge is filled by a C_{UD} roving.

As seen in figure 4.10, the final step before closing the halves is the placement of the foam core

halves, which were previously covered with SGL CARBBON - SIGRAPREG® F 147-E322/100% epoxy film-adhesive. The aforementioned trailing edge roving is subsequently placed and the connector is placed between the core halves in the recess.

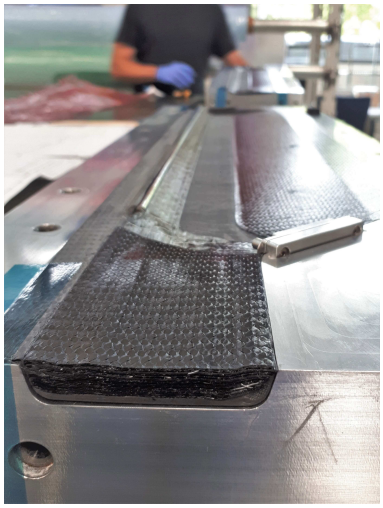

(a) monolithic blade attachment

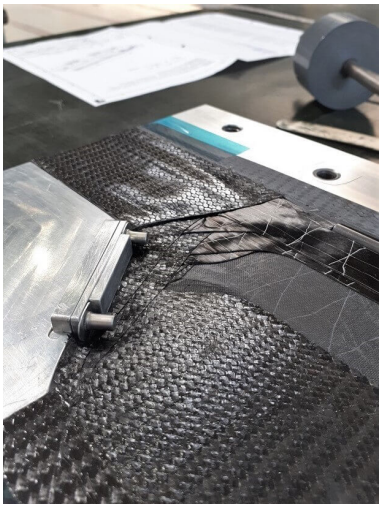

(b) scarfed transition with connector dummy

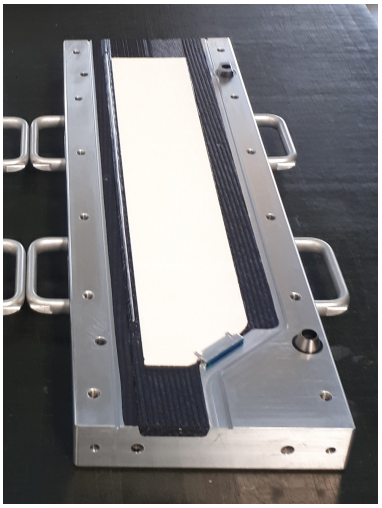

(c) foam core placed in the lower mold

Figure 4.10

When the two mold halves are centered on top of each other, the screws are hand-tightened without compressing the core. Finally, the end plates are attached and the molds are placed in an oven while thermocouples monitor the temperature of the mold at the center, tip and blade attachment. The cure cycles has an initial heating ramp-rate of 1°C/min from room temperature to 80°C that is maintained for 4h. The mold halves are compressed once the monitored thermocouple temperature reaches 77°C. After the first ramp the temperature is increased to 100°C at 1°C/min with a dwell of 8h.

Postprocessing

The excess material is removed using a diamond circular saw (figure 4.11a) and brought to the exact specified dimensions using a belt grinding machine with the help of scribelines and airfoil stencils.
The holes for the blade bushings are drilled using the mold as drill jig with integrated bushings by removing the centering plugs and replacing two of them with flat aluminum plugs to ensure that no delamination of the lowest layers occurs when the drill passes through. Because of the high abrasive behavior of carbon fibers, a carbide reamer is used to create a ∅ 13 mm H7 fit. No cooling fluids are used, so care must be taken to prevent overheating of the laminate as this could lead to a

loss of strength of the laminate [149].
As shown in figure 4.11b the hole for the balancecell is inserted by vertically mounting the rotorblade in a specifically designed drilling, machining and postprocessing jig, which can be used to precisely machine holes and grooves into the blade or blade shells for the integration of sensors.

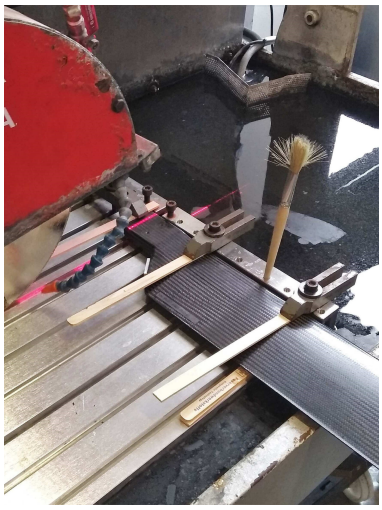

(a) cut excess material

(b) monolithic blade attachment

Figure 4.11

The blade bushings feature three circumferential position noses that have a ∅ 13 mm h7 fit to match the hole diameter to ensure an exact position and even bond line thickness of 0.15 mm. In prior to the application of the adhesive the bushings are sandblasted and all surfaces are thoroughly cleaned (see figure 4.12a). The two component epoxy adhesive Scotch-Weld® 9323 B/A is used for all structural bonding applications of the blade. Besides providing high shear and peel strengths it has a high resistance to oils, fuels and damp heat.
To guarantee an exact fit of the blade bushings with respect to the blade clamps, the blade is mounted in such during gluing. To cure the adhesive, the blades are heated for 2 hours at 65 ± 2 °C. A bonding protocol with adhesive sample provides a minimum required process control.

Balancing

The blades are statically balanced on a 3-axis force/torque sensor (K3R70 20N/0,2Nm by ME-Messsysteme) which is mounted between a base plate and an adapter plate to attached the rotor blades (illustrated in figure 4.13. This work was assisted by ROTH2020 during his bachelor's thesis, in which he designed the scale and verified its performance and achievable measurement accuracy

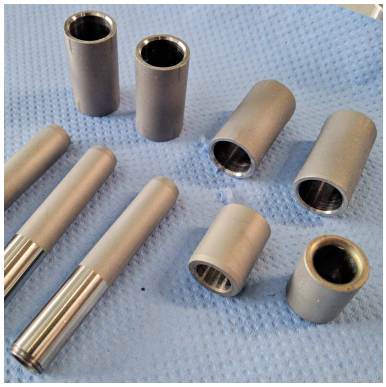

(a) sandblasted blade bushings

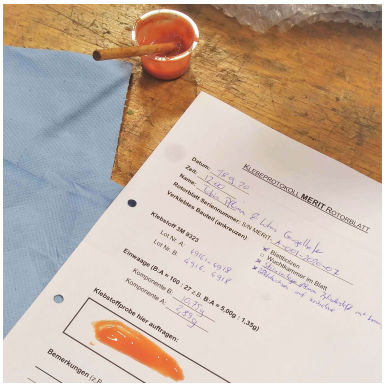

(b) Bonding protocol with adhesive sample

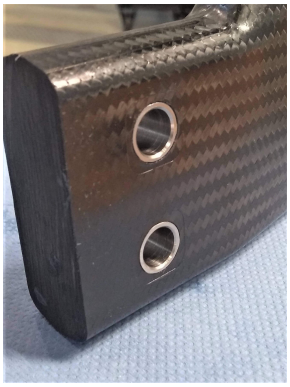

(c) finished blade attachment

Figure 4.12

of 20 gmm in various test series.
The measurement crosstalk between the axis $M_{x,0}(F_z)$, $M_{y,0}(F_z)$ was calibrated with the use of machined discs of different weight. Both $M_{x,0}(F_z)$ and $M_{y,0}(F_z)$ were found to be linear functions passing through the origin with which the zero-point offset is compensated.

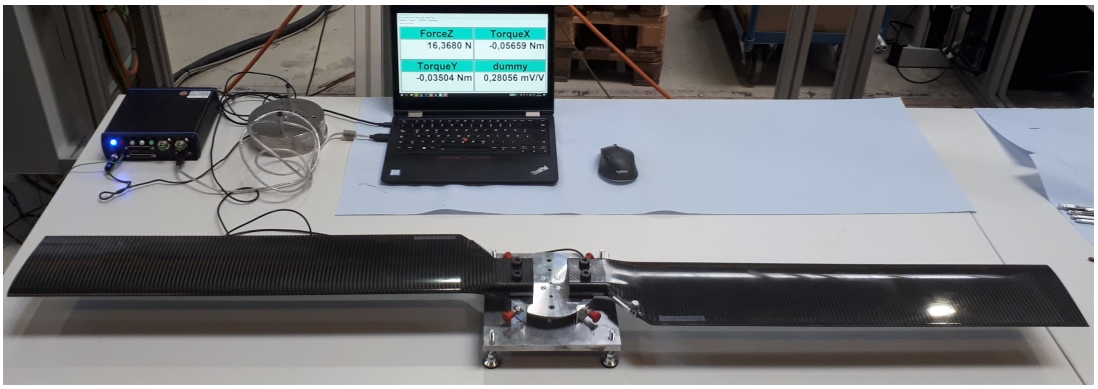

Figure 4.13: 3-axis force/torque balancescale

4.3.5 Destructive and Non-Destructive Testing

Before the rotor blades could be put into operation for the first tests at the MERIT rotor test stand, destructive and non-destructive tests (NDT) were performed on the first two prototypes. The first investigations were performed with the help of Testia GmbH using a high-resolution three-dimensional computer-tomograph (Diondo, D2, 160kV) with a detector resolution of 3008×3008 px. The resulting voxel size for the rotor blade was accordingly 0.0497 × 0.0497 × 0.05 mm. The aim of the investigations with the first two prototypes was to determine the positioning of the foam

Figure 4.14: Finished set of rotorblades *S/N: MERIT-A-006-2021-03, S/N: MERIT-A-007-2021-03, S/N: MERIT-A-008-2021-04*

core, since these were manufactured using two slightly different foam cores with different outer dimensions. Furthermore, the manufacturing process was to be investigated for large voids or resin pockets. The region of interest was the transition region with the embedded connector.
In the institute's research project *iRoB* it is planned to integrate fiber optical sensors with Fiber-Bragg Gratings (FBG) into the rotor blade structure. A sub-objective of the NDT investigations was therefore to evaluate the possibility to use CT-Scans as a quality assurance and verification method of sensor position and orientation.

As can be seen in the pictures in figure 4.15b and 4.15c, the connector dummy is nicely embedded in the fiber laminate. Also visible are the two blind rivet nuts with the small retainer sheets, which provide a form-fit interlocking connection.
In figure 4.15c, the two steel bushings of the blade connection can also be seen. Unfortunately, the large differences in density of the materials used (lead trim mass, steel bushings, titanium balancing chamber, aluminum plug, and steel blind rivets) led to some radiation artifacts around areas of high density. This was particularly noticeable in the homogeneous area with the lead trim mass, which meant that these areas were insufficiently evaluable. In conclusion, it can be said that the production quality of both test specimens is satisfactory.

In addition to the non-destructive tests to verify the general component and process quality, two critical tensile strength tests were conducted to verify the operational safety. Because the high operating rotational speed of the rotor MERIT testrig generates considerable axial loads on the

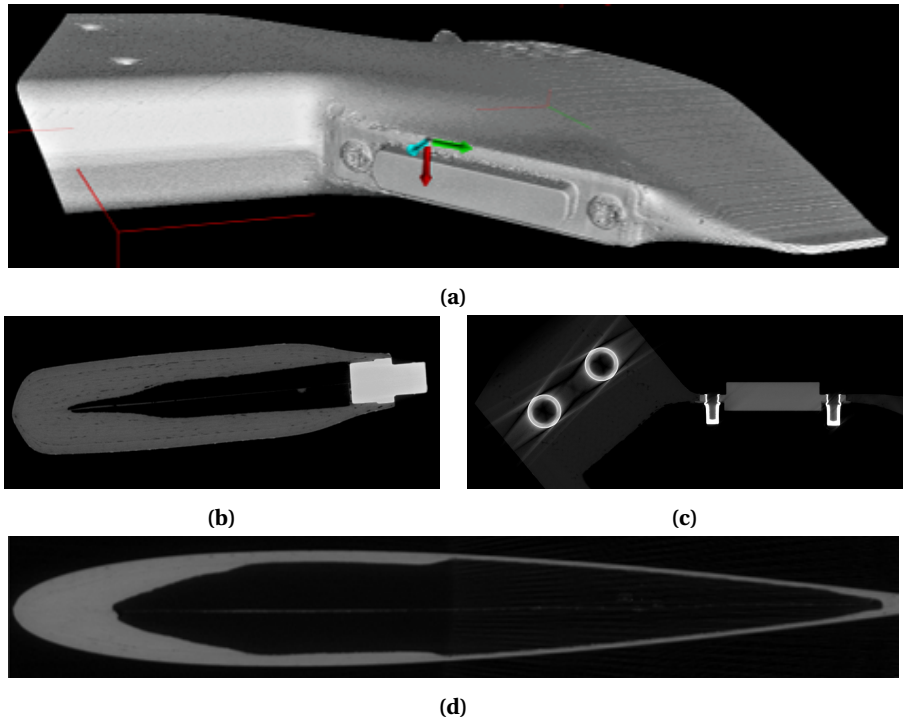

Figure 4.15: CT-Scan of the transition area of *S/N: MERIT-A-001-2020-07*

glued-in balancing chamber and the blade connection, the failure load and mode were evaluated in experimental tests. The results are partially published in ERF2021B.

For the blade attachment tensile test, the homogeneous section of the blade was reinforced with an addition C_{TW} and C_{TW} plies in 0°,90° and ±45° orientation to create a bearing laminate which was bonded and bolted to the steel load interface (see figure 4.16a). The region of interest, the transition and attachment area were pretreated and painted with a stochastic black and white color pattern as well as optical reference markers. A GOM Aramis 5M DIC system with its two stereo-cameras and additional illumination were set up to capture the deformation and strains in the area of interest during the experiments.
Interlaminar shear failure between the skin and the UD C-Spar at the start of the shafted reinforcement occurred at an axial load of 185.8kN, which by far exceeds the defined Ultimate Load of 80.7kN [67].

Figure 4.17a and figure 4.17b shows the load vs. the virtual extensometer strain $\varepsilon_{11,L}$ and the corresponding axial strain field ε_{11} at the maximum load of 185.8kN. The principal strain directions are represented by the vector field. Most notably in this figure is the axial strain gradient in chordwise direction at the homogeneous part of the blade and the low strain at the monolithic attachment.

(a) Experimental setup blade attachment tensile test

(b) Color pattern and failure mode

Figure 4.16: Experimental setup of tensile strength test of MERIT blade attachment

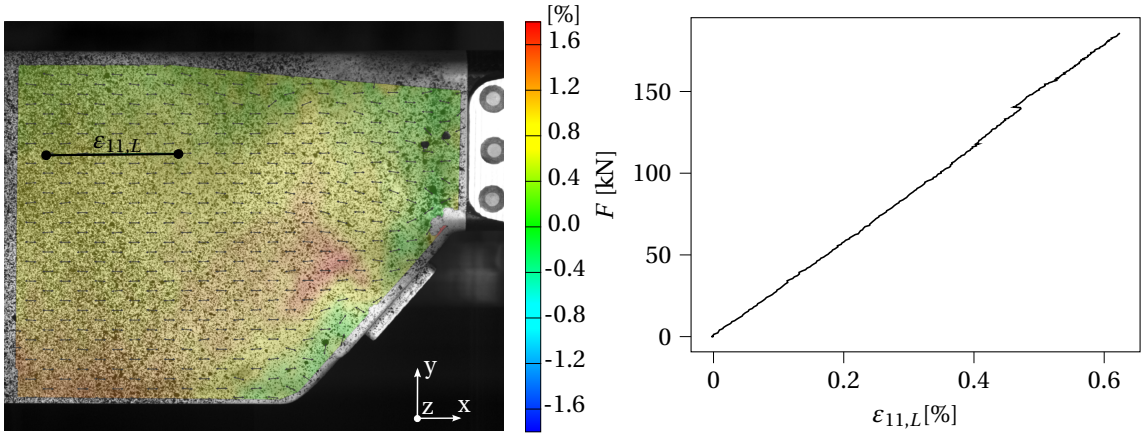

(a) axial strain field ε_{11} and principal strain directions at maximum load 185.8kN

(b) axial load F_1 vs. extensometer strain $\varepsilon_{11,L}$

Figure 4.17: Tensile strength test strain distribution and axial load

The titanium balance chamber insert is glued into the monolithic blade tip and closed off by a screw in combination with a stainless steel screwlocking thread insert and threadlocking adhesive. To provide operational safety, all limit and ultimate load requirements were exceed in a second tensile test in which a threaded pin adapter connected the balance cell to the clamp of the tensile testing machine [67].

4.4 Material Constitutive Behavior

In this section the experimental setup and the identification of the constitutive behavior of the selected composite materials is described. The characterization of strength properties were secondary objectives of this investigation. The results are analyzed and used in the following structural analysis. Parts of this collaborative work was published by Henschel [65] and was assisted by PIET2018 in his semester thesis.

The stress-strain relationship for an orthotropic material with two mutually orthogonal planes of symmetry with 9 independent coefficients is defined as

$$\underline{\varepsilon} = \underline{\underline{S}} \cdot \underline{\sigma} \tag{4.23}$$

$$\begin{Bmatrix} \varepsilon_{11} \\ \varepsilon_{22} \\ \varepsilon_{33} \\ 2\varepsilon_{23} \\ 2\varepsilon_{31} \\ 2\varepsilon_{12} \end{Bmatrix} = \begin{bmatrix} \frac{1}{E_1} & -\frac{\nu_{21}}{E_2} & -\frac{\nu_{31}}{E_3} & & & \\ -\frac{\nu_{12}}{E_1} & \frac{1}{E_2} & -\frac{\nu_{32}}{E_3} & & & \\ -\frac{\nu_{13}}{E_1} & -\frac{\nu_{23}}{E_2} & \frac{1}{E_3} & & & \\ & & & \frac{1}{G_{23}} & & \\ & & & & \frac{1}{G_{13}} & \\ & & & & & \frac{1}{G_{12}} \end{bmatrix} \cdot \begin{Bmatrix} \sigma_{11} \\ \sigma_{22} \\ \sigma_{33} \\ \sigma_{23} \\ \sigma_{31} \\ \sigma_{12} \end{Bmatrix}.$$

In the particular case of transversely isotropic material such as the unidirectional C_{UD}, rotational symmetry with respect to the 1-axis exists, which is perpendicular to the isotropic 2-3 plane. Therefore the number of independent coefficients reduces to 5.

4.4.1 Coupon specimen

The plane stress engineering constants E_1, E_2, G_{12} and ν_{12} can be measured experimentally in tensile tests with specimen of different fiber orientation. The experiments were conducted according to the European Standards Aerospace Series. They specify the method of determination of the ultimate tensile strength, tensile modulus, the Poisson's and the elongation at failure of carbon fiber reinforced plastics. DIN EN 2561 : 1995-11 [3] is applicable to unidirectional specimens where the load-axis is parallel to the direction of the fibers. For the C_{TW} specimen, the general EN ISO 527 [134] was applied. DIN EN 2597 : 1998-08 [4] applies when the load direction is perpendicular

to the fibers. EN 6031:2015 [31] defines the determination of the shear modulus and the shear strength of laminates with fiber orientations of ±45° to the specimen axis.
Table 4.4 lists the specification of the specimen including the number of plies (Lay), number of samples (No) and free length (L). The width (w) and the thickness (t) are measured using a micrometer at three representative locations and therefore the arithmetic mean and standard deviation (SD) are given. It is important to note that the small batch size of 6 samples can contribute to outliers and therefore the results cannot be considered statistically significant. Furthermore the specimens were manufacture from the same material batch and the same composite plate.

		Standard	Lay.	No.		L [mm]	w [mm]	t [mm]
C_{UD}	0°	DIN EN 2561[3]	2	6	Mean	120	15.00	1.14
					SD	-	0.03	0.05
	90°	DIN EN 2597 [4]	4	6	Mean	130	25.01	2.12
					SD	-	0.03	0.04
	±45°	EN 6031:2015 [31]	8	6	Mean	150	25.01	4.26
					SD	-	0.02	0.05
C_{TW}	0°/90°	EN ISO 527 [134]	8	6	Mean	150	25.00	1.64
					SD	-	0.02	0.02
	±45°	EN 6031:2015 [31]	8	6	Mean	150	24.99	1.65
					SD	-	0.02	0.01

Table 4.4: Coupon specimen specifications: fiber orientation, test standard, Number of Plies (Lay.), Number of Samples (No.), length (L), width (w) and thickness (t) in terms of arithmetic mean and Standard Deviation (SD).

The specimen were manufactured by stacking the cut plies together with a peel ply onto 300 mm x 300 mm cleaned and with release agent coated plates while paying attention to the correct fiber orientation (see figure 4.18). To ensure a symmetric and balanced layup, eight plies are stacked according to the following lay-up: $[+45°, -45°, +45°, -45°]_S$ for the ±45° specimen. The stack-up is completed by covering it with peel ply, perforated release film and breather fabric before sealing it into a vacuum bag. The specimen are cured under vacuum condition (minimum of -0.7 bar) at 90°C (with a 1°C/min heat-up rate) at 3.5 bar autoclave pressure for 6 hours.

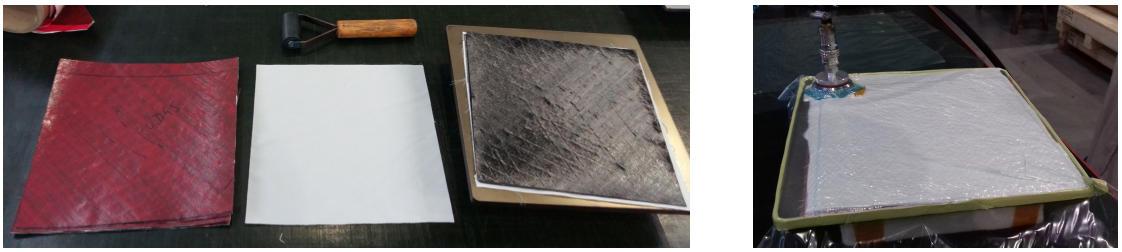

Figure 4.18: Layup: Steel plate, release agent, peel ply, composite pre-preg layup, peel ply, perforated release film, breather fabric, sealed vacuum bag

Using a diamond circular saw, the specimens were cut into the specified dimensions respecting the fiber orientation. Damaged fibers were removed by scrubbing the edges with sandpaper. 1 mm thick end tabs of ±45° glass-epoxy laminate are bonded with epoxy adhesive onto the sand-blasted and cleaned surface (see figure 4.19a) of the specimens.

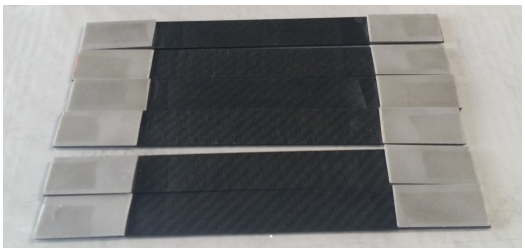

(a) ±45° reinforced GFRP end tabs

(b) Spray-painted stochastic speckle pattern

Figure 4.19

4.4.2 Experimental Setup

An stochastic color pattern was spray-painted onto the specimens homogeneous surface by using a compressed-air spray gun. Initially, three layers of matte white color were applied before matte black dots were distributed by adjusting pressure and distance of the stray gun aiming for an equal amount of black and white parts. Pattern templates helped to adjust the dots to the correct size according to the spatial camera resolution. Figures 4.19b shows the pattern of the $C_{UD,0°}$ specimens.
The experimental setup is shown in figure 4.20, where the *GOM ARAMIS 5M* sensor with stereo-cameras and an adjustable base is positioned horizontally on a tripod in front of the *Instron*® universal testing machine, which is equipped with a calibrated 100 kN load cell to measure the loads during the experiment. Digital Image Correlation was used to measure the surface strains of specimen. Figure 4.21 shows the virtual extensometers used to measure the strains $\varepsilon_{11,L}$, $\varepsilon_{22,L}$. The stochastic pattern quality has an average value of 7.2.

4.4.3 Results

According to the referred standards, the elastic properties were derived by the secant modulus of the resulting stress-strain relations. To reduce errors from measurement noise a 1D Gaussian filter of size 3 was applied to all signals. The obtained stress-strain graphs are shown in figure 4.22 and 4.23 respectively. Those experimental results allowed to determine the plane elastic quantities

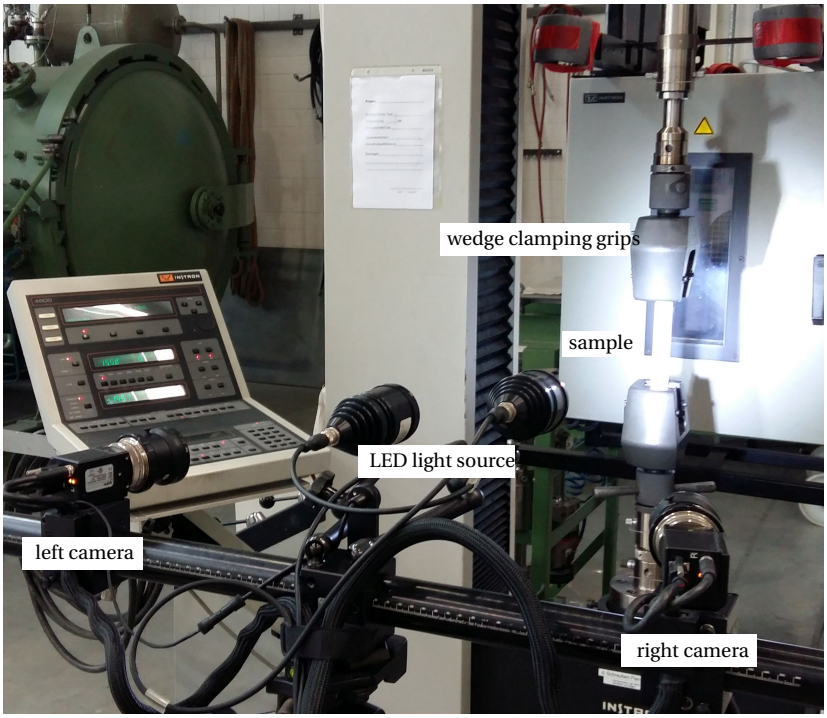

Figure 4.20: Tensile test experimental setup

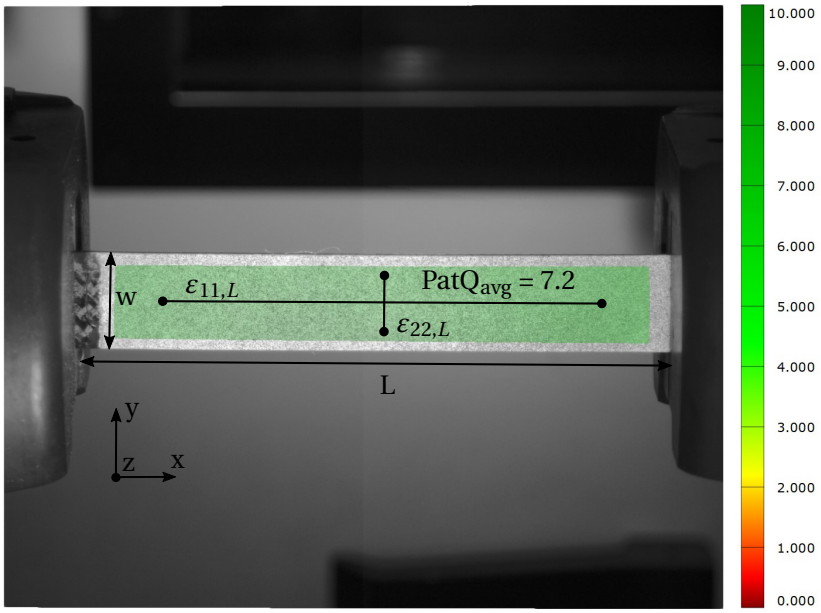

Figure 4.21: Digital evaluation of virtual extensometers

E_1, E_2, G_{12} and ν_{12}, which are sufficient to determine the constitutive behavior for the plane stress state, which is present in thin-walled components. However, for thick-walled structural components, it is necessary to extend the stress and deformation analysis to spatial stress states. Although

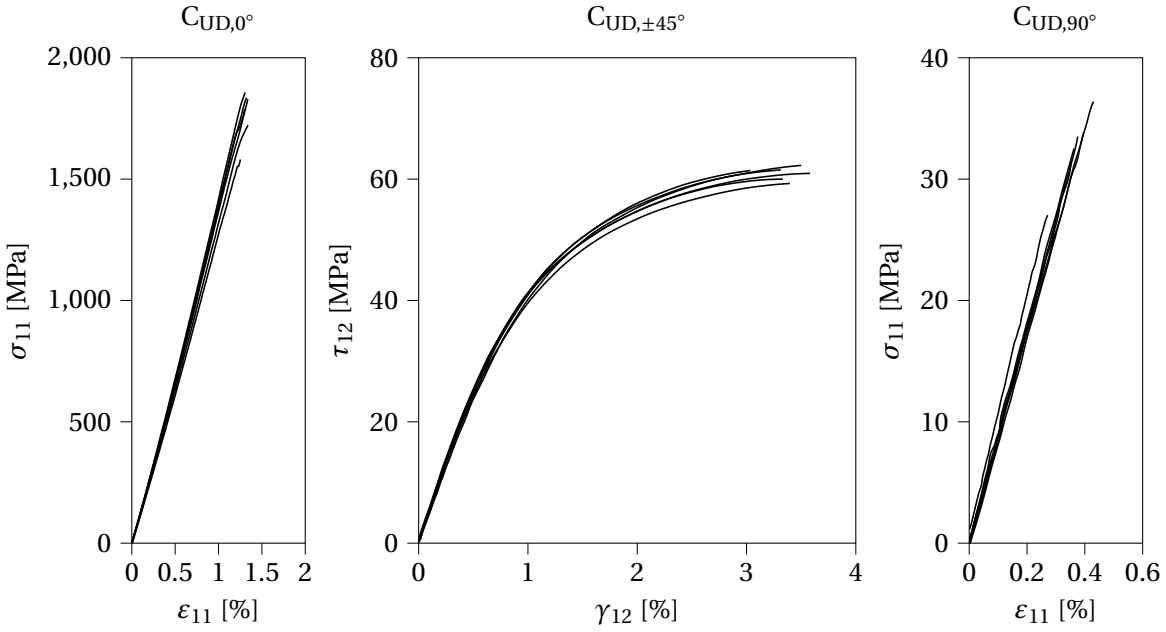

Figure 4.22: Measured stress-strain relation of C_{UD}

the out-of-plane material properties were not derived from the tensile experiments, they are derived from a micro- and mesomechanic approach where the elastic quantities of the UD material are determined from the respective fiber and matrix values [149].
Table 4.5 and 4.6 summarize the material properties in terms of arithmetic mean, standard deviation and coefficient of variation. Values denoted with (*) are derived from the micro- and mesomechanic approach. Values denoted with ($^+$) are taken from the suppliers technical data-sheet (TDS) [153], [154].

The remaining elastic properties of C_{UD} are derived with *SwiftComp Micromechanics*™, a general-purpose micromechanics code for homogenization and dehomogenization of heterogeneous materials [181]. The desired properties for the C_{TW} 2x2-twill fabric are derived by generating a 3D solid finite-element model for the textile composite with *TexGen* [98], [101], an open-source geometric textile modelling software package for textile composites. Parameters such as yarn width and spacing were adjusted to match the average measurements and values of fiber volume content of the specimens. Periodic boundary conditions were selected for the elastic analysis with an assigned voxel seed of 30, 30 and 15 with respect to x, y, z coordinates. The dimensions and layout of the fabric is illustrated in figure 4.24. Subsequently, *Swiftcomp* was used again to approximate the orthotropic material behavior.

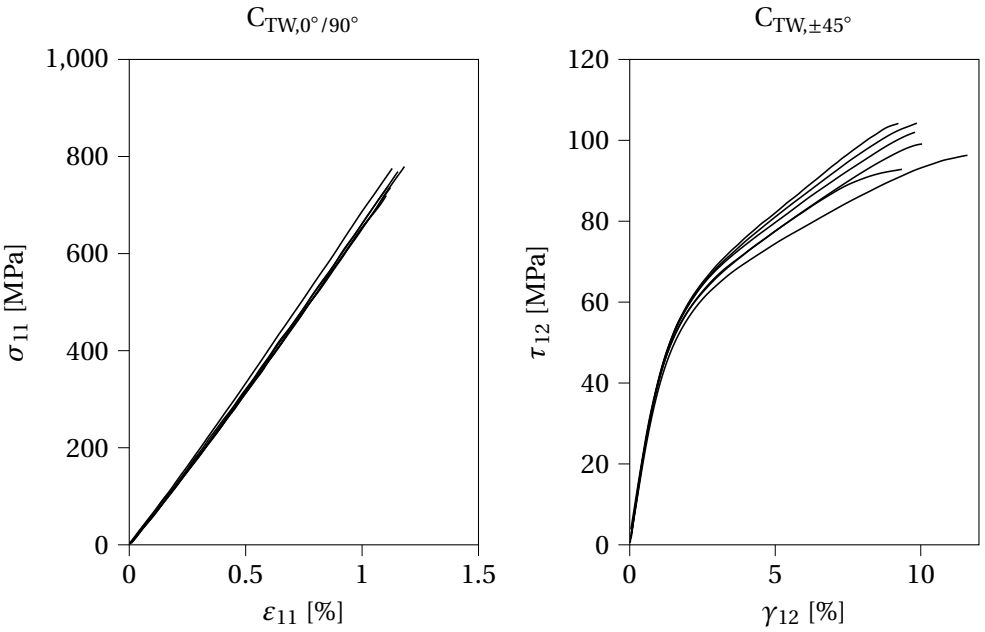

Figure 4.23: Measured stress-strain relation of C_{TW}

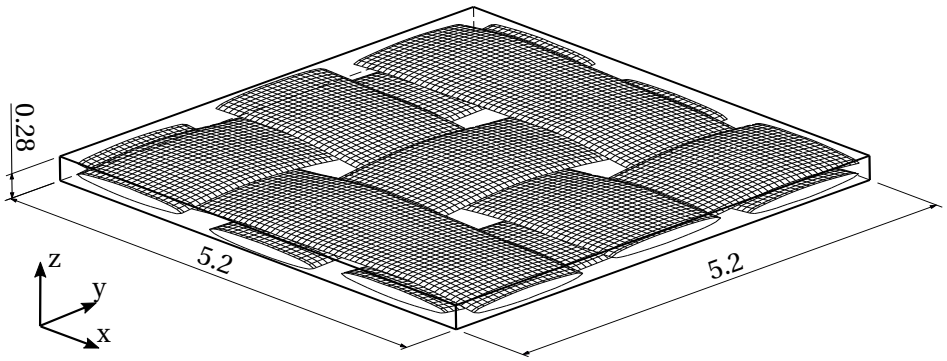

Figure 4.24: Dimensions of mesomechanic 2x2-twill fabric modeled with TexGen[98], [101] and analyzed with SwiftComp by Analyswift [181]. Yarn-spacing = 1.72, yarn-width=1.36, yarn-height=0.255, fiber-volume-fraction=0.549

Parameter	Unit	Mean	SD	COV [%]
Elastic Properties				
E_1	[GPa]	134.6	5.2	3.9
$E_2 = E_3$	[GPa]	9.02	0.41	4.6
$\nu_{12} = \nu_{13}$	[-]	0.336	0.051	15.3
ν^*_{23}	[-]	0.388		
$G_{12} = G_{13}$	[GPa]	4.75	0.1	2.2
G^*_{23}	[GPa]	3.02		
Strength				
σ_1	[MPa]	1784	97.6	5.5
$\sigma_2 = \sigma_3$	[MPa]	32.9	2.89	8.8
$\tau_{12} = \tau_{13}$	[MPa]	60.9	0.99	1.6
τ^+_{23}	[MPa]	75		

Table 4.5: Material properties of SIGRAPREG® C U600-0/SD-E501/33% in terms of arithmetic mean, Standard Deviation (SD) and coefficient of variation (COV).

Parameter	Unit	Mean	SD	COV [%]
Elastic Properties				
$E_1 = E_2$	[GPa]	65.3	1.16	1.8
E^*_3	[GPa]	11.7		
ν_{12}	[-]	0.077	0.037	48.4
$\nu^*_{23} = \nu^*_{13}$	[-]	0.34		
G_{12}	[GPa]	4.58	0.12	2.6
$G^*_{13} = G^*_{23}$	[GPa]	4.34		
Strength				
$\sigma_1 = \sigma_2$	[MPa]	762	22.6	3.0
τ_{12}	[MPa]	99.7	4.18	4.2

Table 4.6: Material properties of SIGRAPREG® C W200 TW2/2 E503/45% in terms of arithmetic mean, Standard Deviation (SD) and coefficient of variation (COV)

4.5 Experimental Setup

As described through the governing equations in section 4.1, the plane surface strains ($\varepsilon_{11,e}, \varepsilon_{12,e}, \varepsilon_{22,e}$) and their corresponding cross-sectional coordinates need to be determined under at least six precisely known linearly independent load cases ($F_x, F_y, F_z, M_x, M_y, M_z$) at three or more points of the cross-section. To determine the sectional stiffness properties along the span, this measurement needs to be repeated at multiple cross-sections. By measuring the forces and moments at the blade root as the loads are applied at the tip, it is possible to calculate the forces and moments acting in every blade sections using a free-body diagram. To account for geometric non-linearities the deformation of the blade needs to be measured and accounted for as well.

The test stand shown in figure 4.25 was specially built for this purpose. It uses the sturdy steel frame, previously used for rotor blade investigations by Hajek et. al. [61] and Suesse [166].
The blade is mounted with two ∅10 mm bolts vertically onto a 6-axis load cell with an adapter that has the same geometry and material as the original MERIT blade clamps. The load cell itself is in turn attached to an base plate that is screwed to aluminum flat sections on the floor.
All loads are applied at the tip of the blade via steel cables and a system of pulleys. Aluminum profiles are used to equip the steel-frame with modular components that allow to vary the mounting position of cable pulleys. The force is introduced via a hydraulic cylinder in combination with a hand actuated hydraulic pump. The advantages are large forces, simple equipment, great damping characteristics and precise load repeatability.

4.5.1 Load Application

It is important to highlight that the experiments are nondestructive, which means that neither the applied loads exceed the strength capacity of the blade structure nor that the load-interface at the tip of the blade prevents further usage.
The blades are manufactured with the quasi-isotropic monolithic tip layup extending 34 mm over the finished engineering edge of part that is used for a tough load-interface by inserting a cylindrical steel pin at the pitch axis at 25% chord and two steel bushings. Again the two-component 3M 9323 A/B adhesive is used.

In figure 4.26 the experimental setup of the load cases are shown. Considering the coordinate system of the blade, F_x is the axial force along the longitudinal axis, F_y is the transverse force in lead-lag direction and F_z in flap direction. Analog, the torsional moment about the longitudinal

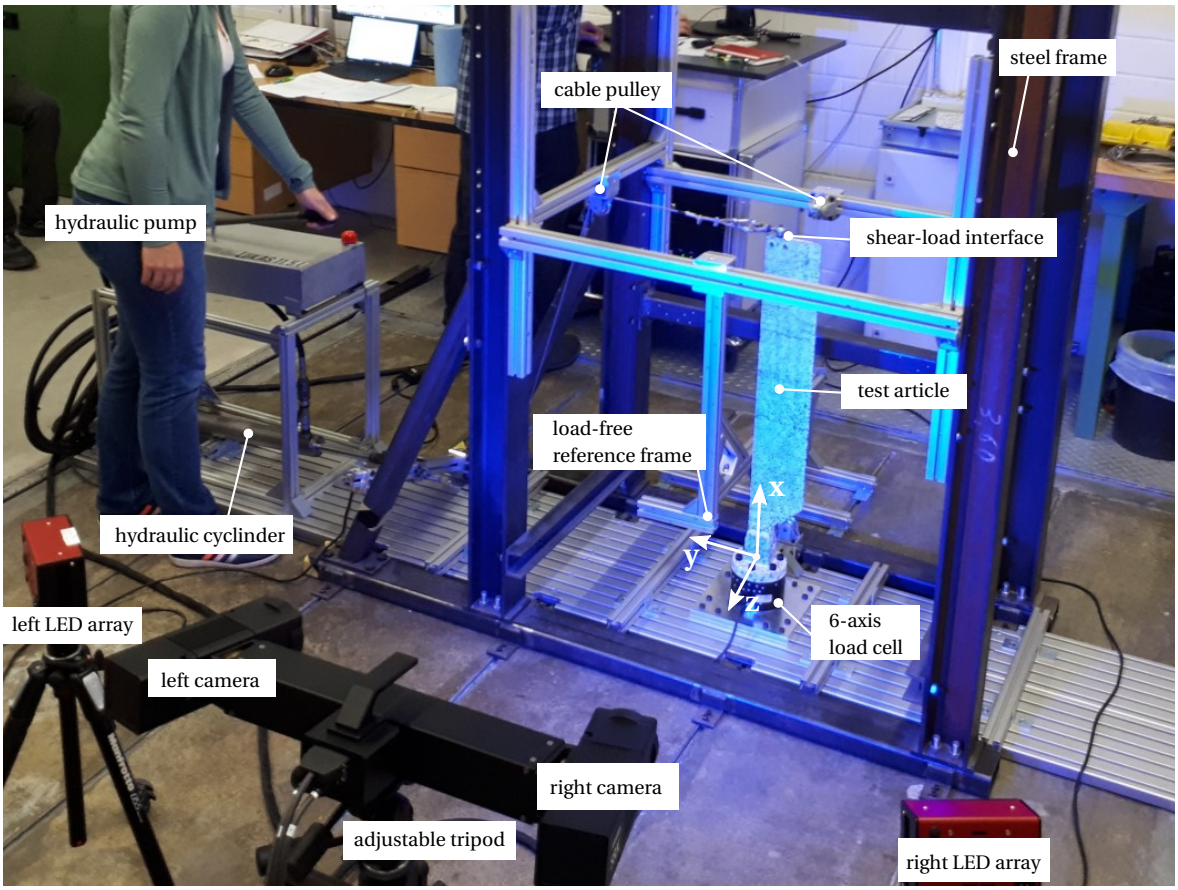

Figure 4.25: Experimental Setup: Testbench for load application and DIC system measurement setup

pitch axis is denoted M_x, the bending moment in flap direction M_y and M_z in lead-lag direction. All loads are applied in positive and negative direction, except for the negative axial force due to the potential risk of buckling, leaving 11 load-cases shown in figure 4.26 and 4.27

For the axial load case, the two integrated bushings are used to connect a steel cable via a adapter as shown in figure 4.26. This allows coupling relations of the stiffness-matrix to become more visible during the experiment as the movement in the other directions is less counteracted. Due to the load capacity of the pulleys the axial load was limited to 10 kN. To reduce undesired forces and moments, the transverse forces F_y (4, 5) and F_z (2, 3) are applied precisely at the pitch axis with the help of the glued-in cylindrical pin via a spherical rod end. A ring nut transfers the applied forces of the hydraulic cylinder from the steel cable to the rod end. Note that, depending on the spanwise position, the transverse forces at the tip induce a sectional bending moment.
A force couple of equal and opposite magnitude is introduced to a frame that transfers the torsional moment M_x (6, 7) via blade clamps onto the blade. The clamps are secured with two cylindrical

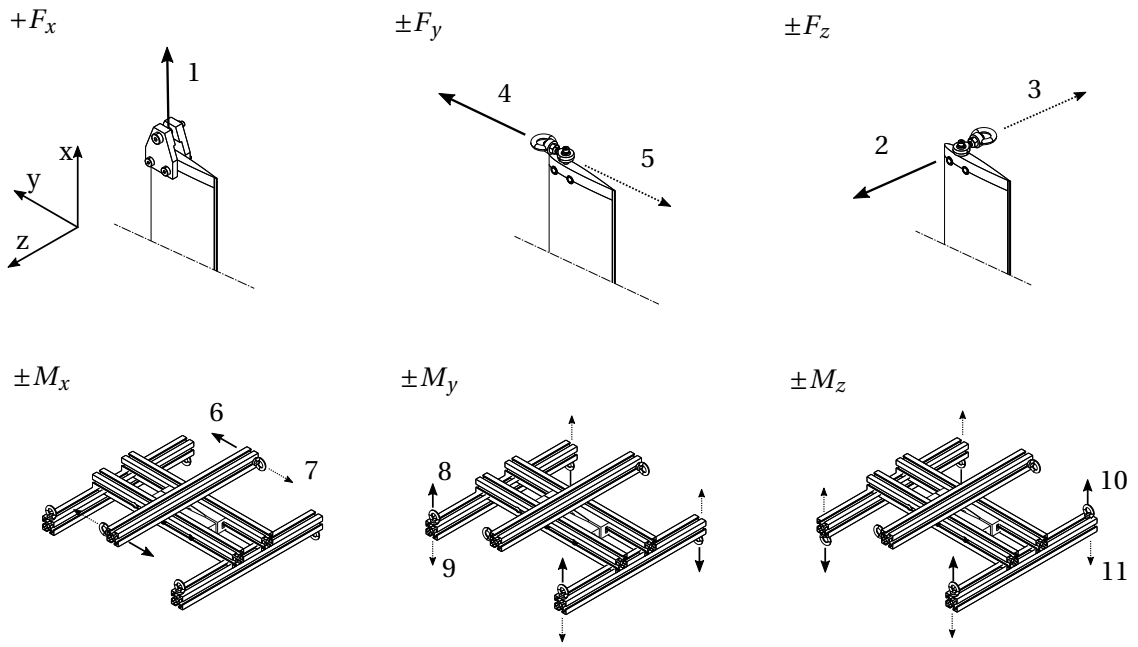

Figure 4.26: Independent load cases in positive (solid) and negative (dashed) direction, the index indicates the corresponding test case.

pins through the blade bushings to prevent undesired movement. To ensure equal force magnitudes the steel cable is routed back through pulleys at the hydraulic cylinder.
The bending moments M_y (8, 9) and M_z (10, 11) are applied with the same load frame. However, four forces instead of two are now applied with the same magnitude and opposite direction at the outer corners to provide a free image area in front of the blade surface. Again, to ensure equal force magnitudes the steel cable is routed back through pulleys at the hydraulic cylinder which are attached at a hinged bar.

4.5.2 Metrology

Load Cell

Accurate measurements of the applied loads are the basis of the described method. The 6-axis multi-component sensor (*K6D130 5kN/500Nm MP11* by *ME-Meßsysteme GmbH* [112]) for forces and moments $\underline{F}^T = \{F_x, F_y, F_z, M_x, M_y, M_z\}$ was specifically selected for the desired operating

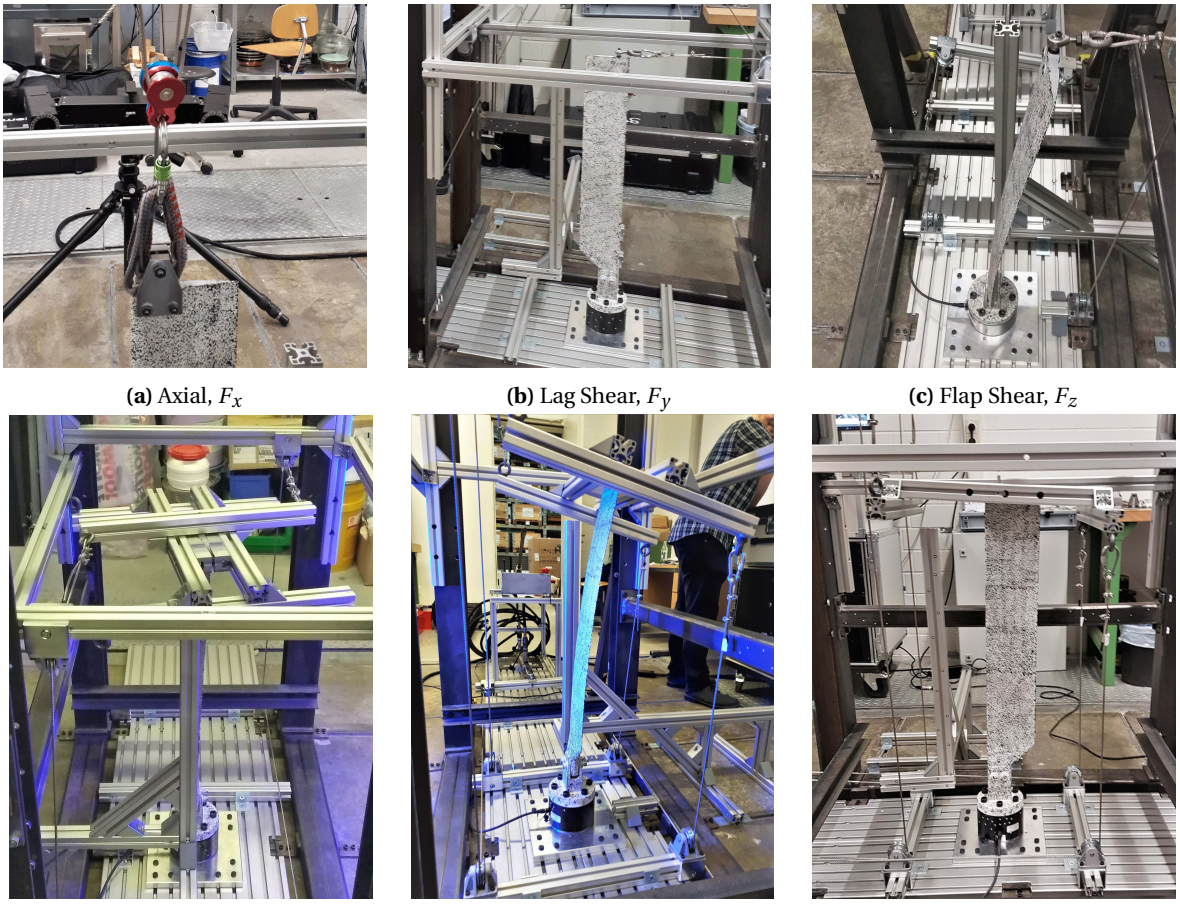

(a) Axial, F_x **(b)** Lag Shear, F_y **(c)** Flap Shear, F_z

(d) Torsion, M_x **(e)** Flap Bending, M_y **(f)** Lag Bending, M_y

Figure 4.27

range to obtain the best compromise between maximum load capacity and measuring accuracy. To obtain a high signal to noise ratio of the strain measurements, the target loads are calculated with the structural model of SONATA for a corresponding target strain estimate of ~ 0.3%. The nominal forces and moments (full scale (FS)) of the load cell are provided in table 4.7.
Sinotte [160] stated that the hardest part of getting good measurements with their test setup was obtaining accurate measurements of the applied loads, which is why they performed an elaborate calibration and uncertainty study to reduce the errors in the load measurements.
In this case, the calibration was carried out under consideration of the requirements of DIN EN ISO/IEC 17025 with measuring equipment according to national standards DIN EN ISO 9001 and DIN EN ISO 10012 by the manufacturer *ME-Meßsysteme GmbH*. The calibration matrix describes the relationship between the displayed voltages of the measuring amplifier and the components of the load vector $\underline{F}$. To determine the calibration matrix, 11 load vectors were applied three times using a reference force or reference weight with or without a reference lever. The direction of the

reference forces and reference moments on the sensor was ensured by different mounting positions of the sensor in the calibration device. Before each load application, a zero adjustment is performed [111]. With a probability of 95%, the measurement results have the uncertainties listed in table 4.7.

Technical Data *K6D130 5kN/500Nm MP11*			
Channel	Rated Forces/Torque (FS)	95% Confidence Interval	Operating Limit
F_x [N]	15000	±31.5	45000
F_y [N]	5000	±4	15000
F_z [N]	5000	±12	15000
M_x [Nm]	500	±0.5	1500
M_y [Nm]	500	±0.6	1000
M_z [Nm]	500	±0.65	1000

Table 4.7: Technical data *K6D130 5kN/500Nm MP11* [112], [111], note that the coordinates are given in the blade reference frame as opposed to the manufacturers coordinates)

The signals of the load-cell were processed by the amplifier GSV-8DS SubD44HD also by *ME-Meßsysteme GmbH* which tranformed the signals according to the calibration matrix, scaled each load individually and transmitted it to the GOM ARAMIS DIC system via coaxial 50Ω BNC cables. After start-up, a signal drift was be detected, that disappeared after the instruments have reached operating temperature. More measures of precision and crosstalk are given by the manufacturer and are summarized in table 4.8.

Precision and Crosstalk		
Accuracy class	0.2	%
Relative linearity error	0.1	%FS
Relative zero signal hysteresis	0.1	%FS
Temperature effect on zero signal	0.1	%FS/K
Temperature effect on characteristic value	0.01	%RD/K
Relative creep	0.1	%FS
Relative repeatability error	0.5	%FS
Crosstalk	1	%FS

Table 4.8: Precision and crosstalk specifications of the *K6D130 5kN/500NM MP11* load cell. Full Scale (FS) refers to the rated load of table 4.7

DIC Setup

To fill the remaining components of the governing equation (4.7), the plane surface strains ($\varepsilon_{11,e}, \varepsilon_{12,e}, \varepsilon_{22,e}$) and their corresponding cross-sectional coordinates ($\underline{Z}_i$) and orientation $\underline{R}_e$ are determined using Digital Image Correlation (DIC).

Sinotte and Bauchau [160], [161] generated a high local resolution by subdividing their specimens into multiple spanwise images and later reassembled them, yet used a high filter size to smoothen the data afterwards. In contrast to that, it was decided to use a camera setup and measurement volume that can capture the full surface of the blade, the blade clamp, load-cell and a load-free reference frame for a rigid-body motion correction.
An ARAMIS SRX 600 MV1200 sensor by *GOM* was used to capture images for full-field and point-based measurements with a resulting calibrated field of view of 920 mm × 1140 mm × 920 mm with an image size of 4096 × 3068 pixels leaving enough in depth space for large deflections under flap bending loads. The two stereo-cameras with a focal length of 24 mm are oriented 25.533° inwards to obtain 3D measurements. The sensor needed to reach its operating temperature in order to achieve thermal equilibrium. Otherwise thermal expansion of the beam, camera sensor or lenses can cause a drift in the intersection deviation. Additional LED arrays provided a homogeneous illumination of the test articles.

4.5.3 Sample Preparation

Before distributing the stochastic color information to the rotor blade and blade clamp, the surfaces of both were sanded and cleaned. Three to four layers of matte white 2-component epoxy resin-based primer (*Spay Max*®- *2K Epoxy Primer*) were applied to generate a smooth white primary coat before applying the matte black stochastic pattern (liquid acrylic paint of *Bob Ross*) with a brushlike sponge. (see figure 4.28a)
The ideal pattern size and distribution was determined prior to the experiments by evaluating various pattern samples on paper by the DIC Software in the test configuration.
The ideal pattern is as pronounced and as evenly distributed as possible and has a texture with about three to four contrast points per facet and optimum color ratio of 50% black and 50% white parts. The facet size can be adjusted to some extent during the post-processing of the images.
Figure 4.28b shows the prepared test articles in the test configuration. Figure 4.28c shows the 50 mm×50 mm cutout of the pattern illustrating a resolution of approximately ~3px/mm on the test article.

∅5 mm retro reflective reference point markers are distributed on the load-free reference frame, the cylindrical surface of the blade clamp, and the surface of the load cell. Additionally, a touch probe with reference point markers permitted to make point measurements of hidden areas such as the full cylindrical surfaces or flat plane of blade clamp. The capture of these distinct geometric objects allows the reference of a coordinate system.

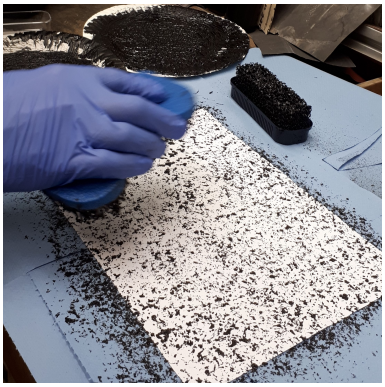

(a) Speckle patter application with a soft plastic sponge

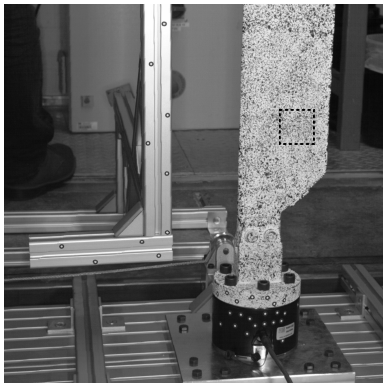

(b) Prepared test articles

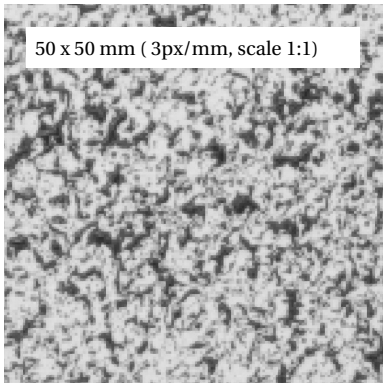

(c) True to scale cutout of the speckle pattern

Figure 4.28

4.5.4 Quality

A pattern quality measure is implemented within the GOM Correlate 2020 software and gives a numerical value of the stochastic pattern within the facet. A value of > 4 is considered sufficient. A variation in facet-size can increase or reduce the stochastic information and can be adjusted accordingly. [57]. Table 4.9 lists the arithmetic mean, standard deviation (SD) as well as the min max values of the pattern quality for a facet size of 23x23px and the intersection deviation over the surface of the test article. As described above, the intersection deviation is a quality measure of the sensor calibration.

	pattern quality [-]				intersection deviation [px]			
	mean	min	max	SD	mean	min	max	SD
Top	8.999	5.217	11.214	1.268	0.018	0.001	0.057	0.012
Bottom	8.135	4.271	10.764	1.101	0.037	0.000	0.109	0.023

Table 4.9: Quality measures of the DIC setup

4.5.5 Test Envelope

The tests was conducted by applying the previously described 11 load cases. The load amplitudes were selected based on preliminary structural calculations to achieve a targeted maximum strain of about 0.3% to ensure a high signal to noise ratio, but at the same time leaving safety margins. For most load cases, the load was applied in three amplitude steps. The test envelope of the highest loads levels is summarized in table 4.10. Again, a negative axial load $-F_x$ was not applied due to concerns about buckling.

		Measured Maximum Loads					
Load Case	Test #	F_x [N]	F_y [N]	F_z [N]	M_x [Nm]	M_y [Nm]	M_z [Nm]
Axial, F_x	L1.2	**10045**	-198	-4	0.7	-3.2	-104.9
	U1.2	**10040**	-83	-78	0.3	22.8	-24.5
Lag Shear, F_y	L2.2	79	**659**	-50	-0.3	-1.5	597.2
	U2.2	159	**659**	-44	0.0	0.1	604.4
	L3.2	66	**-734**	-20	0.7	-2.7	-673.2
	U3.2	139	**-735**	-44	1.3	-0.6	-672.9
Flap Shear, F_z	L4.3	40	-13	**-502**	-1.1	458.2	-7.3
	U4.3	49	-11	**-501**	-0.4	440.1	-2.0
	L5.3	63	6	**504**	0.9	-461.5	0.7
	U5.3	55	16	**503**	0.5	-455.3	7.8
Torsion, M_x	L6.3	-74	11	-51	**179.8**	33.4	2.8
	U6.3	-66	22	-17	**179.5**	-2.4	15.1
	L7.3	-67	-5	-16	**-123.8**	4.7	-2.2
	U7.3	-68	4	-14	**-123.6**	-2.8	5.4
Flap Bending, M_y	L8.3	-43	-29	30	-4.6	**300.3**	-28.9
	U8.3	-123	-12	-38	0.3	**300.3**	-2.6
	L9.3	-22	-27	-68	1.7	**-301.0**	-27.9
	U9.3	-186	-9	-42	2.1	**-301.5**	-5.0
Lag Bending, M_z	L10.3	-63	-42	-53	1.7	8.5	**469.8**
	U10.3	-143	-79	-34	0.9	-1.7	**470.7**
	L11.3	-88	0	-24	2.1	-4.3	**-604.8**
	U11.3	-165	-39	-28	2.5	-9.6	**-606.3**

Table 4.10: Test envelope of the measure load at the load cell, Test # refers to the (L:lower, U:upper) surface. 20 images per load lase

All experiments were conducted for the upper and the lower surface of the rotor blade by rotating the base plate together with the load cell and the blade by 180°. The test number listed here refers to the surface, load-case and load level (e.g L6.3; L:lower surface, 6: +torsion, 3:3rd load application step).

Independent load cases were targeted by reducing the off-diagonal terms of the test envelope table. Additionally, it was targeted to match the load cases of both sides.

For each test, 20 images were taken with a frequency of 2 Hz to offer the possibility to average the data over time.

4.6 Postprocessing

The momentary capture of the combined set of stereo images and analog signals from the load cell is hereinafter referred to as stage. All stages are further processed with the DIC software *GOM Correlate Professional 2020*.
For the initial alignment of the measurement data with respect to a coordinate system, the cylindrical and the plane surfaces of the blade clamp are used that were previously captured with the 3D touch probe.
When generating the surface component, the software finds square facets in the captured images. The software identifies facets in all captured images using the stochastic pattern structure and identifies all facets of the left camera image in the stochastic pattern of the right camera image. The software merges all calculated measuring points from valid facets into one surface component. The surface-component with a facet size of 23 px and a facet spacing of 11 px covers almost the entire visible surface of the blade from R241 to R878 with exceptions at the very front of the leading and the trailing edge. The suface-component of the top surface under flap bending loads are illustrated in figure 4.29.

The CAD description of the blade is superimposed on the undeformed reference state within the software to align the coordinate system to the original target data using a best-fit. Figure 4.30 and table 4.11 show the top and bottom deviation of the surface-component versus the CAD data after the best fit was performed.

The very low surface deviation to the CAD design of the rotor blade indicates a precise machining and sanding of the molds, no distortion of the blade during curing, good airfoil compliance along the span and a uniform paint and stochastic pattern application.

In order to obtain a better support of the individual punctual measured values for the strain tensor calculation, the software takes into account further neighboring points of radius 3 surrounding the point under consideration for the calculation.
Note that the strains are recovered in material, i.e. in local coordinates moving with the specimen. Therefore, each point has its own coordinate system. That is, the software calculates the strains of the sections in the moving coordinate systems $\mathcal{E}$ instead of in the stationary global coordinate system. The $\underline{e}_3$-axis points in thickness direction. To ensure a common orientation, the software uses the normal of a local equalization plane around the point under consideration as the Z direction. The local $\underline{e}_1$-axis results from the cross product of the normal vector $\underline{n}_{LP}$ of the plane and the global X-axis. The local $\underline{e}_2$-axis then results from the cross product of the local $\underline{e}_3$-axis and the local $\underline{e}_1$-axis. [57]

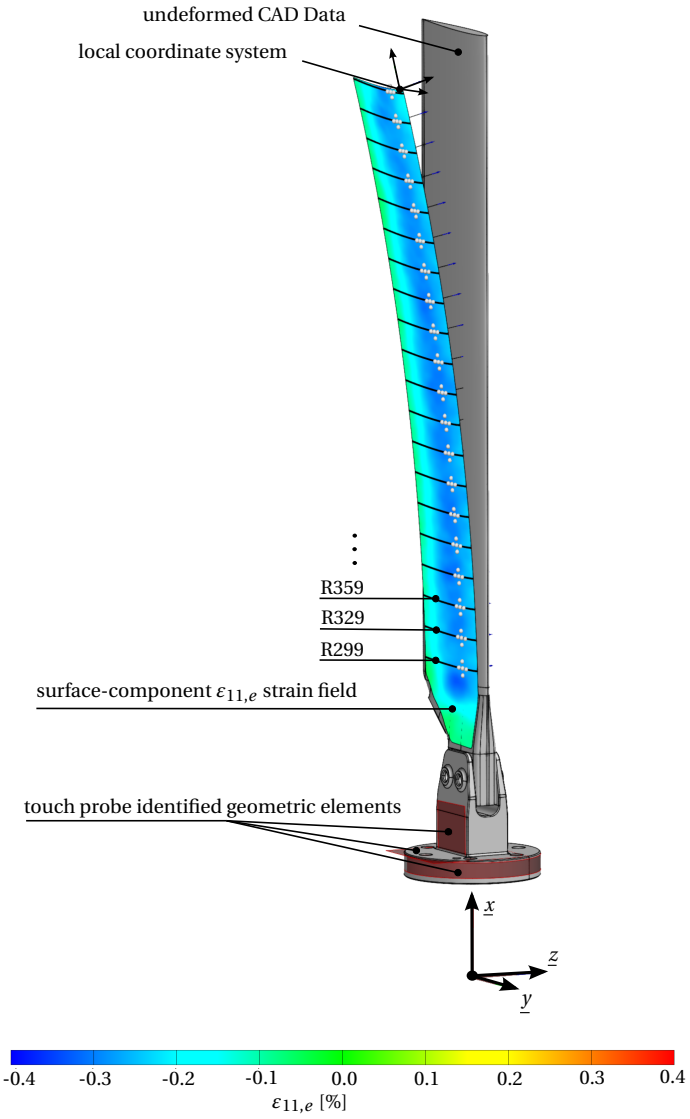

Figure 4.29: Postprocessing setup under load case L8.3 - Flap Bending, each radial section set combines a facet-point-component that is connected to a coordinate system at the beam axis.

The measured strain field is split into multiple radial sections every 30 mm. To recover the deformed local coordinate system $\mathcal{C}$ of each section a facet-point-component with 5 facets of size 23 px is introduced as shown in figure 4.31. They are placed around 25% chord of the airfoil and sit right above the pitch and beam axis of the blade. The facet-point-component links the coordinate system at the beam axis with a rigid body motion. Note that this local sectional coordinate system coincides with the local coordinate system of the deformed beam.

To obtain the sectional loads at each radial station the measured load and moment vectors of the

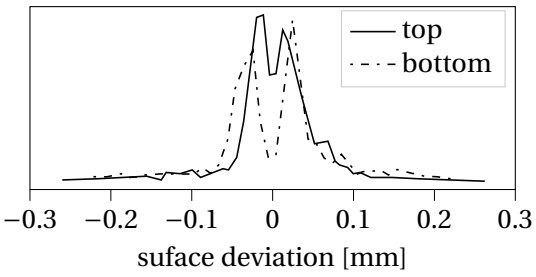

Figure 4.30: Reference surface deviation histogram of the best-fit surface-component versus CAD

	surface deviation [mm]			
	mean	min	max	SD
top	0.016	-0.49	0.16	0.06
bottom	0.01	-0.19	0.20	0.05

Table 4.11: Reference suface-component deviation

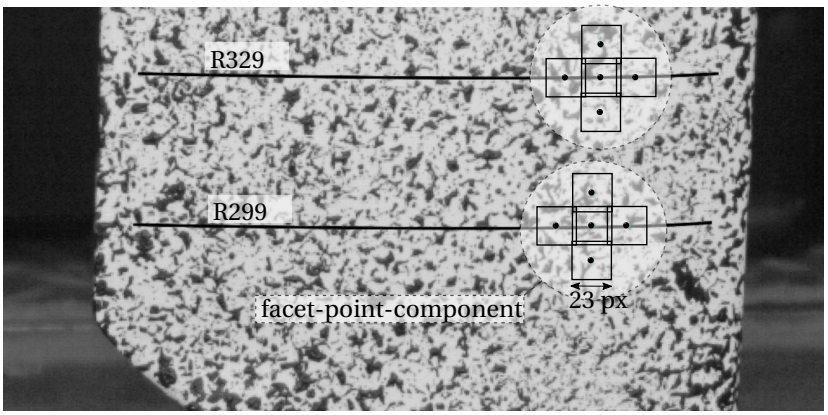

Figure 4.31: Facet-point-component definition on the bottom surface of the blade at R299 and R329 with a facet size of 23 x 23 px.

load-cell are transformed according to the following relationship from the global coordinate system $\mathcal{G}$ to the local sectional coordinate system $\mathcal{C}$. $\underline{p}^{(\mathcal{G})}$ is the position vector of the coordinate system and $\underline{\underline{A}}_{\mathcal{C}\mathcal{G}}$ is the transformation matrix containing the unit vectors of $\mathcal{C}$.

$$\begin{aligned} \underline{F}^{(\mathcal{C})} &= \underline{\underline{A}}_{\mathcal{C}\mathcal{G}}\underline{F}^{(\mathcal{G})} \\ \underline{M}^{(\mathcal{C})} &= \underline{\underline{A}}_{\mathcal{C}\mathcal{G}}(-\underline{p}^{(\mathcal{G})} \times \underline{F}^{(\mathcal{G})} + \underline{M}^{(\mathcal{G})}) \end{aligned} \tag{4.24}$$

4.6.1 Finite Element Model

The hybrid approach of this method requires the experimental results to be mapped onto the finite element discretization by SONATA. The structural analysis of the rotor blade uses the previously described framework SONATA in conjunction with VABS and ANBA4. The outer surface of the blade of the SONATA model is described by the closed surface geometry extracted from the CAD in the form of a .stp file (see figure 4.32).

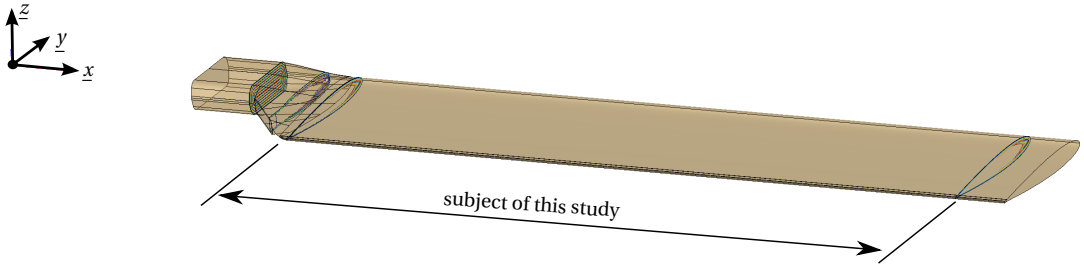

Figure 4.32: SONATA topology of MERIT rotor blade

Figure 4.32 shows different cross sections of the fiber composite topology in addition to the extracted surface. As it was not possible to carry out an entire series of tests with several rotor blades, the primary subject of this study is to focus on the homogeneous blade area, which has identical cross-sections with exactly the same composite structure over the entire length. Deviations along the length are therefore either indicators of fluctuations in the manufacturing process or can provide information about the influences of the test setup, since the deflection as well as the sectional loads change steadily toward the blade tip . Note that the governing equations are evaluated independently of each other every 30 mm along the span with the recovered sectional data.

Figure 4.33b shows the finite element model of the homogeneous cross-section developed during the preliminary design with SONATA in comparison to the sectional view of the second prototype blade *S/N: MERIT-A-005-2020-08* (figure 4.33a). It is well recognized that the model represents the resulting structure of the manufactured rotor blade very accurately. Especially in the context of the fact that the position of the trim mass is not fixed in advance in the manufacturing process, it agrees satisfactorily with the position from the preliminary design model. The position of the spar layers and the shape of the C spar also correspond well to the model and the finished rotor blade. Only the steps of the individual layers are modeled too discretely. An adjustment of the layer cut-off definition in the SONATA model (see section 2.2) could smooth this even further.
In addition, the parting plane of the two foam core halves, which is filled with an extra thin layer of film adhesive, is not represented in the SONATA model. However, this should only have a negligible effect on the resulting stiffness properties.

Note that the even tough the surface deviation compared to the CAD data is very low (see figure 4.30), small discrepancies are still noticeable when the experimental sections are transformed in local coordinates under deformation. This is especially noticeable under torsion and is increasing towards the tip. Figure 4.33b shows both the datapoints of the DIC measurements with the described offset. The surface-strains are therefore mapped onto the nearest nodal locations by linear

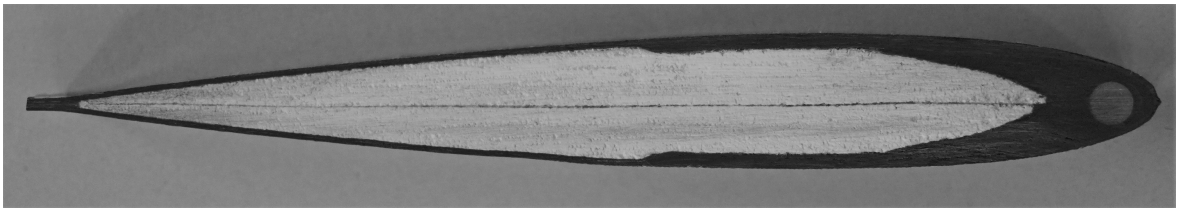

(a) Homogeneous cross-section of *S/N: MERIT-A-005-2020-08*

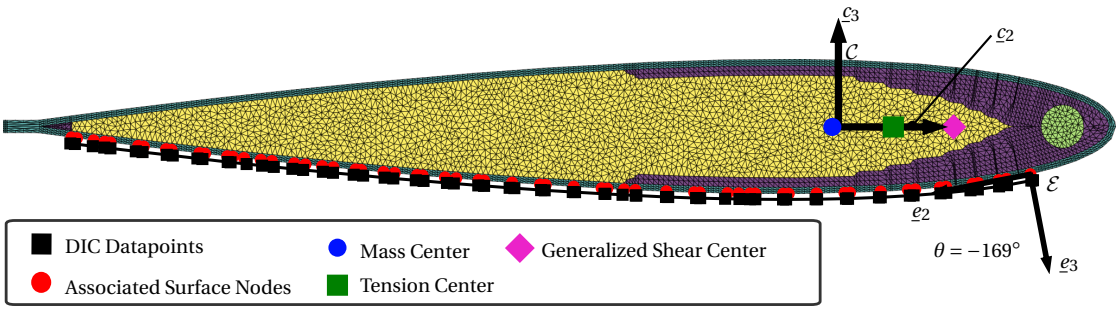

(b) Finite element discretization of the homogeneous cross-section created by SONATA showing the maximum deviation of the measured nodal values at the R869 during torsion (L7.3)

Figure 4.33: SONATA Finite Element model vs. reality of the homogeneous section of the MERIT rotor blade

interpolation. The partial derivatives of the calculated warping field are also recovered by linear interpolated derivatives over the mesh. Figure 4.33b also shows the calculated location of the mass, tension and shear center. Together with the calculated stiffness-properties they will be compared to the results in the next section.

4.7 Results

This section examines the sectional stiffness matrix of the *MERIT-A-001-2020-07* composite blade over the homogeneous region. First, the axial strain distributions are examined under selected load conditions before the numerically determined strains are compared to the measured strains under the six major load cases at section R329. Following this pre-examination, the results of the governing equations are shown and compared and evaluated to the numerically predicted results.

4.7.1 Strain Distributions

The axial surface strains ($\varepsilon_{11,e}$) are illustrated in figure 4.34 for the flap shear load case (U4-3). Under this load, the inevitable flap bending moment creates an axial strain distribution that has its sectional maximum at the maximum thickness location at 30% chord and decreases linearly along the span.

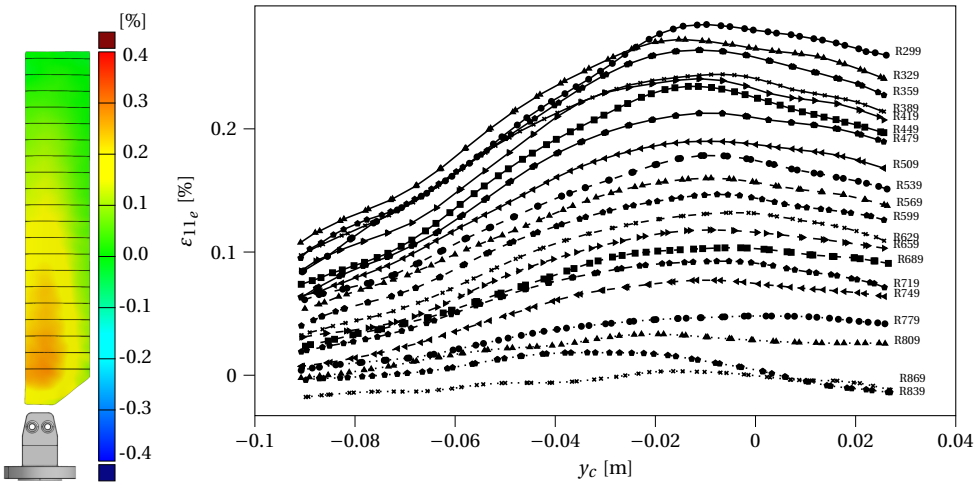

Figure 4.34: DIC axial top surface strain distribution ($\varepsilon_{11,e}$) under positive flap shear (U4.3, +Flap Shear)

The axial surface strains ($\varepsilon_{11,e}$) are illustrated in figure 4.35 for pure flap bending (U9-3). Under this load, the flap bending moment creates a similar strain distribution with a sectional maximum at 30% chord but varies little over homogeneous region along the span. Note, that the outermost radial section R869 already has additional plies within the layup to embed the balance chamber into the structure, which leads to a decreased axial strain amplitude towards the tip. Similarly, the strain decreases towards the blade attachment as the sections becomes thicker and embed more material. Figure 4.36 shows the top surface strain distribution ($\varepsilon_{11,e}$) under negative lag bending

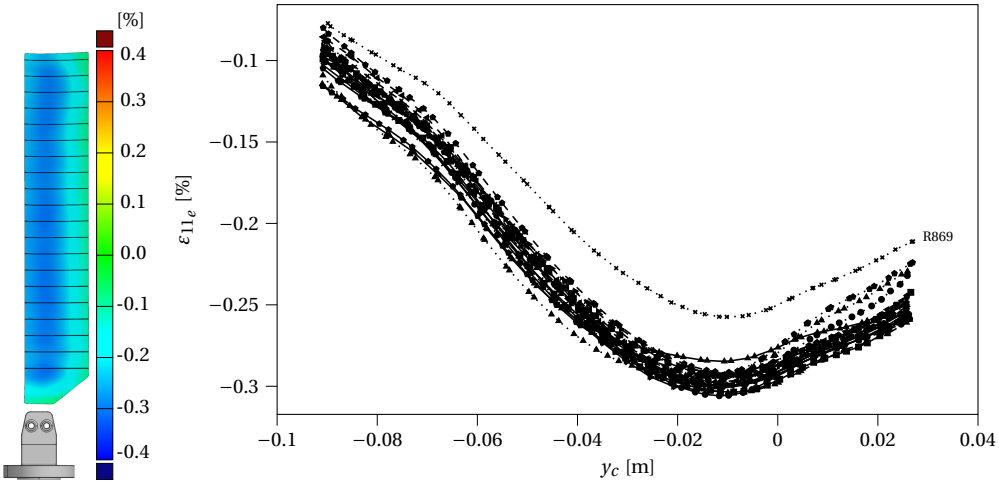

Figure 4.35: DIC axial top surface strain distribution ($\varepsilon_{11,e}$) under positive flap bending (U9.3, +Flap Bending)

(U10.3, -Lag Bending). Comparable to the previous load case the sectional strain distribution varies little along the span with the exception of the outermost section and towards the blade attachment. The axial strain decreases in chordwise direction towards the trailing edge.

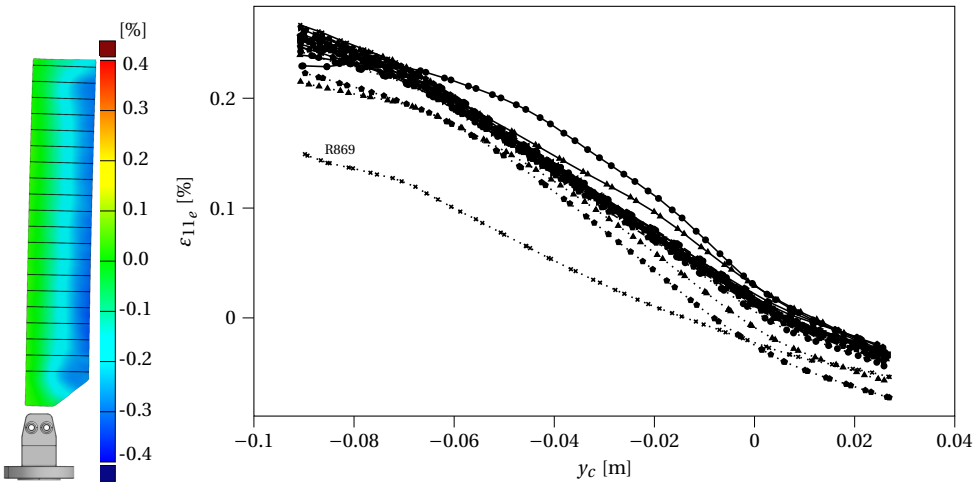

Figure 4.36: DIC axial top surface strain distribution ($\varepsilon_{11,e}$) under negative lag bending (U10.3, -Lag Bending)

Figure 4.37 not only presents the measured surface strains ($\varepsilon_{11,e}$,$\varepsilon_{12,e}$,$\varepsilon_{22,e}$) in six different load cases, but compares them with the numerically determined strains of the finite element model described in section 4.6.1. ANBA4 was used for this purpose. This figure takes the data extracted from the experiments which measured the surface on the upper side of the blade (see figure 4.37a in the local surface coordinate system denoted with subscript $(.)_e$.

In the experiment, as described, only low axial loads could be applied, resulting in a mean axial strain of only 420 $\mu\varepsilon$ at the surface (see Figure 4.37b). At the same time, there was a decrease in axial strain $\varepsilon_{11,e}$ along the blade chordline towards the leading edge. This is explained by the position of the tension center of the cross section which doesn't align with the applied load vector. This coupling relation is is expressed by the coefficient K_{16} of the stiffness matrix. While the finite element model calculates an ideal linear distribution, the experiment shows a slight deviation from this. As expected, the transverse strains $\varepsilon_{22,e}$ have an opposite sign as the axial strains and to a certain extent mirrors this behavior.
Noteworthy is the shear strain distribution $\varepsilon_{12,e}$ that has a significant characteristic with a change in signs near the location of maximum thickness as opposed to the near zero predicted values. Note that for better visualization the scale of the y-axis of this plot is not the same as the other ones.

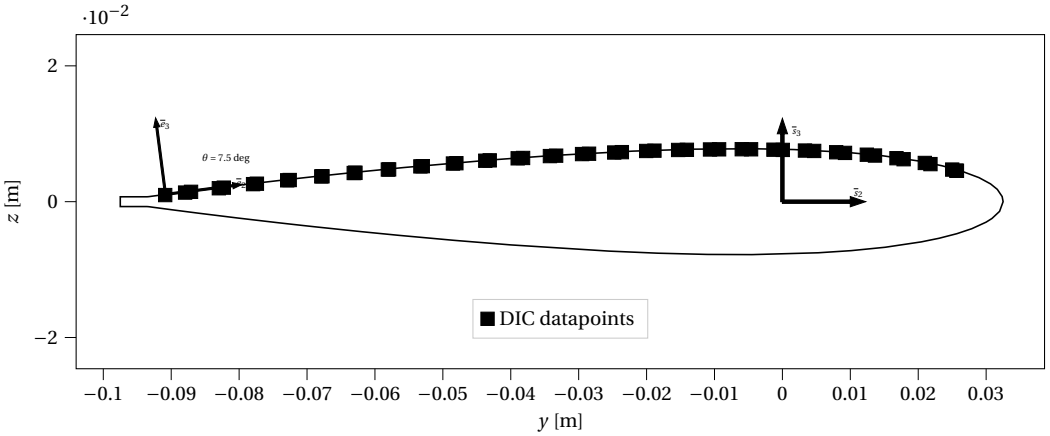

(a)

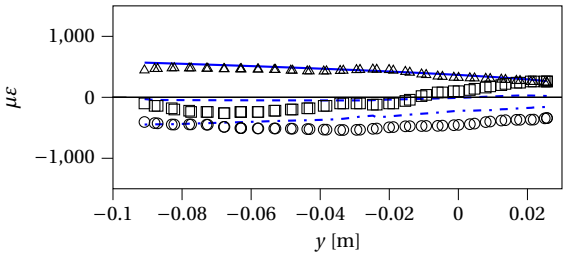

(b) U1.2, +Axial

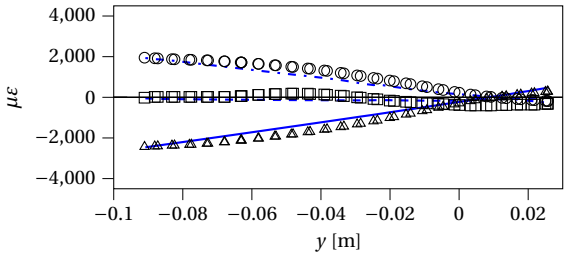

(c) U3.2, +Lag Shear

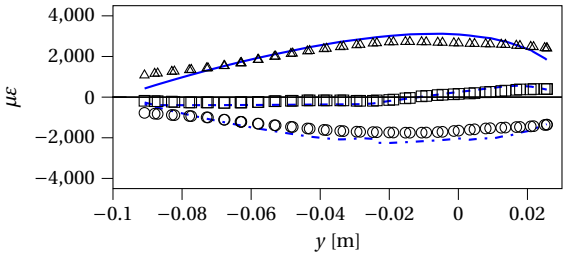

(d) U4.3, +Flap Shear

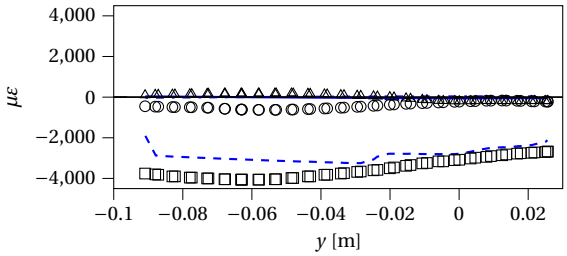

(e) U6.3, +Torsion

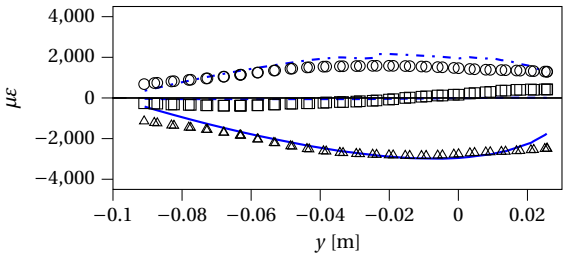

(f) U9.3, +Flap Bending

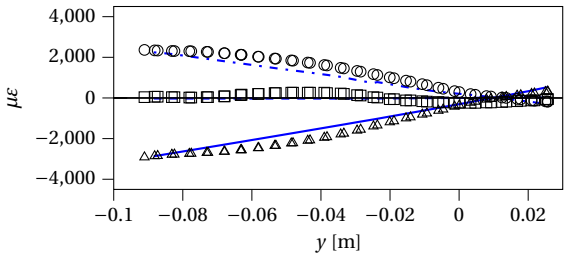

(g) U11.3, +Lag Bending

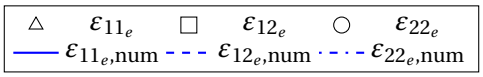

Figure 4.37: Numerically determined strains versus measured strains at section R329.

The numerically predicted strain distributions are very similar when comparing flap shear and flap bending. It is no suprise that the bending moment induced by the concentrated load at the blade tip generates the same axial and transverse strain distribution as in the case under pure bending moment. The difference becomes apparent in the shear strain field. While under additional shear force a shear strain distribution with sign change at the point of maximum thickness is predicted by the numerical model, under pure bending moment the shear strain distribution is close to zero. The experimentally recorded axial strain data reproduce the predicted strains well in both cases, whereas the measured data have a shape will less gradient which leads to a deviation especially at the trailing edge and the leading edge of the rotorblade. The transverse strains are consistent with this observation. The recorded shear strains show in both cases a very similar non-zero distribution, which corresponds to the previously mentioned distribution of the flap-shear load case. An analogous behavior can be observed for the lag-shear and the pure lag-bending load cases. The axial strains of the induced bending moment dominates the stress state, so that both with and without lag shear forces, the strain distribution on the surface of the cross-section is very similar. The experimentally determined axial strains follow the linear behavior numerically predicted strains, although not quite as ideal linear. The shear-strain distribution was predicted to be close to zero for the pure bending lead-lag and non-zero for the case with additional lag shear loads. Yet, the experimental data shows a very similar distribution for both cases in which the order of magnitude ranges from -400 $\mu\varepsilon$ to 260 $\mu\varepsilon$. The torsional load case is predicted to produces primarily shear strains, which is confirmed by the experimental data. The experimentally determined shear strain matches the distribution of the numerical prediction especially in the front part of the cross-section where the thick C-spar is present. The correlation reduces in the direction of the trailing edge. There, the measured strains were higher than predicted by the model.

4.7.2 Sectional Stiffness Matrix

The following section provides the results derived from the governing equations and compares them to the numerically predicted results. This is also accompanied by the analysis of the effects of the presented measurement uncertainties on the results which are calculated by the means of Monte Carlo Simulations.

The dimensionless form of the stiffness matrix is used to determine the significance of the measured off-diagonal coefficients. According to equation (4.25), the coefficients along the diagonal will take the value 1. If the normalized coefficients on the off-diagonal are much smaller than 1, they are insignificant for the overall behavior of the beam, i.e. for the static and dynamic behavior

[159].

$$K_{n,ij} = \sqrt{\frac{K_{ij}^2}{K_{ii}K_{jj}}} \tag{4.25}$$

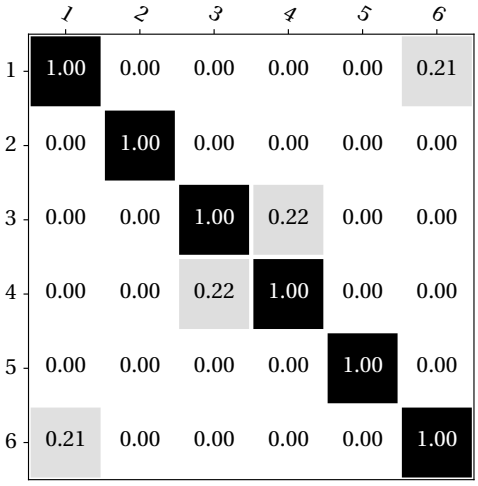

Figure 4.38: Numerically predicted normalized stiffness matrix K_n

K_{11}	3.54e+07	N
K_{16}	-1.83e+05	Nm
K_{22}	5.77e+06	N
K_{33}	2.44e+05	N-m^2
K_{44}	7.28e+02	N-m^2
K_{34}	2.96e+03	N-m
K_{55}	8.04e+02	N-m^2
K_{66}	2.06e+04	N-m^2

Table 4.12: Significant coefficients of the numerically predicted sectional stiffness matrix

The MERIT rotor blade has a symmetric NACA0012 airfoil, a symmetric layup and no twist. Therefore the numerical simulation predicted many off-diagonal coupling relation coefficients to be very small (see figure 4.38). One of the remaining significant off-diagonal coupling relations is K_{16} (= K_{61}) which describes the lead-lag bending moment in response to an axial sectional strain ϵ_1 and vice versa. It is also characterizes the x_{t2} location of the tension center. From figure 4.38 it can be concluded that the tension-center has a significant offset from the coordinate origin of the reference coordinate system which coincides with the pitch axis and the quarter-chord line of the airfoil.
The off-diagonal coupling relation K_{34} (= K_{43}) describes the relationship between the torsional moment and the chordwise transverse sectional shear strain ϵ_2 and therefore contributes to an x_{s2}-offset of the shear center.

Figure 4.39 shows the relative variation of the experimentally determined stiffness properties along the span of the rotor blade compared to the numerically predicted values. The axial stiffness (K_{11}), torsional stiffness (K_{44}), flap bending stiffness (K_{55}) and lead-lag bending stiffness (K_{66}) are all within a 10 to 15% range to the numerically predicted values. The increase of lead-lag and flap bending stiffness towards the tip of the blade is explained by the additional plies that begin to scarf towards a monolithic tip structure. The measured torsional stiffness K_{44} is on average 9% and the flap bending stiffness K_{55} 8% higher than the predicted value of the numerical simulation. The axial stiffness K_{11} is 1.3% and the lead-lag bending stiffness K_{66} is 1.6% lower than the predicted

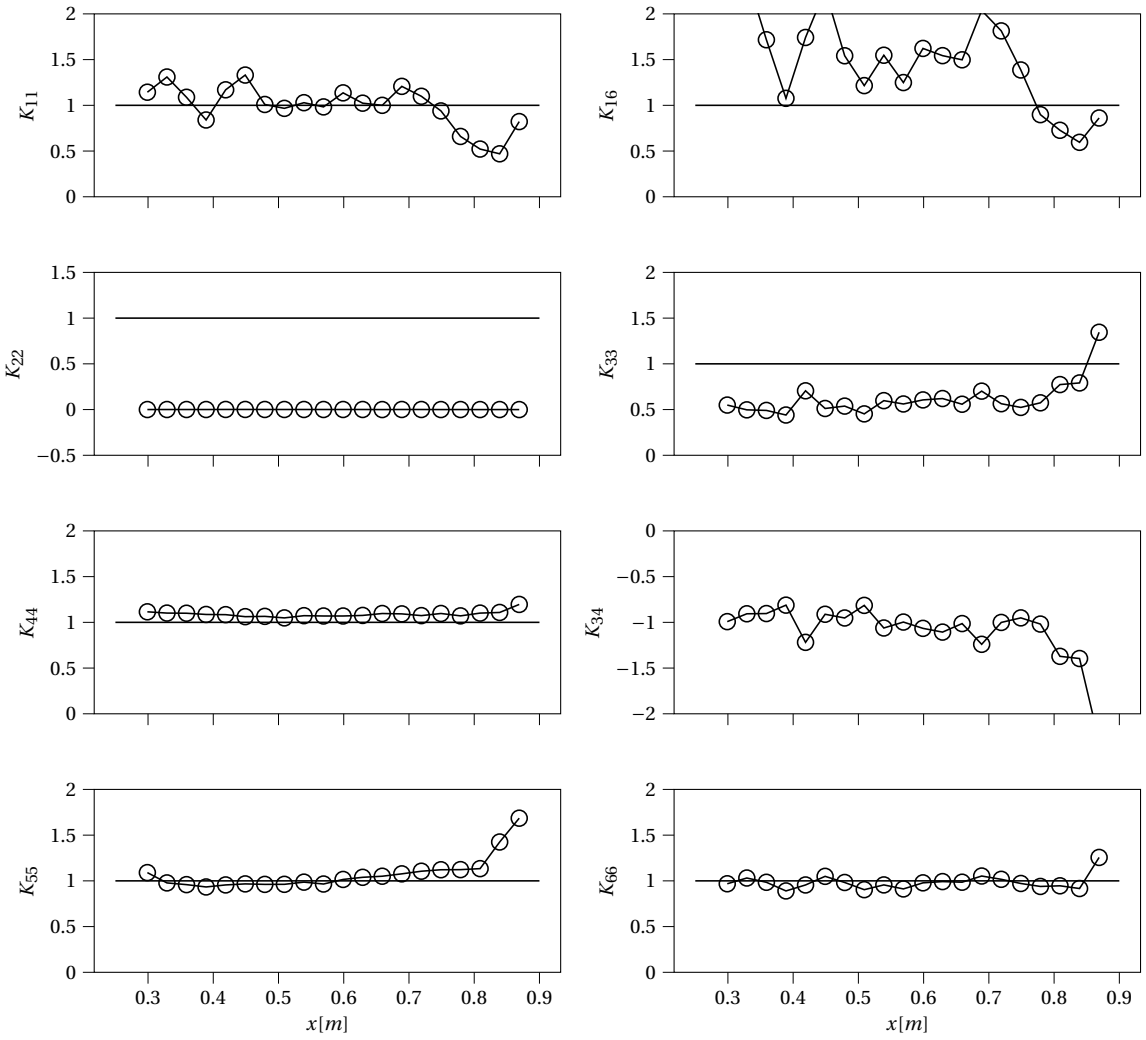

Figure 4.39: Spanwise distribution of sectional stiffness coefficients $K_{\text{exp}}/K_{\text{num}}$

value of the numerical simulation.

Table 4.13 summarizes the results illustrated in figure 4.39 as spanwise mean of the significant stiffness properties along the homogeneous region. The right hand side of the table shows the spanwise mean of the coefficient of variation (COV) of both Load-Cell (LC) and the DIC uncertainty studies described later in this section.

The axial stiffness coefficient K_{11} is on average just 1.3% lower than the predicted value of the numerical simulation but varies along the span with a coefficient of variation of 22.9% with a trend to an increased stiffness towards the blade root and a decreased stiffness towards the blade tip. A similar trend and shape is evaluated for the off-diagonal coupling relations K_{16}. The chordwise

tension center is described by the ratio K_{16}/K_{11} and is illustrated in figure 4.40. It matches well the predicted location along the span with a location of ($x_{t2} = 7.66$, $x_{t3} = -0.85$) mm with a standard deviation of ($x_{t2} = 1.05$, $x_{t3} = 1.04$) mm compared to the predicted location ($x_{t2} = 5.165$, $x_{t3} = 0.00$) mm. This increased chordwise tension center offset of 2.49 mm contributes to an increased coupling coefficient K_{16} compared to the numerical predicted value.

The transverse shear coefficients show a more than significant offset from the predicted values. By looking at both the spanwise mean of the normalized stiffness matrix in figure 4.41 and the strain distributions under lag and flap shear in figure 4.37c and 4.37d it is noticed that a shear strain distribution with sign change at maximum thickness is registered under transverse shear forces in chordwise direction. Which was expected to be especially apparent for the transverse flap shear loadcase. This is one explanation for the large transverse coupling relation K_{23} of figure 4.41. The large differences of all transverse shear coefficients especially K_{22} and K_{33} challenges the inherently inverse hybrid method itself and point out the biggest weakness of this method. With the fundamental assumption that the warping corrections are determined from a numerical model the model itself has to be an adequate representation of the real problem. In other words, the warping function was solved from a cross-section which assumed to have a different compliance matrix to be obtained from the governing equations. In fact, if the compliance matrix is different, then the warping function will also be different.

The torsional stiffness K_{44} is on average 9% higher than the predicted values and has a low variation along the span of only 2.7% with a slight increase towards the tip. The flap-shear torsion coupling relation K_{34} mirrors the shape of the transverse flap-shear stiffness K_{33} and is for the most part responsible for the chordwise shear-center position. The negative relative value of figure 4.39 indicate an opposite location compared to the numerical prediction. The shear-center location, illustrated in figure 4.40, shows a average location of ($x_{s2} = -21.4$, $x_{s3} = -0.6$) mm compared to the predicted location of ($x_{s2} = -12.1$, $x_{s3} = 0.00$) mm and thus a pitch up instead of a pitch down deformation as a result of lifting transverserse shear forces $+F_3$. This difference gives reason to become critical and once again question the results and the inverse method. To anticipate the outlook, in the future alternative studies should verify this behavior.

The flap bending stiffness K_{55} is 8% higher than the predicted values with a coefficient of variation of 16.4%. The slight overshoot of the mean and the variation are primarily explained by the more than 50 percent increase in stiffness at the blade tip. The same but not so pronounced increase at the tip is also observed for the lead-lag bending stiffness K_{66}, which also matches the predicted values up until that point very well with an average difference of 1.6% and variation of 7.8%. The increase of lead-lag and flap bending stiffness towards the tip of the blade is explained by the additional plies that begin to scarf towards a monolithic tip structure.

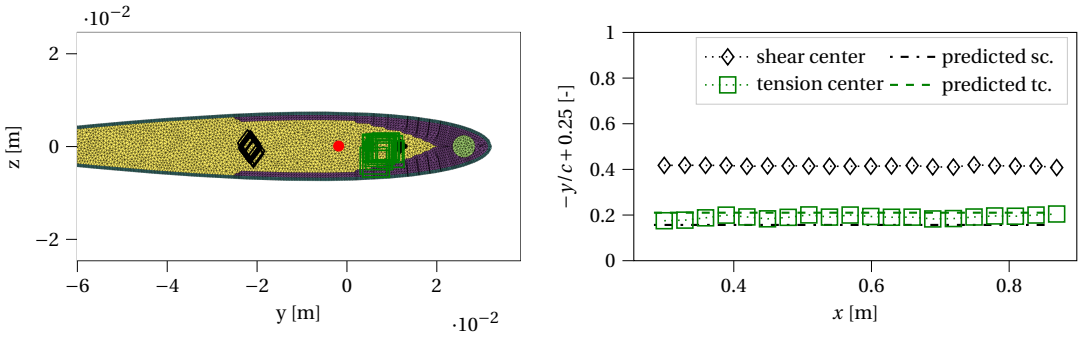

Figure 4.40: Spanwise location of the shear center (SC) x_{x2} and tension center (TC) x_{t2}

	1	2	3	4	5	6
1	1.00	1.20	0.02	0.01	0.10	0.34
2	1.20	1.00	2.57	0.73	0.10	0.34
3	0.02	2.57	1.00	0.29	0.03	0.03
4	0.01	0.73	0.29	1.00	0.02	0.01
5	0.10	0.10	0.03	0.02	1.00	0.05
6	0.34	0.34	0.03	0.01	0.05	1.00

Figure 4.41: Spanwise mean of the normalized stiffness matrix K_{exp}

If the transverse lag shear coefficients of row and column 2 are excluded from the figure 4.41, the reduced 4×4 normalized classical Bernoulli stiffness matrix is obtained. It can be seen that the remaining coupling coefficients have only a very small influence, which matches the predicted behavior.

4.7.3 Uncertainty Evaluation

An integrated uncertainty analysis of the results of the different measurement systems is an important goal of this study. This is one way to assess the validity of this novel measurement methodology and to draw conclusions for improvements. For this purpose, the associated uncertainties of the DIC sensor system and the load cell were investigated independently of each other. Monte Carlo Simulations are once again used as a technical numerical tool to study the effect of these two uncertainties independently and obtain an value of accuracy of the performed experiments and this method.

In this case the complete set of experiments are evaluated 500 times in which the added random uncertainties were extracted from probability distributions.
The systematic error of the strain measurements is estimated based on 30 undeformed reference images of the top surface and 30 images of the bottom surface. The residual sum of squares estimates was used to recover a best fit theoretical distribution for the empirical distributions out of 89 possible. Figure 4.42 shows both the empirical distribution, the best fit theoretical distribution and the upper and lower indication of the 95% confidence interval. The recovered distributions

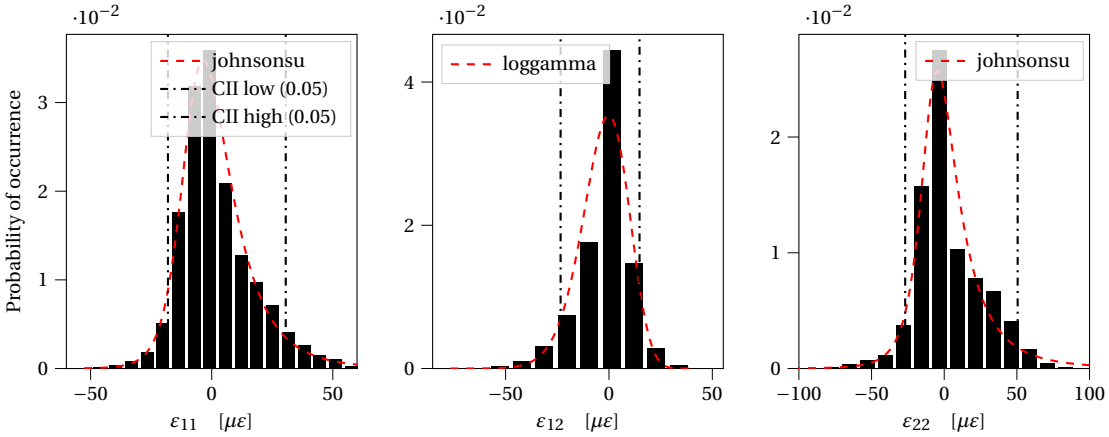

Figure 4.42: Probability of occurrence of strains over 60 undeformed reference images.

of ε_{11}, ε_{12} and ε_{12} show all a minor asymmetry towards positive values. The 95% confidence interval is represented by the black dash-dotted lines with the axial strains ε_{11} in the range between [-18;30] $\mu\varepsilon$, the transverse strains in the range between [-26;50] $\mu\varepsilon$ and the shear strains in the range between [-23;14] $\mu\varepsilon$.
The uncertainty associated with the load measurements of the load cell was determined in advance by the manufacturer during calibration (see table 4.7) and are assumed to follow a Gaussian distribution.

Figure 4.43 shows the spanwise distribution of the same coefficients of the stiffness matrix as the previous graph. Now, the mean value and the standard deviation of the Monte-Carlo simulation are presented for the separate analysis. At first glance, the large difference in the variation bandwidth between the two studies is noticeable. The uncertainty of the load-cell measurements exceeds the uncertainties of the strain measurement considerably. The reason why the uncertainties caused by the DIC strain measurements result in only very small effects is assumed to be not so much because of the absolute measurement accuracy but in how the uncertainties were added to the equations. Since for each measuring point i a sample is taken from the probability distribution, the errors average out over the cross-section with multiple data points and loadcases. As a summary,

the mean coefficients of variation of the two studies are shown on the right side of table 4.13. Since the basis for the load-cell study are symmetric Gaussian probability distributions, the mean of the study is equivalent to the solutions from Figure 4.41. The DIC study involves asymmetrical distributions that explain the recovered mean offset of both studies. With a mean value of 3.3%, the coefficient of variation is lowest for the lead-lag bending stiffness K_{66}. The pure bending load case, which is the main contributor to the determination of this parameter, has a relatively high signal to noise ratio, which can be seen in the relationship of the applied load to the rated value of the load cell. However, the value of 3.3% exceeds the accuracy class of the load cell, because in order to determine the resulting moment at the radial section, a sum of moments is represented, to which the transverse shear forces multiplied by the lever arm are also added.
This effect is particularly evident in the increasing standard deviation of the flap bending stiffness K_{55} towards the blade tip. This results in a spanwise mean coefficient of variation of 6.25%. For the axial stiffness K_{11} and the torsional stiffness K_{44} a mean LC COV of 14.2% and 10.6% results. The largest uncertainty concerns the transverse shear terms K_{22}, K_{33}, and K_{44} in which the rated load of the load-cell is much higher than the actual applied load. In summary, it can be said that similar to the discoveries from Sinotte [160], the load cell proves to be crucial for a good accuracy. Especially the transverse shear load measurements (F_y, and F_z) proved to be mainly responsible for the large standard deviation of the results.

	K_{exp}	$\frac{K_{\text{exp}}}{K_{\text{num}}}$ [%]	COV [%]	COV LC [%]	COV DIC [%]
K_{11}	3.50e+07 N	98.7	22.9	14.2	1.11
K_{16}	-2.73e+05 Nm	150	33	19.5	1.73
K_{22}	2.55e+03 N	0.044	91.1	153	1.97
K_{33}	1.51e+05 N-m^2	62.0	30.8	97.4	0.522
K_{44}	7.93e+02 N-m^2	109	2.73	10.6	0.0451
K_{34}	-3.26e+03 Nm	-110	28.7	96.7	0.512
K_{55}	8.65e+02 N-m^2	108	16.4	6.25	0.159
K_{66}	2.03e+04 N-m^2	98.4	7.78	3.27	0.351

Table 4.13: Spanwise mean of the significant stiffness properties along the homogeneous region. The right hand side of the table shows the spanwise mean of the coefficient of variation (COV) of both Load-Cell (LC) and the DIC uncertainty studies.

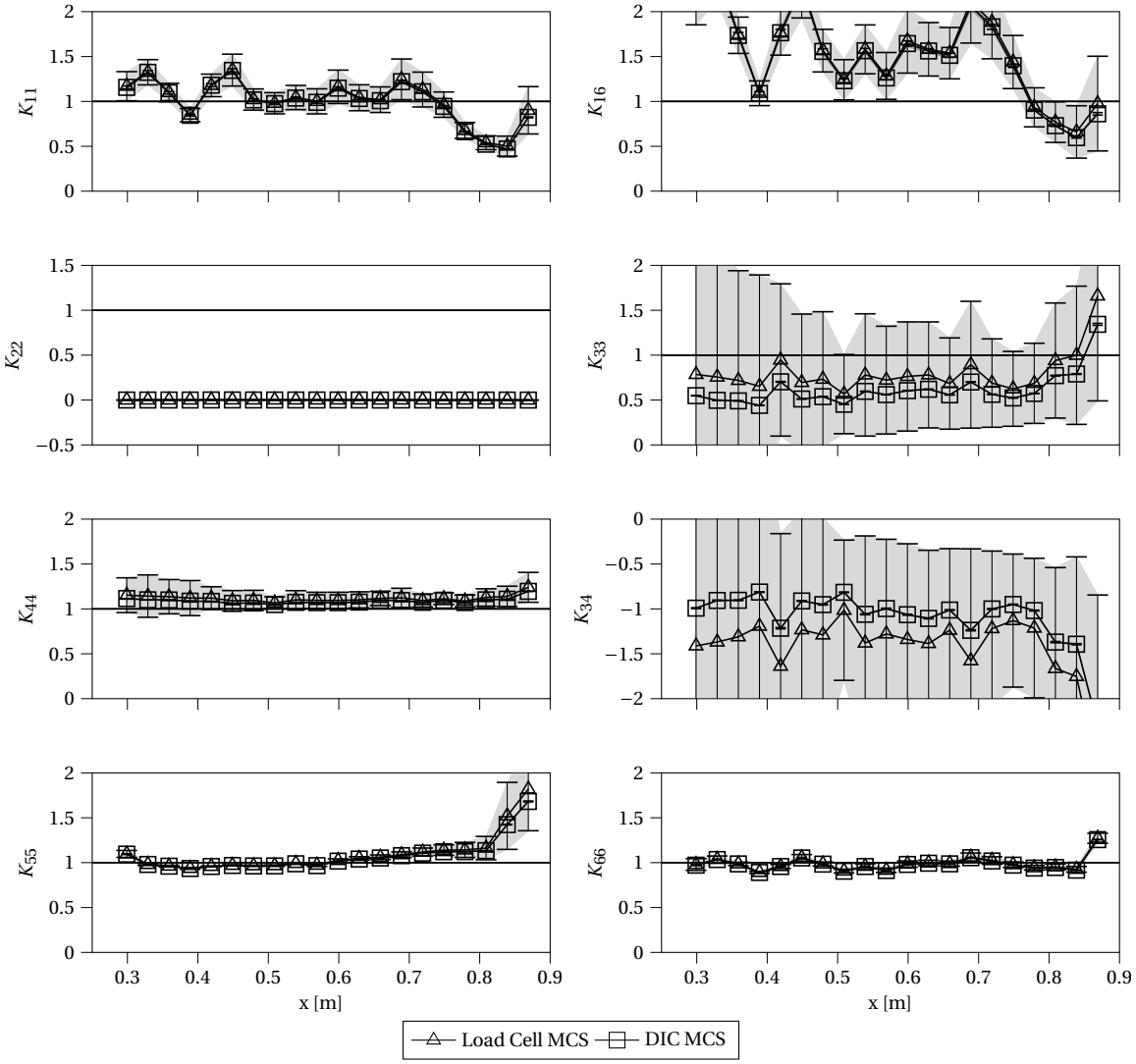

Figure 4.43: Spanwise distribution of mean and SD of sectional stiffness coefficients $K_{\text{exp}}/K_{\text{num}}$ for Load-Cell and DIC MCS

4.7.4 Discussion

To conclude the discussion of the presented methodology, first of all, the good agreement of the two bending and torsional stiffnesses along the radius between experiment and prediction by the numerical model can be pointed out. Also the good agreement of the axial stiffnesses and the position of the tension center is worth mentioning. For the helicopter engineer, these characteristics are the most important properties when determining the dynamic behavior of the rotor. Differences in the shear stiffness properties of even an order of magnitude have an insignificant effect to the dynamic response of rotor blades and are often neglected and set to infinity in rotor analyses [161].

The relevant dynamic responses can be characterized as low-frequency / long-wavelength effects. When higher frequency effects are investigated, the bending modes have a shorter wavelength and thus the transverse shear deformations have an increasing importance [70], [71]. Nevertheless, it should be explicitly mentioned here that the transverse shear results are considered critically and with great skepticism as they show a large deviation from the numerical predicted values. I do not consider these properties to be set in stone, but rather see them as an incentive for further research.

In the associated uncertainty study it became evident that the accuracy of the load cell is decisive for the quality of the results, which supports the discoveries and results from Sinotte [159]. Especially the transverse shear load measurements (F_y, and F_z) proved to be mainly responsible for the large standard deviation of the results. A suggestion for future applications is to adapt the 6-axis load cell even better to the designed load case to balance the signal to noise ratio between transverse forces and bending moments. Also, further investigation with a more in-depth study of the uncertainties of the DIC system in particular is desirable for further research projects.

Although, the material constitutive behavior, foundation of the numerical model, was determined experimentally and great attention was paid to an accurate representation of the numerical model, small and large discrepancies were observed between the measured and numerical values. The large discrepancies were particularly evident in the transverse lag shear properties. Those differences reveal the weakness of this inherently inverse methodology. With the fundamental assumption that the warping corrections are determined from a numerical model, the model itself has to be an adequate representation of the real problem. As it was stated above, if the results are different to the prediction, then the warping function will also be different. Following discussions with Wenbin Yu, highlighted that the key issue is to identify what is measured by experiments while not captured in the cross-sectional analysis, thus created the difference between the measured and predicted results. He suggested to treat these factors as unknowns, using machine learning to figure out these unknowns so that the measured and predicted differences can be minimized. Some of the fundamental ideas can be found in the following two publications [99], [100].

A second apparent weakness of the hybrid experimental approach is that to determine the nonuniform beam properties, one needs a 2D finite element model of each cross section of interest. In the future, a fully experimental method is desirable.
One approach for this strain-based method could be to investigate how to extract the warping displacement field from the experimental DIC data as well. The governing-equation chosen here describes the displacement as a superposition of the average sectional displacement of the rigid-section motion and the nodal warping. The experimental data of the DIC system consists of relative displacements in the differential neigborhood of the point of interest and provides both the strain

information in the form of the material deformation gradient tensor as well as the general warping displacement. Problems and issues that can be addressed in future research include the separation of the nodal displacements to extract the warping field. In particular, an appropriate choice of defining facet-point-components can play a decisive role to extract the average sectional displacement. Compared to the post-processing presented here, more facet-points could be distributed along the chord.
The second problem is that the warping displacement is a very small displacement in the range up to μm, which is partially lost in the measurement noise. It is therefore suggested to perform fundamental experiments with smaller measurement volumes on simple isotropic rectangular and open thin-walled beam cross-sections.

5 Conclusion and Outlook

Beam stiffness properties of rotor blades differ from the design values due to uncertainties in the manufacturing process and varying material properties but also because the structural model of current predesign methods often have an inaccurate level of detail.

In the first substantive chapter of this thesis, the parametric finite element preprocessor for slender fiber composite beam structure SONATA is described. The two-dimensional approach is based on the principle that the slender but inherently 3D problem can be separated into a linear 2D analysis and a nonlinear 1D beam analysis.
Leveraging the power of the seamlessly integrated CAD Kernel opencascade, the presented method is able to provide a rapid transition from and to commercial CAD systems. The generation of the internal cross-sectional topology was inspired by composite manufacturing processes, where layers are consecutively placed on top of each other to avoid complex boundary conditions and constraints and meet the interface requirements of a multidisciplinary rotor-blade design optimization framework while at the same time, enabling a detailed and realistic representation of the cross-sectional layup with many design freedoms not restricted to predefined topologies.
The discretization follows the same principle, using the layer structure of the generated topology to create a finite element representation through orthogonal projections and corner-style differentiation. Additional secondary structural elements such as trim masses can be sewn into this basic discretization by a layer preserving mapping algorithm. Applications of SONATA range from beams with simple geometries to sophisticated helicopter rotor blade cross-sections with multiple webs, trim masses, and an elaborate shafted spar structure to wind turbine rotor blade cross-sections with multiple shear webs, spar caps trailing edge filler, etc. At the same time, the computing time on a currently standard computer is only a few seconds for most applications. The use of SONATA in the development and design of the MERIT rotor blade has shown that the resulting structure of the manufactured rotor blade is very well reproduced (compare chapter 4) and most structural important properties are confidently predicted. To complete this development, mesh convergence as well as validation studies are performed for prismatic composite box beams and a generic wind turbine blade with both VABS and ANBA4.

The second main part of this work reaffirms the research hypothesis that improvements in numerical and experimental structural beam analysis methods are necessary for the development of helicopter rotor blades to be used in multidisciplinary optimizations. Studies of the effect of material and manufacturing uncertainties of a generic UH-60A composite rotor blade on beam properties, rotational natural frequencies, aeroelastic response, and vibration loads in hover and forward flight, provide the answers to this question.
Monte Carlo Simulations are used as a technical tool to perform two independent analyses on material and manufacturing uncertainties. The deterministic simulation model is executed in both cases with 1000 Latin Hypercube samples from normal distributions. It is based on a flexible multibody system analysis with DYMORE with a rotor model similar to the UH-60A main rotor. The baseline generic UH-60A composite rotor blade of the simulation model has a realistic internal fiber composite structure and the dynamic properties of this generic rotor correspond to a reasonable design with carefully placed natural frequencies with sufficient distance to the rotor harmonics at nominal rotor speed.
The results of the investigations showed that the variation resulting from the manufacturing tolerances and deviations in the material properties are of such magnitude that they cause the rotor system performance and vibratory hub loads to change significantly. This emphasizes the importance of accurate knowledge of the rotor blade beam characteristics, both by predicting the beam properties in predesign with sufficient accuracy and reasonable computational expenses and by measuring them with an experimental procedure that includes not only off-diagonal coupling relations but also non-uniformity along the span. The goal is reached when the remaining uncertainties no longer have a significant effect on the dynamic rotor behavior.

The third and last element of this work addresses the objective to apply, refine, and evaluated the strain-based measurement method by Sinotte and Bauchau to experimentally determine beam stiffness properties of the first rotor blade specifically developed for the Munich Experimental Rotor Investigation Testbed (MERIT). This hybrid method relies on the measurement of the strain field and combines it with a numerically determined warping field.
The details of the design and manufacturing of the rotor-blade specimen are described in the same way as the tests carried out to determine the material properties used. The test setup and the post-processing of the measurement data are also described in depth.
The strain field and deformations are measured using Digital Image Correlation (DIC), while a 6-axis load-cell monitored the linearly independent load cases. The data is combined during the evaluation of the governing equations with the warping field that was derived from a numerical analysis with ANBA4 with the previously generated SONATA model.
The results can be expressed in the following way: When comparing the experimental results and the prediction by the numerical model, the two bending and torsional stiffnesses have a deviation of under 10% and there is also a good agreement of the axial-stiffness and the position of the

tension center. For the helicopter engineer, these characteristics are among the most important properties when determining the dynamic behavior of the rotor. However, the transverse lag shear coefficients of the stiffness matrix deviate significantly from the predictions, so no final verdict can be made in this respect. For instance, the shear center determined by the model lies in front of the pitch axis, whereas the experiment determined it behind it. I consider this an incentive for further research.

To better evaluate the significance of the results, Monte Carlo simulations were performed on the effects of the uncertainties of the load cell and the DIC strain measurement. It became evident, that the accuracy of the load cell is decisive for the quality of the results with the lowest coefficients of variation for the lead-lag bending stiffness K_{66} and the highest for transverse shear coefficients.

Despite the fact that the material constitutive behavior, which is the basis for the numerical model, was determined experimentally and great care was taken to represent the numerical model accurately, some small and large differences were observed between the measured and numerical values. Large discrepancies were particularly evident in the transverse lag shear properties. These differences reveal a weakness in this inherently inverse hybrid methodology. Since the warping corrections are determined from a numerical model, the model itself must accurately represent the problem. If the results are different from the prediction, then the warping function will also be different. Following discussions with Wenbin Yu, highlighted that the key issue is to identify what is measured by experiments while not captured in the cross-sectional analysis, thus creating the difference between the measured and predicted results. It is suggested for future research to treat these factors as unknowns, using machine learning to determine these unknowns so that the measured and predicted differences can be minimized. Some of the fundamental ideas can be found in the following two publications [99], [100]. Further potential research in this area could also include and combine the information of both strain and global deformation of the rotor blade to produce a seamless as well as accurate stiffness property estimate.

Similarly, a second apparent weakness of the hybrid experimental approach is that in order to calculate nonuniform beam properties, a finite element model of each cross-section of interest is necessary. A fully experimental method should be developed in the future.
Using this strain-based approach, one could study how to extract the warping displacement field from the experimental DIC data as well. The governing equation chosen here describes the displacement as a superposition of the average sectional displacement of the rigid-section motion and the nodal warping. The experimental data of the DIC system consists of relative displacements in the differential neighborhood of the point of interest and provides both the strain information in the form of the material deformation gradient tensor as well as the general warping displacement. Problems and issues that can be addressed in future research include the separation of the nodal

displacements to extract the warping field. In particular, an appropriate choice of defining facet-point components can play a decisive role to extract the average sectional displacement. Because the warping displacement is very small, it is suggested to perform fundamental verification experiments with smaller measurement volumes on simple isotropic rectangular and open thin-walled cross-sections.

Bibliography

[1] AARONIA AG, *Technical Datasheet - Aaronia-Shield®, Rev 1.8-20.09.2016*, Sep. 2016.

[2] Adelman, H. M. and Mantay, W. R., "Integrated Multidisciplinary Optimization of Rotorcraft: A Plan for Development," NASA, Tech. Rep., 1989.

[3] *Aerospace series - Carbon fibre reinforced plastics - Unidirectional laminates, Tensile test parallel to the fibre direction*, DE, EN, Standard, Normenstelle Luftfahrt (NL), 1995.

[4] *Aerospace series - Carbon fibre reinforced plastics, unidirectional laminates - Tensile test perpendicular to the fibre direction*, DE, Berlin: Normenstelle Luftfahrt, 1998.

[5] Army Materiel Command, A. V., *Engineering Design Handbook - Helicopter Engineering, Part Two - Detail Design: (AMCP 706-202)*. Defense Technical Information Center.

[6] Atilgan, A. R. and Hodges, D. H., "Unified nonlinear analysis for nonhomogeneous anisotropic beams withclosed cross sections," *AIAA journal*, vol. 29, no. 11, pp. 1990–1999, 1991.

[7] Atilgan, A. R., Hodges, D. H., and Fulton, M. V., "Nonlinear deformation of composite beams: Unification of cross-sectional and elastic analyses," 1991.

[8] Bain, J. J., Sankar, L. N., Prasad, J. V. R., Bauchau, O. A., Peters, D. A., and He, C., "Computational Modeling of Variable-Droop Leading Edge in Forward Flight," *Journal of Aircraft*, vol. 46, no. 2, pp. 617–626, 2009.

[9] Bansemir, H., "Leichtbau im Hubschrauber - Unter Berücksichtigung Multifunktionaler Eigenschaften," *Themenheft Forschung - Leichtbau, Universität Stuttgart*, no. 3, pp. 22–31, 2007.

[10] Bauchau, O. A., *Flexible Multibody Dynamics*. Springer-Verlag GmbH, Oct. 23, 2010.

[11] Bauchau, O. A. "SectionBuilder User's Manual." EN. (2021), [Online]. Available: http://www.sectionbuilder.com/.

[12] Bauchau, O. A., Bottasso, C. L., and Nikishkov, Y. G., "Modeling Rotorcraft Dynamics With Finite Element Multibody Procedures," *Mathematical and Computer Modelling*, vol. 33, no. 10-11, pp. 1113–1137, May 2001.

[13] Bauchau, O. A. and Craig, J. I., *Structural Analysis - with Applications to Aerospace Structures*. Springer-Verlag GmbH, Aug. 3, 2009.

[14] Bauchau, O. A. and Han, S., "Three-Dimensional Beam Theory for Flexible Multibody Dynamics," *Journal of Computational and Nonlinear Dynamics*, vol. 9, no. 4, Jul. 2014.

[15] Bauchau, O. A. and Hodges, D. H., "Analysis of Nonlinear Multibody Systems with Elastic Couplings," *Multibody System Dynamics*, vol. 3, no. 2, pp. 163–188, 1999.

[16] Beer, S. M., "Uncertainty Quantification of Composite Rotor Blade Cross-Sections," Semester thesis, Technical University of Munich, 2019.

[17] Beran, P., Stanford, B., and Schrock, C., "Uncertainty Quantification in Aeroelasticity," *Annual review of fluid mechanics*, vol. 49, pp. 361–386, 2017.

[18] Berdichevski, V. L., "On the Energy of an Elastic Rod," *PMM*, vol. 45s, pp. 518 –529, 1982.

[19] Bernardini, G., Serafini, J., Enei, C., Mattioni, L., Ficuciello, C., and Vezzari, V., "Structural Characterization of Rotor Blades through Photogrammetry," *Measurement Science and Technology*, vol. 27, no. 6, p. 065 401, Apr. 2016.

[20] Bernhardt, J. P. "lamipy: Laminated composites engineering simulations in Python." (2017), [Online]. Available: https://github.com/joaopbernhardt/lamipy.

[21] Bielawa, R. L., *Rotary Wing Structural Dynamics and Aeroelasticity*. AIAA, 2006.

[22] Blasques, J. P. and Stolpe, M., "Multi-material topology optimization of laminated composite beam cross sections," *Journal of Composite Structures*, vol. 94, pp. 3278–3289, 2012.

[23] Blasques, J. P., "Multi-material topology optimization of laminated composite beams with eigenfrequency constraints," *Composite Structures*, vol. 111, no. Denmark, pp. 45–55, May 2013.

[24] Blaut, J., "Auslegung und Konstruktion eines verstellbaren Hubpropellers in Faserverbundbauweise für VTOL Fluggeräte," M.S. thesis, Technical University of Munich, 2018.

[25] Böhler Edelstahl GmbH & Co KG, *Technical Data Sheet - BÖHLER N352 Extra*, May 2018.

[26] Bouhaouel, F., "FMEA (Failure Mode and Effects Analysis) für strukturelle Faserverbundwerkstoff-Klebungen," Semster thesis, Technical University of Munich, 2016.

[27] Bousman, W. G., *Airfoil Dynamic Stall and Rotorcraft Maneuverability*. National Aeronautics and Space Administration, 1998.

[28] Bousman, W. G. and Kufeld, R. M., "UH-60A Airloads Catalog," 2015.

[29] Bowen-Davies, G. M., "Performance and Loads of Variable Top Speed Rotorcraft at High Advance Ratios," Ph.D. dissertation, University of Maryland, 2015.

[30] Brunton, S. L. and Kutz, J. N., *Data Driven Science and Engineering: Machine Learning, Dynamical Systems, and Control*. Cambridge University Press, 2019.

[31] CEN - European Committee for Standardization, *Aerospace series – Fibre reinforced plastics – Test method – Determination of in-plane shear properties (± 45° tensile test);* German and English version, 2015.

[32] Cesnik, C., Mok, J., Parikh, A., and Shin, S., "Optimum Design Framework for Integrally Twisted Helicopter Blades," in *45th AIAA/ASME/ASCE/AHS/ASC Structures, Structural Dynamics & Materials Conference*, American Institute of Aeronautics and Astronautics (AIAA), Apr. 2004.

[33] Cesnik, C. E. S. and Hodges, D. H., "VABS: A New Concept for Composite Rotor Blade Cross-Sectional Modeling," in *American Helicopter Society 51st Annual Forum*, 1995.

[34] Cesnik, C. E. S., Mok, J., Morillo, J. A., and Parikh, A. S., "Design Optimization of Active Twist Rotor Blades," in *30th European Rotorcraft Forum*, 2004.

[35] Chakravarty, U. K., "On the Modeling of Composite Beam Cross-sections," *Composites Part B: Engineering*, vol. 42, no. 4, pp. 982–991, 2011.

[36] Chakravarty, U. K., "Section Builder: A Finite Element Tool for Analysis and Design of Composite Beam Cross-sections," Ph.D. dissertation, Georgia Institute of Technology, 2008.

[37] Chandra, R. and Chopra, I., "Experimental and Theoretical Analysis of Composite I-beams with Elastic Couplings," *AIAA journal*, vol. 29, no. 12, pp. 2197–2206, 1991.

[38] Chatterjee, T., Essien, A., Ganguli, R., and Friswell, M. I., "The Stochastic Aeroelastic Response Analysis of Helicopter Rotors Using Deep and Shallow Machine Learning," *Neural Computing and Applications*, pp. 1–20, 2021.

[39] Chen, H. and Yu, W., *Manual of PreVABS*, Utah State University, Logan, Utah, 2008.

[40] Chen, H., Yu, W., and Capellaro, M., "A Critical Assessment of Computer Tools for Calculating Composite Wind Turbine Blade Properties," 6, vol. 13, Wiley Online Library, 2010, pp. 497–516.

[41] Cornette, D., Kerdreux, B., Michon, G., and Gourinat, Y., "Aeroelastic tailoring of helicopter blades," *Journal of Computational and Nonlinear Dynamics*, vol. 10, no. 6, 2015.

[42] Datta, A. and Johnson, W., "Three-Dimensional Finite Element Formulation and Scalable Domain Decomposition for High-Fidelity Rotor Dynamic Analysis," *Journal of the American Helicopter Society*, 2011.

[43] Davis, S. J., "Predesign Study For a Modern 4-Bladed Rotor for the RSRA," NASA, Tech. Rep. 16155, Mar. 1981.

[44] Drechsler, K., *Konstruktion von composite-strukturen mit catia v5*, Vorlesungsskriptum, 2013.

[45] Eckart, C. and Young, G., "The Approximation of One Matrix by Another of Lower Rank," *Psychometrika*, vol. 1, no. 3, pp. 211–218, 1936.

[46] Enei, C., Bernardini, G., Serafini, J., Mattioni, L., Ficuciello, C., and Vezzari, V., "Photogrammetric Detection Technique for Rotor Blades Structural Characterization," *Journal of Physics: Conference Series*, vol. 658, p. 012 003, Nov. 2015.

[47] Evonik, *Product Information - Rohacell® RIMA*, Mar. 2020.

[48] Feil, R., Pflumm, T., Bortolotti, P., and Morandini, M., "A Cross-sectional Aeroelastic Analysis and Structural Optimization Tool for Slender Composite Structures," *Composite Structures*, vol. 253, p. 112 755, Dec. 2020.

[49] Friedmann, P. P., "Helicopter Vibration Reduction Using Structural Optimization with Aeroelastic/multidisciplinary Constraints - A Survey," *Journal of Aircraft*, vol. 28, no. 1, pp. 8–21, Jan. 1991.

[50] Fuhrmann, S., "Parametrische Modellierung von Hubschrauber Rotorblattquerschnitten," Bachelor's thesis, Technical University of Munich, 2016.

[51] Gaertner, E., Rinker, J., Sethuraman, L., *et al.*, "Definition of the IEA 15 MW Offshore Reference Wind Turbine," International Energy Agency, Tech. Rep. NREL/TP-75698, 2020.

[52] Garre, W., Amri, H., Pflumm, T., Paschinger, P., Mileti, M., Hajek, M., and Weigand, M., "Helicopter Configurations and Drive Train Concepts For Optimal Variable Rotor-Speed Utilization," in *Deutscher Luft- und Raumfahrtkongress, Braunschweig, Germany*, Sep. 2016.

[53] Garre, W., Pflumm, T., and Hajek, M., "Enhanced Efficiency And Flight Envelope by Variable Main Rotor Speed For Different Helicopter Configurations," in *42nd European Rotorcraft Forum, Lille, France*, Sep. 2016.

[54] Gaugelhofer, L., "Hybrid Experimental Measurement of Sectional Stiffness Properties of a Composite Rotor Blade with Digital Image Correlation," M.S. thesis, Technical University of Munich, Nov. 2020.

[55] Geuzaine, C. and Remacle, J.-F., "Gmsh: A 3-D finite element mesh generator with built-in pre-and post-processing facilities," *International Journal for Numerical Methods in Engineering*, vol. 79, no. 11, pp. 1309–1331, 2009.

[56] Giavotto, V., Borri, M., Mantegazza, P., Ghiringhelli, G., Carmaschi, V., Maffioli, G. C., and Mussi, F., "Anisotropic beam theory and applications," *Computers & Structures*, vol. 16, no. 1-4, pp. 403–413, Jan. 1983.

[57] GOM GmbH, *GOM Testing - Digital Image Correlation and Strain Computation Basics*, GOM GmbH, Braunschweig, 2020.

[58] Graf, S., "Mission and Performance Analysis of Landing Gears for the Helicopter EC135," Semester thesis, Technical University of Munich, 2019.

[59] Gray, J. S., Hwang, J. T., Martins, J. R. R. A., Moore, K. T., and Naylor, B. A., "OpenMDAO: An Open-Source Framework for Multidisciplinary Design, Analysis, and Optimization," *Structural and Multidisciplinary Optimization*, vol. 59, pp. 1075–1104, 4 2019.

[60] Gunduz, M. E., "Software Integration for Automated Stability Analysis and Design Optimization of a Bearingless Rotor Blade," Ph.D. dissertation, Georgia Institute of Technology, 2010.

[61] Hajek, M., Manner, S., and Suesse, S., "Blade Root Integrated Fiber Bragg Grating Sensors-A Highly Redundant Data Source For Future HUMS," in *Annual Forum Proceedings-AHS International*, 2015.

[62] Hamade, K. S. and Kufeld, R. M., *Modal Analysis of UH-60A Instrumented Rotor Blades* (NASA Technical Memorandum). National Aeronautics, Space Administration, Office of Management, Scientific, and Technical Information Division, 1990.

[63] Han, S. and Bauchau, O. A., "Nonlinear three-dimensional beam theory for flexible multibody dynamics," *Multibody System Dynamics*, vol. 34, no. 3, pp. 211–242, Oct. 2014.

[64] Han, S. and Bauchau, O. A., "On Saint-Venant's Problem for Helicoidal Beams," *Journal of Applied Mechanics*, vol. 83, no. 2, pp. 021 009–021 009, Dec. 2015.

[65] Henschel, K. A., "Biocomposites in Aviation Structures on the Example of Flax and its Hybrids," Dissertation, Technical University of Munich, München, 2019.

[66] Heuschneider, V., Berghammer, F., and Hajek, M., "Numerical and Experimental Study on the Modal Characteristics of a Rotor Test Rig," in *Topics in Modal Analysis & Testing, Volume 8*, Dilworth, B. and Mains, M., Eds., Cham: Springer International Publishing, 2021, pp. 315–321.

[67] Heuschneider, V., Berghammer, F., Pflumm, T., and Hajek, M., "Development and Initial Hover Testing of the Mach Scaled Rotor Test Rig MERIT," in *47th European Rotorcraft Forum, United Kingdom*, 2021.

[68] Ho, J., Yu, W., and Hodges, D., "Energy Transformation to Generalized Timoshenko Form by the Variational Asymptotic Beam Sectional Analysis.," in *51st AIAA/ASME/ASCE/AHS/ASC Structures, Structural Dynamics, and Materials Conference, Orlando, Florida*, 2010.

[69] Ho, J. C., Yeo, H., and Ormiston, R. A., "Investigation of Rotor Blade Structural Dynamics and Modeling Based on Measured Airloads," *Journal of Aircraft*, vol. 45, no. 5, pp. 1631–1642, 2008.

[70] Hodges, D. H., *Nonlinear Composite Beam Theory*. American Institute of Aeronautics and Astronautics, 2006.

[71] Hodges, D. H., Atilgan, A. R., Cesnik, C. E. S., and Fulton, M. V., "On a simplified strain energy function for geometrically nonlinear behaviour of anisotropic beams," *Composites Engineering*, vol. 2, no. 5, pp. 513–526, 1992, Use of Composites in Rotorcraft and Smart Structures.

[72] Howlett, J. J., "UH-60A Black Hawk Engineering Simulation Program. Volume 1: Mathematical Model," NASA, Tech. Rep., 1981.

[73] Hu, T., "A Validation and Comparison About VABS-IDE and VABS-GUI," M.S. thesis, Utah State University, 2012.

[74] Hwang, H. J., Ahn, J. H., Chang, S., Jung, S. N., Kalow, S., and Keimer, R., "Digital Twin Approach for Structural Property Evaluation of Next Generation Active Twist Blades," in *Vertical Flight Society 76th Annual Forum*, 2020.

[75] Jaksch, C., "Experimentelle Bestimmung der strukturellen Rotorblatteigenschaften eines koaxialen Ultraleichthubschraubers," Semester thesis, Technical University of Munich, 2015.

[76] Johnson, W., "A History of Rotorcraft Comprehensive Analyses," in *American Helicopter Society 60th Annual Forum*, 2013.

[77] Jung, S. N., You, Y. H., Dhadwal, M. K., Hagerty, B. P., Riemenschneider, J., and Keimer, R., "Blade property measurement and its assessment on air/structural loads of HART II rotor," in *70th Annual Forum. American Helicopter Society*, 2014.

[78] Jung, S. N. and Lau, B. H., "Determination of HART I Blade Structural Properties by Laboratory Testing," NASA, Tech. Rep. NASA/CR–2012-216039, 2012.

[79] Jung, S. N., You, Y. H., Lau, B. H., Johnson, W., and Lim, J. W., "Evaluation of Rotor Structural and Aerodynamic Loads Using Measured Blade Properties," *Journal of the American Helicopter Society*, vol. 58, no. 4, 1–12, Oct. 2013.

[80] Jung, S. N., Nagaraj, V., and Chopra, I., "Assessment of composite rotor blade modeling techniques," *Journal of the American Helicopter Society*, vol. 44, no. 3, pp. 188–205, 1999.

[81] Kallähn, F., "Integrationsstudie einer Enteisungsanlage in ein Rotorblatt für einen modularen lagerlosen Hauptrotor," Master's thesis, Technical University of Munich, 2016.

[82] Kerrick, D. "From Wood to Composite Materials - The Evolution of the Rotor Blade." EN, Helicopter Maintenance Magazine. (Jan. 2011), [Online]. Available: https://helicoptermaintenancemagazine.com/article/wood-composite-materials-evolution-rotor-blade.

[83] Königsberger, R., "Analysis of Ice Accretion and Strategies of Ice Protection for a Helicopter Main Rotor Blade," Semester thesis, Technical University of Munich, 2016.

[84] Ku, J., Volovoi, V., and Hodges, D., "Multilevel-Multiphase Optimization of Composite Rotor Blade with Surrogate Model," in *48th AIAA/ASME/ASCE/AHS/ASC Structures, Structural Dynamics, and Materials Conference*, 2007, p. 1900.

[85] Kumar, D. and Cesnik, C. E., "New Hybrid Optimization for Design of Active Twist Rotors," in *54th AIAA/ASME/ASCE/AHS/ASC Structures, Structural Dynamics, and Materials Conference*, American Institute of Aeronautics and Astronautics (AIAA), Apr. 2013.

[86] Kumar, D. and Cesnik, C. E. S., "Optimization Framework for the Dynamic Analysis and Design of Active Twist Rotors," in *American Helicopter Society 68th Annual Forum*, 2012.

[87] Kuntze-Fechner, G., *Design Guide for Static Balancing Devices of Rotor Blades*. Airbus Helicopter, 2014.

[88] Kuntze-Fechner, G., *Einführung in die Hubschraubertechnik*. Eurocopter Deutschland GmbH, 2004.

[89] Langer, S., "Machbarkeitsstudie einer Fenestron®-Nabe aus Faserverbundwerkstoffen für einen mittelschweren Hubschrauber," M.S. thesis, Technical University of Munich, 2016.

[90] Lee, D. and Hodges, D. H., "Multi-Flexible-Body Analysis for Application to Wind Turbine Control Design: September 10, 1999 – October 31, 2003," *Tech. rep., NREL Report*, Sep. 2004.

[91] Leishman, J. G., "State-space model for unsteady airfoil behavior and dynamic stall," *30th Structures, Structural Dynamics and Materials Conference*, 1989.

[92] Leishman, J., *Principles of Helicopter Aerodynamics* (Cambridge Aerospace Series). Cambridge University Press, 2006.

[93] Li, L., Volovoi, V. V., and Hodges, D. H., "Cross-sectional Design of Composite Rotor Blades Considering Manufacturing Constraints," in *American Helicopter Society 63rd Annual Forum*, American Helicopter Society, May 2007.

[94] Li, L., "Structural Design of Composite Rotor Blades with Consideration of Manufacturability, Durability, and Manufacturing Uncertainties," Ph.D. dissertation, Georgia Institute of Technology, Aug. 2008.

[95] Li, L., Volovoi, V., and Hodges, D., "Probabilistic Design Optimization of Composite Rotor Blades," in *49th AIAA/ASME/ASCE/AHS/ASC Structures, Structural Dynamics, and Materials Conference; 16th AIAA/ASME/AHS Adaptive Structures Conference;*, American Institute of Aeronautics and Astronautics, Apr. 2008.

[96] Li, L., Volovoi, V. V., and Hodges, D. H., "Cross-Sectional Design of Composite Rotor Blades," in *American Helicopter Society 63rd Annual Forum*, 2007.

[97] Lim, J., Shin, S., and Kee, Y., "Optimization of Rotor Structural Design in Compound Rotorcraft with Lift Offset," *Journal of the American Helicopter Society*, vol. 61, no. 1, pp. 1–14, Jan. 2016.

[98] Lin, H., Brown, L. P., and Long, A. C., "Modelling and Simulating Textile Structures Using TexGen," in *Advances in Textile Engineering*, ser. Advanced Materials Research, vol. 331, Trans Tech Publications Ltd, Oct. 2011, pp. 44–47.

[99] Liu, X., Tao, F., Du, H., Yu, W., and Xu, K., "Learning Nonlinear Constitutive Laws Using Neural Network Models Based on Indirectly Measurable Data," *Journal of Applied Mechanics*, vol. 87, no. 8, May 2020, 081003.

[100] Liu, X., Tao, F., and Yu, W., "A Neural Network Enhanced System for Learning Nonlinear Constitutive Law and Failure Initiation Criterion of Composites Using Indirectly Measurable Data," *Composite Structures*, vol. 252, p. 112 658, 2020.

[101] Liu, X. and Yu, W., *TexGen4SC*, Sep. 2016.

[102] *Lochleibungsproben programm 5, edm-aerotec gmbh,* 2013.

[103] Löffler, P., "Faltkonzepte für einen modularen lagerlosen 5-Blatt Hauptrotor," M.S. thesis, Technical University of Munich, 2018.

[104] Lynch, C. E., *Advanced CFD Methods for Wind Turbine Analysis*. Georgia Institute of Technology, 2011.

[105] Mack, M. D., "Konstruktive auslegung eines hauptrotorblattes für einen modernen ultraleichtkleinhubschrauber und herstellung einer prototypenkomponente," Diplomarbeit, Hochschule München, edm-aerotec GmbH, 2011.

[106] McAlister, K., Pucci, S., McCroskey, W., and Carr, L., *An Experimental Study of Dynamic Stall on Advanced Airfoil Sections. Volume 2. Pressure and Force Data*. Defense Technical Information Center, 1982.

[107] Mccroskey, W., *An experimental study of dynamic stall on advanced airfoil sections. Volume 1: Summary of the experiment*. Defense Technical Information Center, 1982.

[108] Mccroskey, W., *The phenomenon of dynamic stall*. Defense Technical Information Center, 1981.

[109] *Mechanical vibration - Rotor balancing - Part 11: Procedures and tolerances for rotors with rigid behaviour (ISO 21940-11:2016)*, DIN Deutsches Institut für Normung e. V., 2017.

[110] Mendoza, N. R., Feil, R., Johnson, N., and Anderson, B., "Conceptual Designs of the Structure of Inflatable Blades for Enabling Larger Turbines," in *AIAA Scitech 2021 Forum*.

[111] ME-Meßsysteme GmbH, *Calibration Certificate 20562699-1 - K6D130 5kN/500Nm SN:17402398*, Sep. 2020.

[112] ME-Meßsysteme GmbH, *Technical Datasheet - 6-Axis Force Sensor K6D130 5kN/500Nm/MP11*, May 2021.

[113] Meyn, L., "Rotorcraft Optimization Tools: Incorporating Rotorcraft Design Codes into Multi-Disciplinary Design, Analysis, and Optimization," in *AHS Specialists Conference on Aeromechanics Design for Transformative Vertical Flight*, San Francisco, California: AHS, Jan. 2018.

[114] Mok, J. W., "Design Optimization for Active Twist Rotor Blades.," Ph.D. dissertation, University of Michigan, 2010.

[115] Morandini, M., Chierichetti, M., and Mantegazza, P., "Characteristic behavior of prismatic anisotropic beam via generalized eigenvectors," *International Journal of Solids and Structures*, vol. 47, no. 10, pp. 1327–1337, May 2010.

[116] Murugan, S., Ganguli, R., and Harursampath, D., "Aeroelastic Response of Composite Helicopter Rotor with Random Material Properties," *Journal of Aircraft*, vol. 45, no. 1, pp. 306–322, 2008.

[117] Murugan, S., Harursampath, D., and Ganguli, R., "Material Uncertainty Propagation in Helicopter Nonlinear Aeroelastic Response and Vibratory Analysis," *AIAA Journal*, vol. 46, no. 9, pp. 2332–2344, Sep. 2008.

[118] Murugan, S., Ganguli, R., and Harursampath, D. K., "Stochastic Aeroelastic Analysis of Composite Helicopter Rotor," *Journal of the American Helicopter Society*, vol. 56, no. 1, pp. 12 001–1 200 113, Jan. 2011.

[119] Norman, T., Shinoda, P. M., Kitaplioglu, C., Jacklin, S., and Sheikman, A., "Low-Speed Wind Tunnel Investigation of a Full-Scale UH-60 Rotor System," in *American Helicopter Society 58th Annual Forum*, 2002.

[120] Oliver Olivella, X. and Agelet de Saracibar Bosch, C., *Continuum Mechanics for Engineers. Theory and Problems*. 2017.

[121] Onkar, A. K., Upadhyay, C. S., and Yadav, D., "Stochastic finite element buckling analysis of laminated plates with circular cutout under uniaxial compression," *Journal of applied mechanics*, vol. 74, no. 4, pp. 798–809, 2007.

[122] Pancar, E., "Performance Analysis of a Coaxial and Compound Helicopter with Variable Rotor Speed," Bachelor's Thesis, Technical University of Munich, 2016.

[123] Park, J.-S., Jung, S. N., Park, S. H., and Yu, Y. H., "Correlation Study of a Rotor in Descending Flight Using DYMORE with a Freewake Model," *Journal of Mechanical Science and Technology*, vol. 24, no. 8, pp. 1583–1594, 2010.

[124] Paviot, T., *pythonOCC, 3D CAD/CAE/PLM development framework for the Python programming language, http://www.pythonocc.org/*.

[125] Pawar, P. M. and Jung, S. N., "Active Twist Control Methodology for Vibration Reduction of a Helicopter with Dissimilar Rotor System," *Smart materials and structures*, vol. 18, no. 3, p. 035 013, 2009.

[126] Pettit, C. L., "Uncertainty Quantification in Aeroelasticity: Recent Results and Research Challenges," *Journal of Aircraft*, vol. 41, no. 5, pp. 1217–1229, 2004.

[127] Pflumm, T., "Auslegung und Konstruktion eines Hauptrotorblattes für ein in extremen Flughöhen operierendes Drehflügel-UAV," M.S. thesis, Technical University of Munich, 2015.

[128] Pflumm, T., Barth, A., Kondak, K., and Hajek, M., "Auslegung und Konstruktion eines Hauptrotorblattes für ein in extremen Flughöhen operierendes Drehflügel-UAV," de, in *Deutscher Luft- und Raumfahrtkongress, Rostock*, Rostock, 2015.

[129] Pflumm, T., Garre, W., and Hajek, M., "A Preprocessor for Parametric Composite Rotor Blade Cross-Sections," in *44th European Rotorcraft Forum, Delft, The Netherlands*, Sep. 2018.

[130] Pflumm, T., Gaugelhofer, L., Heuschneider, V., Berghammer, F., and Hajek, M., "Hybrid Experimental Measurement of Sectional Stiffness Properties of the MERIT Rotor Blade with Digital Image Correlation," in *47th European Rotorcraft Forum, United Kingdom*, 2021.

[131] Pflumm, T. and Rex, W., "Entwicklung eines drehzahlvariablen Rotorsystems : LUFO-V-2 Schlussbericht : TUM-HT-3-2019 : Abschlussbericht : VARI-SPEED," Technische Universität München TiB Hannover, Germany, Tech. Rep., 2019.

[132] Pflumm, T., Willem, Rex, and Hajek, M., "Propagation of Material and Manufacturing Uncertainties in Composite Helicopter Rotor Blades," in *45th European Rotorcraft Forum, Warsaw, Poland*, 2019.

[133] Piet, E., "Structural Evaluation and Optimization of the AREA Rotor Blade," Semester thesis, Technical University of Munich, 2018.

[134] *Plastics - Determination of tensile properties - Part4: Test conditions for isotropic and anisotropic fibre-reinforced plastic composites*, CEN -European Committee for Standardization, 1997.

[135] Popescu, B. and Hodges, D. H., "On asymptotically correct Timoshenko-like anisotropic beam theory," *International Journal of Solids and Structures*, vol. 37, no. 3, pp. 535–558, 2000.

[136] Rabbott Jr, J. P., Paglino, V. M., and Lizak, A. A., "A Presentation of Measured and Calculated Full-scale Rotor Blade Aerodynamic and Structural Loads," United Technologies Corp, Stratford CT, Sikorsky Aircraft Div., Tech. Rep., 1966.

[137] Rex, W., Pflumm, T., and Hajek, M., "UH-60A Rotor and Coupled Rotor-Fuselage Simulation Framework Validation and Analysis," in *45th European Rotorcraft Forum, Warsaw, Poland*, 2019.

[138] Roget, B., "Simulation of Active Twist and Active Flap Control on a Model-Scale Helicopter Rotor," in *24th AIAA Applied Aerodynamics Conference*, 2006, p. 3473.

[139] Roget, B. and Chopra, I., "Individual Blade Control Methodology for a Rotor with Dissimilar Blades," *Journal of the American Helicopter Society*, vol. 48, no. 3, pp. 176–185, 2003.

[140] Rohl, P. J., Kumar, D., Dorman, P., Sutton, M., and Cesnik, C. E. S., "A Composite Rotor Blade Structural Design Environment for Aeromechanical Assessments in Conceptual and Preliminary Design," in *American Helicopter Society 68th Annual Forum*, American Helicopter Society, 2012.

[141] Rohl, P. J., Cesnik, C. E. S., Dorman, P., and Kumar, D., "IXGEN - A Modeling Tool for the Preliminary Design of Composite Rotor Blades," in *AHS Future Vertical Lift Design Conference*, 2012.

[142] Roth, N., "Konzept und Konstruktion einer Auswuchtvorrichtung für Rotorblätter des Experimentellen Rotorprüfstandes MERIT," Bachelor's Thesis, Technical University of Munich, 2020.

[143] Samni, E. and Sabra, R. "Dealing with B-splines in OpenCASCADE." EN. (Jan. 2021), [Online]. Available: https://www.linkedin.com/pulse/dealing-b-splines-opencascade-rashed-sabra.

[144] Saunders, C., "Validating the SONATA mesh pre-processor, and programming an optimization program to determine the design variables of a box beam," Practical Research Experience, Technical University of Munich and University of Alberta, 2017.

[145] Schicker, D. E., "Numerische Optimierung der aerodynamischen Eigenschaften drehzahlgesteuerter Propeller für Multicopter," Dissertation, Technische Universität München, München, 2019.

[146] Schmalfuß, S., "Mechanische Prüfverfahren zur strukturellen Hautreparatur am H135 Hauptrotorblatt," Semester thesis, Technical University of Munich, 2018.

[147] Schöner, M., "Conceptual Design and Optimization of a Deicing System for Small- and Medium-Sized Helicopters," M.S. thesis, Technical University of Munich, 2018.

[148] Schulz, M., Opitz, S., and Riemenschneider, J., "A new concept to determine the mass distribution of an active twist rotor blade," *CEAS Aeronautical Journal*, vol. 3, no. 2-4, pp. 117–123, Apr. 2012.

[149] Schürmann, H., *Konstruieren mit Faser-Kunststoff-Verbunden*. Springer, 2005.

[150] Schwingshackl, C., Aglietti, G., and Cunningham, P., "Determination of honeycomb material properties: Existing theories and an alternative dynamic approach," *Journal of Aerospace Engineering*, vol. 19, no. 3, pp. 177–183, 2006.

[151] SGL Carbon SE, *Product Data Sheet (PDS) - SIGRAPREG® C U600-0/SD-E501/33%*, May 2018.

[152] SGL Carbon SE, *Product Data Sheet (PDS) - SIGRAPREG® C W200 TW2/2 E503/45%*, May 2018.

[153] SGL Carbon SE, *Technical Data Sheet (TDS) - SIGRAPREG® C U600-0/SD-E501/33%*, May 2018.

[154] SGL Carbon SE, *Technical Data Sheet (TDS) - SIGRAPREG® C W200 TW2/2 E503/45%*, May 2018.

[155] Shen, J., Roget, B., Masarati, P., Piatak, D., Singleton, J., and Nixon, M., "Modeling a Stiff-Inplane Tiltrotor Using Two Multibody Analyses: A Validation Study," in *Proceedings of the 64th American Helicopter Society Forum*, Citeseer, vol. 64, 2008, p. 2307.

[156] Shewchuk, J. R., "Triangle: Engineering a 2D quality mesh generator and Delaunay triangulator," in *Applied Computational Geometry Towards Geometric Engineering*, Lin, M. C. and Manocha, D., Eds., Berlin, Heidelberg: Springer Berlin Heidelberg, 1996, pp. 203–222.

[157] Shin, S.-J., Cesnik, C. E. S., and Hall, S. R., "Design and Simulation of Integral Twist Control for Helicopter Vibration Reduction," *International Journal of Control, Automation, and Systems*, vol. 5, no. 1, pp. 24–34, 2007.

[158] Silva, C. and Johnson, W., "Multidisciplinary Conceptual Design for Reduced-Emission Rotorcraft," in *AHS Specialists Conference on Aeromechanics Design for Transformative Vertical Flight*, San Francisco, California: AHS, Jan. 2018.

[159] Sinotte, T. M., "A Strain-Based Experimental Methodology for Measuring Sectional Stiffness Properties of Composite Blades," Ph.D. dissertation, University of Maryland, 2020.

[160] Sinotte, T. M. and Bauchau, O. A., "Experimental Measurement of Sectional Stiffness Properties of Composite Rotor Blades," in *Vertical Flight Society 76th Annual Forum*, 2020.

[161] Sinotte, T. M. and Bauchau, O. A., "Novel Approach for Experimental Measurement of Sectional Stiffness Properties of Composite Rotor Blades," in *45th European Rotorcraft Forum, Warsaw, Poland*, 2019.

[162] Sitaraman, J. and Roget, B., "Prediction of Helicopter Maneuver Loads Using a Fluid-Structure Analysis," *Journal of Aircraft*, vol. 46, no. 5, pp. 1770–1784, 2009.

[163] Sixt, H., "Effekt- und Anforderungsanalyse eines Hubschrauber Hauptrotorsystem für den Einsatz bei variabler Drehzahl," Semester thesis, Technical University of Munich, 2016.

[164] Skjoldan, P. F. and Bauchau, O. A., "Determination of Modal Parameters in Complex Nonlinear Systems," *Journal of Computational and Nonlinear Dynamics*, 2011.

[165] Sobieszczanski-Sobieski, J., Morris, A., Tooren, M. J. L. van, Rocca, G. L., and Yao, W., *Multidisciplinary Design Optimization Supported by Knowledge Based Engineering*, 1st Edition. John Wiley & Sons, Ltd., Sep. 28, 2015, 388 pp.

[166] Suesse, S. and Hajek, M., "Rotor Blade Displacement and Load Estimation with Fiber-Optical Sensors for a Future Health and Usage Monitoring System," in *American Helicopter Society 74th Annual Forum*, 2018.

[167] Tarzanin, F. and Young, D., "Boeing rotorcraft experience with rotor design and optimization," in *7th AIAA/USAF/NASA/ISSMO Symp. Multidiscip. Anal. Optim.*, Reston, Virigina: American Institute of Aeronautics and Astronautics, Sep. 1998.

[168] Tian, S., Liu, X., Du, H., and Yu, W., *PreVABS Documentation - Version 1.3.0*, Feb. 2021.

[169] Tian, S., Liu, X., and Yu, W., *PreVABS, https://cdmhub.org/resources/1597*, Nov. 2017.

[170] Vogl, J., "Konstruktive Auslegung eines 2-Blatt Heckrotorsystem für einen modernen Ultraleicht-Keinhubschrauber und Entwurf eines lagerlosen Heckrotorsystems," Diplomarbeit, Hochschule München, edm-aerotec GmbH, 2012.

[171] Wall, B. G. van der, *Grundlagen der Hubschrauber-Aerodynamik*. Springer, 2015.

[172] Wanhill, R. J. H., Symonds, N., Merati, A., Pasang, T., and Lynch, S. P., "Five helicopter accidents with evidence of material and/or design deficiencies," *Engineering Failure Analysis*, vol. 35, pp. 133–146, 2013, Special issue on ICEFA V- Part 1.

[173] Weller, W. H. and Davis, M. W., "Wind Tunnel Tests of Helicopter Blade Designs Optimized for Minimum Vibration," in *American Helicopter Society 44th Annual Forum*, 1988.

[174] Wirth, D. and Hajek, M., "Probabilistic Methodology for Multi-Fidelity Model-Based Robust Preliminary Design of Rotorcraft," in *American Helicopter Society 3rd Annual Forum*, 2017.

[175] Yeo, H., "Assessment of 1-D Versus 3-D Methods for Modeling Rotor Blade Structural Dynamics," in *51st AIAA/ASME/ASCE/AHS/ASC Structures, Structural Dynamics, and Materials Conference*, 2010.

[176] You, Y. H., Jung, S. N., Pawar, P. M., and Shin, E. S., "Effect of Uncertainty on Hub Vibration Response of Composite Helicopter Rotor Blades," *Journal of aircraft*, vol. 47, no. 1, pp. 151–160, 2010.

[177] Yu, W., Hodges, D. H., and Ho, J. C., "Variational Asymptotic Beam Sectional Analysis – an Updated Version," *Journal of Engineering Science*, vol. 59, pp. 40–64, 2012.

[178] Yu, W., *VABS Manual for Users*, Analyswift, West Lafayette, IN 47906 USA.

[179] Yu, W., Hodges, D., Volovoi, V., and Cesnik, C., "Timoshenko-like Modeling of Initially Curved and Twisted Composite Beams with Oblique Cross Sections," in *41st Structures, Structural Dynamics, and Materials Conference and Exhibit*, 2000, p. 1405.

[180] Yu, W., Hodges, D. H., Volovoi, V., and Cesnik, C. E. S., "On Timoshenko-like Modeling of Initially Curved and Twisted Composite Beams," *International Journal of Solids and Structures*, vol. 39, no. 19, pp. 5101–5121, 2002.

[181] Yu, W. and Liu, X., *SwiftComp*, Jan. 2017.

[182] Yu, W., Volovoi, V., Hodges, D. H., and Hong, X., "Validation of the variational asymptotic beam sectional analysis," *AIAA Journal*, vol. 40, no. 10, pp. 2105–2112, Jan. 2002.

[183] Zhu, W. and Morandini, M., "Multiphysics cross-section analysis of smart beams," *Mechanics of Advanced Materials and Structures*, pp. 1–18, Mar. 2020.

Prior Publications by the Author

ERF2021B Heuschneider, V., Berghammer, F., Pflumm, T., and Hajek, M.: "Development and Initial Hover Testing of the Mach Scaled Rotor Test Rig MERIT", 47th European Rotorcraft Forum, United Kingdom, Virtual, 2021. Reference: [67]

ERF2021A Pflumm, T., Gaugelhofer, L., Heuschneider, V., Berghammer, F., and Hajek, M.: "Hybrid Experimental Measurement of Sectional Stiffness Properties of the MERIT Rotor Blade with Digital Image Correlation", 47th European Rotorcraft Forum, United Kingdom, 2021. Reference: [130]

COMPSTRUC2020 Feil, R., Pflumm, T., Bortolotti, P, Morandini, M.: "A Cross-Sectional Aeroelastic Analysis and Structural Optimization Tool for Slender Composite Structures", 2020, Composite Structures. 253. 112755. Reference: [48]

VARISPEED2019 Pflumm, T., Rex, W.: "Entwicklung eines drehzahlvariablen Rotorsystems : LUFO-V-2 Schlussbericht : TUM-HT-3-2019 : Abschlussbericht : VARISPEED", Technische Universität München, TiB Hannover, Germany, 2019. Reference: [131]

ERF2019B Rex, W., Pflumm, T., Hajek, M.: "UH-60A Rotor and Coupled Rotor-Fuselage Simulation Framework Validation and Analysis", 45th European Rotorcraft Forum, Warsaw, Poland, 2019. Reference: [137]

ERF2019A Pflumm, T., Rex, W., Hajek, M.: "Propagation of Material and Manufacturing Uncertainties in Composite Helicopter Rotor Blades", 45th European Rotorcraft Forum, Warsaw, Poland, 2019. Reference: [132]

ERF2018 Pflumm, T., Garre, W., Hajek, M.: "A Preprocessor for Parametric Composite Rotor Blade Cross-Sections", 44th European Rotorcraft Forum, Delft, The Netherlands, 2018. Reference: [129]

DLRK2016 Garre, W., Amri, H., Pflumm, T., Paschinger, P., Marco, M., Hajek, M., Weigand M.: "Helicopter Configurations and Drive Train Concepts For Optimal Variable Rotor-Speed Utilization", Deutscher Luft- und Raumfahrtkongress, Braunschweig, Germany, 2016. Reference: [52]

ERF2016 Garre, W., Pflumm, T., Hajek, M.: "Enhanced efficiency and flight envelope by variable main rotor speed for different helicopter configurations", 42nd European Rotorcraft Forum, Lille, France, 2016. Reference: [53]

DLRK2015 Pflumm, T., Barth, A., Kondak, K., Hajek, M.: "Auslegung und Konstruktion eines Hauptrotorblattes für ein in extremen Flughöhen operierendes Drehflügel-UAV", Deutscher Luft- und Raumfahrtkongress, Rostock, Germany, 2015. [128]

Students Theses Guided by the Author

PANCAR2016 Pancar, E., "Performance Analysis of a Coaxial and Compound Helicopter with Variable Rotor Speed", Bachelor's Thesis, Technical University of Munich, 2016. Reference: [122]

LANGER2016 Langer, S., "Machbarkeitsstudie einer Fenestron®-Nabe aus Faserverbundwerkstoffen für einenmittelschweren Hubschrauber", Master's thesis, Technical University of Munich, 2016. Reference: [89]

KOENIGSB.2016 Königsberger, R., "Analysis of Ice Accretion and Strategies of Ice Protection for a Helicopter Main Rotor Blade", Semester thesis, Technical University of Munich, 2016. Reference: [83]

FUHRMANN2016 Fuhrmann, S., "Parametrische Modellierung von Hubschrauber Rotorblattquerschnitten", Bachelor's thesis, Technical University of Munich, 2016. Reference: [50]

KALLAEHN2016 Kallähn, F., "Integrationsstudie einer Enteisungsanlage in ein Rotorblatt für einen modularen lagerlosen Hauptrotor" Master's thesis, Technical University of Munich, 2016. Reference: [81]

BOUHAOUEL2016 Bouhaouel, F., "FMEA (Failure Mode and Effects Analysis) für strukturelle Faserverbundwerkstoff Klebungen", Semster thesis, Technical University of Munich, 2016. Reference: [26]

SIXT2016 Sixt, H., "Effekt- und Anforderungsanalyse eines Hubschrauber Hauptrotorsystem für den Einsatz bei variabler Drehzahl", Semester thesis, Technical University of Munich, 2016. Reference: [163]

SAUNDERS2017 Saunders, C., "Validating the SONATA mesh pre-processor, and programming an optimization program to determine the design variables of a box beam", Practical Research Experience, Technical University of Munich and University of Alberta, 2017. Reference: [144]

SCHMALF.2018 Schmalfuß, S., "Mechanische Prüfverfahren zur strukturellen Hautreparatur am H135 Hauptrotorblatt", Semester thesis, Technical University of Munich, 2018. Reference: [146]

SCHOENER2018 Schöner, M., "Conceptual Design and Optimization of a Deicing System for Small- and Medium-Sized Helicopters", Master's thesis, Technical University of Munich, 2018. Reference: [147]

LOEFFLER2018 Löffler, P., "Faltkonzepte für einen modularen lagerlosen 5-Blatt Hauptrotor", Master's thesis, Technical University of Munich, 2018. Reference: [103]

PIET2018 Piet, E., "Structural Evaluation and Optimization of the AREA RotorBlade", Semester thesis, Technical University of Munich, 2018. Reference [133]

BLAUT2018 Blaut, J., "Auslegung und Konstruktion eines verstellbaren Hubpropellers in Faserverbundbauweise für VTOL Fluggeräte", Master's thesis, Technical University of Munich, 2018. Reference: [24]

BEER2019 Beer, S.M., "Uncertainty Quantification of Composite Rotor Blade CrossSections", Semester thesis, Technical University of Munich, 2019. Reference: [16]

GRAF2019 Graf, S., "Mission and Performance Analysis of Landing Gears for the Helicopter EC135", Semester thesis, Technical University of Munich, 2019. Reference: [58]

ROTH2020 Roth, N., "Konzept und Konstruktion einer Auswuchtvorrichtung für Rotorblätter des Experimentellen Rotorprüfstandes MERIT", Bachelor's Thesis, Technical University of Munich 2020. Reference: [142]

GAUGELH.2020 Gaugelhofer, L., "Hybrid Experimental Measurement of Sectional Stiffness Properties of a Composite Rotor Blade with Digital Image Correlation", Master's thesis, Technical University of Munich, 2020. Reference: [54]